

---

# Synthetic Generation of Radar Sensor Data for Virtual Validation of Autonomous Driving

---

Vom Fachbereich Maschinenbau an der Technischen Universität Darmstadt  
zur Erlangung des akademischen Grades Doktor-Ingenieur (Dr.-Ing.)  
genehmigte Dissertation von Martin Friedrich Holder aus Heilbronn  
Tag der Einreichung: 10. November 2020, Tag der Prüfung: 20. Januar 2021

Referent: Prof. Dr. rer. nat. Hermann Winner  
Korreferent: Prof. Dr.-Ing. Erwin Biebl  
Darmstadt – D17

---



TECHNISCHE  
UNIVERSITÄT  
DARMSTADT



FAHRZEUGTECHNIK  
TU DARMSTADT

---

# Synthetic Generation of Radar Sensor Data for Virtual Validation of Autonomous Driving

genehmigte Dissertation von Martin Friedrich Holder

Referent: Prof. Dr. rer. nat. Hermann Winner

Korreferent: Prof. Dr.-Ing. Erwin Biebl

Tag der Einreichung: 10. November 2020

Tag der Prüfung: 20. Januar 2021

Darmstadt – D17

Bitte zitieren Sie dieses Dokument als:

URN: urn:nbn:de:tuda-tuprints-175450

URL: <http://tuprints.ulb.tu-darmstadt.de/17545>

Dieses Dokument wird bereitgestellt von tuprints,

E-Publishing-Service der TU Darmstadt

<http://tuprints.ulb.tu-darmstadt.de>

[tuprints@ulb.tu-darmstadt.de](mailto:tuprints@ulb.tu-darmstadt.de)

Die Veröffentlichung steht unter folgender Creative Commons Lizenz:

Namensnennung – Keine kommerzielle Nutzung – Keine Bearbeitung 4.0 International

<https://creativecommons.org/licenses/by-nc-nd/4.0/deed.de>

Für Frauke und Fritz



# Zusammenfassung

---

Trotz vielversprechenden Präsentationen von Entwicklungsfahrzeugen zum autonomen Fahren rückt in Folge der ersten Unfälle mit selbstfahrenden Autos die Bedeutung ihres Sicherheitsnachweises in den Fokus. Hierbei werden an virtuelle Fahrversuche als wirtschaftliche Alternative zum Realversuch hohe Erwartungen gestellt. Mit seiner Schlüsselposition in autonomen Fahrfunktionen stellt die Modellierung des Radarsensors eine besondere Herausforderung dar. Obwohl eine zunehmende Leistungsfähigkeit der Simulation festgestellt werden kann, fehlt ein systematischer Nachweis der Fidelität der Simulationsmodelle in Bezug auf die korrekte Abbildung radartypischer Anomalien sowie dem korrekten Verhalten von nachgelagerten Datenverbreitungsalgorithmen bei Stimulation mit synthetischen Daten.

Hierauf baut diese Dissertation auf: Zunächst werden aus gezielt durchgeführten Messungen Artefakte extrahiert und für die Relevanz in der Modellierung bewertet. Zur Generierung von synthetischen Radardaten aus einer 3D-Welt wird ein neues, auf Raytracing basierendes Verfahren vorgestellt, das spektrale Radardaten aus einem virtuellen 3D Umfeld unter Berücksichtigung von Mess-, Auflösungs- und Eindeutigkeitsbereichen generiert. Das als "Fouriertracing" bezeichnete Verfahren zeichnet sich dadurch aus, dass insbesondere mehrwegebedingte Artefakte abgebildet sind. Ein Standardsatz an Falsifikationsexperimenten zur Bewertung von Radarmodellen wurde erstellt und damit das entwickelte Fouriertracing Modell gegenüber anderen Modellierungsansätzen und Realdaten bewertet. Schwerpunkte stellen die Untersuchung der Mehrwegeausbreitung hinsichtlich Wellenüberlagerung, Sichtbarkeit verdeckter Objekte, Spiegelzielen und dem Verhalten eines Objekttrackingalgorithmus mit synthetischen Radardaten dar. Hierdurch gelingt es, Teilaspekte der untersuchten Modelle sowie der zugrundeliegenden Annahmen falsifizierbar zu machen und Gültigkeitsbereiche der Radarsimulation zu identifizieren.



# Abstract

---

The first accidents in otherwise promising deployments of autonomous driving fleets has underscored the importance of safety certification. Safety certification is expensive, especially when conducted via real-world driving. As such, high expectations are placed on virtual testing as an economic alternative. Autonomous driving functionality often relies heavily on radar sensors, but adequately modeling these radar sensors presents a particular challenge. While automotive simulation techniques have improved, there have yet to be systematic evaluations to prove that radar simulation models describe typical radar anomalies adequately such that downstream data processing algorithms behave correctly when operated with synthetic data.

This dissertation builds a series of contributions to address this need. First, sensing artifacts are extracted from targeted measurements and evaluated for modeling relevance. A new method based on ray tracing is presented that generates spectral radar data from a 3D virtual environment, while addressing measurement ranges, limited resolution, and unambiguous intervals. This method, called “Fourier tracing”, is of particular note in that it can model multipath related sensing artifacts. This dissertation presents a standard set of experiments for evaluating radar models and applies these to compare Fourier tracing to other modeling approaches using real radar data. The evaluation focuses on multipath propagation with respect to wave superposition, the visibility of occluded objects, on mirror targets, and on object tracking with synthetic data. The analysis makes it possible to falsify aspects of the examined radar sensor models, question their underlying assumptions, and to identify where these methods adequately simulate radar behavior.



# Contents

---

Symbols and Indices . . . . .	IX
List of Abbreviations . . . . .	XV
List of Figures . . . . .	XVIII
List of Tables . . . . .	XXII
<b>1. Introduction</b>	<b>1</b>
1.1. Motivation . . . . .	3
1.2. Thesis outline . . . . .	5
1.3. Terminology . . . . .	7
<b>2. Radar sensors from the modeling perspective</b>	<b>9</b>
2.1. A brief history of radar in automobiles . . . . .	9
2.2. Radar fundamentals . . . . .	10
2.2.1. Mathematical model of chirp sequence waveform with phased array antenna . . . . .	12
2.2.2. Resolution limits and unambiguous intervals . . . . .	14
2.2.3. Implications for radar sensor modeling . . . . .	14
2.3. State of the art in radar sensor modeling: What is missing in today's radar models? . . . . .	17
2.3.1. The role of "raw data" during signal and data processing of per- ception sensors . . . . .	17
2.3.2. Modeling terminology: Unmerging physics, phenomena, stochas- tic, and integration into the generic sensor modeling process . . . . .	20
2.3.3. Common variants of sensor models . . . . .	24
2.4. Conclusions from existing sensor models . . . . .	33
<b>3. What do we need in a radar simulation for virtual testing of AD?</b>	<b>37</b>
3.1. A methodological approach for deriving relevant features and test cases . . . . .	38
3.2. Research tools . . . . .	41

3.3. Application of artifact qualification method on the example of multipath propagation . . . . .	43
3.3.1. Impact on range and azimuth measurement . . . . .	44
3.3.2. Impact on Doppler measurement . . . . .	46
3.3.3. Wave superposition due to multipath propagation . . . . .	48
3.4. Multipath application case 1: Visibility of occluded objects . . . . .	51
3.4.1. Reference scenarios . . . . .	51
3.4.2. Observations from measurements . . . . .	52
3.4.3. Implications for modeling . . . . .	53
3.5. Multipath application case 2: Repeated reflections at sensor . . . . .	54
3.5.1. Reference scenario . . . . .	54
3.5.2. Observations from measurements . . . . .	55
3.5.3. Implications for modeling . . . . .	56
3.5.4. Falsification criteria . . . . .	56
3.6. Multipath application case 3: Horizontal reflections at guardrails . . . . .	58
3.6.1. Reference scenario . . . . .	58
3.6.2. Observations from measurements . . . . .	59
3.6.3. Implications for modeling . . . . .	59
3.6.4. Falsification criteria . . . . .	59
3.7. Multipath application case 4: Wave superposition patterns and shaking factor . . . . .	61
3.7.1. Reference scenarios . . . . .	61
3.7.2. Observation from measurements . . . . .	61
3.7.3. Implications for modeling . . . . .	68
3.7.4. Falsification criteria . . . . .	69
3.8. Intrinsic uncertainties, noise, and clutter . . . . .	70
3.8.1. Hardware parameters . . . . .	70
3.8.2. Noise of static objects . . . . .	71
3.8.3. Sensitivity of sub-bin estimation to SNR . . . . .	72
3.8.4. Clutter targets . . . . .	73
3.9. Extrinsic uncertainties . . . . .	76
3.9.1. Sensitivity of received power to vehicle body vibrations . . . . .	76
3.9.2. Noise effects due to unsteady movement of traffic . . . . .	77
3.10. Object tracking artifacts . . . . .	78
3.10.1. Reference scenario . . . . .	78
3.10.2. Observation from measurements . . . . .	78
3.10.3. Implications for modeling and falsification criteria . . . . .	79
3.11. Summary of the effects to be included in the radar simulation model . . . . .	80

---

<b>4. Fourier tracing: A new concept for synthetic radar data generation from virtual environments</b>	<b>83</b>
4.1. Assembling the radar simulation ecosystem . . . . .	83
4.2. Architecture of Fourier tracing . . . . .	86
4.2.1. Rendering step: Deriving $\delta$ -peaks from a 3D scene . . . . .	88
4.2.2. Radar cubic formation: Mapping of $\delta$ -peaks into the radar cubic . . . . .	92
4.2.3. Implementation details . . . . .	94
4.3. Parametrization and calibration . . . . .	103
4.3.1. Ray tracing parameters . . . . .	103
4.3.2. Sensor specific parameters . . . . .	104
4.3.3. Calibration of received power . . . . .	104
4.4. Verification . . . . .	106
4.4.1. Separability of point objects . . . . .	106
4.4.2. Separability of extended objects . . . . .	107
4.4.3. Masking weak objects . . . . .	108
4.4.4. Conservation of RCS profiles for calibration objects . . . . .	108
4.4.5. Propagation paths . . . . .	110
4.5. Assumptions for a tractable sensor simulation within currently available virtual environments . . . . .	111
4.5.1. Virtual scenery and 3D geometries . . . . .	111
4.5.2. Radar sensor . . . . .	114
4.6. Chapter conclusion: Generating spectral radar data with ray tracing . . . . .	115
<b>5. Radar sensor model test for falsification</b>	<b>117</b>
5.1. Wave propagation aspects . . . . .	119
5.1.1. Wave superposition pattern with CCR . . . . .	119
5.1.2. Shaking factor . . . . .	121
5.1.3. Relative velocity measurement under multipath propagation . . . . .	122
5.1.4. Repeated reflections . . . . .	125
5.2. Reflectivity behavior of geometries and materials . . . . .	127
5.2.1. Sensitivity of RCS to aspect angle . . . . .	127
5.2.2. Occluded objects . . . . .	132
5.2.3. Material properties: Opacity of glass . . . . .	133
5.3. Measurement uncertainties . . . . .	137
5.3.1. Noise in received power . . . . .	138
5.3.2. Range accuracy . . . . .	139
5.4. Interim conclusion: Revealed modeling errors . . . . .	141

5.5. Stimulation of object tracking with synthetic data . . . . .	143
5.5.1. Object tracking evaluation tools . . . . .	143
5.5.2. Slalom drive . . . . .	145
5.5.3. Car following and evasion . . . . .	148
5.5.4. Object separability . . . . .	150
5.6. Final remarks on object tracking with synthetic data . . . . .	152
<b>6. Conclusion</b>	<b>153</b>
6.1. Modeling scope . . . . .	153
6.2. Radar modeling . . . . .	155
6.3. Sensor model evaluation . . . . .	156
6.4. Recommendations for large-scale data acquisition for sensor models . . .	157
6.5. Further research directions . . . . .	158
<b>A. Appendix</b>	<b>161</b>
A.1. Estimating object height from wave superposition pattern . . . . .	161
A.2. Obtaining SNR . . . . .	162
A.3. 1-ECDF plots for shaking factor determination with different vehicles . .	163
A.4. Sensor model parameters . . . . .	164
A.5. Simulated RCS profiles of vehicles . . . . .	165
A.6. Calibration of the “Measurement2Sim” method . . . . .	169
A.7. Conditioning of ground truth . . . . .	173
A.8. Quadratic interpolation of spectral peaks . . . . .	174
<b>Bibliography</b>	<b>175</b>
<b>Own Publications</b>	<b>197</b>
<b>Supervised Student Theses</b>	<b>199</b>
<b>Danksagung</b>	<b>203</b>

---

## Symbols and Indices

---

### Latin Symbols

Symbol	Unit	Description
$A$	$m^2$	Area
$C$	-	Calibration value
$c$	$m/s$	Speed of light
$d$	$m$	Generic distance between elements
$\partial q$	$m$	Antenna element distance. $\partial q = \partial \Gamma \lambda$
$f$	$Hz$	Frequency
$h$	$m$	Object height
$I$	-	Upper limit of a counting index
$j$	-	Imaginary unit
$k$	-	Coefficient or dimensionless multiplier depending on index
$L$	-	Lens faktor
$\ell$	$m$	Path length of ray or wave
$l$	$m$	Object length
$n$	-	Surface normal vector (denoted $\mathbf{n}$ )
$P$	$W$	Power
$Q$	$dB$	Logarithmic measure for level
$R$	-	Coefficient of determination (denoted $R^2$ )
$\dot{r}$	$\frac{m}{s}$	Radial relative velocity of a point target. Also denoted as $v_r$
$r$	$m$	Range, or radial distance, from center of an antenna element to a (point) object.
$s$	-	Generic real valued array
$T$	$s$	Timespan or duration
$t$	$s$	Time
$U$	-	Signal strength
$V$	-	Shaking factor, defined as $V_{mp}^2$

## Contents

---

Symbol	Unit	Description
$v$	$\frac{\text{m}}{\text{s}}$	Velocity over ground
$W$	-	Window function
$x$	m	x dimension in cartesian frame (“longitudinal”)
$y$	m	y dimension in cartesian frame (“lateral”)
$z$	m	z dimension in cartesian frame (“height”)

## Greek Symbols

Symbol	Unit	Description
$\alpha$	rad	Angle between vectors as found by dot product
$F$	-	(Complex valued) spectrum
$\delta$	-	Dirac delta function
$\Delta$	-	Difference in a signal on same axis, not to confuse with resolution
$\xi$	-	Generic noise function
$\theta$	rad	Elevation (= vertical) angle between target and sensor center. $\theta > 0$ means upright. $\theta = \text{asin}(sz/sr)$
$\iota$	-	Counting index
$\lambda$	m	Wavelength
$\rho$	$1/\text{m}^2$	Hit density
$\sigma$	$\text{m}^2$	Radar Cross Section
$\varsigma$	-	Standard deviation
$\tau$	s	Delay time
$\partial\Gamma$	$\text{m} / \lambda$	Antenna element distance normalized w.r.t. wavelength
$\phi$	rad	Azimuth (= horizontal) angle between target and sensor center. $\phi > 0$ to the left. $\phi = \text{atan2}(sy/sx)$
$\varphi$	rad	Phase angle
$\psi$	rad	Yaw angle
$\omega$	rad/s	Circular frequency

## Indices

Symbol	Description
O	Normalized quantity
abs	Absolute value
add	Additional
$\phi$	Azimuth angle, used as index for $\phi$
B	Baseband, e.g. baseband frequency
b	Angle between outbound specular reflection and eye point
inci	Incidence angle
c	(Centered) carrier frequency of transmitted wave in the center of a chirp
ch	Chirp
diff	Diffuse
D	Doppler frequency
eff	Effective
exp	Exponential distribution
fp	Flat square plate
GT	Ground truth
inc	Increment
lognorm	Log-normal distribution
M	Index for duration of measurement frame, consisting of $I_v$ chirps
meas	Measured
mod	Modified
mp	Multipath
O	Point object
P	Index for duration of pause between two measurement cycles
r	Radial distance or direction, used as index for $r$
$v$	Radial (relative) velocity, used as index for $\dot{r}$
ref	Reference value
ray	Ray launched in simulation

<b>Symbol</b>	<b>Description</b>
rd	Reflection depth, i.e. number of ray interactions
R	Reflection coefficient of a surface
Rx	Received
s	Sampling frequency
S	Sensor
sim	Simulated quantity (used if accent is not available due to readability)
sm	Smoothness
spec	Specular
st	Start/beginning of an event
stat	Stationary
tilt	Tilted
Tx	Transmitted
UO	Unit object, i.e. an object with RCS = 1 m <sup>2</sup>

## Accents and highlighting

<b>Symbol</b>	<b>Description</b>
$\hat{\phantom{a}}$	Amplitude of a quantity in a transformed space
$\sim$	Estimated quantity
$\ddot{a}$	Second time derivative of $a$
$\dot{a}$	First time derivative of $a$
$\sim$	Simulated quantity
$\top$	Vector/matrix transpose
<b>v</b>	Bold indicates a vector valued quantity
<i>f</i>	Italic denotes a variable quantity
$k$	No highlighting indicates a scalar valued quantity
c	Upright denotes a constant quantity

## Transformations and operators

Symbol	Description
*	Convolution
$\langle \mathbf{a}, \mathbf{b} \rangle$	Dot product of vectors $\mathbf{a}$ and $\mathbf{b}$
$\mathcal{F}$	Fourier transform: $\mathcal{F}\{\cdot\}$
$\max(\cdot)$	Maximum operator
$\bar{\mathbf{a}}$	Mean value of vector $\mathbf{a}$
$\min(\cdot)$	Minimum operator
$\propto$	Proportionality symbol
$\square$	Rectangular function: $\square(\cdot)$

## Calligraphic and fraktur symbols

Symbol	Description
$\partial$	Symbol for resolution operator
$\mathcal{G}$	Total amplification of a MIMO antenna array
$\mathfrak{h}$	Hit point as reported by the ray tracer
$\mathcal{N}$	Normal distribution of a random variable
$\mathcal{O}$	Object state vector
$\mathcal{P}$	Probabiliy
$\mathfrak{r}$	Ray direction vector
$\mathcal{U}$	Uniform distribution of a random variable

## Coordinate system notation

$$\text{CoordinateSystem } X_{\text{Index}}^{\text{Exponent}}$$

### Used coordinate systems

Ego: Centered to rear axle, ground level

Sensor (S): Centered to sensor

OOI: Centered to object of interest (OOI), rear axle, ground level

G: Global coordinate system, e.g. centered to the origin of the (virtual) world

## List of Abbreviations

---

ACC	adaptive cruise control
AD	automated or autonomous driving
ADAS	advanced driver assistance systems
ADC	analog-to-digital converter
ADMA	automotive dynamic motion analyzer
AEB	automatic emergency braking
APE	absolute pose error
BRDF	bidirectional reflectance distribution function
CCR	corner cube reflector
CDF	cumulative distribution function
CEM	computational electromagnetics
CFAR	constant false alarm rate
COST	european cooperation in science and technology
CPU	central processing unit
DD	direct-direct multipath combination
deg	degree of arc
DFT	discrete Fourier transformation
DI	direct-indirect multipath combination
ECDF	empirical cumulative distribution function
EM	electromagnetism
EMC	electromagnetic compatibility
ESC	electronic stability control
FFT	fast Fourier transformation
FIR	finite impulse response
FM	frequency modulated
FS	far scan
FT	Fourier tracing

GNSS	global navigation satellite system
GOSPA	generalized optimal subpattern assignment
GPU	graphics processing unit
GT	ground truth
ID	indirect-direct multipath combination
II	indirect-indirect multipath combination
ISO	International Organization for Standardization
KPI	key performance indicator
LoS	line of sight
MIMO	multiple-input and multiple-output
MLE	maximum likelihood estimation
NS	near scan
ODD	operational design domain
OOI	object of interest
OSI	open simulation interface
OSPA	optimal subpattern assignment
PBR	physically based rendering
PCB	printed circuit board
PDF	probability density function
QIFFT	quadratically interpolated FFT
radar	radio detection and ranging
RAM	radiation-absorbent material
RANSAC	random sample consensus
RCS	radar cross section
RGB	red green blue color model
RINEX	receiver independent exchange format
RQ	research question
RSI	raw signal interface
RTK	real-time kinematic positioning

SiL	software in the loop
SLAM	simultaneous localization and mapping
SNP	spectral noise power density
SNR	signal-to-noise ratio
STFT	short time Fourier transformation
SUT	system under test
ToF	time of flight
ULA	uniform linear array
UTD	uniform geometrical theory of diffraction
VRU	vulnerable road users
VTD	Vires Virtual Test Drive



# List of Figures

---

1.1. Thesis organization and research questions . . . . .	6
1.2. Contextualizing of terminology used in this dissertation . . . . .	7
2.1. Chirp sequence waveform . . . . .	11
2.2. Differentiation of terms in relation to sensor data in the context of radar	18
2.3. Generic components of the modeling and simulation process . . . . .	21
2.4. Scattering center reflection model . . . . .	28
3.1. Test equipment used in this thesis. . . . .	41
3.2. Three cases of false targets originating from reflections of off guardrails .	43
3.3. Range and Doppler distortion under multipath propagation . . . . .	47
3.4. Vertical multipath propagation with a CCR . . . . .	49
3.5. Multipath wave superposition pattern . . . . .	50
3.6. Occlusion reference scenarios . . . . .	51
3.7. SNR for occluded VW Crafter . . . . .	52
3.8. RCS over distance for scenario 2 . . . . .	52
3.9. Idealized ray path with specular reflection off the road . . . . .	53
3.10. Reference scenario 3: Repeated reflections at sensor . . . . .	54
3.11. Range and radial velocity for accelerating mirror target. . . . .	55
3.12. Statistical analysis of mirror targets . . . . .	57
3.13. Typical scenario on German motorways with guardrails on both sides. . .	58
3.14. Mirror targets on guardrails induced by multipath propagation . . . . .	60
3.15. Illustration of scenarios 4-6 for quantification of shaking factor . . . . .	62
3.16. Height estimation of CCR based on the Diewald/Schneider method . . .	62
3.17. RCS behavior over time in dynamic scenario . . . . .	63
3.18. Height spectrum for dynamic and static scenario . . . . .	66
3.19. Measurement data in log(1-ECDF) representation . . . . .	67
3.20. Limited repeatability of experiments involving extended objects . . . . .	68
3.21. RCS noise fluctuation of static objects . . . . .	71
3.22. Sensitivity of Doppler measurement under different SNR conditions. . .	72

3.23. Probability distribution of clutter targets . . . . .	74
3.24. Clutter targets under different weather conditions . . . . .	75
3.25. Extrinsic uncertainties during radar measurements . . . . .	76
3.26. Object tracking artifacts . . . . .	79
4.1. Sensor simulation architecture . . . . .	86
4.2. Flowchart of the ray tracing portion in Fourier tracing . . . . .	91
4.3. Illustration of complex addition mechanism . . . . .	93
4.4. Introduction of jitter on angular increments between rays . . . . .	94
4.5. Distance between two hit points with different ray increments . . . . .	95
4.6. Parallel incidence of rays on a flat plate in the far field . . . . .	96
4.7. Illustration of the aliasing problem in radar . . . . .	97
4.8. Depiction of the inverse distance law . . . . .	99
4.9. Notation of $\alpha_b$ . . . . .	100
4.10. Adaption of Phong model as lens factor . . . . .	101
4.11. Separability of point objects . . . . .	106
4.12. Separability of extended objects . . . . .	107
4.13. Masking of two objects . . . . .	108
4.14. RCS profile of flat plate obtained in simulation . . . . .	109
4.15. Visualization of hit points for a trihedral CCR obtained by ray tracing . . . . .	110
4.16. Material segmentation and simulated radar reflectivity . . . . .	113
4.17. Reflective plate at the ego vehicle to facilitate repeated reflections. . . . .	113
5.1. CCR height estimation in simulation and measurement . . . . .	120
5.2. 1-ECDF plot of simulated RCS quantities . . . . .	122
5.3. Range-Doppler plot with simulated quantities . . . . .	124
5.4. Repeated path scenario in simulation . . . . .	126
5.5. Example of a box-shaped panel van and its 3D models . . . . .	128
5.6. RCS profiles of vehicles obtained with Fourier tracing and CarMaker . . . . .	129
5.7. Illustration of the slalom drive . . . . .	130
5.8. Results of slalom drive in measurement and simulation . . . . .	131
5.9. SNR of hidden VW Crafter . . . . .	132
5.10. Experiment setup for studying opacity of glass . . . . .	133
5.11. Measurement results for opacity of glass experiment . . . . .	135
5.12. Range accuracy considering two vehicles . . . . .	136
5.13. Range accuracy in simulation . . . . .	136
5.14. Noise fluctuation range of static objects . . . . .	138
5.15. Range accuracy in measurement and simulation . . . . .	140

---

5.16. Lateral velocity over time (left) and as spectrum (right). . . . .	145
5.17. Scatter plots for visualization of tracking performance in slalom scenario	147
5.18. Car following and evasion scenario for object tracking evaluation. . . . .	148
5.19. Tracking of occluded object . . . . .	149
5.20. Illustration of object separability test scenario . . . . .	150
5.21. Targets and objects obtained in simulation and measurement . . . . .	150
5.22. Qualitative results of object separability experiment . . . . .	151
A.1. RCS fluctuation in (1-ECDF) representation . . . . .	163
A.2. BMW G30 (“BMW 5 Series”). . . . .	165
A.3. Mercedes Benz W222 (“S-Class”). . . . .	166
A.4. Chevrolet Silverado. . . . .	167
A.5. Mercedes Benz W447 (“Vito”). . . . .	168
A.6. Signal reading during calibration . . . . .	171
A.7. Geometric relationships for ground truth conditioning . . . . .	173
A.8. Illustration of parabolic peak interpolation . . . . .	174



# List of Tables

---

- 2.1. Overview of radar sensor models known from literature . . . . . 36
- 3.1. Parameters of the radar sensor used within this thesis . . . . . 42
- 3.2. MLE estimates for distribution fits . . . . . 65
- 5.1. Results of testing the Fourier tracing radar model for falsification . . . . 142
- 5.2. Quantitative tracking results from slalom drive scenario . . . . . 146
- 5.3. Quantitative tracking results in quasi-stationary scenario . . . . . 149
- A.1. Sensor model parameters . . . . . 164
- A.2. Calibration values of “Measurement2Sim” method . . . . . 171



# 1. Introduction

---

“Are we ready for autonomous driving?”<sup>1</sup>. This question is the headline of the scientific publication introducing the KITTI dataset in 2012, the most cited database of lidar and camera data to benchmark perception algorithms for autonomous driving functions to date. As of today, we see more than 400 companies and research institutes across 15 sectors working on the development of autonomous vehicles.<sup>2</sup> The increasing number of prototypes deployed in public roads solidifies the impression that technological challenges around the development of automated or autonomous driving (AD) systems have essentially been resolved. What remains as an unresolved challenge so far is proving safety of a self-driving car: Over the course of the first accidents with self-driving vehicles, the importance of safety certification has once again been pushed to the forefront of public and technological discussion. This is also one of the reasons for adjusting the timelines for market entry and full availability of this new technology to customers.

System testing and safety validation by means of real-world test drives, as it is done with driver assistance systems, has proven to be not feasible for driver assistance systems with level of automation three and higher.<sup>3</sup> Therefore, virtual test methods are expected to facilitate the release of automated driving. Compared to tests in real-world, virtual test drives offer a number of advantages. On the one hand, the controllability of all environmental conditions enables tests to be performed with full reproducibility. On the other hand, a large number of test variants can also be examined in a time and cost efficient and environmentally friendly manner.

Using virtual testing methods is not new in the automotive industry. For example, guidelines such as U.S. Federal Motor Vehicle Safety Standard 126 on braking systems provides a combination of real-world tests and simulations for the homogenization process of electronic stability control (ESC) systems with pre-defined maneuvers.<sup>4</sup> However, no experience is available for the use of virtual test methods in safety validation and

---

<sup>1</sup> Geiger, A. et al.: Are we ready for Autonomous Driving? The KITTI Vision Benchmark Suite (2012).

<sup>2</sup> Orsay Consulting: The Autonomous Vehicles Landscape (2020).

<sup>3</sup> Wachenfeld, W.; Winner, H.: The Release of Autonomous Vehicles (2016), p. 442.

<sup>4</sup> Lutz, A. et al.: Simulation methods supporting homologation of Electronic Stability Control (2017).

certification for the release of AD systems. In this course, publicly funded research projects, such as PEGASUS, ENABLE-S3 and SET Level 4to5, focus on enhancing virtual test methods.

When simulating an AD system, regardless of its level of automation, the focus is not only on the vehicle equipped with AD functionality. It is a matter of representing the traffic situation around the vehicle and the perception by the sensors in the simulation. For conducting meaningful virtual test drives in a simulation environment, synthetic sensor data with a high level of fidelity, which is an abstract measure for the confidence in the simulation result, is required. Apart from synthetic sensor data, the tool chain for virtual testing must cover additional aspects: A comprehensive road description format that allows for arbitrary road configurations with definitions of road geometry, various types of lanes, junctions, logical inter-connection of lanes, roads, and road-side objects. For the former there are open standards such as OpenDRIVE<sup>5</sup> and Lanelet2<sup>6</sup> and road surface properties are defined by the OpenCRG standard<sup>7</sup>. Universal scenario description languages such as OpenSCENARIO<sup>8</sup> and M-SDL<sup>9</sup> describe the dynamic content of scenarios, such as maneuvers, driver actions, as well as the behavior of other traffic participants. For sensor simulation, open simulation interface (OSI)<sup>10</sup> transfers ongoing sensor interface activities<sup>11</sup> to virtual environments.

Radar sensors play a prominent role in the perception system of autonomous cars<sup>12</sup> due to their robustness against adverse weather conditions and their ability to measure radial velocity with high accuracy. During its first automotive use for adaptive cruise control (ACC) applications, object detection was of major interest. Recent developments of radar sensors towards higher resolutions enable their deployment for scene understanding applications<sup>13</sup> such as mapping<sup>14</sup>, localization<sup>15</sup>, as well as semantic segmentation<sup>16</sup>.

---

<sup>5</sup> ASAM: OpenDRIVE (2020).

<sup>6</sup> Poggenhans, F. et al.: Lanelet2 (2018).

<sup>7</sup> ASAM: OpenCRG (2020).

<sup>8</sup> ASAM: OpenSCENARIO (2020).

<sup>9</sup> Hollander, Y.: Foretellix Blog: M-SDL, the autonomous vehicles verification language (2020).

<sup>10</sup> Hanke, T. et al.: Open Simulation Interface (2017).

<sup>11</sup> International Organization for Standardization: ISO23150 (2019).

<sup>12</sup> Dickmann, J. et al.: Radar for Autonomous Driving (2019), p. 121.

<sup>13</sup> Schumann, O. et al.: Scene Understanding with Automotive Radar (2019).

<sup>14</sup> Weston, R. et al.: Probably Unknown: Deep Inverse Sensor Modelling Radar (2019).

<sup>15</sup> Adams, M.: Robotic Navigation and Mapping with Radar (2012).

<sup>16</sup> Schumann, O. et al.: Semantic Segmentation on Radar Point Clouds (2018).

## 1.1. Motivation

---

Generating synthetic radar data from a virtual environment by means of a sensor model is associated with several scientific challenges and is subject of this dissertation. Modeling a radar sensor is particularly challenging due to the complexity of its measurement principle and the interaction of electromagnetic waves, emitted and received by the radar, with the environment. Although sensor data is obtained in real-world tests with the highest fidelity, the feasible test coverage in a measurement series remains limited. It is not possible to conduct driving tests on a test site for an unlimited number of scenario combinations. Offline replay of recorded measurement data and its aggregation into large measurement databases provides an established basis for the development and benchmarking of signal and data processing algorithms, as done with sensor data sets such as KITTI. Recorded sensor data is, however, not suitable for discussing modifications of the sensor setup. Only limited statements can be made about the impact of changing the sensor setup or mounting positions. Also, it will never be possible to gather the so-called “ground truth” in real-world in the same accuracy as it is available in a simulation environment. Conducting virtual test drives in a simulations allows an unlimited variety of combinations and thus performing every imaginable tests. When testing AD systems, however, a valid sensor simulation model is a prerequisite for meaningful tests.

Simulation of radar sensors poses several technological and scientific challenges. For visual wavelength, a rich body of rendering methods that build upon red green blue color model (RGB) textures attached to 3D models exist. Photorealistic rendering methods using ray tracing algorithms allow to synthesize realistic appearing images and are used for simulation of cameras, including their imagers and lenses. At millimeter wavelengths, as employed in automotive radar, the powerful methods available in the field of image synthesis cannot be applied directly. This is due to two aspects: First, the measurement principle of a radar uses the time-of-flight measurement of a modulated electromagnetic wave rather than measuring light intensity as an image sensor in cameras does. On the other hand, the reflectivity of objects also depends on their materials, surface characteristics and aspect angle, and is thus sensitive to different wavelengths. As a rough tendency, it can be said that electrically conductive materials such as metals generally show good reflection properties for radar. If the irradiated surface is inclined, however, the incident wave can be almost completely reflected away in the worst case.

The complexity of radar sensors involves antenna gains, high-frequency circuits and signal processing, and the interaction between the electromagnetic wave and reflecting matter. Developing a simulation model therefore requires an approach to derive the necessary modeling scope to obtain a computationally feasible simulation model while

preserving its validity for the simulation task. Already with the understanding of the physical functionality of a radar sensor, first conclusions about a minimal number of features of the model can be drawn. For example, the resolution and unambiguous intervals result from respective signal processing parameters of the radar. This motivates the use of physically inspired modeling methods.

To date, neither simulation methods for radar sensors that consistently provide realistic results nor methods for evaluating the quality of synthetic data exist. One reason lies in the sensor data reported by radar: Unlike lidar and camera, which have a point-cloud or RGB image as de-facto standard, no such common representation exists for radar sensors. In addition, radar sensor data is notoriously difficult to interpret due to the presence of measurement artifacts caused by multipath propagation, ambiguities, and other factors. This complicates the comparison between real and synthetic sensor data. For a simulation model, this would require a universal representation of sensor data, that is appropriate for all radar sensors and can be addressed by both the real sensor and a simulation model.

In the sense of the famous aphorism of George Box “all models are wrong”<sup>17</sup>, it is to note that it will not be possible to create a simulation model that generates valid data under all circumstances. For this reason, it is even more important to rigorously test the simulation model to verify model assumptions and simplifications in the context of the intended use of the model. The validity ranges of hypotheses about the expected simulation result can be identified by rigorous and targeted tests for falsification. Because discrepancies between reality and simulation are always found at the microscopic level, their consequences must be investigated. For example, if a subsequent data processing algorithm draws the same conclusions from the measured data and synthetic data in the same scenario, the model cannot be proven invalid. This would provide a certificate of fidelity of the model and qualify it for use in virtual tests of AD.

---

<sup>17</sup> Box, G. E. P.: Robustness in the Strategy of Scientific Model Building (1979).

## 1.2. Thesis outline

---

The overview of the state of the art and research in **chapter 2** shows that a large number of approaches for radar simulation for various application purposes already exist. Initial conclusions about the requirements for a simulation model are drawn from the understanding of the operation of radar sensors and its physical relationships. The first research question states as: **RQ1: *What is necessary for an automotive radar simulation and what is not available from existing models?*** The objective is to analyze the current state of the art and to investigate which aspects are not fulfilled by currently available radar models.

Simulation models are a simplified representation of reality and, as indicated, modeling of radar sensors can become arbitrarily complex w.r.t. the underlying physics. Therefore, **chapter 3** investigates definitions, requirements, and test criteria for a tractable radar simulation for virtual validation of AD. This is the basis for **RQ2: *What are the relevant features for the virtual test of AD that a radar simulation must demonstrate?***

As relevant features are found, it is of interest to analyze a model's ability to correctly render them. Such test criteria are the subject of **RQ3: *How are the relevant characteristics defined and what are the requirements and test criteria for modeling?***

With the understanding of the required modeling scope developed, a novel concept for synthesizing radar data from currently available virtual environments is shown in **chapter 4**. Therefore, research question 4 is stated as: **RQ4: *How can one use ray tracing to generate spectral radar data?***

**Chapter 5** presents a benchmark that contains model tests for falsification of assumptions and design choices made during the development of the model. The sensor model developed in chapter 4 is compared to measured data and a commercially available radar simulation model that represents the state of the art in radar sensor modeling. The goal is to answer **RQ5: *Which requirements are not fulfilled by Fourier tracing?*** For this purpose, test cases developed in chapter 3 are used for identification and quantification of modeling errors.

With the awareness that errors are present in the sensor model, the practical impact of model deviations in sensor data processing for autonomous driving functions is investigated. On the example of object tracking, the sensitivity of the resulting deviations to modeling errors is examined and **RQ6: *What is the sensitivity of an object tracking algorithm to deviations between simulation and measurements?*** is studied.

**Chapter 6** summaries the achieved results and gives an outlook on future research directions.

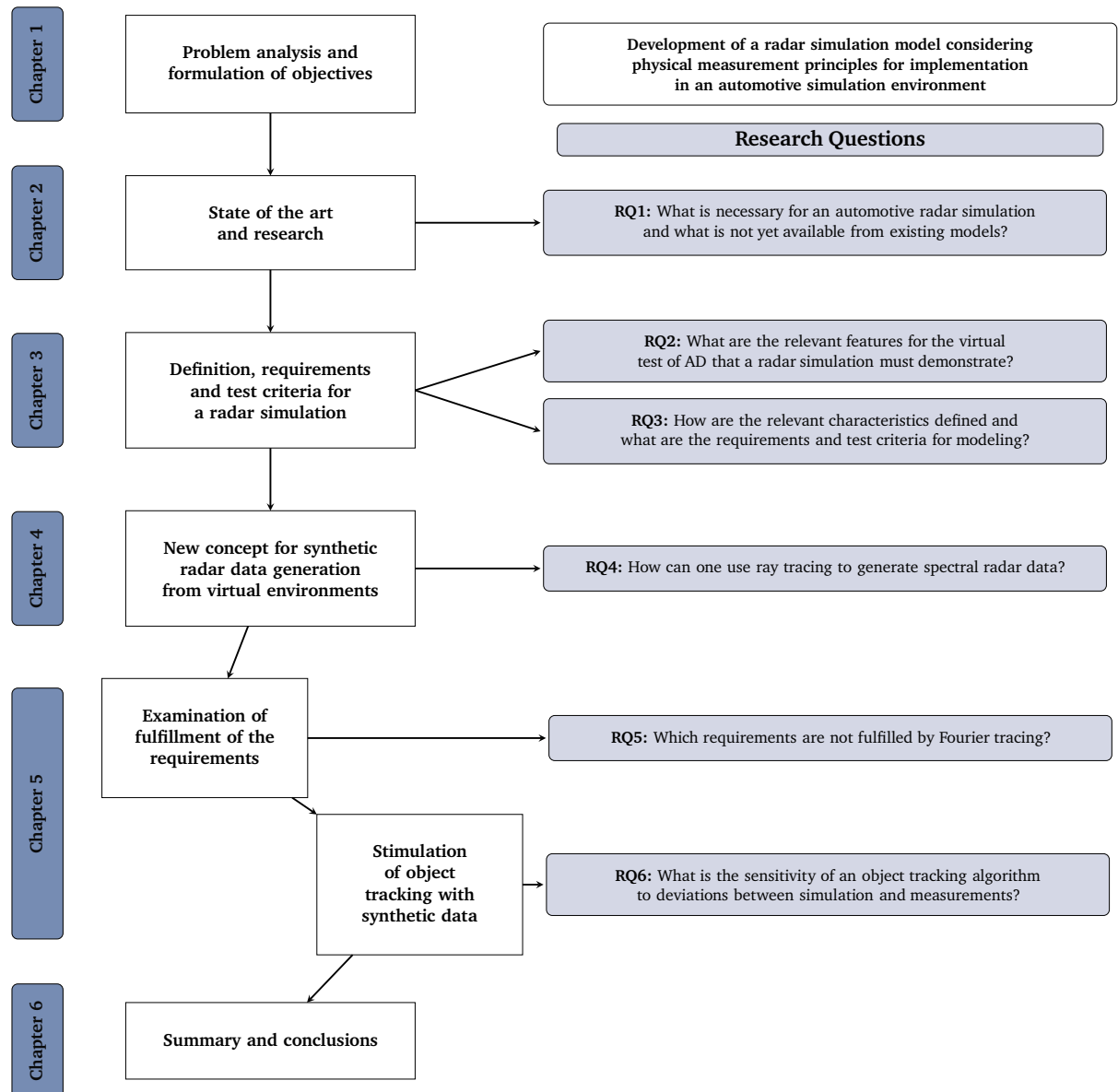


Figure 1.1.: Thesis organization and research questions

## 1.3. Terminology

Frequently used terms in this dissertation are defined in this subsection. They are contextualized against the background of simulation and virtual test drives in figure 1.2.

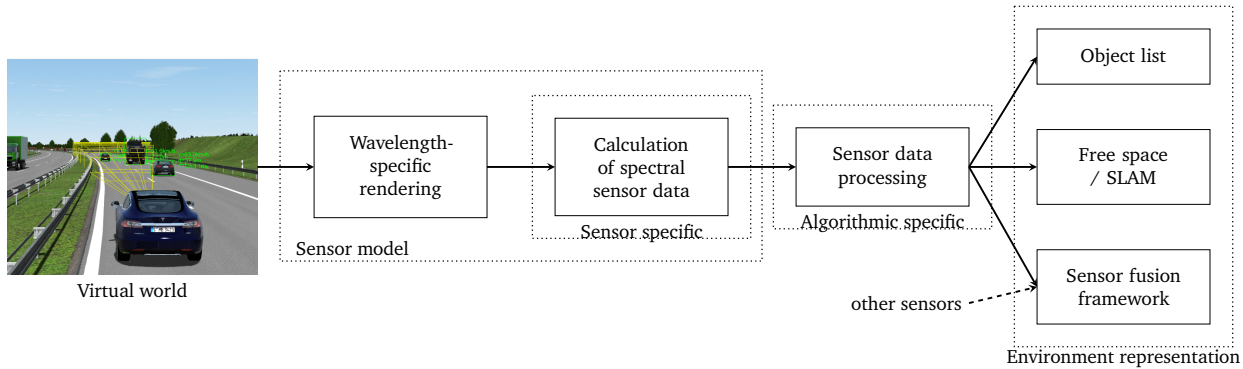


Figure 1.2.: Contextualizing of terminology used in this dissertation

**Sensor:** Unless stated otherwise, sensors in this dissertation are understood as perception sensors such as radar, lidar, and camera. If the term “sensor” is used, this refers to a radar sensor.

**Sensor model:** A sensor model is a mathematical model that gives an approximation of the measurement principle of the sensor. It simulates the output signals of a sensor for a given input. As soon as the output of the sensor model also includes processed data, the term becomes fuzzy: Separation between the model for the sensor measurement principle and the sensor data processing becomes indistinct. In the context of this dissertation, it is therefore defined that the output of the sensor represents spectral sensor data without further processing.

**Sensor data:** This refers to a measurable data stream of a sensor. It can include the initial measurable digitized analog signal, transformed data (e.g. spectral data) up to processed data, which is e.g. an object list. Sensor data is characterized by the fact that it depends on the specification of the sensor and deviations from ground truth are present, even if these can be minimal for reference sensors.

**Ground truth:** As the name implies, this is the true value of a quantity. Whether this can be determined in reality is debatable: Even with highly precise measurement technology, a measurement uncertainty (e.g. due to measurement noise) and thus a deviation from the true value will remain. In simulation, theoretically all quantities can be retrieved. In the simulation software, this is not done via a sensor, but by accessing

variables stored in internal data structures.

**Sensor simulation:** The term sensor simulation describes the process of generating synthetic sensor data using a sensor model. Synthetic sensor data can be used to stimulate a sensor data processing algorithm. A sensor simulation consists of a sensor model along with corresponding parameters and is executed in a virtual environment.

**Synthetic data:** Synthetic data refers to all data generated from a simulation environment. Within this dissertation, quantities generated by a simulation model are understood as synthetic data and are marked with  $\sim$ .

**Object:** An object is an object present in road traffic. This can be a car, vulnerable road users (VRU), or some other arbitrary object such as a reference reflector. Its perception for a sensor depends on its properties (e.g. material, size) and its position relative to the sensor and other objects.

**Object list:** An object list contains measured or estimated information about position, length, width, height, class, and other sensor-specific quantities such as a measure of signal intensity for each object. In simulation, it is available from ground truth. In measurement, it is obtained from a tracking filter and includes all objects identified by the filter. Since the information from the measurements is constantly updated, the content varies between time steps.

**Object of interest:** In the vicinity of the vehicle there is often a large number of objects, only a small number of which are of immediate relevance. One of the number of objects that is of particular interest for a more detailed analysis is called object of interest (OOI).

**Environment representation:** The autonomous vehicle arranges the collected sensor data of its environment in such a way that its perception system can draw conclusions on how to safely navigate through its environment. This is done by using object lists, free space information, map knowledge, and self-localization (e.g., simultaneous localization and mapping (SLAM)). By fusing with other sensors, sensor data can be combined in complementary ways.

**Rendering:** Rendering is the generation of information perceptible to the sensor from a virtual scenery. This can have different degrees of abstraction: It ranges from simple state vectors of objects from which, for example, contours can be extracted up to high-definition 3D objects with corresponding material allocation. Rendering is wavelength-dependent to account for the measurement principle of the sensor technology. For radar sensors, for example, metallic objects usually have a high reflectivity, while their color plays a subordinate role.

**Ego vehicle:** This refers to the vehicle on which the sensor to be simulated is located. It is also referred to as only “ego”.

## 2. Radar sensors from the modeling perspective

---

In the first part of this chapter, automotive radar sensors are reviewed with a focus on modeling and simulation. According to the radar's physical measurement principle, its performance parameters are derived. The second part contains a literature review of existing radar sensor models and modeling approaches. These sensor models are organized with regard to their input and output data and representation of sensing and measurement errors. Given the model description, it is analyzed which features of a radar simulation are covered by the respective model.

The chapter concludes by deriving a list of deficits of current models and addresses **RQ1**: *What is necessary for an automotive radar simulation and what is not yet available from existing models?*

---

### 2.1. A brief history of radar in automobiles

---

Radar is short for **radio detection and ranging**. Originally invented by the German inventor Christian Hülsmeyer as a device for detection of metallic objects<sup>18</sup> it was termed as telemobiloscope. The usability of radar sensors in automotive applications was first described in Germany in the middle of the 20th century.<sup>19</sup> Although its use as a distance warning system was already reported in the 1980s<sup>20</sup>, another 20 years of research and development passed before it went into series production in 1998 in the Mercedes-Benz S-Class<sup>21</sup> as adaptive cruise control (ACC) and branded as “Distronic”. First and early prototypes of automotive radar used frequencies at 10 or 35 GHz.<sup>22</sup> Today, the frequency

---

<sup>18</sup> Hülsmeyer, C.: Verfahren um metallische Gegenstände mittels elektrischer Wellen zu melden (1904).

<sup>19</sup> Fonck, K.: Radar bremsst bei Gefahr (1955).

<sup>20</sup> Ackermann, F.: Abstandsregelung mit Radar (1980).

<sup>21</sup> Automobil-Entwicklung: David und die Goliaths: Simultaneous Engineering (1999).

<sup>22</sup> Meinel, H. H.; Bösch, W.: Radar Sensors in Cars (2016).

band between 76 and 81 GHz is globally available for automotive radar<sup>23a</sup> and consistently used for today's series production radars. Current research trends aim at higher resolution, which traditionally balances cost and package size. While advanced driver assistance systems (ADAS) applications such as ACC require range resolutions within meter ranges<sup>24</sup>, today, advances in semiconductor technology and signal modulation allow cm-resolution in range<sup>25,26</sup>, increased angular resolution, and elevation measurement capability<sup>27</sup>.

---

### 2.2. Radar fundamentals

---

Measurements with radar build upon obtaining phase shifts during the round-trip time i.e. the time of flight (ToF) of an electromagnetic wave transmitted into the scenery and received by the receiving antenna elements. Therefore, it is necessary that the emitted wave is reflected in such a way that it can be received again by the sensor. The reflectivity of a geometry w.r.t. wavelength must be sufficiently high to distinguish the signal strength that is received by the radar from its noise level and ground clutter. Also, electromagnetic waves propagate in the air at a constant speed, which can be approximated by the speed of light.

Today's automotive radar systems are so-called frequency modulated (FM) radars, whereby the transmission frequency is modulated linearly in time. The formerly widely used "slow ramps" method has been almost completely replaced by the chirp sequence waveform. In chirp sequence radars, the transmitted signal consists of a sequence of identical linear frequency ramps, see figure 2.1. The radar equation given in eq. 2.1 describes the relation between transmitted and received power denoted as  $P_{Tx}$  and  $P_{Rx}$ , respectively. It combines factors that influence the received power for a given wavelength  $\lambda$ . The proportionality with the radial distance from the sensor  $s_r$  results from the fact that the wave propagates as an isotropic radiator in all directions for the incoming and outgoing directions. The total gain of a multiple-input and multiple-output (MIMO) antenna array introduces  $\mathcal{G}$  and gives a higher power density for certain directions of the radar wave. It combines the antenna gain of the transmitting or receiving portion

---

<sup>23</sup> Winner, H.: Automotive RADAR (2015). a: p. 371; b: p. 331; d: p. 354.; c: pp. 354-367.

<sup>24</sup> Abou-Jaoude, R.: ACC Radar Sensor Technology, Test Requirements, and Test Solutions (2003).

<sup>25</sup> Fleming, B.: Recent Advancement in Automotive Radar Systems (2012).

<sup>26</sup> Hasch, J.: Driving towards 2020: Automotive Radar Technology Trends (2015).

<sup>27</sup> Brisken, S. et al.: Elevation Estimation with a High Resolution Automotive Radar (2019).

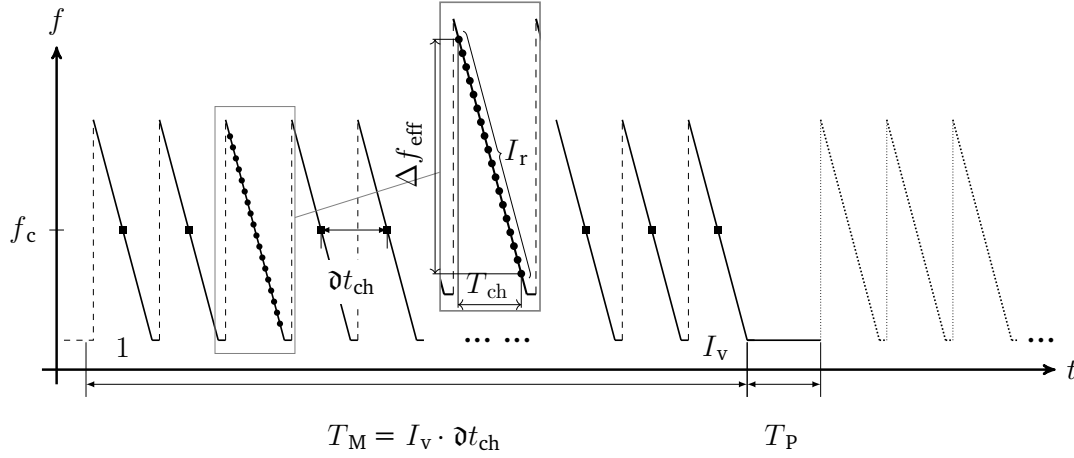


Figure 2.1.: The chirp sequence waveform comprising  $I_v$  chirps, effective sweep bandwidth  $\Delta f_{eff}$  centered around carrier frequency  $f_c$ , chirp duration  $\delta t_{ch}$ , total sequence duration  $T_M$ , and  $T_P$  as period between two adjacent chirp sequence cycles. Sampling each chirp renders in  $I_r$  samples per chirp, where the transient region and beginning and end portion of the chirp is neglected for avoiding side-effects. Note that  $\delta t_{ch} = T_M / I_v > T_{ch}$ .

of the antenna, which are given as separate factors in the otherwise standard notation of the radar equation. The size of the reflective object is governed by its radar cross section (RCS)  $\sigma$ , which indicates its reflectivity. It is depended on the object's materials, size, shape, and wavelength. Winner<sup>23b</sup> extends the traditional radar equation by a shaking factor  $V_{mp}^2$  that considers fluctuations in received power due to multipath wave superposition effects that potentially cause significant distortions.

$$\frac{P_{Rx}}{P_{Tx}} = \frac{\sigma \lambda^2 \mathcal{G}}{(4\pi)^3 s r^4} \cdot V_{mp}^2 \quad (2.1)$$

The statements and derivations in the following paragraph focus on chirp sequence radars with a patch antenna array that comprises  $I_\phi$  equally spaced receiving antenna elements in the lateral direction organized as uniform linear array (ULA). This combination constitutes the current state of the art in automotive radars. A detailed overview of alternative concepts is given by Winner<sup>23c</sup>.

### 2.2.1. Mathematical model of chirp sequence waveform with phased array antenna

A mathematical data model for automotive radar based on the derivations outlined by Engels<sup>28a</sup> is used in the following. The comprehensive derivations of the governing equations are condensed to key aspects that focus on outlining the measurement principle for range, range rate, and azimuth angle along with respective resolution and ambiguity limitations. The nomenclature is adapted to this dissertation.

In the chirp sequence waveform, the radar transmits a linear frequency modulated signal for each of the  $I_v$  chirps over his  $I_\phi$  antenna elements starting at  $t_{st}$ .

$$\sum_{\iota_v=1}^{I_v} \square \left( \frac{(t - t_{st}) - \mathfrak{d}t_{ch} \iota_v}{T_M} \right) \cos [2\pi\varphi((t - t_{st}) - \mathfrak{d}t_{ch} \iota_v)] \quad (2.2)$$

where  $\square$  is the rectangular function and the instantaneous phase is given by

$$\varphi(t - t_{st}) = \left( f_c + \frac{\Delta f_{eff}}{2T_{ch}} (t - t_{st}) \right) \quad (2.3)$$

The received signal observed at each antenna element is a time-delayed instance of the transmitted signal, which is subject to the Doppler effect due to relative motion in radial direction to the sensor. Radial distance, radial velocity, and azimuth angle to an object determines a corresponding phase shift.

Range information is encoded in the time offset of the “ramp height” between the transmitted and received wave. This information is basically identical for all ramps, so that the information of a single frequency ramp would be sufficient for the distance measurement. However, due to a relative movement of the object w.r.t. the sensor, the Doppler effect causes changes in the phase position of the received wave. Thus, the phase position is proportional to the radial velocity of the object. In the following, radial velocity is also referred to as range rate.

Angular measurement is based on the fact that the reflected wave hits each of the horizontally arranged receiving antenna elements with a time offset. The resulting phase offset is proportional to the sine of azimuth angle. If an antenna array is also arranged vertically, an elevation measuring capability can be obtained.<sup>29</sup> The proceeding is then similar to the azimuth measurement, since the phase differences between the antenna elements are again proportional to the elevation angle.

---

<sup>28</sup> Engels, F.: Multidimensional Frequency Estimation in Automotive Radar (2016). a: pp. 71-83; b: p. 77.

<sup>29</sup> Wintermantel, M.: Radar system with elevation measuring capability (2013).

After mixing and low-pass filtering, the baseband signal available from each antenna can be obtained. Commonly, a number of neglects are made for simplification<sup>28b</sup>: Radial velocity of objects satisfies  $\dot{r} \ll c$ , range-Doppler coupling within one measurement cycle is neglectable small, i.e.  $r \ll \dot{r} \partial t_{\text{ch}} \iota_v$ , while the carrier frequency is sufficiently high, i.e.  $f_c \gg \tau \Delta f_{\text{eff}} / (2T_M)$ .

After sampling, the baseband signal, considering a total number of  $I_O$  reflecting (point) objects can be arranged in a 3D, real-valued array s:

$$\begin{aligned}
 \mathbf{s}(\iota_r, \iota_v, \iota_\phi) = \sum_{\iota=1}^{I_O} \hat{\mathbf{s}}_\iota \cos \left( \underbrace{\frac{4\pi \Delta f_{\text{eff}}}{c I_r} r_\iota \cdot \iota_r}_{\omega_{r,\iota}} + \underbrace{\frac{4\pi \partial t_{\text{ch}}}{\lambda} \dot{r}_\iota \cdot \iota_v}_{\omega_{v,\iota}} + \underbrace{2\pi \partial \Gamma \sin(\phi_\iota) \cdot \iota_\phi}_{\omega_{\phi,\iota}} \right. \\
 \left. + \underbrace{\varphi_\iota(r_\iota)}_{\text{range depended phase term}} \right) + \underbrace{\xi(\iota_r, \iota_v, \iota_\phi)}_{\text{Noise term}} \quad (2.4)
 \end{aligned}$$

The index notation is  $1 < \iota_\phi \leq I_\phi$ ,  $1 < \iota_v \leq I_v$  and  $1 < \iota_r \leq I_r$ .

Eq. 2.4 utilizes the representation as composition of sinusoids as used by Engels. Here, each object  $1 \dots I_O$  renders in normalized frequency components associated with range, range rate, and azimuth, i.e.  $\omega_{r,\iota}$ ,  $\omega_{v,\iota}$ , and  $\omega_{\phi,\iota}$ . This representation emphasizes that determining the range, range rate, or angular component of a detection in radar basically corresponds to a frequency estimation problem. The measured quantities assigned to an object are thus given by peaks in the respective frequency spectra obtained by Fourier transformation. The generalized baseband signal shown in eq. 2.4 is now transferred into frequency domain by means of the Fourier transformation under consideration of window functions for range, range rate, and azimuth, denoted  $W_r$ ,  $W_v$ , and  $W_\phi$ , respectively:

$$\begin{aligned}
 \mathcal{F}(\mathbf{s}(\iota_r, \iota_v, \iota_\phi)) &= F(\omega_r, \omega_v, \omega_\phi) \\
 &= \sum_{\iota_r=1}^{I_r} \sum_{\iota_v=1}^{I_v} \sum_{\iota_\phi=1}^{I_\phi} W_r(\iota_r) W_v(\iota_v) W_\phi(\iota_\phi) \mathbf{s}(\iota_r, \iota_v, \iota_\phi) e^{-j(\omega_r \iota_r + \omega_v \iota_v + \omega_\phi \iota_\phi)} \quad (2.5)
 \end{aligned}$$

The representation in eq. 2.5 represents the multidimensional *radar cubic*, a representation that is frequently used in the course of this dissertation. The term “radar cubic” is preferred over the otherwise common term “radar cube”. This is motivated by the fact that the geometric figure of a cubic, unlike a cube, does not require equal edge lengths. Thus, it is taken into account that the resolution cells in a radar sensor have different widths in the respective measurement dimensions. This data structure is a

multi-dimensional matrix and an entry is called a “cell”. For each computing cycle, the measuring ranges, e.g. for range, range rate, azimuth, and elevation (if available), span one dimension. Each measurement dimension is discretized into so-called “bins”, which conceptually correspond to the width of the resolution cells.

### 2.2.2. Resolution limits and unambiguous intervals

A computational efficient spectral density estimation is given by the periodogram, which is the squared magnitude of a signal’s discrete Fourier transformation (DFT). The frequency discretization and resolution limits are specified by the sampling points for each ramp, chirp, and antenna. They can be derived from eq. 2.5:

$$\partial\omega_r = \frac{4\pi\Delta f_{\text{eff}}}{cI_r} \partial r = \frac{2\pi}{I_r} \implies \partial r = \frac{c}{2\Delta f_{\text{eff}}} \quad (2.6)$$

$$\partial\omega_v = \frac{4\pi\partial t_{\text{ch}}}{\lambda} \partial \dot{r} = \frac{2\pi}{I_v} \implies \partial \dot{r} = \frac{\lambda}{2T_M} \quad (2.7)$$

$$\partial\omega_\phi = 2\pi\partial\Gamma\partial\sin(\phi) = \frac{2\pi}{I_\phi} \implies \partial\sin(\phi) = \frac{1}{I_\phi\partial\Gamma} \quad (2.8)$$

Unambiguous measurement ranges result from the requirement that a phase angle can’t exceed  $2\pi$  for range and  $\pm\pi$  for radial velocity and azimuth angle:

$$0 \leq \frac{4\pi\Delta f_{\text{eff}}}{cI_r} r \leq 2\pi \implies r \in \left(0, \frac{cI_r}{2\Delta f_{\text{eff}}}\right) \quad (2.9)$$

$$-\pi \leq \frac{4\pi\partial t_{\text{ch}}}{\lambda} \dot{r} \leq \pi \implies \dot{r} \in \left(\frac{-\lambda}{4\partial t_{\text{ch}}}, \frac{\lambda}{4\partial t_{\text{ch}}}\right) \quad (2.10)$$

$$-\pi \leq 2\pi\partial\Gamma\sin(\phi) \leq \pi \implies \sin(\phi) \in \left(\frac{-1}{2\partial\Gamma}, \frac{1}{2\partial\Gamma}\right) \quad (2.11)$$

### 2.2.3. Implications for radar sensor modeling

In order to model radar sensors, which is subject of this dissertation, several remarks are made at this point.

Based on the derivations shown in the previous section, it becomes clear that object detection with chirp sequence radars can be understood as a frequency estimation problem. The simplest method for this is the presented procedure using the periodogram

which is, however, known for its poor basic resolution. The periodogram method yields in a set of basic performance parameters for the measurement ranges in range, rate rate, and azimuth angle. A number of estimation algorithms to increase the frequency resolution are presented in reviews by Patole et al.<sup>30</sup>, Engels et al.<sup>31</sup> and Sun et al.<sup>32</sup>. These algorithms are characterized by higher computational costs or by additional assumptions, such as a prior estimate about the expected number of objects, but promise higher angular resolutions. In order to maintain generalization over all chirp sequence radars, the periodogram method is used for frequency estimation in this dissertation.

The performance parameters regarding measurement and resolution ranges are given by hardware parameters. The number of simultaneously receiving antennas elements  $I_\phi$ , effective modulation bandwidth  $\Delta f_{\text{eff}}$  and length of a chirp sequence  $T_M$  are key design parameters for resolution. Unambiguous intervals are limited by chirp repetition rate  $\partial t_{\text{ch}}$  and antenna spacing  $\partial \Gamma$ . The relationships derived above are initially only valid for point objects, i.e. objects whose dimension or extension is smaller than one resolution cell.

In order to find a suitable data layer for the output data of a simulation, the data rate is considered. For chirp-sequence radars the baseband signal has a very high data rate, which is due to the required sampling frequency. A simple calculation example shall illustrate this: According to Winner<sup>23c</sup>, sampling rates in the orders of MHz are required to meet the Nyquist-Shannon sampling theorem. With an assumed sampling rate of 10 MHz and when storing each sample with integer resolution (i.e. 32 bit/sample), this results in a data rate of  $I_\phi \cdot 40$  MB/s for the baseband signal in time domain. It is obvious that this poses a challenge in terms of possible real-time requirements for the simulation, not yet taking into account the computational effort required for the Fourier transform. However, also with the radar cubic representation outlined in eq. 2.5 it should be noted that a considerable data rate is also present in Fourier domain: An exemplary radar system with  $I_\phi$  antennas,  $I_r = 256$  range bins,  $I_v = 128$  Doppler bins and a cycle time of 50 ms is given. The complete unthresholded radar cubic requires  $256 \cdot 128 \cdot I_\phi \cdot 32$  bit =  $I_\phi \cdot 20.5$  MB/s when storing the spectral power in each cell as single precision float.

In view of unambiguous intervals, however, the radar cubic has the property that its entries are not unambiguous when it is set up in the dimensions  $I_\phi$ ,  $I_r$ , and  $I_v$ . It is therefore seen as an aliased cubic. For de-aliasing, either several consecutive cubics may be required, or the respective measurement ranges may have to be extended, which increases the data rate. The number of entries that contain the desired signal is small

<sup>30</sup> Patole, S. M. et al.: Automotive radars: A review of signal processing techniques (2017).

<sup>31</sup> Engels, F. et al.: Framework on high-resolution frequency estimation (2017).

<sup>32</sup> Sun, S. et al.: MIMO Radar for Advanced Driver-Assistance Systems and Autonomous Driving (2020).

compared to the number of cells a de-aliased cubic would contain. For data reduction without loss of information, the relevant entries of the cubic can instead be stored as lists or as subspaces of the cubic. The Doppler dimension is particularly dedicated for reducing the data rate, as in the automotive context only a finite number of Doppler cells will be occupied per range-beam cell.

This does not fully apply in the case of objects that show an expansion in speed, as it is the case with pedestrians and cyclists: Here, Micro-Doppler determination provides a highly descriptive feature for the identification of vulnerable road users (VRU)<sup>33,34</sup> and extracting wheel movement<sup>35</sup>. If Micro-Doppler is not specifically evaluated, e.g. by an short time Fourier transformation (STFT), the velocity expansion is reflected in the occupancy of several Doppler cells in which the maximum spectral power migrates between the cells and cycles.<sup>36</sup> The current state of the art in Micro-Doppler evaluation in automotive radar context appears to be mainly suitable for the detection of VRU at close range.

---

<sup>33</sup> Engels, F. et al.: Framework on high-resolution frequency estimation (2017).

<sup>34</sup> Belgiovane, D.; Chen, C.-C.: Micro-Doppler characteristics of pedestrians and bicycles (2017).

<sup>35</sup> Kellner, D. et al.: Wheel extraction based on micro doppler distribution (2015).

<sup>36</sup> Andres, M. et al.: Extraction of Micro-Doppler Signatures using Automotive Radar Sensors (2012).

## 2.3. State of the art in radar sensor modeling: What is missing in today's radar models?

---

### 2.3.1. The role of “raw data” during signal and data processing of perception sensors

The measuring principle of radar sensors was presented in the previous section. Regarding the performance parameters, it was pointed out that there is a smooth transition between hardware (e.g. modulation, antenna design) and software components (e.g. signal processing and frequency analysis). For this reason, the question arises as to which data a radar sensor actually provides and can therefore also be synthetically generated in the simulation. Traditionally, the sensor modeling community debates the definition of sensor data during different sensor data processing stages. This applies especially to the so-called “raw data” that is unprocessed or minimally processed data. The absence of any thresholds or filtering procedures promises the richest information content. In photography, for example, there are the so-called “raw images”, which are standardized in ISO/IEC 14496-12 and contain a series of meta-data in addition to the sensor image data. Because the raw image is unprocessed data from the image sensor, it offers a higher dynamic range and color gamut compared to a developed image. The user can change the image properties after capturing to enhance the image details. Especially for radar sensors, but also for lidar sensors, a comparably sound understanding of raw data is not yet available. The common view is that raw data must be some sort of less pre-processed data: For radar sensors, the first measurable data is available at the output of the respective analog-to-digital converter (ADC) converter at each receiving antenna element. An individual signal sample of the baseband signal is, however, difficult to interpret. Therefore, the next step of signal processing is to perform frequency analysis using a multi-dimensional fast Fourier transformation (FFT) regime, as outlined above. The continuous Fourier transformation is essentially a loss-free transformation. As sampling is only possible at discrete points in a discrete FFT, discretization errors are not significant as long as the sampling frequency does not violate the Nyquist-Shannon sampling theorem. For this reason, the Fourier-transformed spectral data can be considered as “raw data” of an automotive radar sensor and is therefore referred to as “spectral data” in the following.

Figure 2.2 contextualizes the terms “reflection”, “detection”, “target”, and “object”. It is tailored to active sensors that transmit a specific signal which interacts with the environment.

## 2. Radar sensors from the modeling perspective

---

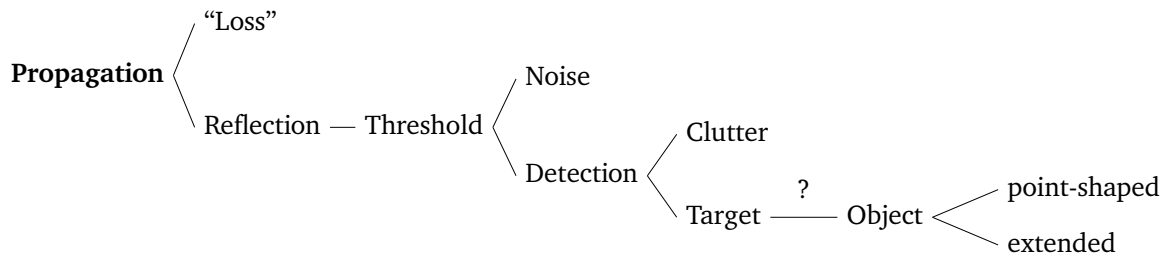


Figure 2.2.: Differentiation and dependencies of terms in relation to sensor data in the context of radar sensors.

After emitting the signal, it can occur that there is no reflection, i.e. the transmitted signal does not return to the sensor, e.g. if the propagation is (partially) directed towards the sky, or because highly absorbing material is hit.

If the signal undergoes a **reflection** towards the sensor, a threshold (either pre-defined or adaptively calculated) determines whether this signal shows an intensity that is sufficiently different from the noise floor. Signal readings below a **threshold** are considered noise. Because they are removed from the signal stream, they are no longer available for subsequent processing. For a signal exceeding the threshold, a peak-value can be determined.

**Detections**, or **peaks**, are formed from the remaining signal. It cannot be assumed that all detections are actually relevant as the detection threshold may be randomly exceeded due to noise. The term **clutter** is therefore used to describe those detections which are characterized by the fact that they cannot be found permanently and, for example, occur only once. Clutter is closely related to weak detections that only marginally differ from noise due to a low signal-to-noise ratio (SNR). At this point false positive or false negative errors can occur: The former results e.g. from clutter detections, the latter as soon as the backscatter of objects does not exceed the detection threshold.

**Targets** is still a widely used term in the (automotive) radar community and is a reminder of the military origin of radar technology. It differs from detections since a target has an unambiguous and physically interpretable state vector, e.g. because ambiguities are resolved. The accuracy of target states can be further improved by means of estimation algorithms (e.g. sub-bin interpolation). If a target can be tracked over time, i.e. it can be found again in successive time steps with an expected state, it can be considered an **object**. In the object tracking community, two types of objects are distinguished: Point-shaped and extended objects. The latter is characterized by the fact that it causes multiple targets due to its geometric extension over multiple resolution

cells w.r.t. the radar cubic. Object-level information can include additional information, e.g. about classification and estimated geometric dimensions.

With regard to the discussion of the term “raw data”, attention should be paid when thresholding is applied. Due to the lossy character of this operation, the term raw data is defined in this dissertation as follows:

**Definition (Raw Data).** Raw data is a lossless representation of machine-interpretable and physical meaningful sensor readings. It is required that unambiguous (non-aliased) sensor readings in at least one physical domain can be calculated from a finite set of subsequent data samples along with knowledge about additional sensor parameters. Raw data is exposed to artifacts in the respective sensor technology.

During continuous processing of sensor data and associated processing by algorithms, measured data is gradually replaced by estimated or interpolated data. It is necessary for an autonomous vehicle to create a comprehensive understanding of the scene in the vicinity of the ego vehicle, from which subsequent algorithms can derive a situation analysis and derive appropriate motion control actions. Therefore, the goal of sensor data processing is to create a comprehensive environment model that makes use of all available sensor measurement data. Ideally, this is done by using the acquired measurement data in a way that is advantageous for the respective sensor technology. With radars, the radial velocity is particularly useful for this purpose, as it can be measured precisely via the Doppler shift. Sensor fusion is expected to play a central role at higher levels of automation.<sup>37</sup> It facilitates the combination of respective technological advantages of sensors. In addition, the reliability of the information obtained can be increased by mutual plausibility checks. Within the development trends towards higher resolutions, there are more and more applications for radar sensors for scene understanding of an autonomous vehicle besides object detection, as it was originally deployed for ACC applications. An overview is given by Dickmann et al.<sup>12</sup>. This emphasizes the need for an universal interface between sensor output data and input data consumed by data processing algorithms also for the task of sensor simulation. This is accompanied by the need for a clear separation between the synthesis of sensor data and the simulation of the behavior of sensor data processing algorithms.

---

<sup>37</sup> Schreier, M.: Environment representations for automated on-road vehicles (2018).

### **2.3.2. Modeling terminology: Unmerging physics, phenomena, stochastic, and integration into the generic sensor modeling process**

The sensor modeling community understands a sensor model as a device that translates ground truth information, as available from simulation, to sensor data, i.e. *synthetic* sensor readings. This understanding applies to every type of sensor and corresponds to the understanding of a sensor as an information receiver. In a simulation environment, information is available with ground truth accuracy. The term “ground truth” should not be overemphasized in the light of simulation environments. Ground truth contains all quantities that are used as input to models in the simulation, with direct access to this data in the simulation environment. However, the completeness of the ground truth information from a modeled environment in the simulation in the sense of an all-encompassing, atomic accuracy is not given. For example, unlike in real-world, friction coefficients can be determined very accurately in simulation, but these quantities only represent the friction coefficient model used within the simulated road and tire model. The resulting offset is conceptually absorbed in the “accuracy” and “precision” of the ground truth. Obtaining ground truth in real-world requires reference sensor technology, which also has an upper limit for the technically achievable accuracy.<sup>38</sup>

For this reason, a perception sensor model must reproduce the same perception uncertainties as the real sensor exhibits. These uncertainties arise from finite accuracy and precision in the real sensor, which translates into a lossy representation of the (ideal) input information available from the simulation environment. More generally stated, a sensor model is the link between input data from the virtual environment to output data reflecting the quantities measured by the sensor. Clearly, this logic merges sensor hardware and sensor software components, and therefore, a closer inspection of sensor models reveals the relationships between their input and output data. An overview of manifestations of sensor models is given in figure 2.3 and is described in the following.

---

<sup>38</sup> Berk, M. et al.: Reliability Assessment of Safety-Critical Sensor Information (2019).

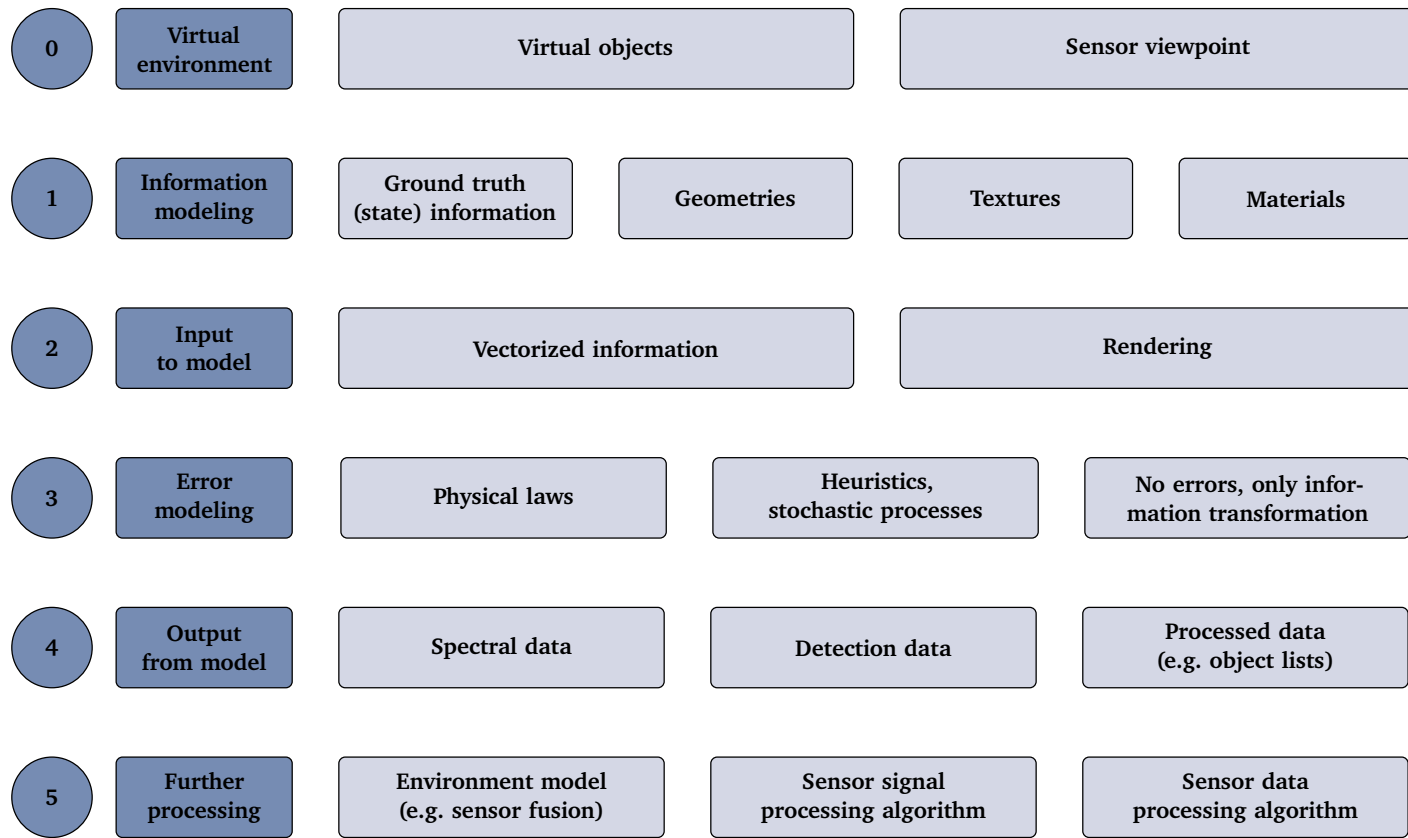


Figure 2.3.: Generic components of the modeling and simulation process for different manifestations of sensor models as found in literature.

A virtual environment must comprise a certain representation of *objects* in order to extract synthetic sensor data. Taking a scenario description perspective, objects are understood as either movable (e.g. traffic participants) or immovable objects (e.g. vegetation), temporal modifications to the road, or as part of the traffic infrastructure (e.g. guardrails, traffic lights, traffic signs).<sup>39</sup>

In a virtual environment all (graphical) content is given by (virtual) objects. The scene is observed by a sensor from a certain viewpoint (i.e. its mounting position) and various information about the appearance can be attributed to these (virtual) objects. In sensor modeling, objects require a representation in the virtual environment. Computer graphics realizes this by decomposing an object into its principal geometries along with textures and material assignments, each of which can have an arbitrary level of detail. The virtual environment also comprises *ground truth* information, that is the comprehensive knowledge of the virtual world such as the internal state of traffic participants, the scenario, its environment conditions, etc. In addition, the aspect angle and the positioning of respective energy sources (e.g. lights, electromagnetic waves) are required to consider specific properties such as reflectivity behavior w.r.t. the sensor's viewpoint. This is summarized as **information modeling** and includes all sources of information from which a sensor model can draw information to obtain synthetic data.

Thus, the **input** to the model is either vectorized information extracted from ground truth (e.g., state vectors, contour information), or is subject to some type of rendering, i.e., processing of the virtual world in a manner consistent with the sensor measurement principle. The object is displayed exactly as it is modeled, and the level of detail can be adjusted in terms of computational cost. Its geometry can be approximated as a rectangular bounding box from the external dimensions, for example, but abstraction errors result when neglecting ground clearance height.

In the rendering stage, a representation is created from the 3D geometry that depends on its properties and aspect angle: The geometry itself, its texture, material as well as surface finish (e.g. roughness). If, for example, the depth information or the occlusion between objects is of interest, this corresponds to hidden surface determination in computer graphics. A wealth of algorithms for this problem has been proposed in the course of research in the field of computer graphics.<sup>40</sup> Today, z-buffering, is frequently used as it is amenable to parallelization on graphic cards. It stores depth information for each pixel<sup>41</sup> but is prone to artifacts due to limited resolution of the depth buffer. In a less abstract perspective, the appearance of objects to a sensor consists of a composition of

---

<sup>39</sup> Sauerbier, J. et al.: Definition of Scenarios for Safety Validation of Automated Driving Functions (2019).

<sup>40</sup> Sutherland, I. E. et al.: A characterization of ten hidden-surface algorithms (1974).

<sup>41</sup> Straßer, W.: Ph.D. thesis, Kurven-und Flächendarstellung auf grafischen Sichtgeräten (1974), p. 6-1.

reflections. Surface normals and reflectance functions are required to calculate reflection paths and intensities. If the lighting conditions and the associated multiple reflections are to be physically “correctly” represented, this is possible with the ray tracing algorithm.

If contour information is available in the ground truth, from which e.g. the ground clearance can be derived, occlusion calculation can also be done without dedicated rendering, but by drawing the object contours according to their transformed position to the sensor. With such considerations, it would also be possible to take into account simple mirror effects.

Automotive radar sensors utilize wavelengths in mm range and wave propagation is a major part of rendering for radar sensor simulation: It determines how the scenery is illuminated and which attenuations are present, also taking into account possible multipath propagation. In the European cooperation in science and technology (COST) Actions 231, 259 and 273 a terminology for distinguishing wave propagation models has been established.<sup>42a</sup> It separates deterministic models that include ray tracing methods, stochastic models, and geometry-based stochastic models. The latter abstracts the radio channel by multidimensional probabilistic functions derived from extensive measurements. Modeling of the interaction of electromagnetic fields with objects, taking into account the wave propagation in the environment, can be formulated using the Maxwell equations. These can be described as partial differential equations and solved by special solution methods (e.g. finite element method) and approximations.<sup>43</sup> This requires support points, which can be obtained by discretizing the surface, known as meshing. There are a number of commercial software products that are of interest for specific sensor development problems: These include the calculation of material attenuation when choosing the installation position of the sensor in the vehicle, the design of the antenna taking into account the manufacturability on printed circuit board (PCB), as well as questions concerning electromagnetic compatibility (EMC). Due to the high computing time, there are also efforts to simplify calculations through approximations. For example, the “high-frequency approximation” allows the mm-wave to be approximated as a beam of light, so that methods such as ray tracing can be used to calculate wave propagation. However, this is associated with limitations as, e.g., diffraction is initially not taken into account.

These considerations are localized in the **error modeling** portion of a sensor model. There are several options for modeling sensor errors. If the sensor measurement principle is modeled as close as possible to physical laws, one speaks of “physical” models because internal calculations are mainly based on physical models. The term is not as sharp

---

<sup>42</sup> Bonek, E.: MIMO Propagation and Channel Modeling (2011). a: p. 31; b: -.

<sup>43</sup> Sefi, S.: Ray tracing tools for high frequency electromagnetics simulations (2003), p. 4.

as it promises. Many physical laws only apply within certain assumptions and arise from real-world observations, so that the concept of phenomenology is brought closer. A prominent example is Newtonian mechanics, which can be falsified once relativistic effects are taken into account. A conceptual remedy would be the term “physically inspected” (error) modeling.

Observations of sensor behavior in the real-world can be described as heuristics for reasons of simplification. Stochastic models are created to represent a particular phenomenon as closely as possible to the underlying physics without explicitly modeling it. Finally, there are cases in which consideration of perception errors are not relevant because, for example, a “best-case” estimate is of interest. Then, error modeling is reduced to transforming ground truth information into the sensor coordinate system and clipping the field of view according to the sensor specification.

The **output** of the model is based on the sensor output, which in turn is determined by the application of the model. The raw data interface, which emphasizes the separation between sensor hardware and sensor software simulation, is suitable for component tests. Here, only unprocessed data is available (e.g. time or frequency spectra), from which subsequent algorithms extract information.

If parts of the sensor software is included in the simulation model, detections or objects can be calculated from the model. In contrast to lidar<sup>44</sup> or camera<sup>45</sup>, outputting free space information from radar simulation models is rather unusual, although a radar sensor is often used for this purpose.<sup>46</sup>

The sensor data synthesized by the sensor simulation model is **further processed** and is integrated in the perception stack. There are many different forms of this, which will not be examined in detail at this point. Therefore, only the increasing importance of comprehensive perception models, in which the information of all sensors is combined via sensor fusion approaches, should be pointed out. This can be done at object level, detection level or raw data level, with information from any sensor.

### 2.3.3. Common variants of sensor models

Permutation of the model inputs and outputs results in several variants that can be derived from the generic modeling process. Almost all models known from the literature can be classified in this process. It should be emphasized that almost all mixed forms are possible.

---

<sup>44</sup> Schaermann, A. et al.: Validation of vehicle environment sensor models (2017).

<sup>45</sup> Reway, F. et al.: Test Methodology for ADAS Algorithms with an Automotive Camera (2018).

<sup>46</sup> Werber, K. et al.: Automotive radar gridmap representations (2015).

- Object in Object out (OIOO)
- Object in Detection out (OIDO)
- Object in Reflection out (OIRO)
- Rendering in Object out (RIRO)
- Rendering in Detection out (RIDO)
- Rendering in Reflection out (RIRO)

Software in the loop (SiL) models, i.e. simulation models of the sensor software do not represent sensor models in the strict sense, but can be integrated into the structure: A SiL simulation of a thresholding algorithm based on raw data generates detections. The SiL module of the tracking filter consumes targets and calculates the object list on this basis. However, SiL models can be part of a sensor system model and their stimulation with synthetic data is possible via OIRO or RIRO models.

Each of the aforementioned manifestation is briefly reviewed in the following in terms of examples, areas of application and individual strengths and weaknesses.

### **Object in Object out (OIOO)**

OIOO models utilize the fact, that in principle any information about objects present in a scene can be retrieved directly from ground truth as provided by the simulation environment. Rendering can be kept simple and is limited to the reproduction of the object dimensions, bounding box information and, if necessary, information about occlusions. A coordinate transformation is necessary if the desired object information from the simulation environment is only available in world coordinates and has to be transferred to a sensor or ego vehicle centered coordinate system. Therefore, user-definable parameters include the sensor's mounting position and orientation and the reference point. With appropriate class affiliation information as directly available from ground truth, it is also possible to filter different object types such as vehicles, pedestrians, but also lane markings, etc. to simulate the detection sensitivity of a sensor. The output of such a model is thus a state vector reflecting the (transformed) ground truth information. The state vector can capture all ground truth information, such as object dimensions and class affiliation. This would correspond to an ideal estimator for these quantities.

It covers geometric (i.e. distance to object), kinematic (e.g. relative movement w.r.t. ego) and additional sensor specific properties, such as a rough estimate of the object's backscatter intensity. As the calculation in such a model renders down to information transformation from ground truth, no noise or other distortions are superimposed to the detection or measurement behavior. The (non-uniform) nomenclature in the literature

refers these models as “ground truth” models, “perfect sensors”<sup>47</sup>, “ideal sensors”<sup>48</sup>, or “idealized sensors”<sup>49</sup>. If the object dimensions from which contour information can be derived are also known via ground truth information, then it is also possible to recreate the image of a simulated camera using semantic segmentation. Also for the (idealized) simulation of object lists of radar sensors, information such as ground clearance is helpful for the occlusion calculation.

Machine perception, however, is subject to uncertain domains of state, existence and class.<sup>50</sup> The aforementioned “ideal” models do not reflect any of these uncertainties. The sensor modeler is aware of deviations between “ground truth” and the actual sensor behavior. By observing the measurement behavior of a sensor, empirical conclusions can be drawn. In this context, the terms “phenomenological”<sup>51</sup>, “stochastic”<sup>52</sup>, “statistical”<sup>53</sup>, and “behavioral”<sup>54</sup> model appear in the literature. Their goal is to mimic the error characteristics (i.e. imperfections) of sensors by incorporating stochastic properties to those quantities that are consumed from ground truth and “in general a phenomenological model appears to be an arbitrarily-chosen mathematically-expressed correlation of physical parameters from which the empirical laws of some domain can be derived”<sup>55</sup>.

In a typical stochastic model, a stochastic behavior is superimposed on the object’s state vector, as available from ground truth, to simulate the measurement errors, such as noise. Such a model is described by Bernsteiner et al.<sup>51</sup> to name one of the early examples of this category.

The consideration of sensor technological aspects is possible in OIOO models. For example, conclusions about occlusions can be drawn from the geometric arrangement of the bounding boxes. In a radar model, the visibility of an occluded object can thus be allowed, whereas this should not be possible in a lidar or camera model.

OIOO models, whether idealized or phenomenological, require only little computing power because the involved arithmetic calculations (e.g. coordinate transformations, binary operations) are of low complexity. One challenge is to parameterize the OIOO

---

<sup>47</sup> Miegler, M. et al.: Hardware-in-the-loop test of advanced driver assistance systems (2009).

<sup>48</sup> Feilhauer, M.; Häring, J.: A multi-sensor model to validate ADAS in a virtual environment (2017).

<sup>49</sup> Roth, E. et al.: Analysis and Validation of Perception Sensor Models (2011).

<sup>50</sup> Dietmayer, K.: Predicting of Machine Perception for Automated Driving (2016), pp. 412-418.

<sup>51</sup> Bernsteiner, S. et al.: Radar Sensor Model for the Virtual Development Process (2015).

<sup>52</sup> Hanke, T. et al.: Generic architecture for simulation of ADAS sensors (2015).

<sup>53</sup> Rasshofer, R. et al.: Generalized modeling of radar sensors (2005).

<sup>54</sup> Haider, A. et al.: Automotive Radar Sensor Behavioral Models (2019).

<sup>55</sup> McMullin, E.: What do Physical Models Tell us? (1968).

model so that it matches the empirical behavior of real data processing algorithms. For example, a real tracking algorithm must be abstracted by models, which in turn corresponds to a “phenomenological” sub-model. Promising methods are presented by Hirsenkorn et al.<sup>56</sup> who shows a non-parametric probability distribution fit. Zec et al.<sup>57</sup> utilize Hidden Markov Models to model the object’s behavior as seen by the sensor over time. A purely-analytical approach is shown by Stolz and Nestlinger<sup>58</sup> who explicitly account for occlusion phenomena. Stellet et al.<sup>59</sup> focus on modeling of object detection in stereo vision and derive a statistical model of object detection for a disparity image.

In contrast to ideal models, phenomenological models require additional parameters: These consist of the probability distributions that characterize noise behavior but also RCS maps for calculating the received power in radar and resolution cells for mimicking merging of objects that are no longer separable.<sup>60</sup>

By outputting the object list, however, OIOO models rather describe the sensor software, i.e. the object detection and tracking component. They address sensor technology-specific features only through empirical relationships and not through physical causal relationships. OIOO models are therefore suitable for simulator studies in which, for example, a worst- or best-case estimate of the performance of the sensor system is to be found.

### **Object in Detection out (OIDO)**

This class of sensor models is based on the assumption that radar reflections “can be understood as a superposition of the reflected signals from a high number of scattering centers”<sup>61a</sup>. Here, the object-level representation is extended to include point reflection centers or scattering center models, which aim to simplify the complex scattering properties of objects to a few significant scattering centers as illustrated in figure 2.4. In the approach by Bühren et al.<sup>62</sup>, the scattering centers are parametrized heuristically, i.e. manually fitted to real radar data. Eder et al.<sup>63</sup> proposes a data-driven by means of neural networks or density estimators.

---

<sup>56</sup> Hirsenkorn, N. et al.: A non-parametric approach for modeling sensor behavior (2015).

<sup>57</sup> Zec, E. L. et al.: Statistical Sensor Modelling for Autonomous Driving (2018).

<sup>58</sup> Stolz, M.; Nestlinger, G.: Fast generic sensor models for testing highly automated vehicles (2018).

<sup>59</sup> Stellet, J. E. et al.: Statistical Modelling of Object Detection (2015)

<sup>60</sup> Dörr, D.: Radar Sensor in IPG CarMaker (2017)

<sup>61</sup> Schuler, K. et al.: Extraction of Virtual Scattering Centers (2008).a: p. 1; b: -.

<sup>62</sup> Bühren, M.; Yang, B.: Simulation of Automotive Radar Target Lists (2006).

<sup>63</sup> Eder, T. et al.: Data Driven Radar Detection Models (2019).

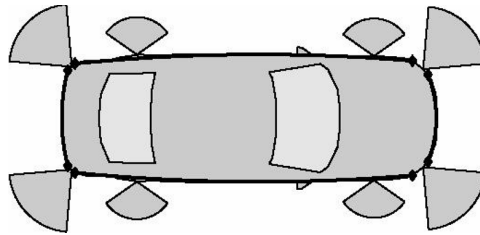


Figure 2.4.: Scattering center reflection model of a vehicle according to Bühren with 8 reflection centers: 4 at each corner and at the wheel houses. ©2006 IEEE

OIDO simulation bypasses the detection and thresholding step in sensor signal processing and reports detections for each point reflection center that is visible to the sensor. The intensity of a detection is based on the parametrization of the respective reflection point in the scattering model. OIDO models are of interest in applications where the sensor's detection plane is to be simulated. As with OIOO models, the challenge remains to parameterize the nearly infinite variety of objects and prove their validity.

### **Object in Raw data out (OIRO)**

It is also possible to render raw sensor data based on an object model or object state vector: The reflectivity behavior of objects can also be generated in a fully data-driven fashion, e.g. by conditional variational autoencoders as shown by Wheeler et al.<sup>64</sup> which does not require detailed meshing of the geometry. A geometry description based on object information is not very detailed. Basically, only a cuboidal representation by a bounding box or object contours can be derived from the ground truth state vectors. Therefore, for this kind of models further meta-information like the reflection centers known from OIDO are used. Weinmann<sup>65</sup> shows the calculation of reflection intensity at scattering centers by means of electromagnetic field distributions, but emphasizes that this is not suited for large problems due to the required computational effort. As described above, ray tracing is a common choice when modeling wave propagation at wavelengths much smaller than the objects in the scene. The principle of shooting and bouncing rays allows the calculation of the scattering properties of arbitrary object geometries under the assumption of geometric optics. Ray tracing simulations allow a significant improvement in computation time when computing large geometries, such as cars, compared to computational electromagnetics (CEM) methods. Nevertheless,

---

<sup>64</sup> Wheeler, T. A. et al.: Deep stochastic radar models (2017).

<sup>65</sup> Weinmann, F.: Ray Tracing with PO/PTD for RCS Modeling (2006).

there is no claim to real-time performance. Contributions to this class of models include the work from Buddendick<sup>66</sup> and Schuler<sup>61b</sup>. A radar sensor simulation that focuses on modeling the high frequency fronted for evaluating adaptive beam control is presented by Dudek<sup>67a</sup>. He calculates the channel impulse response based on reflectivity of objects found with the method from Buddendick with 12 scattering centers. In contrast to the OIDO model, however, the output data in OIRO models is available on signal level. This indicates the intensity of a reflection, but no extraction of detections has taken place.<sup>67b</sup>

The model of Haider et al.<sup>54</sup> strikes a middle course between OIDO and OIRO: Here, the object information from ground truth is formulated as an open simulation interface (OSI) message to the model, which then calculates the baseband signal. The signal is now further processed by a typical radar signal processing chain which comprises the FFT regime and a constant false alarm rate (CFAR) algorithm for obtaining detections. Because the output of raw data is based on object information, the model is classified as OIRO.

#### **Rendering in Object out (RIOO)**

It is obvious that an object description by a bounding box represents reality on a rather abstract level. In order to better represent the geometric reflection properties of real objects, a more sophisticated rendering step is necessary. The advantage of such rendering based models is that a much higher adaptation to the respective sensor is possible because performance parameters such as resolutions, measuring ranges and antenna patterns are explicitly considered. This is accompanied by higher demands on the description of the 3D geometries in terms of detailing, material assignment, and texturing. A rendering engine calculates the appearance resulting from the reflections of the geometries based on this kind of information.

In the method proposed by Cao<sup>68</sup>, the object state vector obtained from the ground truth is discretized. It takes sensor separability intervals of the respective measurement dimensions into account. Rendering of the vehicle reflectivity is approximated by overlapping Poisson window functions.

Object tracking algorithms are based on a so-called “measurement models” that mathematically describe the sensor measurements in terms of uncertainties. Therefore, there are numerous research projects such as the work by Hammarstrand et al.<sup>69</sup> and Berthold

---

<sup>66</sup> Buddendick, H. et al.: Bistatic scattering center models (2010).

<sup>67</sup> Dudek, M.: Towards automotive safety applications based on radar sensors (2015), a: - ; b:p. 116.

<sup>68</sup> Cao, P.: Ph.D. thesis, Modeling Active Perception Sensors (2018), p. 103.

<sup>69</sup> Hammarstrand, L. et al.: Extended Object Tracking using a Radar Resolution Model (2012).

et al.<sup>70</sup> dealing with the refinement of the underlying measurement model to achieve better tracking performance.<sup>71</sup> These are not sensor simulation models in the sense of this dissertation. Instead, they would fit as SiL models that consume detections based on an object description extended by rendering and calculation of object information.

Aust<sup>72</sup> proposes a lidar sensor model that combines reflections available from a ray tracing engine with ground truth object information in order to mimic state, existence and class-uncertainties. The key idea is to map occlusion information, distance, and orientation of objects to the resulting uncertainties. For example, the model offers a parameter that describes how many reflections are required to keep an object as member of the object list and what percentage of overlap is allowed between objects before object separation fails. It is a hybrid approach, as both rendering information and ground truth information about objects are processed. The advantage of this method is that the rendering information allows the sensor measurement principle to be considered more detailed. Because object information from ground truth can also be used, the generic behavior of tracking algorithms can be simulated without the need to implement the tracking algorithm itself.

### **Rendering in Detection out (RIDO)**

Since the detection behavior of the sensor is simulated, the detection step, i.e. the comparison of the reflected intensity against a threshold value, is part of models that belong to the RIDO category. In a simple implementation, each hit from a ray tracing engine would be considered a detection. For radar sensors, this assumes that the rendered input data (e.g. from the ray tracer) is correct in that effects such as multipath propagation, decay of signal intensity, and Doppler shifts are correctly modeled. This modeling approach is especially common in lidar simulation, where it is assumed that a hit of the ray tracing algorithm defines a point in the point cloud. Exemplary applications can be found in CARLA<sup>73</sup> and LGSVL simulator<sup>74</sup>. CARLA also offers a radar sensor model<sup>75</sup> that provides distance, angular position, and relative speed for each detection, but not the backscattered intensity.<sup>76</sup>

---

<sup>70</sup> Berthold, P. et al.: An Abstracted Radar Measurement Model for Extended Object Tracking (2018).

<sup>71</sup> Koch, W.: Advanced Sensor Models for Tracking Applications (2007).

<sup>72</sup> Aust, P.: Master's thesis, Entwicklung eines lidartypischen Objektlisten-Sensormodells (2019).

<sup>73</sup> sergi-e; DSantosO: Carla LIDAR raycast sensor (2020).

<sup>74</sup> <http://lgsvlsimulator.org>: Lidar sensor plugin - LGSVL Simulator (2020).

<sup>75</sup> sergi-e; DSantosO: Carla v: 0.9.9 Radar sensor (2020).

<sup>76</sup> <http://carla.org>: Carla v: 0.9.9 Radar Detection (2020).

This type of model is also deployed in sensor stimulation, where a real radar receives synthetically generated reflections from so-called target simulators. Maier et al.<sup>77</sup> describe a method for calculating the “radar signature”, which corresponds to the reflection intensity for radar waves of an object for a given aspect angle. Their work adapts the Phong reflectivity function for calculating the RCS of geometries<sup>78</sup> and the work by Gadringer et al.<sup>79</sup> shows the hardware architecture for calculating detections (denoted as targets in their work) based on reflections at the input.

### Rendering in Raw data out (RIRO)

Under this paradigm, the models that come closest to understanding the so-called “physical” sensor models can be found because the mathematical models used to calculate the output data are closer to the actual sensor physics.<sup>80</sup>

A precise surface description of the geometry of virtual objects is of great importance in this approach. Besides a more detailed discretization in the shape of a mesh, materials and textures are usually also taken into account and described with radar-typical reflection properties. CEM programs such as CST Studio Suite, ESI CEM One and ANSYS HFSS and SBR+ fit into this range, to name just a few.

Ray tracing is the foundation for the calculation of wave propagation, also in applications outside the automotive domain.<sup>81,82</sup> Radar simulation models, as supplied in commercial automotive simulation environments such as IPG CarMaker, Vires VTD 2020, COSMOsim and TASS PreScan, build upon ray tracing to calculate wave propagation: For example, IPG CarMaker<sup>83a</sup> contains a radar sensor model which uses a ray tracing engine and provides individual detections that are calculated from reflections of rays within the virtual scene. Here, the reflectivity of objects is influenced by their geometric shape as well as their materials.<sup>83b</sup>

Based on reflections reported by the ray tracer, the baseband signal can be calculated

---

<sup>77</sup> Maier, F. M. et al.: Environment perception simulation for radar stimulation (2018).

<sup>78</sup> Maier, F. M. et al.: Adapting Phong into Stimulation of Automotive Radar Sensors (2018).

<sup>79</sup> Gadringer, M. E. et al.: Virtual reality for automotive radars (2018).

<sup>80</sup> van Driesten, C.; Schaller, T.: Overall Approach to Standardize AD Sensor Interfaces (2019), p. 53.

<sup>81</sup> Yun, Z.; Iskander, M. F.: Ray Tracing for Radio Propagation Modeling (2015).

<sup>82</sup> Felbecker, R. et al.: Electromagnetic wave propagation using OptiX GPU ray tracing (2012).

<sup>83</sup> Herrmann, M.; Schön, H.: Sensor Development Using Raw Signal Interfaces (2019), a:-, b: p. 36.

as shown by Hirsenkorn et al.<sup>84</sup>. A similar approach is also presented by Herz et al.<sup>85</sup> which adds multiple distortions, such as noise, smoothing, and antenna effects etc. to the ray tracing result when obtaining raw data. Thieling et al.<sup>86</sup> propose a modular framework for simulating spectral range Doppler maps considering material properties that exhibit different reflection modes (diffuse, specular) and attenuation by rainfall.

In the domain of lidar sensor simulation, there is related work by Berger et al.<sup>87</sup> that computes depth information from geometric information of the virtual environment. By using projective structures on the graphics card, calculations can be parallelized and thus accelerated. CARLA has also announced the support of such a modeling layer and takes up the concept of separating the rendering of the environment from the calculation of the sensor model.<sup>88</sup>

Such “physical based” approaches promise the highest agreement between simulation and measurement data and, at the same time, the highest flexibility regarding the scenario and sensor setup to be simulated. Disadvantages are the higher computational effort and the need for further computational steps to obtain interpretable data from the synthesized raw data, which can then be processed into object lists by further algorithms to be stimulated. Furthermore, this approach requires a large number of parameters, not only about the sensor to be modeled, but also about the environment in terms of materials and their reflection behavior.

---

<sup>84</sup> Hirsenkorn, N. et al.: Ray launching for modeling an FMCW radar system (2017).

<sup>85</sup> Herz, G. et al.: Sophisticated Sensor Model Framework (2017).

<sup>86</sup> Thieling, J. et al.: Scalable and Physical Radar Sensor Simulation (2020).

<sup>87</sup> Berger, C.; Rumpe, B.: Nutzung der GPU für automotive Sensorsimulationen (2009).

<sup>88</sup> CARLASimulator: CARLA Talks 2020 - The External Sensor Interface (ESI) (2020).

## 2.4. Conclusions from existing sensor models

---

The overview of the state of the art and research regarding modeling of radar sensors given in this chapter is summarized w.r.t. still existing deficits. Individual deficits in some models may be less significant, but not completely eliminated. The chapter derives answers for **RQ1**: *What is necessary for an automotive radar simulation and what is not available from existing models?*

### **Model scope and requirements**

The sensor models presented in this section are listed in table 2.1 and structured regarding the implemented effects and the model validation approach. Based on the presented sensor models, no systematic approach could be identified according to which aspects the sensor artifacts (“features”) to be captured by the sensor model were selected. The capabilities of a sensor model to render certain sensing artifacts are often designed as a binary list, i.e. “available” or “not available”. There is little or no discussion about the fidelity with which artifacts are modeled. Instead, simulation results are either not compared to measurements, or are compared to measurements on a per time step basis. The parameterization of the models is often limited to the sensor specification such as resolution and measurement ranges. However, it is unclear how the models handle artifacts such as measurement errors, multiple reflections, and other effects that are the characteristics of radar measurements and vary under certain circumstances. The model scope therefore lacks a deductive method for deriving requirements. In a work by Ponn et al.<sup>89</sup> it is shown how the overall sensor system of an autonomous vehicle can be designed with the help of phenomenological sensor models. Stellet et al.<sup>90</sup> derive performance bounds found in automatic emergency braking (AEB) systems caused by noisy sensor measurements that can be used to derive sensor accuracy constraints. What is missing, however, is the reverse approach: Starting from the existing sensor setup of an autonomous vehicle: What are the quality requirements for a meaningful sensor simulation?

### **Proof of validity and model benchmarking**

None of the sensor models examined provides a detailed description of the respective validation method. Rosenberger et al.<sup>91</sup> provides initial approaches to describe a holistic method w.r.t. a conceptual sensor model validation strategy focusing on lidar. There is,

---

<sup>89</sup> Ponn, T. et al.: Systematic Analysis of the Sensor Coverage of Automated Vehicles (2019).

<sup>90</sup> Stellet, J. E. et al.: Derivation of performance bounds of autonomous emergency brake systems (2016).

<sup>91</sup> Rosenberger, P. et al.: Towards a Validation Methodology for Sensor Models (2019).

however, no experience yet with the application of that method to sensor simulation. Instead, most papers compare individual measurements samples with with an instantaneous simulation result as basis for qualitative comparison. A systematic proof that sensor characteristics are correctly represented in the model is not provided. There are very few studies that compare different sensor simulation models on benchmark scenarios, for example the work of Rosenberger et al.<sup>92</sup> for the lidar domain. For this reason, it would be desirable for a simulation model to compile a test report from a set of standard scenarios specifically designed for the required sensor model specification. A benchmark derived from such scenarios would then provide a basis and criteria for an objective evaluation. Based on the resulting degree of fulfillment with the required specification, a statement about the validity of the model can be drawn.

### **Separation between hardware and software**

In a strict sense, sensor modeling ends at level of sensor raw data. The information content of this data stream is exclusively determined by hardware components. All subsequent signal or data processing steps can be clearly assigned as components of sensor software. By gradually replacing measured data with estimated data, it can change the information content as desired. Models that output any kind of processed data thus already implicitly mimic a mathematical representation of the behavior of the involved algorithms. There is a wide variety of algorithms for many data processing steps, such as object tracking, which in turn have a very large number of parameters. Non-raw data models therefore correspond to a regressive model that matches an assumed, empirically derived behavior of such data processing steps. This results in a sensor model that represents only a particular variant of an algorithm with a specific set of parameters. One example is the sensor processing model described by Stellet et al.<sup>59</sup>, which summarizes the complexities of object detection in stereo cameras through static models. Generalizability, e.g. to another set of parameters of the same algorithm, is not given if the statistical behavior of the algorithm is significantly affected by the changed parameters. The solution to this problem is strict modeling at the sensor raw data level, i.e. at the level of data processing, which is not subject to any modifications by data processing algorithms.

It is noticeable that most sensor models deal with an object list, while other environment model representations are of little interest from the current sensor modeling perspective. Consequently, such models are not suitable for testing automated or autonomous driving (AD) functionalities that are explicitly not based on the object list. This is a major drawback considering the current development trends towards the use

---

<sup>92</sup> Rosenberger, P. et al.: Benchmarking and Functional Decomposition of Lidar Sensor Models (2019).

of machine learning algorithms on unprocessed sensor data. With the availability of more powerful on-board networks (Flexray, Automotive Ethernet), it is also possible to provide higher data rates of unprocessed sensor data to a fusion architecture. These “early fusion” paradigms cannot be addressed with object list models.

Therefore, a model that outputs an object list or any processed data implies two models: A sensor model and a data processing model. Thus, it is necessary to prove that the data processing model matches the behavior of the data processing software.

### **Sensor model assumptions**

Because modeling is always a simplification of reality, it is necessary that the model assumptions are made transparent regarding the intended application area of a sensor model. While an operational design domain (ODD) is provided in the autonomous vehicle, a similar scope and validity of the models presented in the literature is not explicitly described. If the model assumptions made were explicitly stated, the scope of the model could be inferred. With the exception of the open source implementations in Carla, LGSVL and Apollo, the publicly available information is limited to descriptions of how the models work, based on scientific publications or user manuals for the software. There is little or no insight into the implementation of the models. Instead, only the description of certain implemented effects is available, but not the assumptions made for them.

For models that use ray tracing to simulate wave propagation, there is no in-depth discussion of the parameterization and limitations of ray tracing for simulating the propagation of mm-waves. Consideration of reflections outside specular reflections (e.g. transmission or diffuse scattering) is not given. Since diffraction cannot be represented with ray tracing<sup>93</sup>, the resulting deviations between measurement and simulation are not discussed. Errors in the model output, i.e. deviations between expected and actual value, can then only be attributed to two possibilities by the user: Either there is a user error in the use of the model (e.g. incorrect parameterization), or the model is used outside its specification, i.e. the desired simulation task cannot be handled with the model.

---

<sup>93</sup> this would require uniform geometrical theory of diffraction (UTD)

Table 2.1.: Overview of radar sensor models known from literature with covered effects and validation approach.

Author	Model principle	Covered effects	Validation method
Bernsteiner	OIOO	“Imperfections” in object states	Qualitative comparison with measurement in one scenario
Rasshofer	OIOO	Power loss over range, clutter	Simulation results in one scenario
Hirsenkorn	OIOO	“Imperfections” in object states	Simulation results
Zec	OIOO	“Imperfections” in object states	Trajectory error from comparison with measured sequences
Stolz	OIOO	Measurement ranges	none
Dörr	OIOO	“imperfections” in object states, object separability	none
Wheeler	OIRO	Power loss over range, clutter	Qualitative comparison with measurement in three static scenarios
Haider	OIRO	Object states in spectra	Simulation results from one dynamic scenario
Dudek	OIRO	Irradiation pattern	Simulation results
Bühren	OIDO	Resolution limits, power loss	Qualitative comparison with measurement in one static scenario
Eder	OIDO	Aspect angle dependency	Simulation results
Cao	RIOO	Object separability, power loss	Qualitative comparison with static measurements
CARLA	RIDO	Measurement noise	Simulation results
Herrmann	RIRO	Multipath propagation	Simulation results
Hisenkorn	RIRO	Multipath propagation	Qualitative comparison with measurements in three static scenarios
Herz	RIRO	Measurement noise, irradiation pattern	Simulation results
Thieling	RIRO	Measurement resolution	Simulation results in two static scenarios

### 3. What do we need in a radar simulation for virtual testing of AD?

---

In the previous chapter, the operating principle of radar sensors was presented and an overview of the current radar sensor modeling landscape was given. The high complexity of radar sensors and the individual components at the microscopic level could be transferred into highly detailed mathematical models. To keep the effort for sensor model development, execution, verification and validation within reasonable limits, it is desirable to systematically derive the required model scope together with the level of detail. Due to physical laws, there can be no ideal, i.e. error-free sensor in reality. As a consequence, distortion mechanisms are inevitable and present in every sensor technology. A sensor model must therefore map these distortions to the simulated quantities.

Measurements with a radar sensor show distinct characteristics that must be considered in all radar-based applications in the autonomous vehicle, albeit to varying degrees. In the broadest sense, measurement errors of radar sensors can be considered as anomalies due to the physical measurement principle of a radar, and measurement errors can be called “artifacts”. The online dictionary Dictionary.com defines an artifact as “a spurious observation or result arising from preparatory or investigative procedures” and “any feature that is not naturally present but is a product of an extrinsic agent, method, or the like”<sup>94</sup>. These definitions also apply to the nature of radar measurements, showing e.g. spurious clutter returns, mirror reflections, and ghost targets. Based on the operating principle of radar sensors, upper categories of artifacts are found by deduction. In the course of data collection and analysis of measurement data, further artifacts can be found, which are assigned to specific category. From these considerations the term artifact is defined as follows:

**Definition** (Radar Artifact). An *artifact* in a radar measurement is a noticeable deviation from ground truth in the sensor readings that is inherent in the sensor measurement principle and its system design.

---

<sup>94</sup> Dictionary.com: Definition of Artifact at Dictionary.com (2020).

### 3. What do we need in a radar simulation for virtual testing of AD?

---

For sensor modeling, this implies that considering a dedicated model conception for a particular artifact is seen as a “feature” of the sensor model. An artifact is characterized by a mechanism of formation, a description model, and an exemplary test or measurement setup for reproduction in real-world experiments and simulation. This chapter<sup>95</sup> focuses on the needs of a radar sensor simulation from the perspective of virtual testing of radar based autonomous driving functions. The methodical procedure for the elaboration of the particularly important features of a radar simulation is presented in the first part. The chapter is embedded in the context of **RQ2**: *What are relevant features for virtual testing of AD that a radar simulation must demonstrate?*

With regard to the development and testing of a simulation model, concrete requirements for the simulation model can be created that provide an answer to **RQ3**: *How are relevant characteristics defined and what are the requirements and test criteria for modeling?*

---

## 3.1. A methodological approach for deriving relevant features and test cases

---

As indicated in the previous chapter, a “wish list” of features to be implemented into a sensor model can be compiled from “expert knowledge”. It will not be possible to achieve completeness in the creation of such a list, and there is the potential for domain-specific bias. There is no way to ensure that a panel of experts will have a complete and indisputable overview of the necessary features for a radar sensor simulation. Instead, a methodology is needed that separates out those “features” that are actually relevant from such a “wish list” and translates them into falsifiable validity criteria for a simulation model. The methodology allows the modeling scope to be formulated in such a way as to establish a sensor model that has been proven in defined test cases for the intended application.

A feature to be considered in the model must be of significant relevance. Thus, the model can be falsified if a certain feature is not represented in the required quality. Therefore, the following methodology is proposed to deduce relevant features for sensor simulation.

---

<sup>95</sup> Portions of this chapter were previously published in: Holder M. et al. “Modeling and Simulation of Radar Sensor Artifacts for Virtual Testing of Autonomous Driving” (2019). Here, the artifact definition was introduced as well as some of the artifacts presented in this chapter were explained.

### **Step 1: Artifact allocation within the radar signal processing pipeline**

An artifact must be attributable to at least one source within the radar signal processing chain in order to derive a model concept about the cause of its origin. This is easily possible with a large number of artifacts: Reflections of the radar wave off surfaces can make objects appear multiple times (as mirror targets), but also makes occluded objects visible. During data processing, measurement errors occur at resolution limits and when unambiguous intervals are exceeded. Artifacts can also occur during later stages of data processing, e.g., due to the incorrect assignment of motion hypotheses during object tracking. A distinctive feature of the latter category is the cause of these artifacts. They are mainly influenced by parameters or the behavior of the data processing algorithm exposed to the data at hand.

However, it is not always possible to clearly assign a particular artifact to a specific category. For example, radar targets associated with false-positive and false-negative errors can be explained on the software side by an inappropriately chosen detection threshold. On the hardware side, on the other hand, high measurement noise in the radar or insufficient dynamic range may cause such errors as a “natural” consequence due to the specification of the sensor.

### **Step 2: Qualification of artifacts**

An artifact must be sufficiently different from an isolated single observation of random nature. This ensures that a systematic approach to the occurrence of the artifact is recognizable, even though the artifact itself may be stochastic in nature. This results in the following requirements for qualifying an artifact as a relevant feature:

- The circumstances under which an artifact occurs during a measurement must be known and described to facilitate its reproduction. From this, it must be possible to determine the sensitivity of the artifact in relation to the radar sensor used, the installation position and the environmental or test conditions. This enables the reproduction of the generation processes in the simulation.
- An artifact requires a description model. This enables the formulation of a theoretical explanation for modeling and thus a falsification experiment to verify the theory and its correct modeling in the simulation.
- An artifact must have a relationship to a driving maneuver or scenario. This qualifies the artifact as one that can be observed in real-world road

### 3. What do we need in a radar simulation for virtual testing of AD?

---

traffic and thereby outside of controllable laboratory conditions. Thus, a discussion can take place about the relevance of the artifact in view of the operational design domain (ODD) of the autonomous system.

- An artifact must be distinguishable from random measurement noise. Thus, a connection to a physical cause can be established. This is given if the artifact manifests itself in a clear pattern in the measurement data.
- The sensitivity of the artifact to environmental conditions must be known so that a reproduction in simulation is possible.

#### **Step 3: Quantification by measurements**

When presenting artifacts from measurements, it must be ensured that the artifact under investigation can be viewed in isolation. This means that an observation in the measurement does not result from the superposition of different artifacts. An ordinal scale can be used to rank the frequency of occurrence against the background of the circumstances of occurrence.

#### **Step 4: Synthesizing an description model**

In the course of the evaluation of the measurement data, descriptive models of the respective artifact are sought for modeling according to the “Occam’s Razor” principle. This states that of several explanations for one and the same situation, the simplest theory is preferable to all others. By rigorous comparison with measurements, the ranges of validity of the chosen description model can be narrowed until invalidity is determined. The range of validity is then compared to the intended use of the model, from which its fitness for purpose is determined.

#### **Step 5: Derivation of a falsification experiment**

The final step is the formulation of a test case for the sensor model. A test case for sensor simulation is derived by executing a faithful reproduction of the reference scenario in the simulation. One objective is to test the model assumptions for falsification by identifying inconsistencies with the description model that forms the basis for the implementation. If no falsification is possible, validity intervals, i.e. areas in which the sensor model is not demonstrably invalid, can be obtained by evaluating the test cases.

## 3.2. Research tools



(a) August Euler airfield in Griesheim comprising a 1.1 km runway with multiple lanes and respective lane markings. Reprinted with permission.



(b) 2008 Honda Accord Touring test vehicle with retrofitted additional sensors.

Figure 3.1.: Test equipment used in this thesis.

The basis of the investigation of relevant features is the deduction from theoretical considerations and the evaluation of measurements from which implications for the sensor model are derived. Measurement data used in this dissertation is collected with an automotive grade radar sensor that is deployed in series production. Its technical details are given in table 3.1. Measured variables available from the radar include unprocessed spectral data (radar cubic), detections, and targets from the near scan (NS) and far scan (FS) mode. An object list is available as well. The sensor has been retrofitted to a 2008 Honda Accord Touring (see figure 3.1b), which also has a radar-based adaptive cruise control (ACC) system to control the time gap to the vehicle in front. In the remainder of this dissertation, the term “ego vehicle” refers to the Honda Accord, i.e., the vehicle carrying the radar sensor being modeled, unless specified otherwise. The global navigation satellite system (GNSS) based inertial measurement system automotive dynamic motion analyzer (ADMA) by Genesys Offenburg GmbH in the variant “ADMA-G-PRO+” is used to measure vehicle dynamics in terms of position, accelerations, and angular rates. The precision of the system is increased by the real-time kinematic positioning (RTK) method and the high accuracy of the measured values qualifies their use as reference values. In experiments where the relative position and speed of an additional vehicle w.r.t. the ego vehicle are of particular interest, the second vehicle (i.e. the object of interest (OOI)) is also equipped with an ADMA system. Relative movement and position between vehicles can thus be determined with a high level of fidelity.

Further test vehicles available include a Volkswagen Golf 5 (codenamed VW Golf Mk

### 3. What do we need in a radar simulation for virtual testing of AD?

---

5), Volkswagen Golf 7 (codenamed VW Golf Mk 7), Audi A3 Sportback (codenamed Audi 8V) and a BMW i3. The vehicles are assigned to the B or C segment, which represents the largest market share on European roads.<sup>96</sup> Furthermore, a Volkswagen Crafter is used as a representation of a large vehicle.

Targeted measurements are carried out at the August Euler airfield in Griesheim and on public roads near Darmstadt, Germany. The design of experiments aims at making the respective artifact visible as isolated as possible. Generally, three replicates of each test scenario are intended. If this is not possible, e.g. because the test conditions do not allow control of the influencing factors, a particularly representative measurement trial is used for further evaluation. The test vehicle and the test site is shown in figure 3.1.

Table 3.1.: Technical parameters of the radar sensor used within this thesis

	NS	FS
$f_c$ in GHz	$\approx 76.5$	
$f_s$ in Hz	$\approx 14$	
<b>Range</b>		
$I_r$	240	112
$\Delta f_{\text{eff}}$ in MHz	360	80
$\partial r$ in m	0.42	1.8
<b>Range rate</b>		
$I_v$	256	512
$\partial \dot{r}$ in m/s	$\approx 0.12$	$\approx 0.105$
<b>Azimuth (MIMO)</b>		
$I_\phi$	16	16
$\partial \Gamma$	2.25	1.41
<b>Mounting position, antenna center</b>		
$E_{\text{go}}x$ in m	3.61	
$E_{\text{go}}y$ in m	-0.16	
$E_{\text{go}}z$ in m	0.61	0.64

---

<sup>96</sup> Thiel, C. et al.: Vehicle fleet CO2 emission regulation in the European Union (2014).

### 3.3. Application of artifact qualification method on the example of multipath propagation

When radar waves propagate, they can reflect off pavement, road infrastructure (e.g. guardrails), or traffic participants, including the ego vehicle. With respect to their reflection properties for mm-wavelength in automotive radar, many surfaces are known to cause mirror reflections that settle as mirror detections. This so-called multipath propagation alters the measurements of a radar and is well studied for the two-dimensional case under the assumption of quasi-optical radar wave behavior.<sup>97</sup> This allows to handle radar waves as a infinitely thin rays and enables automated identification schemes as shown by Roos et al.<sup>98</sup> and Prophet et al.<sup>99</sup>. The emergence of mirror reflections is not a fundamentally unwanted effect, since multipath propagation enables the detection of road users who are initially obscured.<sup>100</sup>

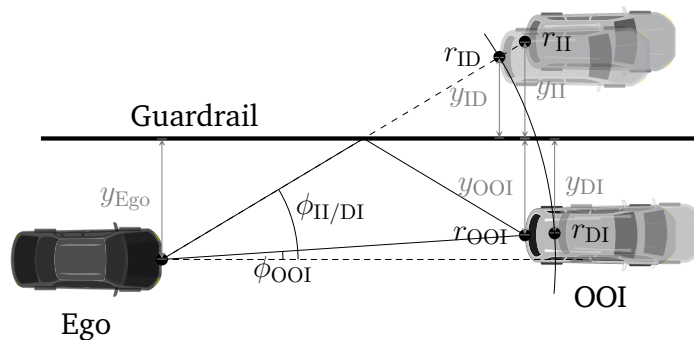


Figure 3.2.: Three cases of false targets originating from reflections off guardrails. The OOI can spawn three mirror targets at ranges  $r_{ID}$ ,  $r_{II}$  and  $r_{DI}$  that are caused due to ID, II, and DD propagation. All quantities are given in sensor centered coordinate frame.

By permuting the propagation paths for the outbound and inbound direction, there are four variants: direct-direct multipath combination (DD), indirect-indirect multipath combination (II), indirect-direct multipath combination (ID), and direct-indirect multipath combination (DI). Three combinations, i.e. II, ID, and DI, potentially produce

<sup>97</sup> Kamann, A. et al.: Automotive Radar Multipath Propagation in Uncertain Environments (2018).

<sup>98</sup> Roos, F. et al.: Ghost target identification by analysis of the Doppler distribution (2017).

<sup>99</sup> Prophet, R. et al.: Instantaneous Ghost Detection Identification in Automotive Scenarios (2019).

<sup>100</sup> Scheiner, N. et al.: Non-Line-of-Sight Detection and Tracking Using Doppler Radar (2020).

false-positive targets as illustrated in figure 3.2. The DD case, i.e. a direct reflection by the OOI, which does not cause a false positive target, is regarded as “canonical case” in the following. Multipath propagation is possible in both horizontal and vertical directions, so the following locations must be considered for reflection:

- Reflections off infrastructure elements (e.g. guardrails, tunnel walls, building façades)
- Reflections off pavement
- (Repeated) reflections at traffic participants (including the ego vehicle)

It is immediately clear that multipath propagation results in an extension of the signal path, denoted  $\ell_{mp}$ . Assuming no further separability via angle or Doppler, two cases can be distinguished:

**Case 1**  $\ell_{mp} < 2\partial r$  : The additional path length caused by multipath propagation results in a shift of the phase angle, which causes constructive or destructive interference during wave superposition.

**Case 2**  $\ell_{mp} \geq 2\partial r$  : Multipath propagation leads to a false target because the separability condition is satisfied in the range domain.

In this context, “interference” refers to the constructive or destructive superposition of electromagnetic waves. This is to be distinguished from the interference caused by the mutual interference of radar sensors. These effects were investigated in detail within the “MOSARIM” project<sup>101</sup>. For better delimitation, in the following the term “wave superposition” is used when referring to constructive or destructive wave interference in the course of multipath propagation.

Because the extension of the path length is reflected in a change of the phase position, false targets also appear in the radial velocity or angular domain once respective separability conditions are fulfilled. In the following, the effects of multipath propagation on the respective measured variables are derived analytically.

#### 3.3.1. Impact on range and azimuth measurement

The setup depicted in figure 3.2 considers horizontal multipath propagation. The targets through ID and DI paths share the same radial distance to the sensor. These targets show different lateral distances to the sensor, i.e.  $y_{ID} < y_{DI}$ ,  $y_{DI} < y_{OOI}$  and  $y_{II} = y_{OOI}$ . These distances result from the geometrical relations assuming ideal reflections.

---

<sup>101</sup> Kunert, M.: The EU project MOSARIM (2012).

The mirror targets through ID and II propagation are critical from a functional point of view, because they are displayed at the wrong azimuth angle. The importance of correctly modeling respective multipath reflections in a simulation model is derived by the following consideration, based on the standard cross section of motorways and country roads. Many German motorways are built according to RQ 31<sup>102</sup> and have two lanes that are separated by guardrails. For a radar sensor located in the middle of the right lane, this results in a lateral offset up to the guardrail of about 7.5 m.

Changes in path length resulting for the direct or indirect path are estimated by geometric considerations. This is done under the following assumptions: Quasi-optical wave propagation, one target per object located at the center of the rear of the OOI, and the reflecting surface represented by a guardrail is stationary and ideally straight. For the trivial case of direct path,  $r_{OOI}$  denotes the shortest distance between the sensor and OOI. As shown by Kamann et al.<sup>97</sup> and Roos et al.<sup>98</sup>, the distances for the indirect cases result from the lateral position to the guardrail (denoted as  $y_{OOI}$  and the position of the OOI w.r.t. the ego vehicle:

$$r_{DD} = r_{OOI} \quad (3.1)$$

$$r_{DI} = r_{II} = \frac{r_{OOI} + r_i}{2} \quad (3.2)$$

$$r_i = \sqrt{r_{OOI}^2 + (2y_{Ego})^2 - 4r_{OOI}y_{Ego} \sin(\phi_{OOI})} \quad (3.3)$$

The azimuth angle results from the direction of the reflecting beam:

$$\phi_{II} = \phi_{DI} = \arctan\left(\frac{2y_{Ego} - r_{OOI} \sin(\phi_{OOI})}{r_{OOI} \cos(\phi_{OOI})}\right) \quad (3.4)$$

$$\phi_{OOI} = \phi_{DD} = \phi_{ID} \quad (3.5)$$

Figure 3.3a shows the additional range component added to the radial distance to the OOI due to multipath propagation. The dotted lines show the azimuth angle  $\phi_{II}$  (left) and  $\phi_{DI}$  (right) in degrees. The solid contour lines represent the additional path length in m due to indirect propagation. It can be seen that the difference in lateral distance is more pronounced for the II case compared to DI/ID. The measured azimuth angle for the mirror targets results from the reflection path: If it is indirect, the mirror target will be found at the corresponding angle.

---

<sup>102</sup> RQ denotes "Regelquerschnitt" and indicates the normal cross section in meter of all paved lanes on a road.

### 3.3.2. Impact on Doppler measurement

Recall that the Doppler frequency  $f_D$  is proportional to the temporal change of path length traveled by the wave between sender and receiver, denoted as  $\ell_{Tx,Rx}$ :

$$f_D \propto \frac{d\ell_{Tx,Rx}}{dt}. \quad (3.6)$$

Distortion of radial velocity measured by Doppler shift occurs when a difference in time derivatives of direct and indirect path lengths exists. Considering multipath propagation, this means that Doppler shifts are accumulated along the wave propagation direction. Formally, this relationship can be expressed by the scalar product of  $\ell_0$ , which is the normalized vector-valued Cartesian direction of the electromagnetic wave, and the absolute vector-valued Cartesian velocity at each of the  $I$  interaction points:

$$\dot{r}_{\text{abs}} = \sum_{\iota=0}^I \langle \ell_{0,\iota}, \mathbf{v}_\iota \rangle \quad (3.7)$$

Here,  $\mathbf{v}_\iota = [v_{k,x}, v_{k,y}, v_{k,z}]$  is the absolute velocity of an object at  $\iota$ -th wave interaction point. Assuming a pure longitudinal movement for the ego and OOI, the following radial velocities result:

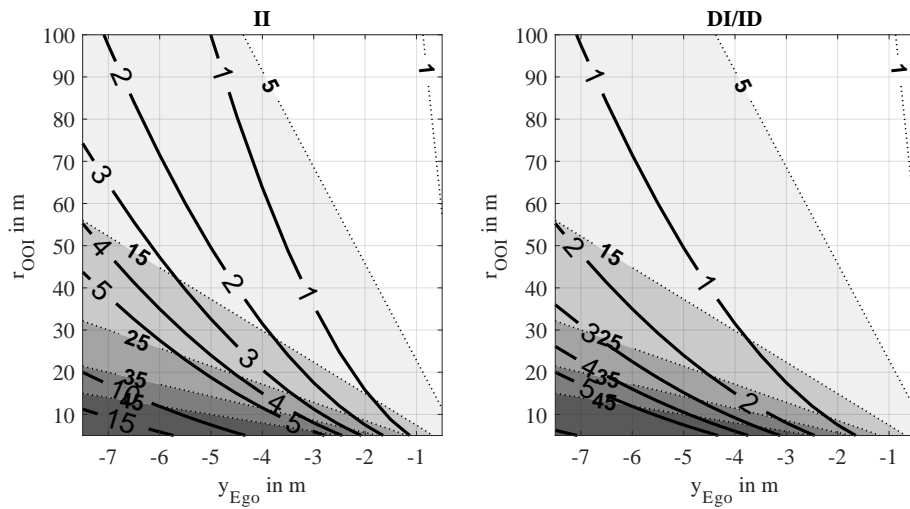
$$\dot{r}_{\text{rel,II}} = (v_{\text{OOI}} - v_{\text{Ego}}) \cos(\phi_{\text{II}}) \quad (3.8)$$

$$\dot{r}_{\text{rel,DI/ID}} = v_{\text{OOI}} \cos\left(\frac{\phi_{\text{II}}}{2}\right) - v_{\text{ego}} \left(\frac{1 + \cos(\phi_{\text{II}})}{2}\right) \quad (3.9)$$

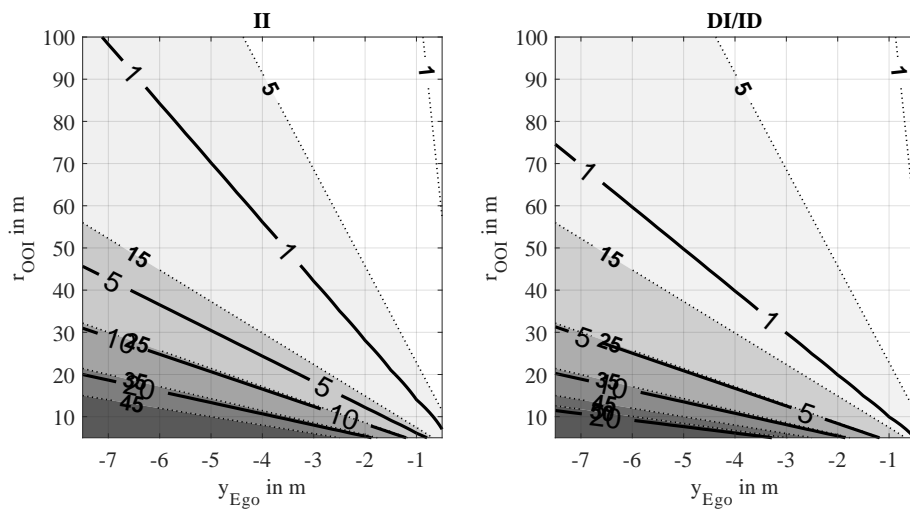
In the multipath propagation scenario presented above, the Doppler shift for the II propagation is purely exposed to the angular position, and for the ID/DI case it is composed of the angular component of the velocity of the OOI.

The deviation of the radial velocity for mirror targets is shown in figure 3.3b: It deviates significantly for the II case compared to ID or DI, especially at greater distances. As with distance, the velocity deviation for the II case is more distinct. It is expected that this case will be easier to identify from measurements than the DI/ID case. A higher relevance of the II path constellation is emphasized for modeling purposes, since it leads to larger measurement errors.

So far, only the case of horizontal multipath propagation has been investigated. For vertical multipath propagation, caused by reflections off the pavement or tunnel walls, geometrically similar conditions arise. Vertical multipath propagation over the road surface shows a negligible influence if sensor installation heights in the range below 1 m are considered.



(a) Range distortion



(b) Doppler distortion

Figure 3.3.: Range and Doppler distortion under multipath propagation. Solid lines denote the relative difference compared to the canonical case. Dashed lines denote contour lines for the respective azimuth angles for the mirror targets.

### 3.3.3. Wave superposition due to multipath propagation

Wave superposition manifests itself in fluctuation of received power, since the electromagnetic waves can superpose constructively or destructively, depending on the phase difference of the direct or indirect propagation path. This phenomenon is a well-known feature in (automotive) radar measurements. Regarding the formation of wave superposition, it is irrelevant whether multipath propagation occurs in horizontal or vertical direction, since only the phase difference between respective paths is the determining factor. The instantaneous phase is calculated from the distance  $\ell$  traveled by the wave that shows an initial phase shift  $\varphi_0$ :

$$\varphi = \varphi_0 + 2\pi \bmod \frac{\ell}{\lambda} \quad (3.10)$$

Electromagnetic waves are superimposed constructively for even and destructively for odd multiples of  $\pi$  in phase difference. Under the assumption of a point object, in the well-known book by Skolnik<sup>103a</sup> it is shown that the resulting amplitude fluctuation takes the form of a harmonic oscillation with angular frequency  $\omega_{mp}$ . When using a corner cube reflector (CCR), which reflects the incident wave back in the same direction, this frequency is proportional to the CCR and sensor height, denoted as  $h_{CCR}$  and  $h_S$ , respectively. The reflection off the road surface thus results in an indirect propagation path with the designation  $\ell_I$ , which differs from the direct propagation path by an additional path length  $\ell_{mp}$  and thus by a different phase angle. The received power signal then shows a harmonic oscillation over reciprocal range, i.e.

$$P_{Rx} \propto 16 \sin^4 \left( \underbrace{\frac{2\pi h_{CCR} h_S}{\lambda}}_{\omega_{mp}} \frac{1}{r} \right) \quad (3.11)$$

Eq. 3.10 and 3.11 assume that the superposition phenomenon occurs as the direct and indirect propagated waves merge at the (point) object. If waves superimpose at the receiver, i.e. direct and indirect paths merge at the receiving antenna,  $\omega_{mp}$  doubles due to the double path length.

A typical reference scenario for wave superposition is observed when approaching a CCR as shown in figure 3.4. If the object remains at a certain height during the approach, a sinusoidal oscillation (see eq. 3.11) can be seen if the amplitude is plotted over the interpolated reciprocal distance. The distinction of over/under-driveability of objects

---

<sup>103</sup> Skolnik, M. I.: Introduction to Radar Systems (2001). a: pp. 484-486; b: p. 66.

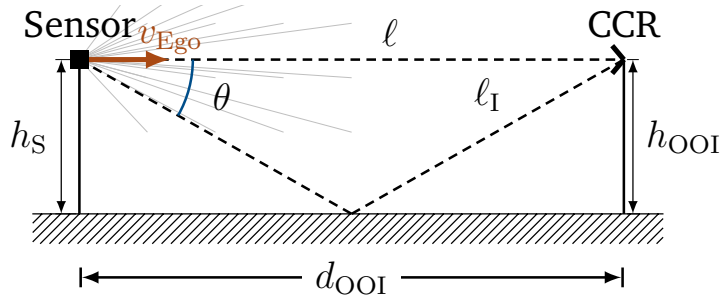


Figure 3.4.: Vertical multipath propagation with a CCR at distance  $d_{OOI}$  from a sensor that travels with  $v_{Ego}$  straight towards a CCR. The length of the direct and indirect path is denoted as  $l$  and  $l_I$ , respectively. Note that  $l_{mp} = l_I - l$ . The indirect path is incident on the sensor under elevation angle  $\theta$  while assuming ideal specular reflection off the pavement.

can be made by evaluating the wave superposition patterns according to a patent filed by Schneider<sup>104</sup>. The method is based on the assumption of a monostatic radar in which wave superposition occurs at the object. Distinct wave superposition pattern results for variable object heights and distances, as shown in figure 3.5. It is to be postulated that automotive radar measurements are principally exposed to superposition effects due to the presence of multipath propagation (e.g. over the pavement).

In order for wave superposition effects to occur in dynamic scenarios, the reflection induced by multipath propagation must not settle at more than twice the radar cubic cell width of the direct reflection, which means that no separability criterion is fulfilled. This requires  $l_{mp} < 2\delta r$  in range measurement domain, see p. 44. This condition is satisfied for azimuth during a straight approach towards a CCR. Separability in Doppler domain, which usually resolves particularly fine in automotive radar, represents the sharpest criterion. The temporal change of path length results in a different radial velocity of the indirect path. For longitudinal movement, it is assumed that  $\dot{l} = \dot{d} = v_{Ego}$ . Given a point object with height  $h_{OOI}$  located at distance  $d_{OOI}$  (see figure 3.4) target separability via Doppler can be excluded if the velocity difference between the direct and indirect path is significantly smaller (e.g. by a factor of 10) than the Doppler resolution cell  $\delta \dot{r}$ . When choosing  $h_S = h_{OOI}$  as simplification, it follows:

$$\cos(\theta) = \frac{d_{OOI}}{l_{mp}} = \frac{d_{OOI}}{\sqrt{d^2 + (2h)^2}}; \quad \dot{l}_{mp} = \frac{\partial l_{mp}}{\partial t} = \frac{d_{OOI}}{\sqrt{d_{OOI}^2 + (2h)^2}} \dot{d} = \cos(\theta) \dot{d}_{OOI} \quad (3.12)$$

<sup>104</sup> Schneider, R.: Method for processing radar signals (1999).

### 3. What do we need in a radar simulation for virtual testing of AD?

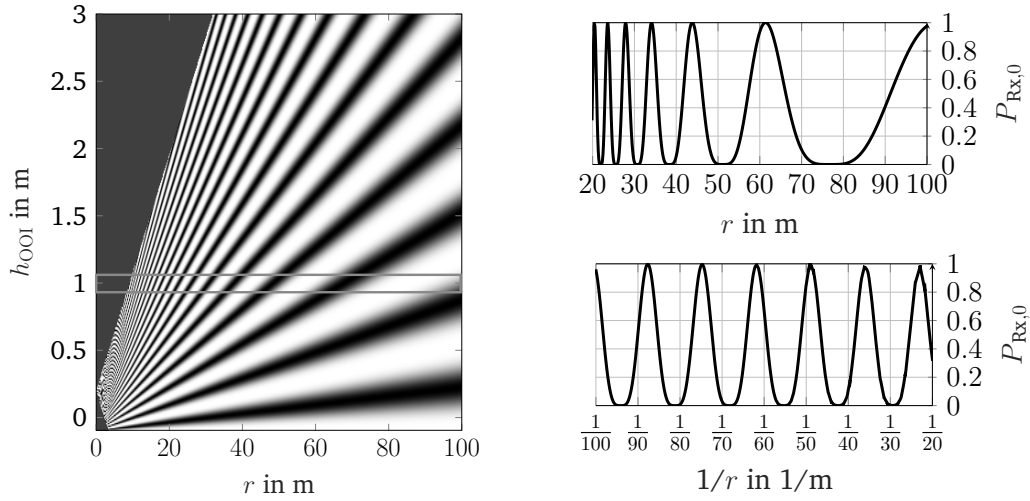


Figure 3.5.: Wave superposition pattern caused by multipath propagation for a given sensor and object height (left) and received normalized power of  $P_{\text{Rx},0}$  over reciprocal distance reveals harmonic oscillation due to multipath wave superposition (right). Additional signal attenuation is neglected for clarity.

Thus, for the estimation of the maximum velocity difference between the paths with which superposition effects are to be expected, the following is obtained:

$$\dot{\ell} - \dot{\ell}_{\text{mp}} = v_{\text{Ego}} - v_{\text{Ego}} \cdot \cos(\theta) < 1/10 \cdot \partial \dot{r} \quad \text{where } \tan(\theta) = \frac{2h_{\text{OOI}}}{d_{\text{OOI}}} \quad (3.13)$$

$$\implies d_{\text{OOI}} > \frac{2h_{\text{OOI}}}{\tan\left(\arccos\left(1 - \frac{\partial \dot{r}}{10v_{\text{Ego}}}\right)\right)} \quad (3.14)$$

Eq. 3.14 results in a lower boundary for  $d_{\text{OOI}}$  of about 14 m for the radar mounting height used in this dissertation (see table 3.1). Below this distance, multipath wave superposition pattern would not be observable because no wave superposition occurs in the affected cells of the radar cubic as separability via Doppler is given.

In the course of multipath wave superposition investigations during dynamic scenarios within this dissertation, it is assumed that these additional conditions (no separability by Doppler or azimuth angle) are met because the investigated distances are larger than the identified critical distance.

### 3.4. Multipath application case 1: Visibility of occluded objects

Electromagnetic waves emitted by a radar sensor can reach objects that are not in the direct line of sight due to multipath propagation.

#### 3.4.1. Reference scenarios

An occlusion scenario is created by a vehicle that is between the ego vehicle and another vehicle: In the selected scenario, a BMW i3 cruises with about 40 km/h in front of the ego vehicle which adjusts a constant time gap via ACC. A VW Crafter drives at about 50 km/h in front of the BMW i3. Thereby, the distance between BMW i3 and VW Crafter increases over time, see figure 3.6a. The visibility of the occluded VW Crafter in the radar measurements is examined during three measurement repetitions. In a second variant, a convoy consisting of three vehicles traveling in the same lane is studied. All vehicles maintain their speeds by means of ACC, resulting in a quasi-stationary scenario. At time  $t_1$ , car 2 changes lanes and accelerates, see figure 3.6b. The visibility of objects is examined by means of the received power reported for the central radar beam in the respective Doppler cell.

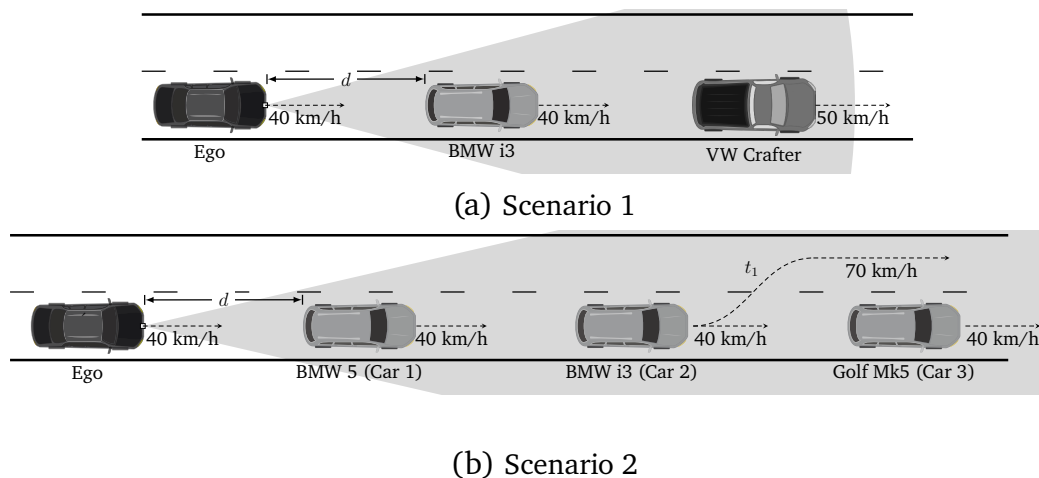


Figure 3.6.: Occlusion reference scenarios. Top: Masked vehicle in front with the distance between the vehicles in front increasing continuously, Bottom: Convoy with a vehicle leaving at time  $t_1$ .

### 3.4.2. Observations from measurements

Those radar cubic cells that are occupied by the VW Crafter are evaluated in terms of their signal-to-noise ratio (SNR). Its calculation rule is given in appendix A.2. Based on the vehicle dimensions, it should be noted that the BMW i3 is about 20 cm narrower than the VW Crafter. According to the intercept theorem, direct visibility of the VW Crafter to the sensor is given only up to 30 m after its starting position. Afterwards, the VW Crafter can only be seen through the glass panes of the BMW i3, by refraction or via multipath propagation when reflected off the pavement. It can be seen from figure 3.7 that the SNR decreases in accordance with the distance law (i.e.  $\propto 1/sr^4$ ). The maximum distance up to which the VW Crafter is visible is limited by the noise floor.

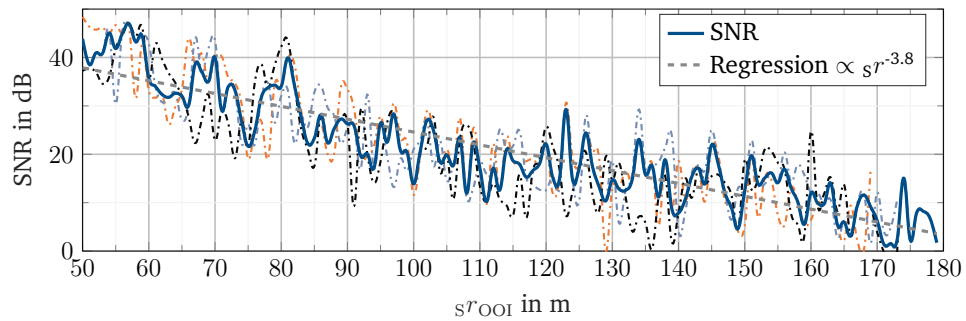


Figure 3.7.: SNR for occluded OOI (here: VW Crafter) in scenario 1: Measurements from three trials are depicted and the averaged value is highlighted.

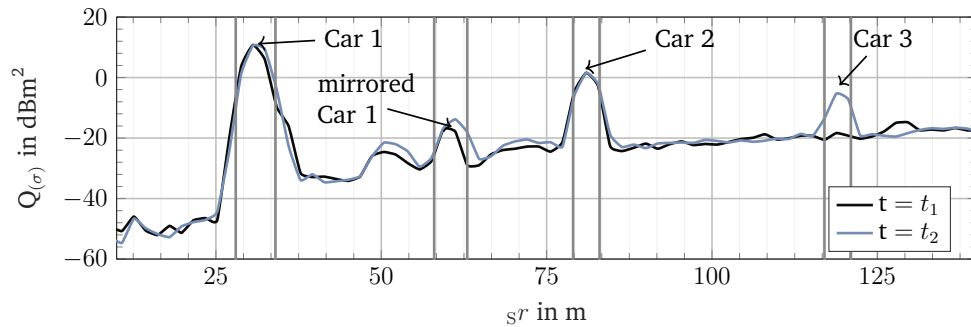
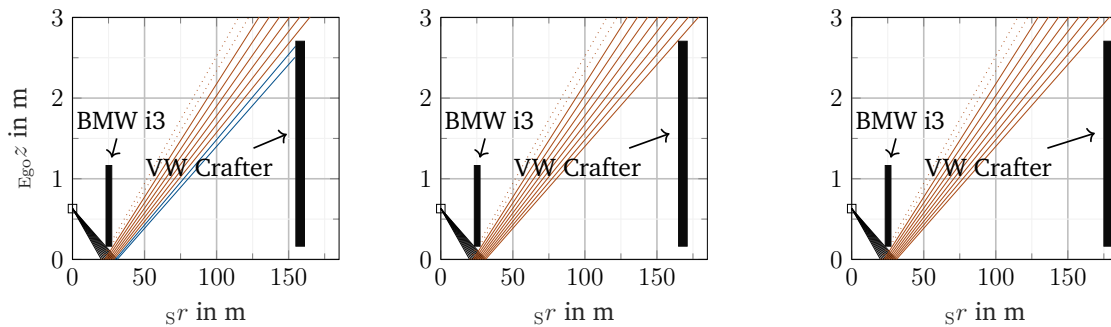


Figure 3.8.: RCS over distance for scenario 2: As car 2 moves out at time step  $t_2$ , car 3 becomes visible.

The evaluation of the convoy scenario shows that one occluded vehicle is reliably detected: Just as soon as car 2 moves out, car 3 becomes visible (i.e.  $SNR \gg 0$ ). A mirror reflection of car 1 can be detected at twice the distance.

### 3.4.3. Implications for modeling



(a) VW Crafter at 155 m

(b) ... at 165 m

(c) ... at 175 m

Figure 3.9.: Idealized ray paths with specular reflection off the pavement. The BMW i3 is located about 23 m from the ego vehicle with the sensor mounted at 0.63 m. By specular reflection, the Crafter is visible up to 165 m. Line color assignment: Rays from sensor to pavement (—), rays obscured by BMW i3 (.....), reflected rays (—), subset of reflected rays that reach the VW Crafter (—).

A trivial explanation for the visibility of hidden objects results from the assumption of specular reflection properties at the road surface. Figure 3.9 shows the idealized ray path including reflections off an ideally smooth road surface with a VW Crafter at different distances to the sensor. The result for the convoy scenario (scenario 2) can also be explained by reflection: Here, car 2 is located at approx. 80 m. Assuming an object height similar to the BMW i3, there are rays intersecting with car 2, but no ray path to the occluded car 3 exists. As soon as car 2 moves out, the intersection of a ray with car 3 is possible. The detection ability of occluded objects, however, cannot be fully explained by specular reflections off the pavement. It is expected that reflection paths outside the directions of specular reflections exists. This is due to uneven surfaces and inhomogeneous surfaces roughness of the pavement: Then, detectability of occluded objects is limited by the dynamic range of the sensor and the total reflectivity of occluded objects in the distance.

For model falsification, the reference scenarios 1 and 2 are executed in the simulation. The received power determined by the sensor model is examined for the retention of the described characteristics.

### 3.5. Multipath application case 2: Repeated reflections at sensor

---

When a radar wave bounces repeatedly between reflecting surfaces, for example originating from the radar in the ego vehicle, reflecting off the OOI, then back to the ego vehicle and again towards the OOI, an effect similar to the infinite mirror effect<sup>105</sup> occurs. Such a repeated reflection can be perceived by a radar sensor as long as the receiving power is above the noise floor. As the wave travels twice the distance, the mirror target appears at twice the distance between the sensor and OOI. Since the Doppler shift is added along the path, the mirror target shows a doubling of its measured radial velocity.

#### 3.5.1. Reference scenario

An exemplary reference scenario that causes this artifact is shown in figure 3.10.

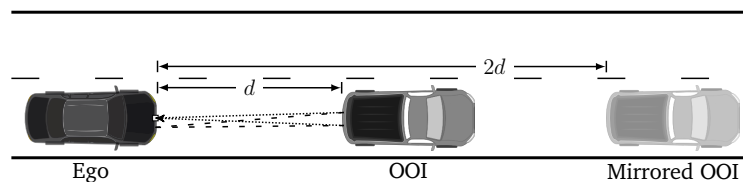


Figure 3.10.: Reference scenario 3: The wave bounces multiple times between ego and OOI before returning to the sensor.

The OOI starts at about 10 m in front of the ego vehicle and leaves the longitudinal measuring range of the radar. To evaluate the influence of the ego vehicle, the test is also performed with the sensor mounted on a wooden test stand as well as with the sensor mounted in the ego vehicle. Two aspects of the experiment are considered:

1. The speed of the mirror target is compared to the speed of the OOI, which is determined by the ADMA.
2. To characterize the effect in terms of sensitivity to different types of vehicles, the test is repeated with different vehicles. The reliability with which the mirror target occurs is investigated.

---

<sup>105</sup> Two or more parallel mirrors create a series of ever smaller reflections that seem to continue to infinity.

To make the measurements robust to uncertainties due to the unevenness of the pavement, the tests are repeated three times at four different locations along the runway of the August Euler airfield. Targets are extracted from the radar cubic and are used for the sensitivity study in relation to the vehicle type. As it is assumed that a repeated path is present until the signal intensity of the multipath reflection is no longer different from the noise, the SNR is analyzed.

### 3.5.2. Observations from measurements

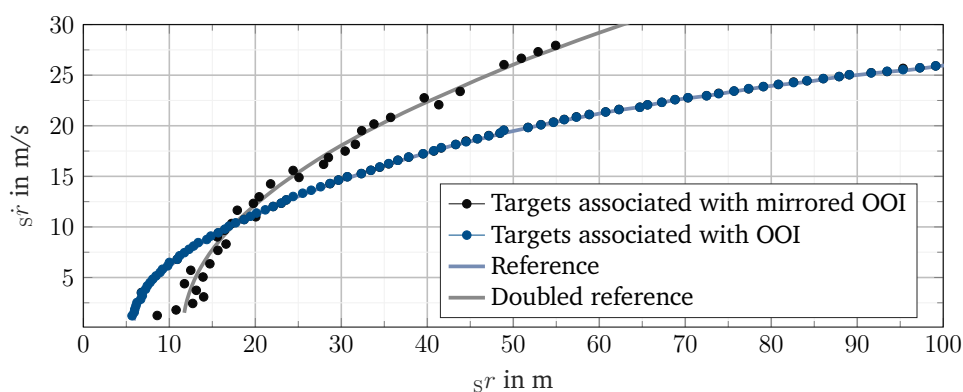


Figure 3.11.: Range and radial velocity for accelerating mirror target.

The theory of the Doppler shift adding up along the path extension is confirmed in the evaluation of the measurements in test variant 1, depicted in figure 3.11. As expected, the mirrored targets, which are located at twice the distance, are consistently measured at twice the speed of the OOI. The reference is found from the ADMA device that is mounted in the OOI. It is noteworthy that the radar's precision in measuring the mirrored targets decreases.

Regarding the longitudinal distance up to which the mirror target can be measured, the cumulative distributions of the measured values for all three vehicles show a homogeneous picture, cf. 3.12. The left column shows the distances to the targets that can be assigned to the real or the mirror target as empirical cumulative distribution function (ECDF) plot. In the right column, the SNR values of the real targets and mirror targets are compared. In NS and FS measurement mode, 90 % of the measured values assigned to the mirror target appear within up to 50 % of the respective maximum range. It is noticeable that the BMW i3 shows higher backscatter intensity and therefore its

### 3. What do we need in a radar simulation for virtual testing of AD?

---

mirrored targets are visible even at greater distances. The backscatter intensities for the Golf Mk5 and the Golf Mk7 are similar.

The SNR analysis shows that the intensities of the mirror targets are about 21-27 dB lower than the intensities of the targets that belong to the actual object. This is motivated by two contributions: The doubled distance absorbs  $10 \log_{10}(2^{-4}) \approx -12$  dB. An additional signal attenuation results from the ratio between the areas of the OOI (estimated as 2 m in width and 1 m in height, i.e.  $A_{OOI} = 2 \text{ m}^2$  and the sensor (estimated with an area  $A_S = 0.1 \text{ m}^2$ ). Therefore:

$$10 \log_{10}(A_S/A_{OOI}) = 10 \log_{10}(0.1 \text{ m}^2/2 \text{ m}^2) = -13 \text{ dB}. \quad (3.15)$$

Both contributions lead to a SNR attenuation of about -25 dB, which can be seen in the measurements.

#### 3.5.3. Implications for modeling

It has been shown that the cause of reflection is caused by the sensor itself and is slightly amplified by potentially reflective parts of the ego vehicle's body (radiator grille, metallic coatings, etc.). The electromechanical design of a radar sensor with the antenna mounted on a printed circuit board (PCB) plate shows very good reflection characteristics for mm-waves. This facilitated reflection of the incident wave back to the OOI. Examination of the mirror targets by wave reflection at the sensor shows that this artifact occurs with high reproducibility with various compact class vehicles. The decrease of the signal strength in relation to the SNR is explained by the doubled path length and the size ratios of the reflecting surfaces.

#### 3.5.4. Falsification criteria

Obviously, this effect is present in all investigated vehicles, so that it has to be represented in the simulation with compact class vehicles. Although isolated outliers at larger distances can be identified w.r.t. mirror targets caused by the BMW i3, the tendency for all investigated vehicles is that the mirror effect can be represented in a simulation model up to 40 % of the maximum sensor range. Here, the speed of the mirror targets must be twice the speed of the OOI.

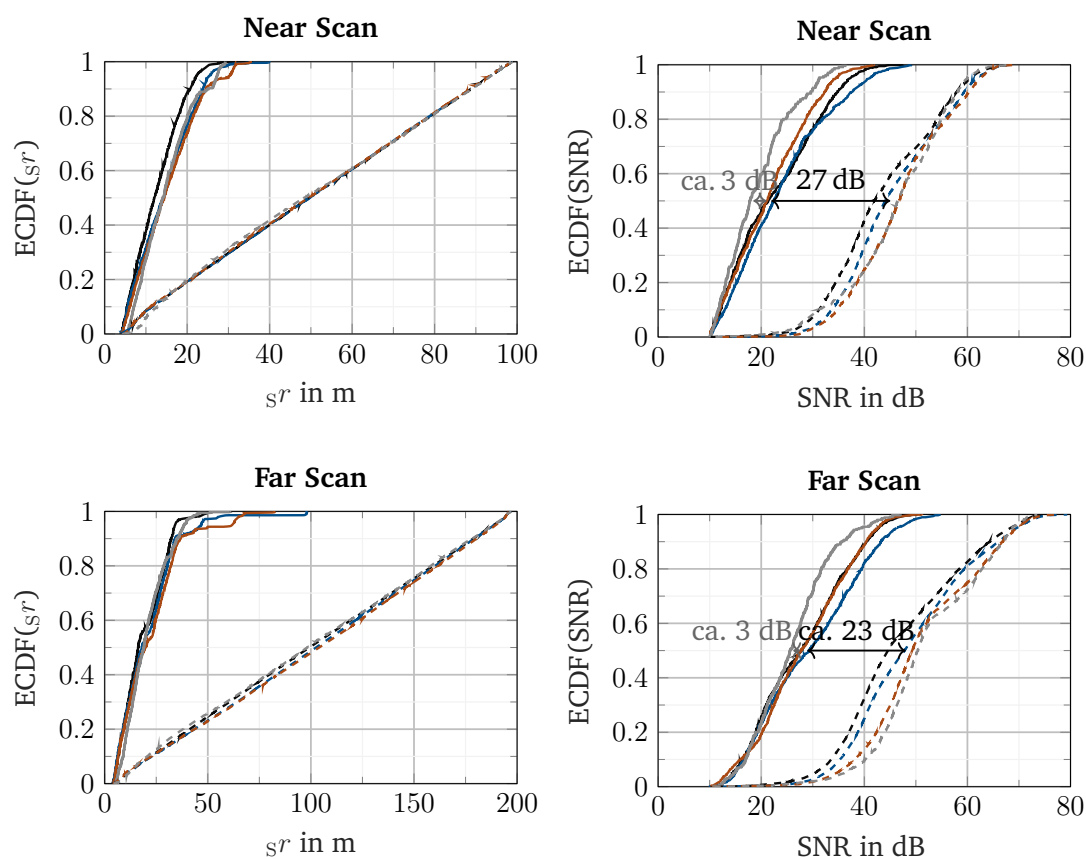


Figure 3.12.: Statistical analysis of mirror targets due to repeated reflections off the sensor. Solid line refers to mirrored targets, dashed line to real target. The mirror targets are visible up to about 30 % of the maximum sensor range. The drop in SNR is between 23 and 27 dB for NS or FS. Line color assignment: Golf Mk5 (—), Golf Mk7 (—), BMW i3 (—), BMW i3 with radar sensor mounted on a wooden bench (—).

### 3.6. Multipath application case 3: Horizontal reflections at guardrails

---

This paragraphs analyzes mirror targets that are associated with horizontal multipath propagation paths as shown in figure 3.2.

#### 3.6.1. Reference scenario

Metallic crash barriers on both sides are often found on motorways. Figure 3.13 shows the german motorway A6 (E50) as an example. The selected reference scenario is based on figure 3.2 where the ego vehicle, driving on the right lane, is overtaken on the left. In the selected test drive, the BMW i3 was observed over a distance of about 260 m.



(a) Google Street View image of an exemplary Autobahn situation with guardrails on both sides. Source: "E50 Mannheim, Baden-Württemberg." 49°55'47.12" N and 8°49'82.96" E. Google Earth. May 2009. June 12, 2020.



(b) Guardrails obstructed by vegetation on A6 near Darmstadt on August 19, 2020.

Figure 3.13.: Typical scenario on German motorways with guardrails on both sides.

### 3.6.2. Observations from measurements

The radar measurements are analyzed on the target level, cf. 2.2. As the BMW i3 is equipped with an ADMA, its relative position and movement is known and facilitates the assignment of targets reported by the radar. All generated mirror targets are examined w.r.t. their position and speed.

Figure 3.14a shows the expected location of mirror targets according to the theory presented in section 3.3.1 and 3.3.2 for all four permutations of reflection paths occurring at the left and right barrier. It can be seen that the measured targets settle at locations according to the theoretical consideration. The position of the guardrail is estimated by means of a random sample consensus (RANSAC) filter identifying static targets on a straight line. The estimation is facilitated because the guardrail can be assumed to be straight in the section under investigation, as shown in figure 3.13a. Based on the distance between sensor and OOI, a differentiation regarding the actual propagation path is not possible due to the small difference in path length. More insights can be obtained by examining the radial velocity component, which differs noticeably for the II and DI path, see figure 3.14b.

It is noticeable that mirror targets induced by the right guardrail are only visible above a certain distance. Obviously, the angle-dependent reflection properties of the OOI and the guardrail only adjust at this distance in such a way that mirror targets can emerge.

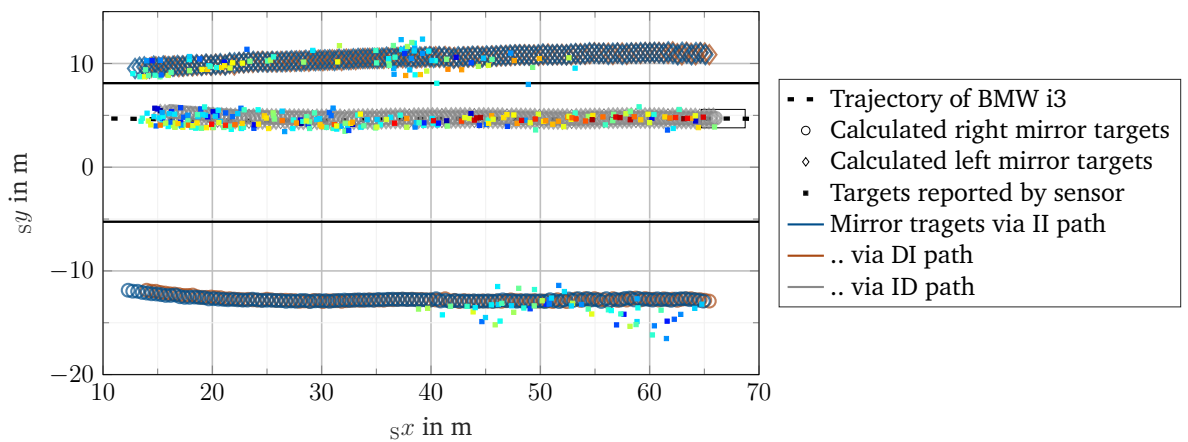
### 3.6.3. Implications for modeling

The examination of the mirror targets on the selected route section shows that both II and DI/ID propagation paths form and must be considered by the sensor model. Although these mirror targets tend to follow the mathematical description model, they are subject to considerable noise. It should be noted that the theoretical model assumes ideal reflections and even small deviations would render as noise. The collection of data on the motorway in normal traffic conditions is difficult because possible propagation paths may be temporarily obscured by other road users, local damages, or vegetation, cf. 3.13b. Due to the obviously high sensitivity, a stable occurrence of this artifact under real conditions is not to be expected.

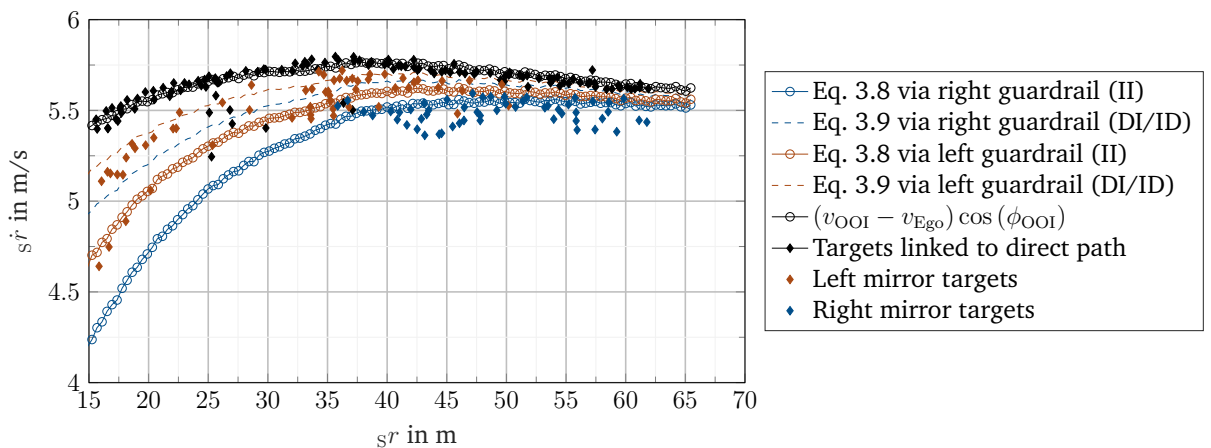
### 3.6.4. Falsification criteria

In a scenario with a guardrail, mirror targets must be formed by direct and indirect wave propagation during exposure over a longer period of time.

### 3. What do we need in a radar simulation for virtual testing of AD?



(a) Spatial distribution of (mirror) targets linked to the OOI. Minor differences in path lengths between II and DI as well as direct path and ID make respective separation barely possible. Targets are colorized according to RCS.



(b) Range - range rate distribution of targets linked to the OOI. Separation by propagation path is facilitated by differences in range rate.

Figure 3.14.: Mirror targets on guardrails induced by multipath propagation.

## 3.7. Multipath application case 4: Wave superposition patterns and shaking factor

---

Wave superposition patterns are particularly easy to observe when approaching a CCR, see figure 3.5. However, it cannot be assumed that the point object assumption holds for large objects, such as vehicles, as they do not exhibit the same backscatter characteristics as a CCR. Therefore, the characteristics of wave superposition patterns for large objects are examined in two steps. First, the wave superposition pattern for CCR of different sizes is extracted from respective measurements. Then, the wave superposition pattern as caused by vehicles is analyzed. The shaking factor in the radar equation (eq. 2.1) is determined by the fluctuations of the received power induced by wave superposition.

### 3.7.1. Reference scenarios

The ego vehicle approaches a CCR, which is mounted at a fixed height, starting at a distance greater than the maximum range of the sensor, see figure 3.15a. The experiment is conducted with two CCR having a radar cross section (RCS) of  $Q_{(\sigma),CCR1} = 4.3 \text{ dBm}^2$  and  $Q_{(\sigma),CCR1} = 26.6 \text{ dBm}^2$  and three repetitions, respectively. In this notation the RCS value in logarithmic scale reads  $Q_{(\sigma)}$  and is of unit  $\text{dBm}^2$ . It is used to denote a level value. Consequently,  $\sigma$  designates an RCS value in the linear range.

To examine the behavior of extended objects, two tests are conducted: In the first test variant, the ego vehicle remains stationary while the OOI moves out of the radar's distance measurement range (cf. 3.15b) at  $v_{OOI} = 10 \text{ km/h}$ . Then, both vehicles move but the OOI moves a little faster (i.e.  $s\dot{r}_{OOI} = 10 \text{ km/h}$ ) so that it gradually moves out of the measuring range of the radar, cf. 3.15c. The test was performed with four vehicles and three repetitions each: Golf Mk5, Golf Mk7, Audi A3 8V and BMW i3. The weather conditions were the same in all tests (cloudy, dry asphalt, approx. 7-15 °C air temperature). The selected section of track was characterized by a homogeneous slope so that the reflective properties of the pavement were not influenced by hilltops or sinks.

### 3.7.2. Observation from measurements

The evaluation of the measurements is performed based on the targets reported by the radar. If several targets can be assigned to the OOI, the strongest reflection w.r.t. the RCS is selected. The received power is transferred into the linear RCS range and interpolated linearly into an equidistant  $1/r$ -range. After smoothing with a Savitzky-

### 3. What do we need in a radar simulation for virtual testing of AD?

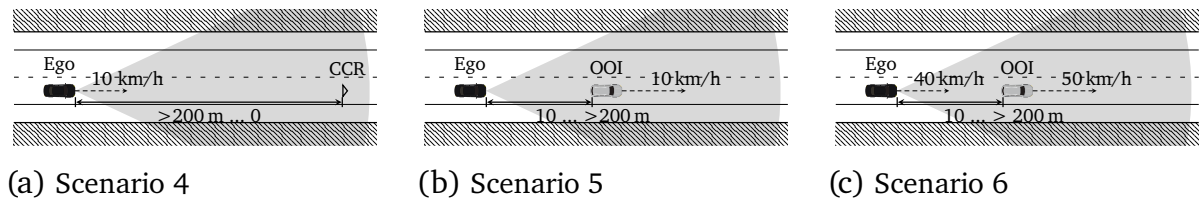


Figure 3.15.: Illustration of scenarios 4-6 for estimating shaking factor. CCR approach (scenario 4), static ego (scenario 5), and dynamic ego (scenario 6) for quantification of shaking factor.

Golay filter of third order with a frame length of five samples, frequency analysis is performed by a discrete Fourier transformation (DFT). The height spectrum according to Diewald/Schneider is used as an evaluation tool, from which the expected superposition-related periodicity is visible as object height over ground. A more detailed description of the procedure is given in appendix A.1.

#### Verification of the “point object” assumption

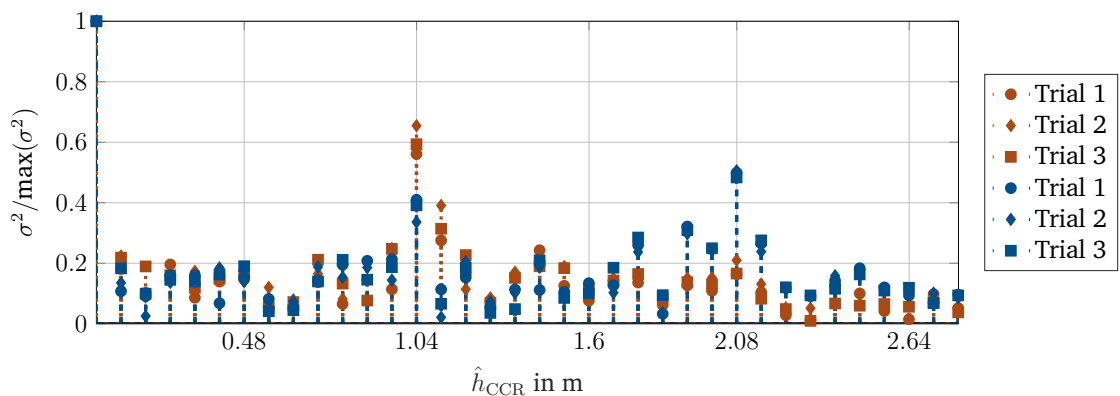


Figure 3.16.: Object height estimation based on the Diewald/Schneider method with two CCR mounted at  $h_{CCR,GT} = 1.0$  m.  $Q_{(\sigma),CCR1} = 4.3$  dBm<sup>2</sup> (—),  $Q_{(\sigma),CCR2} = 26.6$  dBm<sup>2</sup> (—). The ordinate is nominated to the respective maximum RCS value in linear scale.

The measurements evaluated in figure 3.16 reveal that the point object assumption is no longer fulfilled for the large CCR: The peak value settles at twice the frequency and thus twice the estimated height when considering the large CCR. Taking into account that Diewald/Schneider method assumes a point object where wave superposition occurs

at the object, it is shown that this is not the case for large CCR because the height is overestimated by a factor of 2. The resulting duplication of the period length provides an indication that signal cancellation due to destructive wave superposition occurs at the transmitting site (i.e. the sensor) and not at the object.

### Wave superposition with vehicles

The static and dynamic scenario (see figure 3.15b and 3.15c) was conducted with each of the studied vehicles (i.e. Golf Mk5, Golf Mk7, BMW i3, and Audi A3) at four starting positions with three repetitions each. The RCS values observed under the dynamic scenario give the impression of a dominant stochastic noise as seen in figure 3.17. The figure shows RCS behavior over time in the dynamic scenario during one of the trials with the Golf Mk5 and BMW i3, respectively. In contrast to the experiment with a CCR, no clear wave superposition patterns are observed. After filtering by means of a moving median filter over 10 s, the RCS shows a smoother curve of about 15-20 dBm<sup>2</sup>.

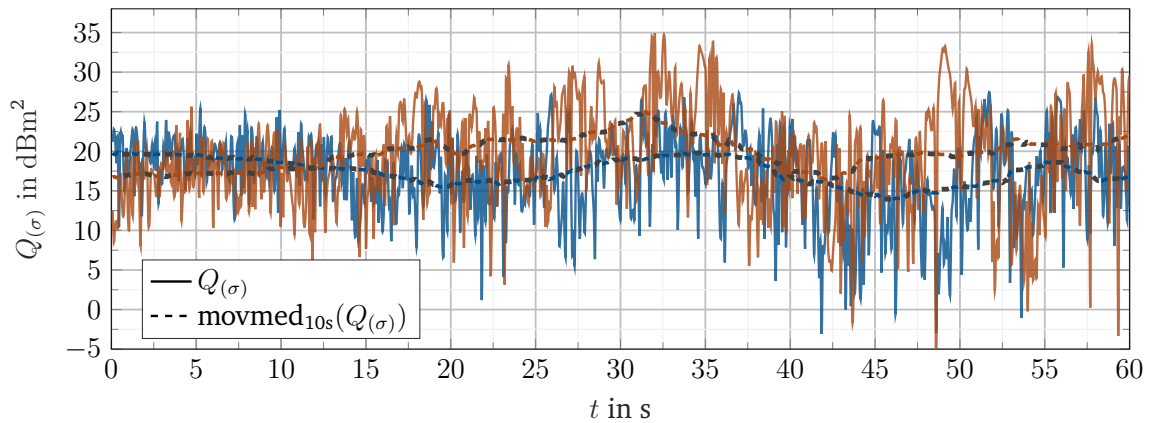


Figure 3.17.: RCS behavior over time in a dynamic scenario. The diagram shows unprocessed RCS values and after smoothing by a moving median filter over 10 s. Line color assignment: Golf Mk5 (—), BMW i3 (—).

Figure 3.18 shows the respective height spectra observed for NS and FS. The static scenario shows isolated significant oscillations in the height spectrum in only one to two out of 12 trials. No pattern of regularity can be seen in the dynamic scenario. The observation is confirmed for all four vehicles in the used vehicle collective.

In order to examine the stochastic character in the fluctuation of RCS in more detail, first its “stationary” contribution, which is available via moving median filtering, is

### 3. What do we need in a radar simulation for virtual testing of AD?

---

subtracted and transferred to linear range after delogarithmization:

$$\sigma_{\xi} = \text{delog} \left( Q_{(\sigma),\text{OOI}} - \text{movmed}_{10s} \left( Q_{(\sigma),\text{OOI}} \right) \right) \cdot \text{m}^2 \quad (3.16)$$

In order to describe the stochastic character of  $\sigma_{\xi}$ , i.e. the portion of fluctuation that is superimposed on the RCS, two probability distribution functions provide a physically plausible explanation: The log-normal distribution is capable of representing values that range between arbitrarily small and a limited upper maximum values. This captures the conditions of received power in a radar measurement. On the other hand, the exponential distribution describes the random path length and hereby a random phase of each received signal. When considering the presence of wave superposition, this reflects the stochastic character of the received power.

In general radar technology, Swerling models are widely used for describing amplitude fluctuation.<sup>106,103b</sup> These models originate from airspace surveillance radar systems and aim at mapping variable backscatter characteristics of objects between measurement cycles. The Swerling 1 model describes an exponential distribution and assumes that the OOI consists of a number of equally large isotropic reflectors while the Swerling 3 model expects one dominant reflector that is superimposed by multiple small reflectors.<sup>107</sup> It corresponds to a the Chi-squared distribution with four degrees of freedom. The Swerling models would also apply to measurement conditions in automotive radar, although multipath superposition effects are not explicitly considered.

All measured values obtained during the test repetitions with all vehicles in each case are considered. A stochastic description of the amplitude variation of all tested vehicles is examined. A detailed analysis by vehicle can be found in the appendix A.3. A log-normal distribution as well as a Swerling 1 and 3 model are parameterized using the maximum likelihood estimation (MLE) method. Respective estimated parameters are given in table 3.2. Samples from the obtained distributions are shown in the diagram. The exponential distribution comprises a scale parameter  $\sigma_{\text{exp}}$ . Its cumulative distribution function (CDF) can be rewritten into a linear function:

$$\begin{aligned} \text{CDF}_{\text{exp}}(\sigma_{\xi}) &= 1 - e\left(-\frac{\sigma_{\xi}}{\sigma_{\text{exp}}}\right) \\ 1 - \text{CDF}_{\text{exp}}(\sigma_{\xi}) &= e\left(-\frac{\sigma_{\xi}}{\sigma_{\text{exp}}}\right) \\ \log(1 - \text{CDF}_{\text{exp}}(\sigma_{\xi})) &= -\frac{\sigma_{\xi}}{\sigma_{\text{exp}}} \end{aligned} \quad (3.17)$$

---

<sup>106</sup> Gamba, J.: Radar Target Detection (2019), p. 53.

<sup>107</sup> Swerling, P.: Probability of detection for fluctuating targets (1960).

A number of observations can be made from the shape of ECDF depicted in figure 3.19: Apparently, the log-normal distribution overestimates the frequency of occurrence of large RCS values. The Swerling 1 model (i.e. exponential distribution) balances drifting between the data points from the static and dynamic experiment. The Swerling 3 model cannot capture the fluctuation range of the RCS. When analyzing the range of small RCS values, a “tilted” exponential distribution provides a higher quality of description for small RCS values.

The slope of the exponential function in the 1-ECDF plot can be tilted by introducing an exponent  $n_{\text{tilt}}$ :

$$\text{CDF}_{\text{exp,tilt}}(\sigma_{\xi}) = 1 - e\left(-\frac{\sigma_{\xi}}{\sigma_{\text{tilt}}}\right)^{n_{\text{tilt}}} \quad (3.18)$$

Both shape parameters  $\sigma_{\text{tilt}}$  and  $n_{\text{tilt}}$  are determined from the  $\log(1 - \text{ECDF})$  plot through linear regression and are given in table 3.2.

The probability density function (PDF), which shows a distribution of the RCS values to describe the amplitude fluctuation, is derived from the CDF:

$$\text{PDF}_{\text{exp,tilt}}(\sigma_{\xi}) = \frac{n_{\text{tilt}}\sigma_{\xi}^{n_{\text{tilt}}-1}}{\sigma_{\text{tilt}}} e\left(-\frac{\sigma_{\xi}}{\sigma_{\text{tilt}}}\right)^{n_{\text{tilt}}} \quad (3.19)$$

Sampling from this distribution describes the shaking factor  $V_{\text{mp}}^2$  in the radar equation which represents the additional fluctuating part of the RCS of the OOI.

Table 3.2.: MLE estimates for distribution fits describing fluctuation of RCS

Exponential distribution	Tilted exponential distribution ( $R^2 = 0.98$ )	Log-normal distribution
$\check{\sigma}_{\text{exp}} = 1.43$	$\check{\sigma}_{\text{tilt}} = 1.49$	$ \check{\sigma} _{\text{lognorm}} = -0.11$
	$\check{n}_{\text{tilt}} = 1.04$	$\check{\zeta}_{\text{lognorm}} = 1.05$

### 3. What do we need in a radar simulation for virtual testing of AD?

---

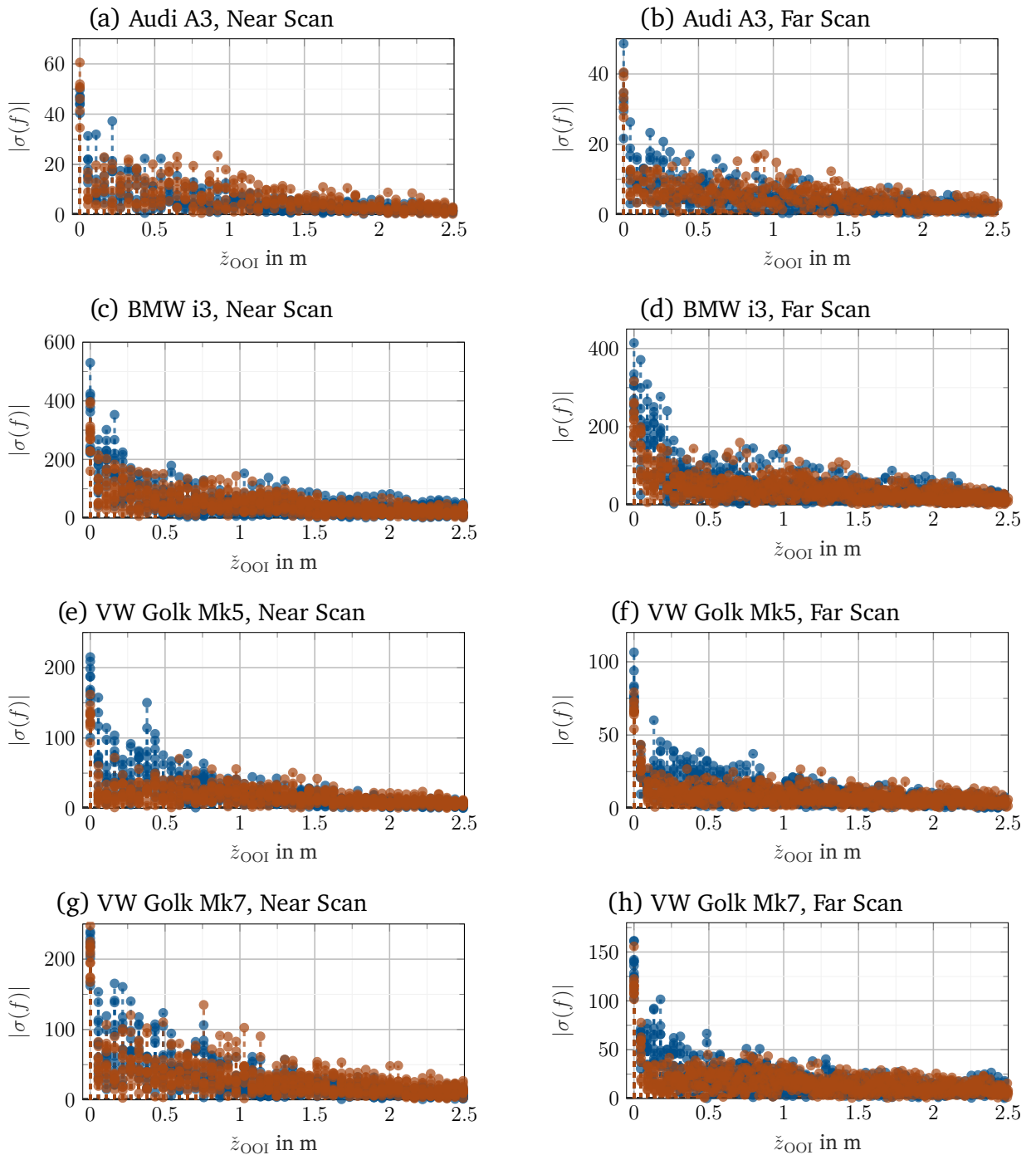


Figure 3.18.: Height spectrum for dynamic and static scenario, evaluated for all four cars on near scan (left) and far scan mode (right). Line color assignment: Dynamic scenario (—), static scenario (—).

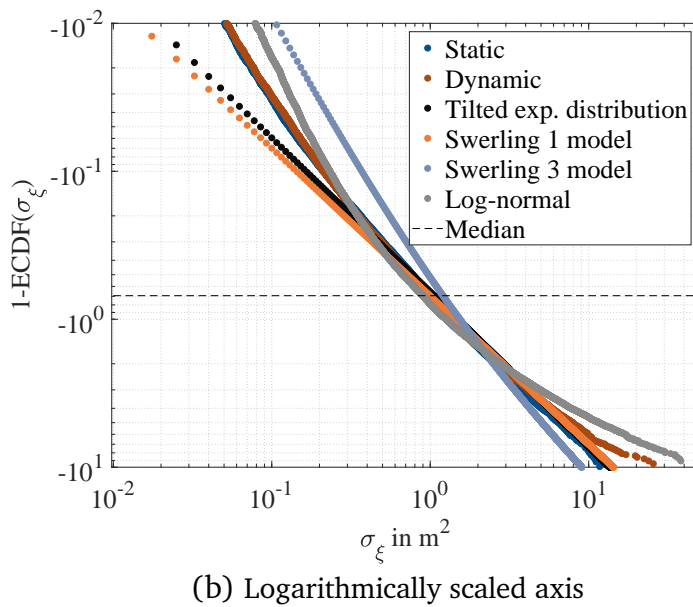
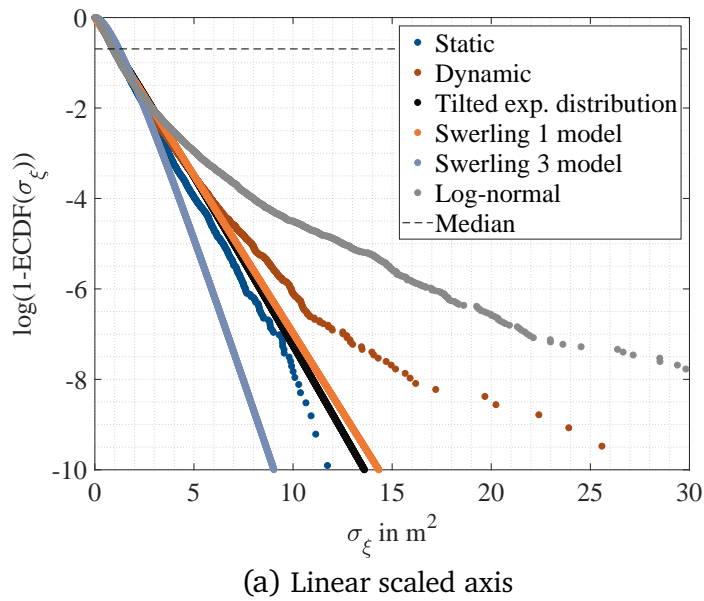


Figure 3.19.: Measurement data from the static and dynamic test in  $\log(1-ECDF)$  representation. Additionally, the fitted log-normal distribution as well as Swerling 1 and 3 models are shown. Because the number of very small random numbers decreases rapidly, the plots show less data points for very small RCS values.

### 3. What do we need in a radar simulation for virtual testing of AD?

---

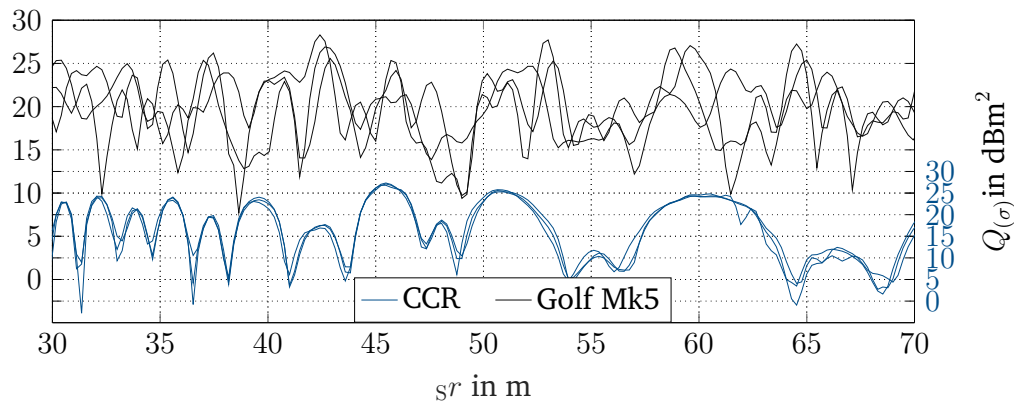


Figure 3.20.: Limited repeatability of experiments involving extended objects (here: Golf Mk5) compared to a CCR is seen from the deviations of the measured values between several repetitions.

#### Remark on repeatability

It is important to note that repeatability of radar measurements is difficult for complex geometries such as vehicles. Figure 3.20 compares the measured RCS value between an experiment where a CCR is approached (scenario 4) and the dynamic scenario using a VW Golf Mk5 (scenario 6). The CCR measurement is characterized by high repeatability. This can also be seen from object height estimation in figure 3.16. When performing the experiment using vehicles, however, only trend statements can be made at best.

### 3.7.3. Implications for modeling

In order to model wave superposition-induced fluctuations in the amplitude of received power, it has been shown that multipath superposition occurs at the receiver for non-point objects and thus at twice the frequency of ideal point objects. The point object assumption is obviously violated with large CCR. Measurements with vehicles did not reveal wave superposition patterns with the same clarity as with a CCR. In the static experiment (scenario 5) a few attempts show tendencies in which a rather clear wave superposition pattern is visible. In the dynamic experiment (scenario 6), however, no wave superposition patterns can be determined. Both the dynamic and static experiment are characterized by poor repeatability. The random character of the amplitude fluctuation can be described by a tilted exponential distribution.

Considering the task of sensor modeling, a description function for the noise pattern occurring in the dynamic case was identified. Measurements for the stationary case

give weak indications that wave superposition patterns can occur even for complex geometries such as vehicles. The poor repeatability indicates a high sensitivity to the experimental setup (e.g. lateral or angular variation between ego and OOI during the experiment). Modeling this infrequently occurring effect would therefore imply a unreasonably high effort. Instead, the sensor model must demonstrate the stochastic nature of amplitude fluctuation through multipath wave superposition for large objects.

#### **3.7.4. Falsification criteria**

The ability of a simulation to handle multipath wave superposition can be demonstrated by conducting scenario 4 (CCR approach) in simulation. The amplitude fluctuation for large objects has to follow a stochastic pattern that corresponds to the proposed tilted exponential distribution.

## **3.8. Intrinsic uncertainties, noise, and clutter**

---

Uncertainties in the measured quantities of the radar (range, radial velocity, angle) are subject to various influencing factors. In this section intrinsic sources, i.e. during sensor data processing, are investigated.

### **3.8.1. Hardware parameters: Aliasing, limitation of resolution, and dynamic range**

The performance parameters of radar sensors (see section 2.2.2) lead to resolution limits and unambiguous intervals. It follows from the DFT resolution limits in the radar cubic concept that there must be at least one free resolution cell in either dimension between two (point) objects for successful separation. The data rate required by the sampling theorem places high demands on the calculation. Therefore, practical system design allows this to be violated, but at the expense of ambiguities due to aliasing effects. This mainly concerns the measurement of radial velocity in the widely used chirp sequence modulation. Regarding the azimuth angle, the unambiguous intervals are given by the distance between antenna elements. These cannot be chosen arbitrarily small considering a desired angular resolution and dimensions of the antenna. If no countermeasures are taken and plausibility considerations fail, the deviations between measured and true value are in the order of magnitude of one unambiguous interval in the worst case.

Limitations in performance of a radar is reflected in all measurements. Reference scenarios can be synthesized from scenarios in which a quantity to be measured is at the limits of the performance parameters. Here, aliasing effects can be observed, e.g. once unambiguous intervals are exceeded or the separation capability is not met.

The dynamic range of the radar sensor is defined as the bandwidth in which the backscatter of an object can be registered by the radar. It has the noise floor as lower limit and the maximum gain of the analog-to-digital converter (ADC) as upper limit.

This may cause weak reflections to be indistinguishable from noise, even though separability criteria are met. A falsification of the sensor model is obvious if these performance parameters are not represented in the simulation model. This can be examined by means of simple scenarios e.g. by analyzing the simulated received power of a moving reflective object.

### 3.8.2. Noise of static objects

Due to the built-in electronics in a radar sensor, noise processes are unavoidable. They appear among other sources as thermal noise.<sup>108</sup> No additional noise sources are to be expected under stationary conditions for objects with high RCS (e.g. vehicles) at short distances.

#### Reference scenario

Two vehicles (BMW i3, VW Golf Mk5) are placed in front of the radar at distances of 20, 25 and 30 m obtained with measuring tape accuracy. These are typical following distances in traffic at moderate speeds.

#### Observation from measurements

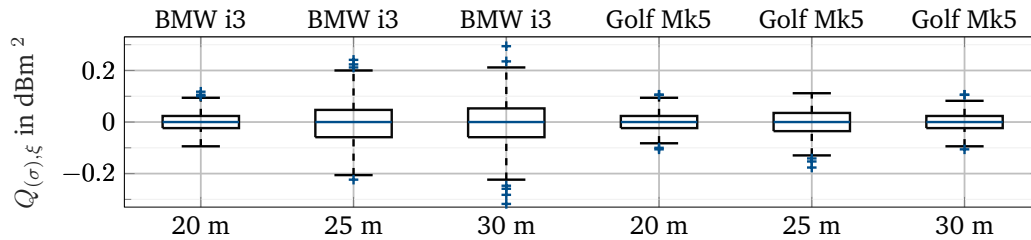


Figure 3.21.: Box plot showing RCS noise fluctuation of static objects located at different distances.

The RCS value observed during a measurement over 30 s in the range/azimuth-cell of the stationary Doppler plane of the radar cubic occupied by the vehicles is analyzed. The range/azimuth-cell showing the highest RCS is considered in each measurement frame. This results in an quantity denoted as  $\sigma_{\text{stat}}$ . A moving median filter over 5 s removes the stationary component of the RCS and the fluctuation in RCS remains as noise level:

$$Q_{(\sigma),\xi} = 10\log_{10} (\sigma_{\text{stat}} - \text{movmed}_{5\text{s}}(\sigma_{\text{stat}})) \cdot \text{dBm}^2 \quad (3.20)$$

The box plot shown in figure 3.21 displays that no significant noise is visible in RCS values for either vehicle.

#### Implications for modeling and falsification experiment

The noise to be modeled fluctuates below  $\pm 1 \text{ dBm}^2$  for vehicles in 20 - 30 m distance. Synthetic data from a sensor model observing a static object can be falsified if it reports considerable higher noise in such a constellation.

<sup>108</sup> Doerry, A. W.: Noise and Noise Figure for Radar Receivers (2016), p. 12.

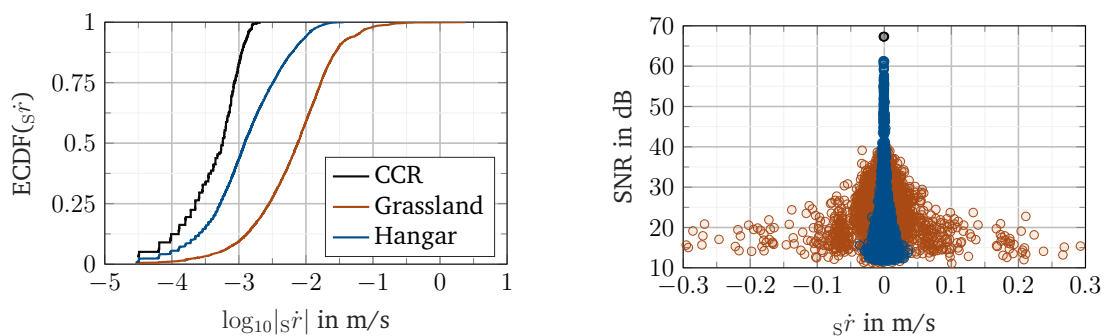
### 3.8.3. Sensitivity of sub-bin estimation to SNR

As described in chapter 2.2.1, range, velocity, and angular measurement with phased array radar sensors is turning into a frequency estimation problem. When these quantities are determined using the DFT spectrum, their accuracy is initially rather low. It can be increased by means of spectral interpolation methods such as quadratically interpolated FFT (QIFFT), which is illustrated in appendix A.8. Such methods exhibit high sensitivity to noise, resulting in noisy estimates for targets with low SNR.

#### Reference scenario

To illustrate the sensitivity to noise, two scenarios are selected under static conditions. When considering scenario 4 (see sec. 3.7) targets with high RCS are assigned to the CCR. The vegetation area and around the August Euler airfield, which contains no moving objects, serves as a reference area for a static environment. An additional radar measurement is performed inside a hangar with the radar illuminating a number of static vehicles and other objects stored inside the facility.

#### Observation from measurements



(a) Distribution of target Doppler components.

(b) Distribution of target SNR.

Figure 3.22.: Sensitivity of Doppler measurement under different SNR conditions.

The sub-bin frequency estimation shows higher noise the lower SNR, see figure 3.22a. A factor of 100 is obtained between the median noise for the high SNR CCR and to the low SNR grassland. Another superimposed effect becomes visible when considering those targets that originate from grassland: Because absolute calm cannot be reached in real-world situations, slight movements of the vegetation (e.g. grass blades at the

roadside) will be shown as “noise”. This is shown in figure 3.22b by grassland targets that have a radial velocity different from 0.

### **Implications for modeling and falsification criteria**

Based on the observation above, it can be concluded that additional artificial noise models do not seem to be necessary for radar modeling. This assumes that the decay of backscatter intensities covered by SNR is taken into account. A simulation model must therefore have higher accuracy for sub-bin estimation for targets showing high SNR. Reflections that originate from vegetation should include a small noise component to reflect the fact that complete static conditions do hardly occur in reality.

### **3.8.4. Clutter targets**

Radar measurements are characterized by targets that show a spontaneous exceeding of the detection threshold. Such targets are known as ground clutter targets. They become visible as random targets that are caused by spurious reflections. A characteristic of clutter is the random character of target occurrence. This also includes weakly reflective surfaces whose reflected power does occasionally exceeds the detection threshold as the orientation changes slightly during the measurement. Conditions for systematic occurrence of clutter targets are therefore present in most scenarios.

#### **Reference scenario**

The (static) grassland area around the August Euler airfield is studied from five different positions (denoted Grassland 1 to 5) with a radar facing towards the vegetation area. For reference, an additional measurement is carried out where the sensor observes an area where a car representing an extended object is present.

Environmental influences, such as precipitation or snow, can lead to clutter targets according to Rohling et al.<sup>109</sup> and Gourova et al.<sup>110</sup>. Therefore, a measurement is conducted where the radar observes a section of the runway at August Euler airfield during different weather conditions (dry, rain, snow).

#### **Observation from measurements**

Figure 3.23 shows the distribution of the clutter targets. It shows the probability that at least one detection is reported for a range bin during a given period of time. Only range bins that were not reported as occupied in the previous measurement cycle are examined. This ensures to consider only non-persistent targets to be regarded as clutter.

---

<sup>109</sup> Rohling, H.; Mende, R.: OS CFAR performance in a 77 GHz radar sensor for car application (1996).

<sup>110</sup> Gourova, R. et al.: Analysis of rain clutter detections in commercial 77 GHz automotive radar (2017).

### 3. What do we need in a radar simulation for virtual testing of AD?

---

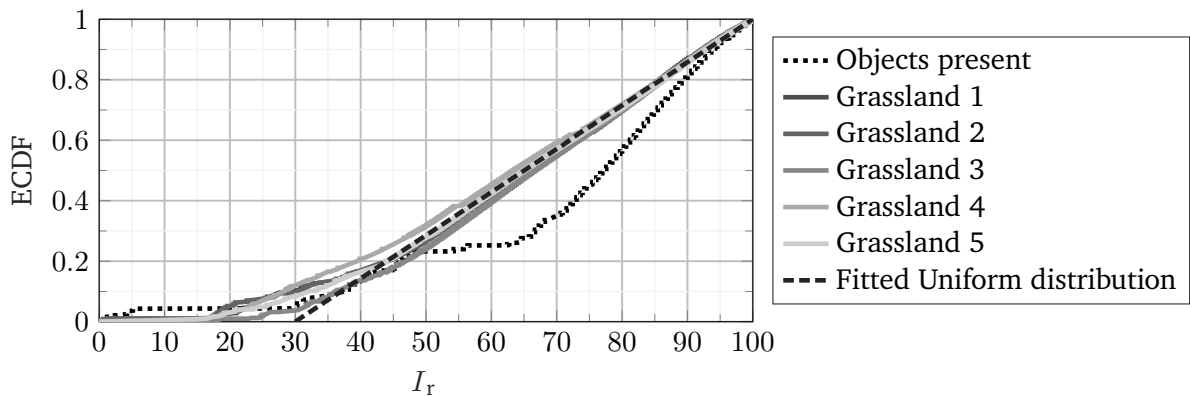


Figure 3.23.: Probability distribution of clutter targets in range bins during observing a static scenario for a period of time.

In particular, for range bins at greater distances from the radar, this probability can be well approximated by a uniform distribution.

Figure 3.24 shows stationary measurements on August Euler airfield under different weather conditions. Here, all targets reported by the radar are accumulated over five time steps. When investigating weather influences, it should be noted that in addition to the atmospheric attenuation by the water droplets in the air, a strongly attenuating water layer can form on the radome of the radar. In the measurements shown in figure 3.24, these influences are not separated from each other, so that only a qualitative trend statement is possible. It is clearly visible, however, that rainfall and snow cover on the runway are perceived as clutter targets at close range. Regarding snow, the lane of the vehicle in front can be detected. A similar characteristics is known from street curbs.<sup>111</sup>

#### **Implications for modeling and falsification criteria**

Clutter measurements have shown that the occurrence of clutter detections by vegetation can be approximated by a uniform distribution. Since terrain reflections are visible over the entire measurement range, the occurrence of clutter detections at longer distances is expected to be limited only by their SNR. As far as the weather influences are concerned, it is shown that both raindrops and snow on the ground become visible as targets. For a more detailed analysis, it is necessary to differentiate between the damping effects of a water layer on the radome and the environment.

---

<sup>111</sup> Ioffe, A. et al.: RCS characteristics of street curbs (2016).

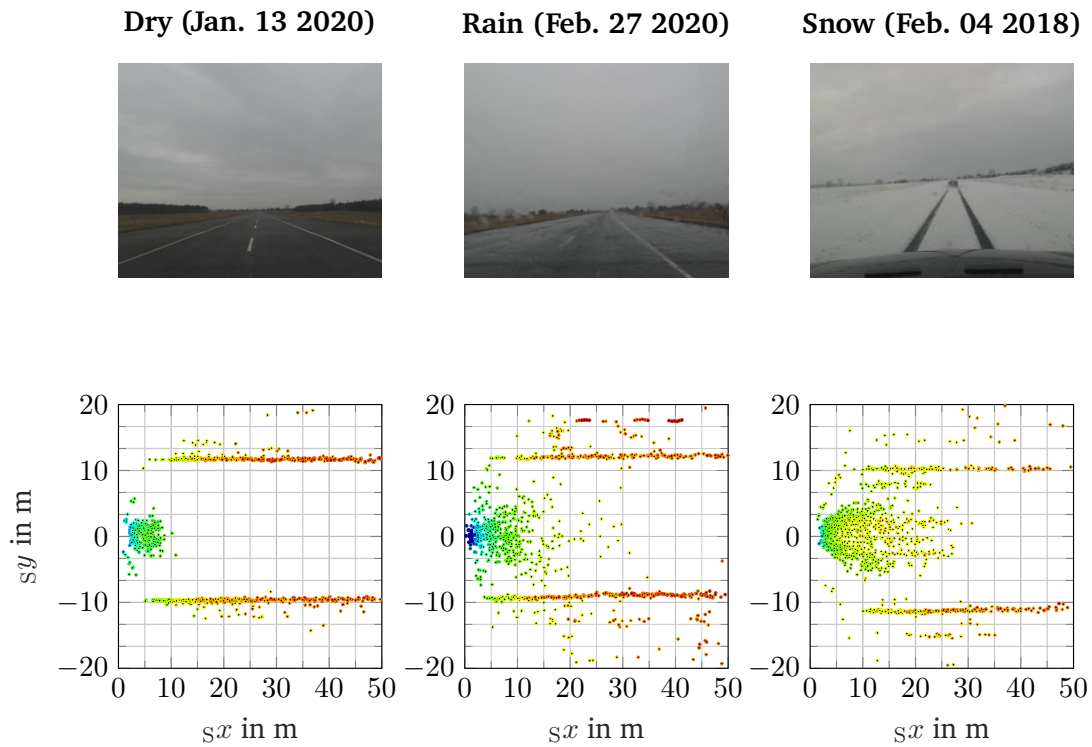


Figure 3.24.: Accumulated clutter targets over 5 measurement cycles at August Euler airfield under different weather conditions. Rain and snow cause significant occurrence of clutter targets at short distances. Color decodes RCS value from blue (low) to red (high).

### 3.9. Extrinsic uncertainties

Extrinsic uncertainties are imposed externally on the system, i.e., they are independent of sensor-internal parameters or data processing procedures.

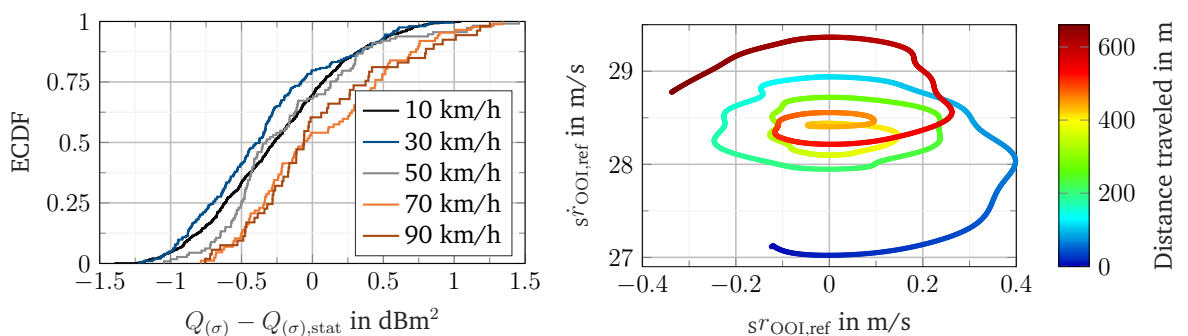
#### 3.9.1. Sensitivity of received power to vehicle body vibrations

The spring-mass damper system of the vehicle body is exposed to various excitations during driving. These include engine vibrations, road surface excitation, as well as body roll, pitch, and yaw movements. It is therefore necessary to investigate whether the simulation model of a radar sensor must take into account influences of complex driving dynamics for the calculation of the sensor's own movements.

##### Reference scenario

The CCR ( $Q_{(\sigma)} = 23.6 \text{ dBm}^2$ ) approaching scenario from section 3.7 is used with slight modifications: In order to avoid multipath wave superposition effects, the CCR is now placed with its flat side on the pavement in the middle of the lane. The unevenness of the road surface causes vibrations of the vehicle body, which are more pronounced at higher speeds.

##### Observations from measurements



(a) Sensitivity of RCS to vehicle body vibrations.

(b) Range-Doppler plot showing the OOI during an ACC drive.

Figure 3.25.: Extrinsic uncertainties during radar measurements due to vehicle body vibration (left) and ACC behavior (right).

Evaluation is performed at the radar target level. Here, targets assigned to the CCR are evaluated. The deviation of the RCS value from the static case at different velocities

is shown as an ECDF plot in figure 3.25a. The measured value of RCS is assumed to be constant due to the absence of wave superposition effects. At higher velocities, fewer measurement samples are available and the median is slightly shifted. Nevertheless, it can be seen that the fluctuation range of the measured RCS value is about  $2 \text{ dBm}^2$  compared to the stationary case with  $Q_{(\sigma)} = 23.6 \text{ dBm}^2$  at all investigated velocities.

### Implications for modeling

Chassis-induced movements of the body and thus of the sensor show no significant influence on the radar's received power. Explicit modeling of the microscopic motion of the sensor is not considered necessary. Since the sensitivity is in the range of  $2 \text{ dBm}^2$ , it is considered negligible small compared to the RCS of the CCR which is  $Q_{(\sigma)} = 23.6 \text{ dBm}^2$ . This does not apply to macroscopic sensor movements, e.g. the vertical swiveling of the antenna during a pitching motion during high longitudinal accelerations: A pitch angle of 1 deg causes a lowering of the boresight of about 1.7 m. Considering the respective vertical extent of objects as well as the antenna gain, this leads to noticeable changes in the received power.

## 3.9.2. Noise effects due to unsteady movement of traffic

Even when using advanced driver assistance systems (ADAS) such as speedometers, ACC, and lane departure warning systems, it cannot be assumed that real traffic moves at constant speed or constant lateral deviation within the respective lane. If these deviations are outside the resolution limits of the radar, they will be reflected as random, noisy deviations from the expected object velocity. This is considered a possible cause of extrinsic uncertainty.

### Reference scenario

The first reference scenario is an ACC scenario in steady state. Here, the OOI maintains its desired speed via cruise control. The ego vehicle follows the OOI via its ACC system at the largest time gap. The absolute speed of the ego vehicle and OOI are recorded via an ADMA available in both vehicles.

### Observations from measurements

The distance and radial velocity between the ego and OOI is shown in figure 3.25b. The values are determined by the ADMAs during an ACC follow-up at 50 km/h observed over about 600 m. The fluctuation interval expands over 2 m or  $\pm 0.4 \text{ m/s}$  with the ACC system in the 2008 Honda Accord. This observation shows that the assumption of constant speed and distance during an ACC following drive is not justified.

### **Implications for modeling**

Due to its high velocity resolution, a radar can measure even minor velocity changes of the OOI. In addition, in scenarios with dynamic content, the impossibility of driving at a constant speed must be taken into account in the simulation. Noise in the measurement of a varying vehicle speed with radar is therefore considered as process noise of the environment and not as measurement noise affecting the Doppler measurement. In this way, it is not justified to impose additional measurement noise on the Doppler dimension of synthetic radar data.

---

## **3.10. Object tracking artifacts**

---

Data processing routines such as object detection and tracking introduce further artifacts. Object tracking algorithms may encounter ghost objects that do not represent an actual object. This occurs as soon as the input data meet the statistical requirements that the estimation algorithm assumes for real existing objects. Such object tracking artifacts are conspicuous by a short lifetime or implausible motion patterns. A radar sensor, however, cannot distinguish them from real objects without further assumptions or observations over a long period of time. This category of artifact also considers the estimation errors of the object state w.r.t. ground truth. Formation of false positive or false negative objects also belongs to this category: Considering geometrically extended objects, such as a tram or truck trailer, multiple objects may be reported by the object tracking algorithm even though they would represent the same object.

### **3.10.1. Reference scenario**

There are no dedicated reference scenarios, as the occurrence of such artifacts can be observed with high frequency. Constellations like roads with metallic guardrails on both sides have a favorable effect on the formation as mirror targets. These can fulfill the conditions for the emergence of a false object.

### **3.10.2. Observation from measurements**

Figure 3.26 shows all dynamic objects that are linked to the OOI and reported by radar during a motorway trip with low traffic and guardrails that facilitates mirror reflections. It is shown that false objects are preferentially spawn at locations where mirror targets

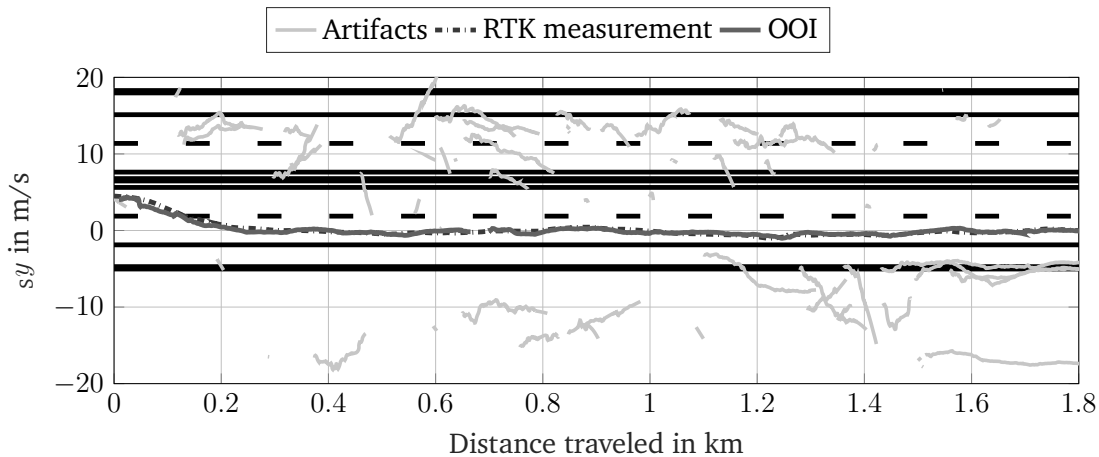


Figure 3.26.: Trajectory of OOI and the associated object tracking artifacts that were observed while driving on a motorway. A few appear geometrically correct on the topmost lane (mirror reflection off guardrail), others do not.

are expected due to multipath propagation, e.g., through guardrails. Significant deviations are found during track initialization or track deletion. Here, the filter algorithm relies on its internal estimates rather than the measurements.

### 3.10.3. Implications for modeling and falsification criteria

The occurrence of such artifacts in the simulation strongly depends on the deployed tracking algorithm and its parameterization. Therefore, it is to be expected that such artifacts also occur in the simulation as the tracking algorithm is stimulated with synthetic data. Explicit modeling is therefore not considered necessary, but is typically performed in stochastic models, see section 2.3.3. Falsification of the model can be achieved if tracking artifacts are completely absent, although the algorithm shows such artifacts when excited with measurement data.

### 3.11. Summary of the effects to be included in the radar simulation model

---

This chapter has highlighted characteristics of radar sensor measurements that are of interest to sensor modeling. Through analysis of real measurements, a set of commonly occurring measurement phenomena in radar measurements was curated. In this process, the term “artifact” was coined to describe such anomalies and translated into properties that a radar sensor model should exhibit. In addition to relevance for modeling, a description model was derived and evaluated for each artifact. The analysis conducted in this chapter is concluded as follows:

- Artifacts can arise from the performance parameters of a radar when exceeding unambiguous intervals and settle as aliasing.
- The change in path lengths resulting from **multipath propagation** affects the measured Doppler velocity. A mathematical description model has been confirmed by measurements. In the case of horizontal multipath propagation (e.g. guardrails) it was shown that both the DI/ID and the II propagation path can be found in measurements. For sensor modeling purposes, it is sufficient to consider the II path, since the total error is small if the DI/ID path is not considered, especially at large distances to the OOI.
- With the assumption of purely specular reflection of radar waves, the visibility of occluded objects cannot be described completely: Although a model for describing multiple **occlusion** is available, the occlusion scenario (i.e. scenario 1) shows that wave propagation in radar also contains components outside specular reflection such as diffraction and diffuse scattering. In this context, the occurrence of diffraction effects can be assumed.
- When investigating wave superposition effects due to multipath, it could be shown that CCR with a sizes starting at  $16.7 \text{ dBm}^2$  do no longer fulfill the point object assumption. The measurements shown in this chapter confirmed that the formation of wave superposition patterns can be explained by **superimposing of waves on the transmitting side**, i.e. as the waves merge when arriving at the sensor. This results in a doubling of the characteristic frequency of the wave superposition pattern compared to the point object.
- No reproducible, stable wave superposition patterns can be obtained for **extended objects**. Although clear wave superposition patterns can be found in isolated cases

in static experiments, there is a lack of repeatability even for different vehicles to derive a relevant effect. In the dynamic case, the measurements of received power are characterized by random noise. It has been shown that a tilted exponential distribution is suitable as a probability distribution to simulate this effect stochastically.

- Clutter originating from many weak or only occasionally strong scatterers linked to the terrain can be described by means of a uniform distribution. The occurrence of **clutter targets** is weather-dependent: Raindrops and snow form reflective targets that cannot be described by purely random processes, but must be modeled in the virtual world.
- Since the determination of range, Doppler, and angle measurements with radar is essentially a frequency estimation procedure, the SNR has a strong impact on the estimation accuracy that can be achieved. Using the example of sub-bin accurate Doppler estimation, it was shown that a supposed stochastic noise of the Doppler measurement is directly related to low target SNR and thus a decreasing estimation quality.
- Unsteadiness in motion of the ego vehicle and other road users creates extrinsic uncertainties that may be outside the resolution limits of the radar. Thus a natural cause of **extrinsic noise** is present. This can be considered a test problem as long as the reproducibility of a test drive is not better than the performance of human drivers.
- In the course of **sensor data processing**, further artifacts are to be expected, resulting from the algorithms used. Their explicit modeling does not seem necessary, since these artifacts are to be expected when the data processing algorithm is stimulated with plausible synthetic data.
- It is likely that the artifacts presented in this chapter are supplemented as part of further research. However, the artifacts presented in this chapter represent a set that can be easily observed by radar measurements in everyday traffic situations.



## 4. Fourier tracing: A new concept for synthetic radar data generation from virtual environments

---

The previous chapter developed the necessary scope of a radar simulation in the context of automated or autonomous driving (AD). This chapter introduces a new approach to radar sensor modeling for rendering synthetic radar data from a virtual scene, as virtual scenes are available in automotive simulation environments. By reinterpreting the ray tracing algorithm, this method is capable of synthesizing radar data using standard object representations from 3D geometric modeling.

This chapter is structured as follows: First, the requirements for the execution environment are analyzed and adjustments for a radar simulation are highlighted. Then a mathematical derivation of the novel synthetic data generation method and its verification is presented. The chapter concludes with a discussion of the assumptions necessary when using ray tracing for automotive radar simulation.

The research question that is answered in this chapter is: **RQ4:** *How can one use ray tracing to generate spectral radar data?*

---

### 4.1. Assembling the radar simulation ecosystem

---

A sensor simulation must process the virtual world in a manner that corresponds to the physical principals that the sensor being modeled. If, for example, a simulation environment for a bat that navigates by ultrasound would be set up, the relevant information would be the depth information regarding the obstacles in relation to the current position of the bat rather than color information that is available from attached red green blue color model (RGB) textures. The task of the sensor data synthesis is to provide a “distortion” process to ground truth available from the virtual environment that is in accordance with the sensor measuring principle. When accessing “ground truth” in the

#### 4. Fourier tracing: A new concept for synthetic radar data generation from virtual environments

---

simulation, full access to the information regarding relative distances, velocities, and angular positions of all objects is given. A sensor model transforms and distorts this information according to the measuring principle and the desired model output and sensor specification. For radar sensor simulation this results in the need for the following components:

- A wave propagation and discretization model that mimics the propagation of electromagnetic waves and allows for multipath propagation between sender and receiver.
- A material description system that links wavelength-specific reflection properties to 3D geometries present in the scene.
- A mathematical method that converts the ranges, radial velocities, and angular positions between the (virtual) sensor and a given scene into Fourier spectra according to the sensor specification (i.e. measurement ranges, irradiation pattern, mounting position, etc.).
- An execution environment for virtual test driving that provides all 3D geometries, a logical street layout, and controls the motion of traffic participants.

Ray tracing is a powerful method that considers complex interactions of light with materials and handles shadows, transmissions, reflections, and caustics in image synthesis. It seeks to calculate the propagation of light by considering the propagation between transmitter (the light source in images) and receiver (the image plane) in terms of the reflective properties at each intersection between a ray and geometry in the scene. The color of each pixel in a 2D image is based on the sum of the individual contributions of the illumination of each point of interaction and the local reflectance is quantified by the bidirectional reflectance distribution function (BRDF). Ray tracing is ideally suited for parallelization due to the mathematical independence of each individual ray, which can be efficiently performed on parallelizable computing architectures such as graphics cards<sup>112,113</sup> or multicore processors<sup>114</sup>. As wavelengths in automotive radar are small compared to the relevant length scales, geometrical optical behavior of waves is assumed. In ray tracing, rays can be sent from the observation point (“eye point”) and from any interaction point of a ray with geometry in the scene in any arbitrary direction that is

---

<sup>112</sup> Parker, S. G. et al.: OptiX: A general purpose ray tracing engine (2010).

<sup>113</sup> Peddie, J.: Ray-Tracing Hardware (2019).

<sup>114</sup> Wald, I. et al.: Embree: a kernel framework for efficient CPU ray tracing (2014).

in accordance with the physics of electromagnetic wave propagation. This makes ray tracing a common method for deterministic radio channel modeling.<sup>42b</sup>

In the reinterpretation of image synthesis for the purpose of radar data synthesis, the counterpart to the 2D image mentioned above would be the 3D radar cubic. It conveys spectral power received at each bin in the range, range rate, and azimuth spectrum with a discretization given by the measurement cell sizes given by the sensor design parameters. In the image plane, each pixel offers four channels: Red, green, blue, and the transparency channel are available for storing radar cubic information that are usually double-precision float exact values. For conserving phase information with a resolution of 0.5 deg and an assumed maximum range of 200 m, a resolution of  $200 \text{ m} \cdot 360 \text{ deg}/0.5 \text{ deg} \cdot 1/\lambda = 3.6 \cdot 10^7$  is required for range which requires a double-precision float value. Since in radar the angle measurement (azimuth or elevation) has the lowest resolution of all measured variables, in simulation it would be possible to store two single-precision float values instead of one double-precision float value, thus allowing for both azimuth and elevation.

In current simulation environments, the description of 3D models is given by means of discretized meshes and material assignment is done by textures that are linked to areas of the geometry. In order to create a “radar world” with currently available 3D representations and file format definitions, the material description system must at least offer surface normal vectors and material attributes. This would provide basic correlations such as the high reflectivity of metallic surfaces and the ability to calculate reflection paths. A widely used open file format is the Wavefront .obj format, which contains polygons defined as a list of vertices and surface material properties in an accompanying .mtl file<sup>115</sup>. In this way it is possible to consider material specific properties regarding transmission, absorption, and dispersion. To improve the quality of the rendering of computer-generated images, there are numerous databases available for BRDF optimized for the wavelength of visible light for the human eye. Due to the wavelength-dependent reflection behavior of materials, it cannot be assumed that these reflectance functions are also valid for mm-waves.

A purposeful extension to the scenario description format is the consideration of extrinsic uncertainties (see chapter 3.9.2). Thereby, sensor-agnostic but “natural” noise of the object poses is provided from outside the sensor model.

---

<sup>115</sup> FileFormat.info: Wavefront OBJ: Summary from the Encyclopedia of Graphics File Formats (2020).

## 4.2. Architecture of Fourier tracing

Generating synthetic sensor data from virtual environments can be framed as a computer graphics pipeline. Here, the task is to generate images from a virtual scenery and in fact, this process shows similarities to the understanding of video sensor simulation within the scope of this dissertation. At the core of synthesizing sensor data is the rendering step that processes information from the virtual environment according to the virtual sensing principle. For this purpose, the “graphics engine” is supplied with material parameters so that reflectivity properties and wave propagation from the current sensor installation position are reflected in the object representation.

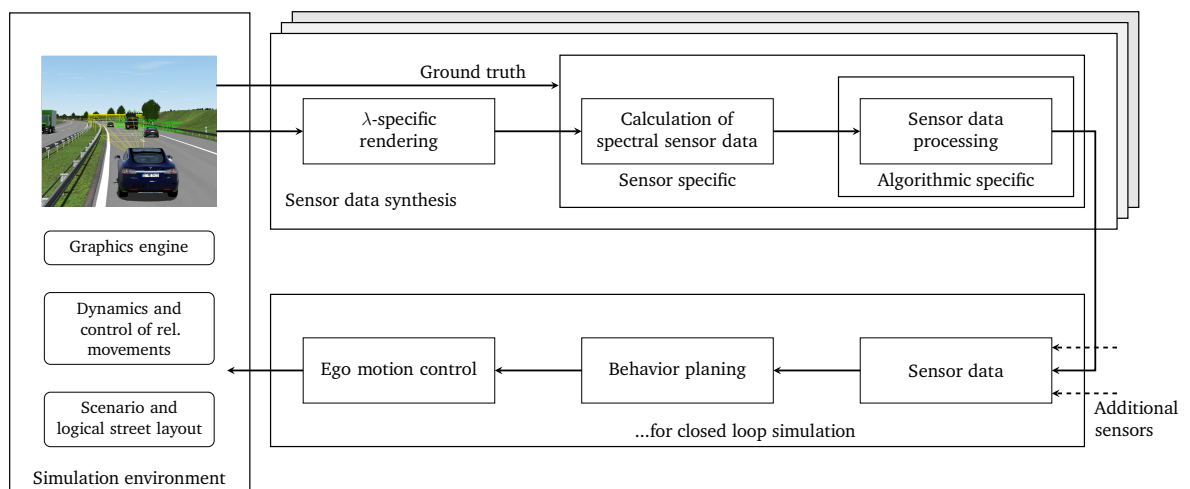


Figure 4.1.: Building blocks of a sensor simulation architecture comprising the simulation environment, the sensor data synthesis and the feedback loop for closed loop simulation. Sensor data synthesis layers indicate different sensor principles.

As the rendered (raw) image of the virtual world is available, it can now be processed according to the sensor parameters. In this step, sensor-specific parameters such as resolutions and unambiguous intervals are taken into account. After this step, the raw sensor data is available and can be further processed using specific algorithms. In radar, this would correspond to spectral sensor data arranged in the radar cubic. Additional information from ground truth, such as object state vectors, are transferred for facilitating calculations such as relative velocities. The execution platform of the simulation controls the course of the simulation and takes into account the interactions of the

traffic participants in relation to the logical road layout. The feedback between sensor data synchronization and execution platform is not predefined in the architecture but is defined by the system under test (SUT). If, for example, synthetic sensor data is used to perform object detection or free space estimation and a trajectory planning control derived from the estimated environment model is selected as the SUT, the resulting ego motion can be returned to the execution platform.

An advantage of this architecture is the separation between the rendering step and the calculation of sensor data. This makes it possible, for example, to calculate different sensor specifications on the same rendering image without having to perform the rendering step again. Although several of the preceding ideas are specifically designed for radar sensors, they can also be applied to other sensor technologies (lidar, camera). In fact, it is essential for a sensor simulation that a virtual world is prepared according to the sensor technology used. The architecture allows any instantiation of several sensor technologies, sensors, or processing algorithms.

This work refers to the generation of spectral radar data, i.e. the Fourier spectra from a virtual world based on ray tracing as “Fourier Tracing”<sup>116</sup>. This term emphasizes the combination of ray tracing with the calculation of Fourier spectra for obtaining the radar cubic. The core idea of Fourier tracing is to populate the radar cubic by applying the ray tracing algorithm to a virtual scene considering radar-specific aspects. Fourier tracing consists of two components:

The first is the ray tracing portion, which calculates the observable signal amplitudes  $\hat{U}$  from a given viewpoint (i.e. sensor position in the virtual world) by projecting rays into the scene, just like the ray tracing algorithm does for image generation. This step is technically sensor-agnostic, as no quantities that are specific to a particular radar sensor fronted specification are required when the rays are projected in an arbitrary direction, length, and to a reflection depth.

In ray tracing for images, the color of each pixel is calculated based on the amount of light that can be observed along the ray path and sets itself to a certain RGB and transparency value for a certain pixel. In Fourier tracing, each pixel of the image plane stores the information about the hit point  $\iota_h$  in terms of its range, denoted as  $r_{\iota_h}$ , range rate  $\dot{r}_{\iota_h}$ , azimuth  $\phi_{\iota_h}$ , as well as the received amplitudes  $\hat{U}_{\iota_h}$  from the direction of the returning ray. The ray tracing result is transferred to a list of hit points.

The second part of the Fourier tracing scheme is a transformation of these hit points into actual sensor quantities, i.e. periodogram values for the respective measurement

---

<sup>116</sup> The term “Fourier tracing” as well as the mathematical principles outlined below were published in advance in this publication: Holder M. et al. “The Fourier Tracing Approach for Modeling Automotive Radar Sensors” (2019).

dimensions. Each hit point that reports a reflection to the sensor is interpreted and referred to as a  $\delta$ -peak in a periodogram and can be expressed in a compact notation using the Kronecker- $\delta$ :

$$\hat{U}_{\iota_h} \cdot \delta(\iota_r - \iota_{r,\iota_h}) \cdot \delta(\iota_v - \iota_{\dot{r},\iota_h}) \cdot \delta(\iota_\phi - \iota_{\phi,\iota_h}). \quad (4.1)$$

In this notation  $\iota_{r,\iota_h}$ ,  $\iota_{\dot{r},\iota_h}$ , and  $\iota_{\phi,\iota_h}$  denote range, range rate, and azimuth values that are normalized to respective bin widths, i.e.

$$\begin{aligned} \iota_{r,\iota_h} &= r_{\iota_h} / \mathfrak{D}r \\ \iota_{\dot{r},\iota_h} &= \dot{r}_{\iota_h} / \mathfrak{D}\dot{r} \\ \iota_{\phi,\iota_h} &= \sin(\phi_{\iota_h}) / \mathfrak{D}\sin(\phi) \end{aligned} \quad (4.2)$$

Unambiguous measurement intervals in the respective domain (see eq. 2.9) are taken into account using the modulo operation. This modular approach makes it possible to run the computation-intensive ray tracing algorithm only once in a specific scenery and then apply different sensor specifications to the list of  $\delta$ -peaks available after the rendering step.

#### 4.2.1. Rendering step: Deriving $\delta$ -peaks from a 3D scene

Rendering in relation to radar sensors means that the “radar view” is computed from the virtual scenery. For this purpose,  $\delta$ -peaks are calculated using conventional ray tracing. Therefore a total number of  $I_{\text{ray}}$  rays are launched into the virtual scene where the initial transmission power, denoted as  $\hat{P}_{\text{Tx}}$ , is evenly distributed among all rays. In optical ray tracing, the transmitter corresponds to the light sources in the scene. In the case of Fourier tracing, the transmitter antenna is modeled as a pinhole camera as a source for the rays that are cast into the scene. Radar-specific quantities are obtained by ray tracing as follows:

**Range:** The range is half the total distance between the sensor and the hit point, following the time of flight (ToF) principle.

**Range rate:** Radial velocity is indicated by the summation of velocity components at the current ray intersection point in direction of the ray along the ray path. This accounts for temporal changes in path length that manifest as a Doppler shift.

**Angle:** This corresponds to the relative angle (azimuth or elevation) between a hit point reporting a reflection to the sensor and the sensor.

**Signal intensity:** The signal intensity represents the relative fraction of the transmitted intensity taking into account attenuation along the propagation and by reflection.

Figure 4.2 depicts the flowchart of the rendering process in Fourier tracing that is executed in parallel for every transmitted ray. A ray tracing engine offers three types of shader programs for the intersection of a ray with geometry: the closest hit shader, the miss shader, and the any hit shader. In addition, each ray provides a so-called **payload**, a data structure that enables data exchanges between shader programs. This payload is initialized for each ray in each simulation cycle. The **closest hit** shader is evoked for the first interaction of the ray with the geometry that is closest to the eye point. To allow for transparency, the any hit shader is used for every interaction along the interval of a ray. In the trivial case, a ray does not interact with any geometry in the scene and the miss shader is executed. To avoid numerical issues, **default values** are stored before the program is terminated for such a ray.

In the Fourier tracing regime, only the closest hit shader program is considered for those rays that do not exceed a predefined upper limit for their length, mimicking the maximal radial measurement range of the radar. The closest hit program checks the material of the hit point, given by its texture, to identify a propagation path back to the sensor after reflection off surfaces while traveling through the scenery.

There are two possibilities how a reflection to the sensor can be realized. The sensor is assumed to be a circular area around the eye point. The first is when a reflective ray actually forms to the sensor. Once the **sensor** is found, the ray's payload, holding the cumulated range, range rate, and received power w.r.t to the current and all previous hit points from that particular ray, is transferred from the ray tracing program in the **saveresults** function and the ray iteration loop is aborted.

When the ray bounces through the scene, it will interact with different surfaces: As pointed out in section 3.8.4, clutter returns are caused by spurious reflections originating from the **terrain**. These have a stochastic character. When a surface that is labeled as "terrain" is reached by a ray, a "**russian roulette**" sampling technique is evoked, which is a well known method to reduce the number of samples in ray tracing: Because every ray that intersects with the terrain texture would trigger the closest hit program, only a randomly chosen subset of hits is further considered. This mechanism models the stochastic character of clutter returns and the underlying probability distribution is parametrized from the distributions shown in figure 3.23.

The **pavement** is modeled as a reflective surface for which a BRDF is given from the work by Schneider. For simplification, the pavement surface is idealized with isotropic reflectivity properties, an assumption that is known only to hold for perfectly smooth surfaces<sup>117a</sup>. The **pavement reflection coefficient** is calculated according to Schneider before a specular reflection is cast.

---

<sup>117</sup> Schneider, R.: Modellierung der Wellenausbreitung für ein Kfz-Radar (1998). a: p. 68; b:-.

All textures that are marked as metallic are considered reflective and are otherwise completely absorbent. If a texture is hit that is neither sensor, terrain, pavement, nor reflecting, the ray tracing program is aborted. In section 3.5 it was pointed out that the antenna front end in the sensor is highly reflective for mm-waves and causes repeated reflections. In order to mimic this behavior, a set of rays that are oriented towards the sensor under low backscatter angle, will not terminate at the sensor but rather undergo an additional reflection when reaching the sensor surface. The set is found by random subsampling that is parametrized according to the ratio between the size of the sensor and the size of the reflecting geometry. This reflects the relationship between the backscatter by the mirror and the real detection. Such a **reflection to the sensor** can only be realized for the first ray iteration (i.e.  $I_{rd} = 1$ ) and leads to the termination of the ray tracing program for this ray after the results from the payload are stored. For each hit point, it is checked whether the **sensor is visible**, i.e. is in direct line of sight (LoS). Hidden objects or objects that can only be reached by mirroring are considered if their mirror image visible on a reflecting surface is in the direct LoS. If the sensor is not visible from the hit point without additional reflection, a further ray iteration is performed with a specular reflection originating at the current hit point, provided that the maximum number of iterations has not been reached. Otherwise the aspect angle to the sensor, denoted  $\alpha_b$  is calculated as the angular difference between a specular reflected ray and a ray that is oriented towards the sensor from the hit point.

For entering the next ray iteration, a **reflection ray is cast** from the hit point that runs through the same sequence. Its payload, holding the range, accumulated range rate and intensities, is updated at each hit point irrespective of whether a reflection toward the sensor can be achieved during the ray's lifetime. To conclude, the sequence terminates when either a propagation path to the sensor is identified, the sensor is hit directly, the maximum permissible ray length is reached, or the maximum ray iteration is reached.

For each pixel of the image plane, that is discretized according to a given increment, one ray is emitted. The payload of those rays that were counted as returning to sensor is now read out and reformulated into a list of  $\delta$ -peaks, see eq. 4.3. Therefore, a total number of  $\delta_{\iota_h}$ -peaks is available after ray tracing.

$$\delta_{\iota_h} = \{r_{\iota_h}, \dot{r}_{\iota_h}, \phi_{\iota_h}, \hat{U}_{\iota_h}\} \forall \iota_h \in I_h \quad (4.3)$$

In this formulation only the azimuth angle was considered. If a radar system also requires that elevation measurements be simulated, the list of  $\delta$ -peaks can be extended by the element for the elevation angle (i.e.  $\theta_{\iota_h}$ ). This completes the ray tracing portion of the Fourier tracing method.

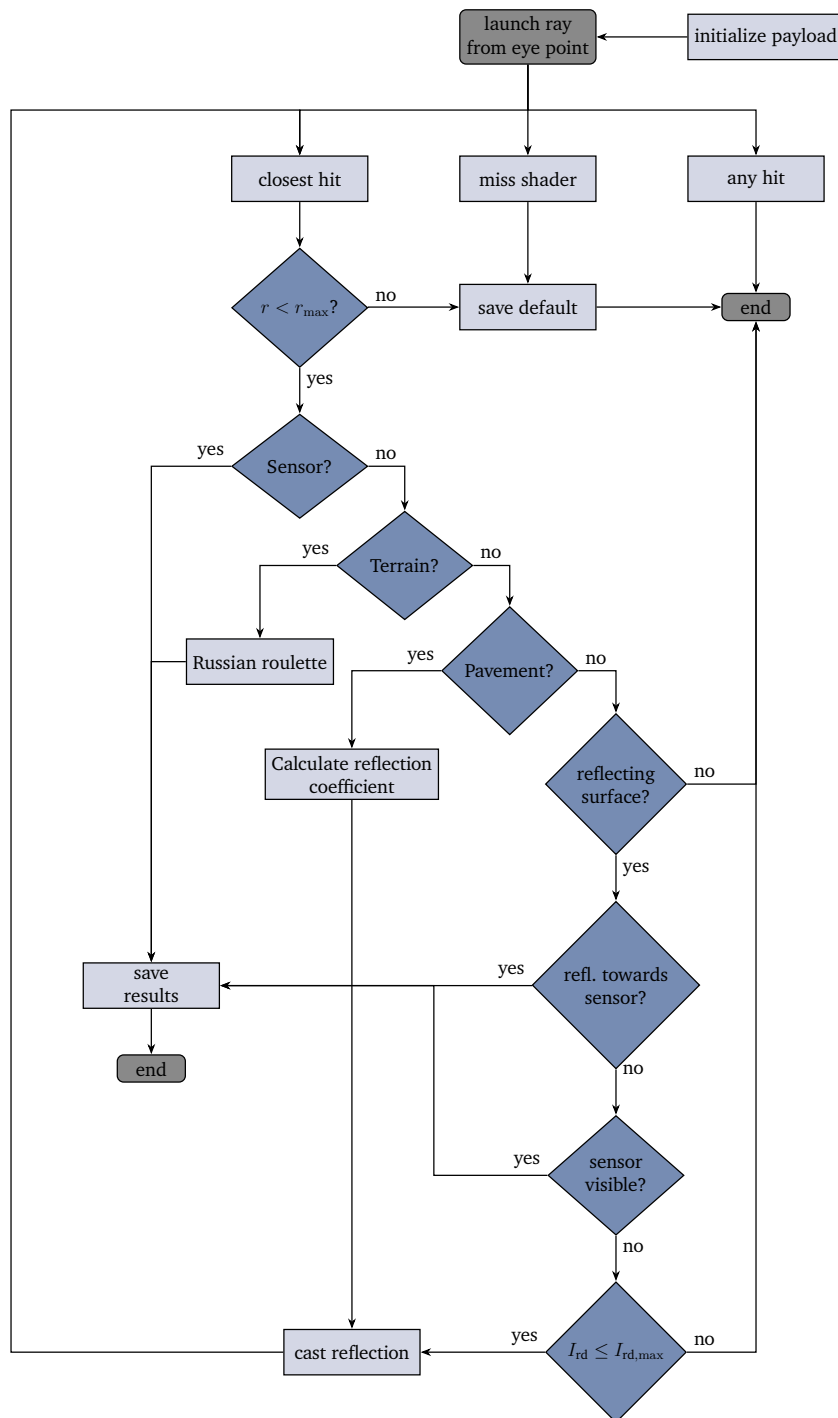


Figure 4.2.: Flowchart of the ray tracing portion in Fourier tracing that is executed for each ray and simulation cycle in parallel.

### 4.2.2. Radar cubic formation: Mapping of $\delta$ -peaks into the radar cubic

Although the actual  $\delta$ -peak location may be in an inter-bin location, in a periodogram, signal peaks can only appear at discrete bins due to discretization during discrete Fourier transformation (DFT). In addition, when calculating the DFT on a signal under limited measurement time and a finite number of samples, peaks do not appear at a single frequency, but affect neighboring bins due to leakage.

In Fourier tracing, assignment of bins that are affected by a given  $\delta$ -peak, i.e. smearing into adjacent bins, is captured in the convolution of eq. 4.1 with respective window functions in the frequency domain, denoted  $\mathcal{F}\{W_r\}$ ,  $\mathcal{F}\{W_v\}$ , and  $\mathcal{F}\{W_\phi\}$ . According to the shifting theorem, the Fourier transform of the window function is shifted on a continuous axis. The amplitude is then calculated at the discrete points given by the binning. This procedure corresponds to the design of a finite impulse response (FIR) filter using the window method where each  $\delta$ -peak corresponds to the passband of the filter. The spectrum is therefore calculated from  $\delta$ -peaks and windows functions as follows:

$$F_{\iota_r, \iota_v, \iota_\phi}(\iota_h) = \hat{U} \cdot \delta(\iota_r - \iota_{r, \iota_h}) * \mathcal{F}\{W_r\} \cdot \delta(\iota_v - \iota_{v, \iota_h}) * \mathcal{F}\{W_v\} \cdot \delta(\iota_\phi - \iota_{\phi, \iota_h}) * \mathcal{F}\{W_\phi\} \quad (4.4)$$

The index notation is  $1 < \iota_\phi \leq I_\phi$ ,  $1 < \iota_v \leq I_v$ , and  $1 < \iota_r \leq I_r$ .  $F_{\iota_r, \iota_v, \iota_\phi}$  gives complex signal strength  $\hat{U} = \sqrt{|\hat{P}_{\iota_h}|} e^{-j\varphi_{\iota_h}}$  for each hit point  $1 \leq \iota_h \leq I_h$  at range, range rate, and azimuth bin locations that are affected by a  $\delta$ -peak. Phase information is particularly important in order to account for wave superposition effects. Phase is given by the length of the  $\iota_h$ -th received ray, denoted  $\ell_{\text{ray}, \iota_h}$ , w.r.t.  $\lambda$ . A reflection off a solid surface introduces an additional phase shift of  $\pi$ .

$$\varphi_{\iota_h} = \frac{2\pi}{\lambda} \text{ mod } (2\ell_{\text{ray}, \iota_h}, \lambda) + n\pi, \quad \varphi \in [0, 2\pi) \quad (4.5)$$

The fraction of the total radiated power  $\tilde{P}_{\text{Tx}}$  for each ray is normalized by the total number of projected rays  $I_{\text{ray}}$ , assuming equal distribution of transmitted energy. The synthetic radar cubic is populated by the absolute power values of the complex-valued  $F_{\iota_r, \iota_v, \iota_\phi}$ .

The summation over all hit points realizes a phase-coherent superposition w.r.t. each rays' individual phase shift. In other words, the resulting power density is available after superposition of  $I_h$  instances of  $F_{\iota_r, \iota_v, \iota_\phi}$ . Ultimately, the simulated power for a given bin

in the radar cubic, denoted  $\tilde{P}_{\ell_r, \ell_v, \ell_\phi}$ , reads:

$$\tilde{P}_{\ell_r, \ell_v, \ell_\phi} = \left| \sum_{\ell_h=1}^{I_h} F_{\ell_r, \ell_v, \ell_\phi}(\ell_h) \right|^2 \quad (4.6)$$

The principle is illustrated by figure 4.3. For illustration purposes, one of the measurement dimensions is considered as an example. Two  $\delta$ -peaks are placed in arbitrary locations. Convolution with the chosen window function (e.g. a Hanning window) corresponds to centering the window at the position of the  $\delta$ -peak. The amplitude, that is formed according to the roll-off behavior of the window function, can be obtained at the discrete bins. The final amplitude in each bin is available after phase-sensitive superimposing amplitudes at each bin. Thus, superposing of multiple  $\delta$ -peaks can result in positive or negative amplification depending on their phasing.

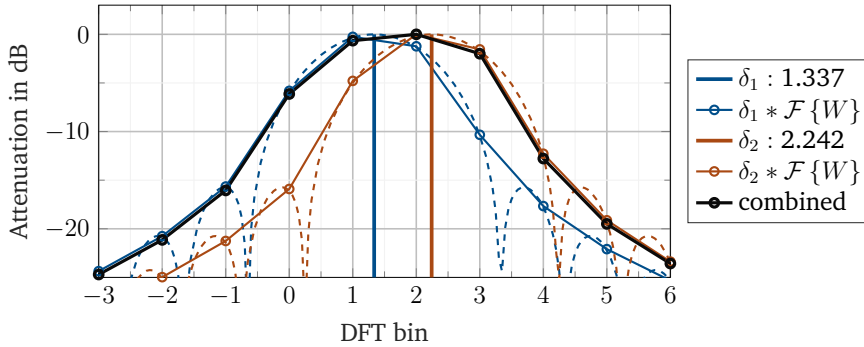


Figure 4.3.: Illustration of complex addition mechanism of two  $\delta$ -peaks in Fourier tracing with a Hanning window.

Sensor-specific parameters are only taken into account when assembling the radar cubic: The size of the radar cubic is determined by the number of bins in each measurement dimension. Assignment to the cubic cells is given by eq. 4.2. Intervals of unambiguity are considered using the modulo operation. The irradiation pattern of the receiving antenna is considered by weighing the signal amplitude according to the azimuth and elevation angle of the incident ray, which is reported by the ray tracing algorithm.

### 4.2.3. Implementation details

#### Remarks on ray discretization

Being a discrete process, aliasing is an inherent issue when generating images with ray tracing: Each ray is assumed to be infinitively thin and is traced through the center of each finite-dimensioned pixel. The value of each pixel is determined from the infinitely small sample taken within its center. As pixels are located at regular intervals, aliasing occurs when the adjacent pixel has abrupt changes in intensity. Aliasing manifests as stair casing and Moiré interference patterns. For mitigation, anti-aliasing techniques in image rendering attempts include improvements of the sampling process: Widely used techniques include supersampling (casting multiple rays per pixel), adaptive sampling (further casting as the intensity registered for each ray varies significantly), and stochastic sampling (tracing the ray through a randomly determined position within the pixel). These techniques thus increase the total number of emitted rays, which has a negative effect on computation time.

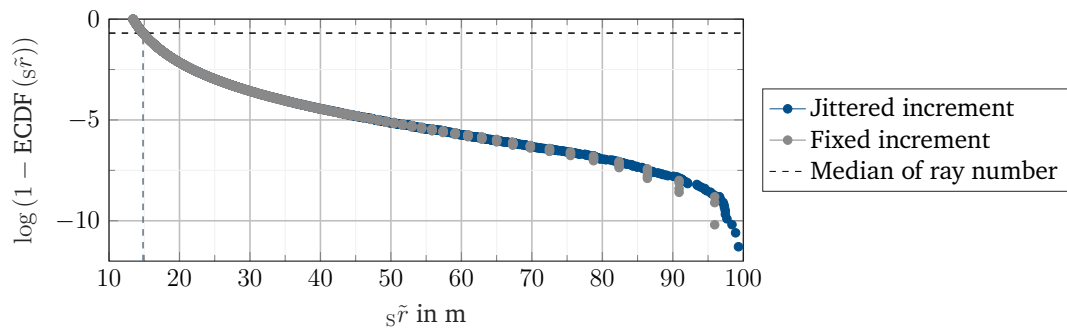


Figure 4.4.: Introduction of jitter on angular increments between rays prevents sampling gaps at greater distances.

In Fourier tracing, the aliasing effect of ray tracing manifests itself as perturbative in multiple places: First, due to ray discretization, fewer rays hit a geometry at greater distances. Second, the staircase effect leads to sudden changes in the number of rays interacting with an object that causes a sudden drop in signal intensity at discretization intervals. Also, searching for propagation paths suffers from fixed angle increments: Similar to point clouds of lidar sensors, gaps between the horizontal ray layers are present due to fixed angle increments in ray tracing. In particular for the calculation of multipath propagation, one is interested in a complete coverage for finding propagation paths, as it would also correspond to the continuity of the electromagnetic wave. Both challenges can be addressed with the anti-aliasing techniques mentioned above. The

simplest implementation is provided by a random angular offset according to a uniform distribution  $\propto \mathcal{U}(-0.5, 0.5)$  over each angular increment. Thus rays are no longer located at a pixel's center and the resulting uneven spacing between rays prevents both effects. The advantage of the so-called "jitter" method is that the total number of rays does not have to be increased and additional computational effort is only required for the calculation and drawing samples for the random distribution for the additional angle increments.

Figure 4.4 shows the effect of introducing jittering on the angular increments of rays where distances between hit points on the pavement in lateral direction at boresight are compared. It can be seen that the jitter distributes the rays more evenly over the entire distance, while the fixed ray increment causes blind spots, which are only considered insignificant if the height of the object always extends over several vertical layers. The median value shows that, due to the sensor perspective, half of the emitted rays do hit the pavement at less than 20% of the sensor range, which is unsatisfactory for reasons of calculation efficiency but unavoidable due to the perspective distortion w.r.t. the eye point.

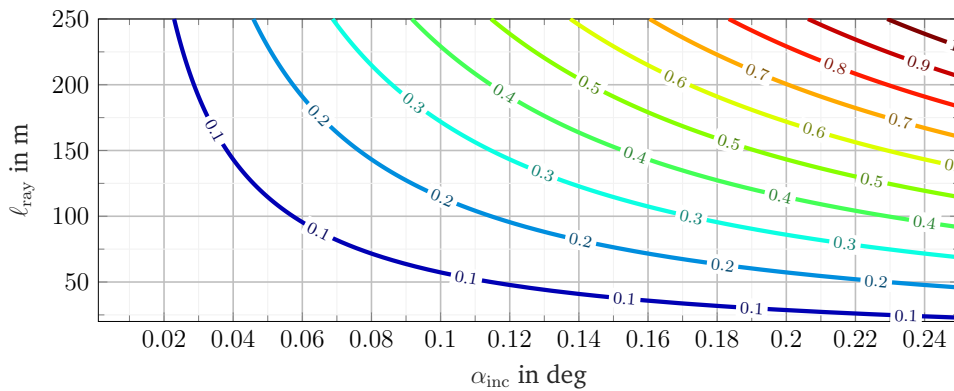


Figure 4.5.: Distance between two hit points with different ray increments. Contour lines indicating distance between two hit points with different ray increments. The contour lines are given in m.

Another problem that cannot be solved by jittering is the increase of the distance between two hit points. This distance is obtained by  $\text{atan}(\alpha_{\text{inc}}) \cdot s\tilde{r}$  and causes considerable distances between rays at larger ranges, see figure 4.5.

### The sampling problem of ray tracing for radar

Application of ray tracing for radar simulation corresponds to sampling the wavefront at discrete sampling points. Phase-sensitive addition requires ray lengths to be sufficiently accurate. Although a ray tracer reports ray lengths with floating point accuracy, ray discretization and associated radiance remain design parameters. From a computational perspective, an infinitely fine discretization is not possible and for given computational resources there is an upper limit for a feasible radiation discretization. Irrespective of this, the problem of decrease of radiance over distance cannot be eliminated, see figure 4.4.

For illustration of the sampling problem, the following experiment is carried out, involving radiating a squared, flat plate with a radar. The backscatter properties of such a plate (denoted “fp”) in far field<sup>118</sup> over yaw angle  $_{fp}\psi$  with dimensions  $A_{fp} = h_{fp}^2$  result from its weighting function which is governed by the sinc function<sup>119</sup>:

$$\sigma_{fp} = \frac{4\pi h_{fp}^4 \cos({}_{fp}\psi)}{\lambda^2} \left[ \text{sinc}(2\pi h_{fp}/\lambda_{fp}\psi) \right]^2 \quad (4.7)$$

When this plate is irradiated with a radiance of  $k \cdot A_{fp} = k \cdot \rho_{fp} \cdot h_{fp}$ , an analogy to the sampling theorem in signal processing becomes visible. Therefore, the plate is rotated around its vertical axis by one angular increment  $_{fp}\psi_{inc}$ . For further considerations, the reduction to the one-dimensional case is made because the same conditions occur over elevation, as shown in figure 4.6.

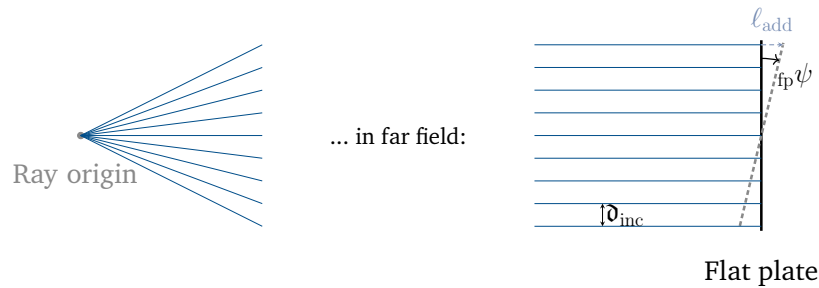


Figure 4.6.: Parallel incidence of rays on a flat plate in the far field. The rays are incremented by  $d_{inc}$  to each other. The plate is rotated by an angular increment of  $_{fp}\psi$  which results in a path extension of  $l_{add}$  for each ray.

Then, a total number of  $\rho_{fp} = \frac{h_{fp}}{d_{inc}}$  will illuminate the plate where  $d_{inc}$  is given by  $1/A_{fp}$

<sup>118</sup> This implies that incident rays are considered parallel

<sup>119</sup> Knott, E.: Radar cross section measurements (1993), p. 185.

and  $\rho$  is radiance. While the plate is rotating each ray will receive an additional path length that renders in a phase shift obtained by

$$\varphi = \text{mod}(2h_{\text{fp}}, \lambda) \cdot \frac{2\pi}{\lambda} \quad (4.8)$$

The additional path length due to rotation of the plate,  $l_{\text{add}}$ , reads:

$$l_{\text{add}} = \tan(\text{fp}\psi_{\text{inc}}) \cdot \mathfrak{d}_{\text{inc}} \quad (4.9)$$

The unambiguous angular range  $\text{fp}\psi_{\text{ua}}$  in far field that can be found for a given ray discretization results from the zeros of the modulo operation:

$$\tan(\text{fp}\psi_{\text{inc}}) \cdot \mathfrak{d}_{\text{inc}} = \lambda \quad (4.10)$$

$$\text{fp}\psi_{\text{ua}} = \text{atan}(\lambda/\mathfrak{d}_{\text{inc}}) \quad (4.11)$$

This shows analogies to angle measurement with phased array antennas: A higher phase resolution is achieved by smaller angle increments when rotating the plate: It increases “measurement duration” for obtaining the instantaneous phase resulting in higher precision, similar to decreasing the patch distance on an antenna. Increasing radiance provides a higher sampling rate and thereby a larger number of sampling points for the phase leading to larger unambiguous intervals, see figure 4.7. This is equivalent to increasing in the number of antennas in the patch antenna.

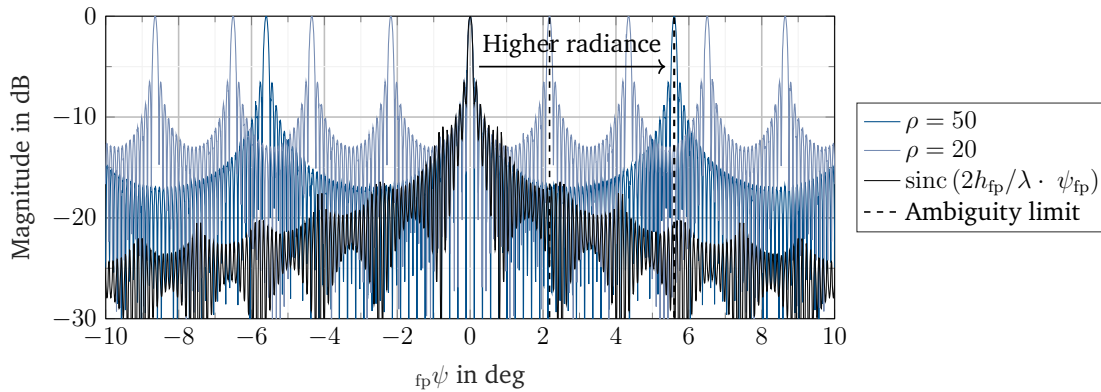


Figure 4.7.: Illustration of the aliasing problem with ray tracing for radar simulation. A rectangular flat plate of 1 by 1 m is illuminated with radiance  $\rho$  of 20 and 50 rays per unit area, respectively. The larger  $\rho$  the larger unambiguous intervals due to the higher number of samples.

This implies that unambiguity is lost at greater distances when utilizing ray tracing with fixed angle increments between rays. As a consequence of the ambiguity problem, there are angular positions of a plate that are not oriented to the sensor and thus clearly exhibit less backscatter, in which the backscatter calculated by ray tracing has the same strength as in the canonical case. To increase the radiance and the associated broadening of the unambiguous interval, more rays are required, which means a significant increase in computing power, especially for large distances.

The analogy to signal sampling can also be used to map the ambiguity problem: The jitter introduced in the previous paragraph is useful as it yields a Monte Carlo-inspired sampling at non-equidistant sampling points. A second countermeasure is to adjust the weighting of rays outside the ambiguity range: This brings in the idea of a low-pass filter in signal processing. A “basic unambiguous interval”, i.e. the angular range under which no aliasing effects occur, corresponds to its passband and rays outside of boresight can still provide considerable parts, as it also corresponds to the backscatter behavior of real objects.

#### **Calculating signal amplitude**

The inverse distance law as shown in figure 4.8 holds for the point-source radiation into three-dimensional space and introduces a  $r^{-2}$  proportionality for the signal amplitude according to the increase of the radiated area element with  $r^2$ . The antenna array of the sensor has a limited geometrical extension and the signal strength dilutes with increasing distance between the hit point and the receiving antenna. If the sensor area is approximated as a circular disk, it corresponds to the partial area of a spherical surface. The solid angle thus decreases with increasing distance from the hit point and implies an additional  $r^{-2}$  proportionality. Including both factors results in the desired  $r^{-4}$  proportionality of the received power w.r.t. range.

The establishment of a ray that reaches the sensor through specular reflections is very unlikely in scenarios that contain complex geometric shapes where specular reflections scatter incident rays in multiple directions. In addition, the decay of the radiance is a challenge in finding those rays that eventually form a reflection back to the sensor. For a given mesh cell on a geometry object, the greater the distance, the lower the radiance and thus the probability that a ray can hit the sensor surface by specular reflection, irrespective of the aforementioned ambiguity problem. Due to their shape, complex geometries such as vehicles initially exhibit only a small number of specular reflections and would therefore show low backscatter in simulation. This is not in line with real-world observations in which vehicles are known to be powerful scatterers. For this reason, the assumption of full specular reflection must be relaxed with the aim of generating a reasonable amount of backscatter even from complex geometries at greater

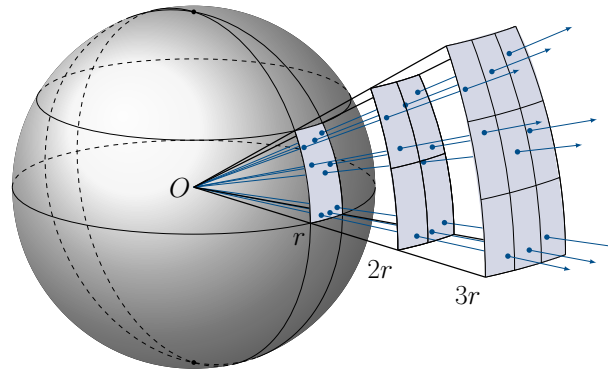


Figure 4.8.: Depiction of the inverse distance law: Geometric dilution corresponding to point-source radiation into three-dimensional space. The arrows demonstrate the homogeneous spreading of the wave across the surface of the sphere. Image source: Gonzalo Medina, <https://tex.stackexchange.com/a/262043>

distances.

While specular reflections dominate the propagation channel at wavelength in the cm range (i.e. 2-4 GHz)<sup>120</sup>, previous research assumes that the received signal at mm wavelengths contains contributions from diffuse scattering on various surfaces<sup>121</sup>, while the dominant contribution originates from specular reflection<sup>122</sup>. From a physical point of view, there is no diffuse radiation component for radar: If the interaction point of the wave on a reflective surface is seen as a microscopic surface, conditions similar to that of a flat plate are present: The plate acts as a transmitting antenna with a sinc weighting function, introduced in eq. 4.7. Its amplitude drops with  $1/\alpha_{\text{inci}}$  where  $\alpha_{\text{inci}}$  is the angle of incidence.

In connection with the mentioned problem of ambiguity due to undersampling, this motivates to adapt the criterion for identifying valid paths back to the sensor: When a ray hits a reflective surface and the sensor is not obscured, its signal amplitude is influenced by the angle under which the wave would propagate towards the sensor. This angle is denoted as the returning angle  $\alpha_b$ . It is assumed that a ray is reflected back to the sensor under angle  $\alpha_b < 90$  deg that represents the portion of the scattered wave that will reach the sensor. This allows a return path to the sensor outside pure

<sup>120</sup> Fan, W. et al.: Measured characteristics of indoor channels at millimetric bands (2016), p. 9.

<sup>121</sup> Goulianos, A. A. et al.: Measurements and Characterisation of Surface Scattering at 60 GHz (2017).

<sup>122</sup> Smulders, P.; Correia, L.: Characterisation of propagation in 60 GHz radio channels (1997), p. 79.

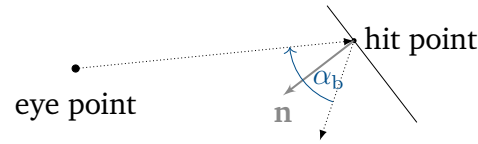


Figure 4.9.: Notation of  $\alpha_b$  found as angle between the eye point and a ray following an ideal specular reflection.  $\mathbf{n}$  denotes the surface normal vector.

specular reflection through quasi-diffusivity, see figure 4.9.

Handling of diffuse reflections is also discussed for the image synthesis of visible light. For this purpose, the concept of gloss and reflection of a surface, known from physically based rendering (PBR), which refers to its smoothness and metalness, is employed: In image synthesis, specularity gives the amount or brightness of the specular reflection and glossiness (or roughness) regulates the sharpness the specular reflection. In previous studies by Peinecke et al.<sup>123</sup> and Maier et al.<sup>78</sup>, the Phong shading model, originally proposed for computer graphics with visual wavelengths<sup>124</sup>, was applied to mm-wave radar simulation. The shading model mimics specular intensity falloff over the returning angle using an integer power of the angle, i.e.

$$L_{\text{Phong}}(\alpha_b) \propto k_{\text{diff}} \cos(k_{\text{edge}} \alpha_b) + k_{\text{spec}} \cos(\alpha_b)^{k_{\text{sm}}} \quad (4.12)$$

where  $k_{\text{sm}}$  controls surface roughness and  $k_{\text{spec}}$  weights the specular component.

As a rule of thumb, rough surfaces in the optical domain are modeled by  $k_{\text{sm}} < 32$ : The higher  $k_{\text{sm}}$ , the smoother the surface and a perfect mirror is given by  $k_{\text{sm}} = \infty$ . The Phong shading model represents a computationally efficient heuristic connection but lacks a rigorous physical justification<sup>125</sup>.

The degrees of freedom of the Phong function, see figure 4.10, allows the weighting of signal amplitudes according to incident angle and act as the desired anti-aliasing filter. Regarding the maximum radar cross section (RCS) it is assumed that all meshes in the virtual environment consist of square flat plates with an edge length of 1.5 cm, resulting in  $\max(Q_{(\sigma), \text{fp}}(\alpha_b)) = -14 \text{ dBm}^2$ .

The choice of surface roughness by  $k_{\text{sm}}$  balances between mapping the specularity of the plate and suppressing ambiguities due to limited radiance. For physically correct modeling, it is recommended to allow for a few of first zeros of the sinc function, which

---

<sup>123</sup> Peinecke, N. et al.: Phong-like lighting for MMW radar simulation (2008).

<sup>124</sup> Phong, B. T.: Illumination for computer generated pictures (1975).

<sup>125</sup> In the language of the sensor modelers it is therefore a phenomenal model.

enables reproducing the RCS profile of a flat plate within the unambiguous interval (see figure 4.7) in simulation. The high decrease in RCS outside this interval does not justify accurate modeling w.r.t. the sensitivity to aspect angle. Weighting of the “diffuse” part via  $k_{\text{diff}}$  is optional: With considerable power drop in order of multiple magnitudes minor or no contribution is expected as  $\alpha_b$  increases. The term  $k_{\text{edge}}$  in eq. 4.12 is not found in the original formula of the Phong model but is added here to modify the “softness” of the diffuse component at the edges. It regulates the zero points of the cosine and allows a softer slope near the zero points. It is set to 1.5, which gives the diffuse component’s zeros at  $\pm 60$  deg. This consideration is based on the assumption that at  $|\alpha_b| > 60$  deg the backscattered intensity of the reflection becomes negligibly small.

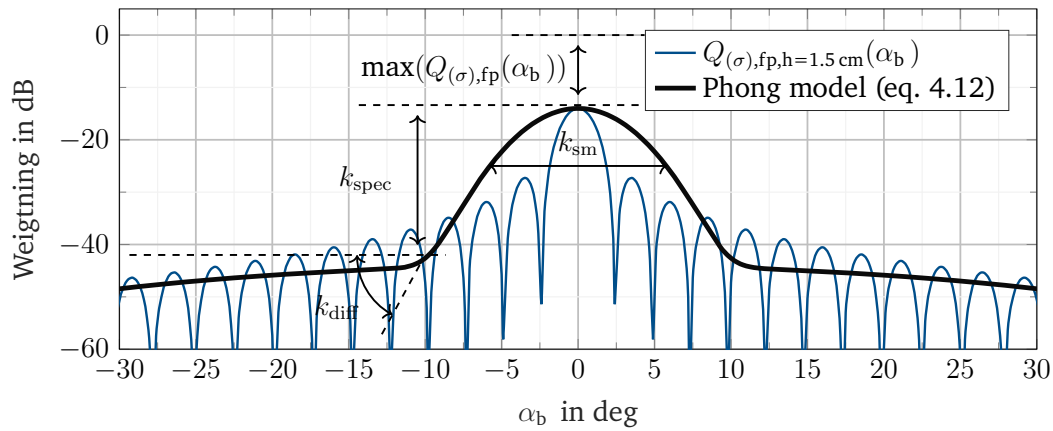


Figure 4.10.: Adaption of Phong as lens factor  $L_{\text{Phong}}$  with three degrees of freedom. In addition an RCS profile of a flat plate with  $h = 1.5$  cm is shown. Further parameters:  $k_{\text{sm}} = 5 \cdot 10^2$ ,  $k_{\text{diff}} = 5 \cdot 10^{-5}$ ,  $k_{\text{spec}} = 5 \cdot 10^{-2}$ .

The signal intensity of each ray that cover the range  $r_{\text{ray}}$  to a hit point and is counted as reflected towards the sensor is ultimately calculated as follows:

$$\hat{U}_{\iota_h} = \underbrace{\left( \prod_{\iota_h=1}^{I_h} k_{R,\iota_h} \right)}_{\text{accumulated reflection coefficients}} \cdot \underbrace{\hat{U}_{\text{init}}}_{\text{initial signal strength}} \cdot \underbrace{\frac{1}{r_{\text{ray}}^2}}_{\text{inverse distance law}} \cdot \underbrace{\frac{A_S}{r_{\text{ray}}^2}}_{\text{solid angle}} \cdot \underbrace{L(\alpha_b, \iota_h)}_{\text{lens factor}} \quad (4.13)$$

### Remarks on calculation of radial velocity

The Doppler shift measured by the radar is caused by the relative radial motion of objects w.r.t. the sensor. The Doppler frequency  $f_D$  is proportional to the temporal change of a signal's path length between the sender and receiver, denoted  $\ell_{Tx,Rx}$ :

$$f_D \propto \frac{d\ell_{Tx,Rx}}{dt}. \quad (4.14)$$

Two methods exist for for extracting relative movements from simulation:

- The (radial) velocity is obtained from the change in an object's position between adjacent simulation time steps.
- For each hit point, the velocity vector of the object is obtained from simulation ground truth and reported to the ray.

The approaches differ in how multipath propagation effects on Doppler frequency are handled: The former method has the advantage of more easily accounting for temporal change of a signal's path length but requires adjacent simulation time steps to be sufficiently small. Also, it requires that the ray tracing engine is able to link hit points across time steps. The latter approach is more intuitive, and only requires access to an object's velocity vector. It is the primary method of velocity determination w.r.t. multipath propagation:

$$\dot{r} = \sum_{\iota_b=1}^{\iota_b} \langle \mathbf{r}_{0,\iota_b} \cdot \tilde{\mathbf{v}}_{\iota_b} \rangle - \langle \mathbf{r}_0 \cdot \tilde{\mathbf{v}}_{ego} \rangle \quad (4.15)$$

Here,  $\mathbf{r}_0$  is the vector-valued normalized direction of the respective ray and  $\tilde{\mathbf{v}}$  is the Cartesian velocity vector holding absolute speeds as available in simulation. The first term represents the absolute range rate, i.e. the summation of the (fractional) velocities that were collected during multiple reflections of each ray. The radial velocity w.r.t. the ego vehicle is obtained from the second term that represents the component of the ego vehicle velocity in the ray's direction. In this way, both direct and indirect returning paths are considered.

## 4.3. Parametrization and calibration

---

Parameter calibration is necessary to adapt Fourier tracing to a specific radar sensor. This section covers how parametrization and calibration is performed.

### 4.3.1. Ray tracing parameters

The input parameters to the ray tracing portion of Fourier tracing are similar to those in general ray tracing, and draw inspiration from the sensor's physical operation.

**Frustum size:** It defines the height and width of the primary field of view of the ray tracing camera for the scene and should match the longitudinal and lateral measurement range of the radar sensor to be modeled. Inappropriate settings would lead to computational overhead. Because there is no hard limit to the field of view in the angular measuring range of a real radar, a margin according to the antenna diagram should be kept to allow for reflections from objects at angles larger than the nominal angular measurement range.

**Ray discretization:** This defines the number of rays in the horizontal and vertical directions. The finer the discretization, the larger intervals of unambiguous results. An angular resolution of 1.5 deg is a reasonable radar ray discretization, and corresponds to a separation ability of 5 m at a distance of 200 m: With ten-fold oversampling it is still possible to place four rays on a 2 m wide car. The horizontal ray discretization should thus be at least 0.12 deg, cf. 4.5. In light of the aforementioned sampling problem, a higher ray discretization is recommended.

**Reflection depth:** This defines the maximum number of interactions that each ray may undergo before the ray is assumed to not return to the receiver. For modeling wave superposition patterns formed by a corner cube reflector (CCR), five reflections (i.e.  $I_{rd,max} = 5$ ) are necessary: Three inside the CCR and two at the pavement for the inbound and outbound ray, respectively.

**Maximum ray length:** A ray is terminated when it does not return to the sensor within its maximal allowed length, irrespective of its reflection depth. In small margin to the maximum range of the sensor can be added in order to account for additional ray length due to multipath propagation. However, no more than 1% path lengthening (e.g. indirect-indirect multipath combination (II) propagation with a 3-lane highway RQ31) is to be expected.

**Camera position:** This defines the viewpoint of the ray tracing camera in the virtual scene. It should correspond to the mounting position and orientation of the radar.

### 4.3.2. Sensor specific parameters

Characteristic radar sensor performance parameters such as range, velocity, and angular resolutions as well as respective measurement ranges, as listed below, are often available from the sensor's technical specification or are defined by its signal processing design. No further algorithm-specific parameters are required when computing the radar cubic with Fourier tracing.

- Range resolution  $\partial r$  and number of range bins  $I_r$
- Velocity resolution  $\partial \dot{r}$  and number of Doppler bins  $I_v$
- Angular resolution  $\partial \sin(\phi)$  and number of virtual antennas (azimuth bins)  $I_\phi$
- Total multiple-input and multiple-output (MIMO) antenna gain  $\mathcal{G}$  w.r.t. azimuth and elevation angle for weighting of the received amplitude
- Window functions  $W$  for either measurement dimension
- Carrier frequency of transmitted wave  $f_c$  and wavelength  $\lambda$

### 4.3.3. Calibration of received power

The objective of the calibration is to objectively compare the received power from simulation to that of real-world measurements. Received power in simulation is calibrated in a manner similar to that of a real radar, using standard calibration objects such as CCR, flat plates, or spheres. Such a geometry with a known RCS profile is inserted into the virtual scenery as a 3D model. The procedure described below has already been used by Mesow<sup>126a</sup> and Matsunami et al.<sup>127</sup> for calibrating of the receiver power for RCS measurements of vehicles and pedestrians. Its application for calibrating simulated radar sensors is straightforward: The radar equation describes the correlation between the RCS and the received power. It is a function of the range and the antenna gain, i.e.  $P_{\text{Rx}} \propto \sigma$ . The magnitude of the spectral power density stored in the radar cubic does not directly correspond to the received power, but contains influences from extrinsic and intrinsic parameters: The extrinsic parameter  $C_{\text{ext}}(r)$  is range-dependent and covers the antenna gain in azimuth or elevation, or the resulting MIMO gain in the case of a MIMO radar. The intrinsic parameter  $C_{\text{int}}$  absorbs any further power factors in the

---

<sup>126</sup> Mesow, L.: Ph.D. thesis, Multisensorielle Datensimulation (2007). a: p. 91; b: -; c: p. 103

<sup>127</sup> Matsunami, I. et al.: RCS measurements for vehicles and pedestrian at 26 and 79GHz (2012).

signal processing chain, such as amplifications, antenna calibration, and gains in the analog-to-digital converter (ADC). In Fourier tracing, the power values stored in the radar cubic are assumed to be tied to the received power via these calibration factors: Thus, the product  $C_{\text{ext}}(r) \cdot C_{\text{int}}$  that combines all power factors in the signal processing chain, is measured in  $1/W$ , resulting in a dimensionless figure for  $P_{\text{meas},0}$ .

Consider a “unit radar object” given by  $\sigma_{\text{UO}} = 1 \text{ m}^2$ , placed at a range of 1 m from the sensor, i.e.  $sr = 1 \text{ m}$ . This object is then measured to have a reference power  $P_{\text{ref},0}$ :

$$P_{\text{ref},0} = P_{\text{meas},0}(\sigma = \sigma_{\text{UO}}, sr = 1\text{m}) = P_{\text{Rx}}(\sigma = 1\text{m}^2, sr = 1\text{m}) \cdot C_{\text{ext}}(1\text{m}) \cdot C_{\text{int}} \quad (4.16)$$

With this reference power, the RCS value can be determined from any received power at a known range to the object, denoted  $\sigma_{\text{equi}}$ :

$$\sigma_{\text{equi}} = \frac{P_{\text{meas},0}(\sigma, sr)}{P_{\text{ref},0}} \cdot \frac{sr^4}{\text{m}^2} \quad (4.17)$$

Considering the compensation of the power loss over the range and because both  $P_{\text{meas},0}(\sigma, sr)$  and  $P_{\text{ref},0}$  are dimensionless figures,  $\sigma_{\text{equi}}$  results in an area in  $\text{m}^2$ .

This means that, apart from the angular position, all factors affecting the received power are calibrated so that the change in received power depends only on the object’s RCS. The angular position could be compensated in a similar way with a known antenna pattern.

In practical application, a calibration experiment with a reference object without additional disturbances is difficult to realize. A trihedral CCR is often used due to its robustness against the angle of incidence. In order to prevent undesired influences due to multipath propagations, the measurement can be carried out in an anechoic chamber or by facing a radar toward the sky and suspending the object from a drone. In both cases a range of  $>25 \text{ m}$  between the radar and the CCR is recommended to fulfill the far field condition. Alternatively, the CCR can be placed with its flat side on a road so that multipath propagation paths are suppressed. In this case, however, the road’s unevenness will lead to uncertainties when obtaining  $P_{\text{ref},0}$ .

For sensor model calibration, an object with known RCS is placed in the virtual environment at an arbitrary (but known) range  $\tilde{r}$  within the radar’s far field. The obtained received power now corresponds to  $\tilde{P}_{\text{ref},0}$ . With this value, an equivalent  $\tilde{\sigma}$  value can be calculated for any  $\tilde{P}_{\text{Rx}}$  with known  $\tilde{r}$ .

This calibration procedure allows the “emitted” power of the radar antenna (i.e.  $P_{\text{Tx}}$ ) in the simulation to be set to an arbitrary value. This is the reason for choosing the initial signal strength of each ray to be 1.

## 4.4. Verification

This section demonstrates the ability of Fourier tracing to capture essential principles of radar sensors. The expected theoretical results are compared to actual simulation results to verify the model.

### 4.4.1. Separability of point objects

Radar resolution and separability are fundamental performance metrics. Fourier tracing represents separability via binning in the respective dimension. In a verification experiment, two CCRs representing point objects are placed on the ground, radially equidistant from the radar without horizontal separation. Their range is then gradually increased by one resolution cell. The experiment was also carried out in simulation, and different window functions were applied.

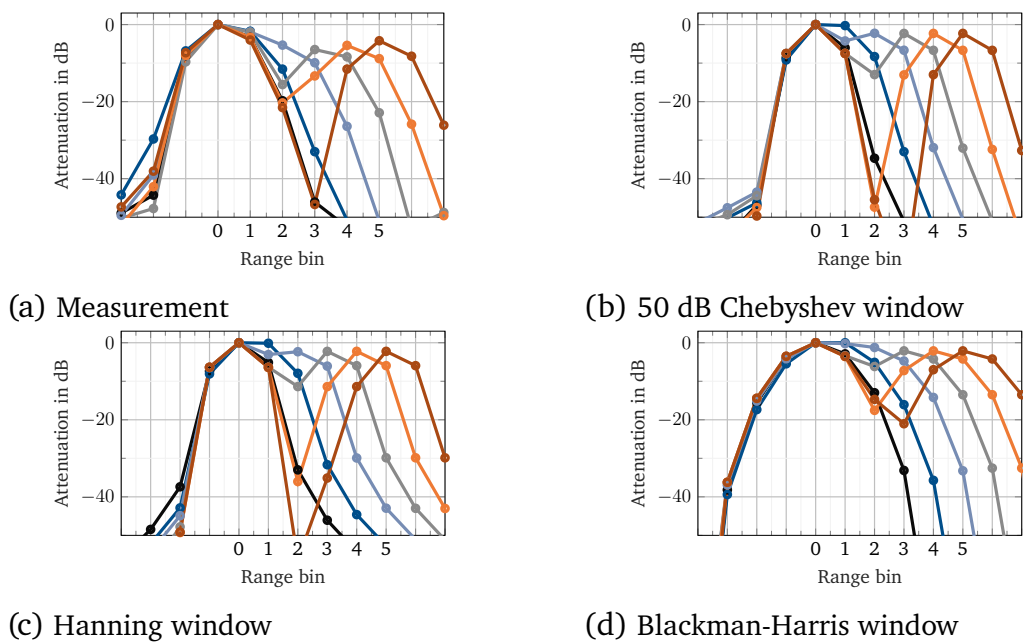


Figure 4.11.: Separability of point objects in measurement and simulation. Objects are placed in integer multiples of the range resolution cell  $\delta r$  from each other. Range bin 0 indicates the bin where the first object is located. Line color assignment:  $0 \delta r$  (—●—),  $1 \delta r$  (—●—),  $2 \delta r$  (—●—),  $3 \delta r$  (—●—),  $4 \delta r$  (—●—),  $5 \delta r$  (—●—).

As confirmed by the measurements, two free bins are required to distinguish point objects. The expected separability of point objects using Fourier tracing is maintained regardless of the window function used, see figure 4.11. This verification experiment is also suitable for selecting an appropriate window function that sufficiently describes the measurement. In the present case, the Chebyshev windows with a side lobe magnitude factor of 50 dB and Hanning windows, are adequate candidates.

#### 4.4.2. Separability of extended objects

Most objects are not well-approximated as point objects, and will create successive  $\delta$ -peaks in short intervals as range resolution results only from the floating point accuracy of the ray tracer. A slightly tilted, ideally smooth, flat plate is assumed. Due to the phase-sensitive complex addition in Fourier tracing, all phases cancel each other out along the extension of an extended geometry. It is only at the edges that the respective antagonistic “phase partners” are missing.

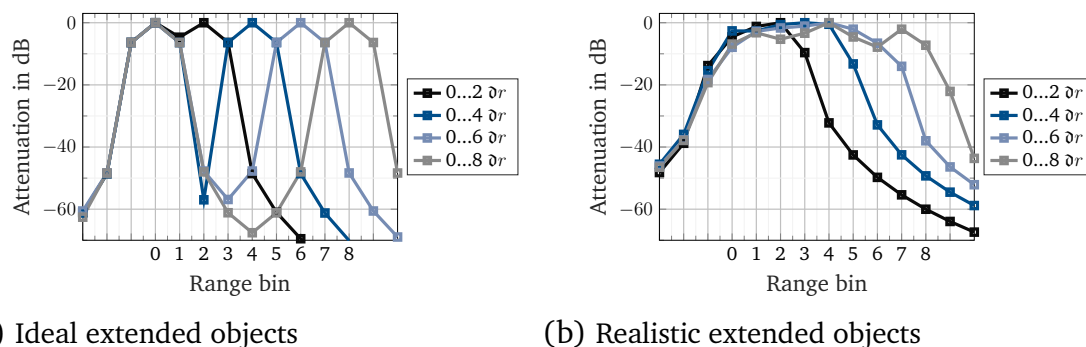


Figure 4.12.: Separability of extended objects: Ideal smooth, flat plate (left) show perfect destructive superpositions at all points but edges. More realistically, minor differences in path lengths prevent destructive phases and extended objects spread over several bins (right). Range bin 0 indicates the range from which the extent of the object begins. The colors indicate the extend of the geometry.

With Fourier tracing, this is inherently considered in the  $\delta$ -peaks reported by the ray tracer: The ray tracer produces a strong peak at the beginning and the end of the geometry with weak returns in between, cf. 4.12a. However, real geometries such as vehicles are not ideally smooth, as would be required for mutual phase cancellation along the geometry. Even the smallest deviations in path lengths and thereby between

phases are sufficient to prevent to meet the conditions for constructive or destructive wave superpositions, which have sensitivities in the scale of the wavelength. In this way, the occupancy spreads over several adjacent bins for extended objects, see figure 4.12b.

### 4.4.3. Masking weak objects

Due to the roll-off behavior of window function, masking effects may occur: If an object that exhibits low backscatter is in close proximity to an object with strong backscatter, the two cannot be separated. This would only be the case if a separation condition in another measurement dimension (radial velocity, angular position) is not fulfilled. This is shown in figure 4.13, which compares this case to the case of identical backscattering of both objects when the two objects are separated by  $2.25 \delta r$ .

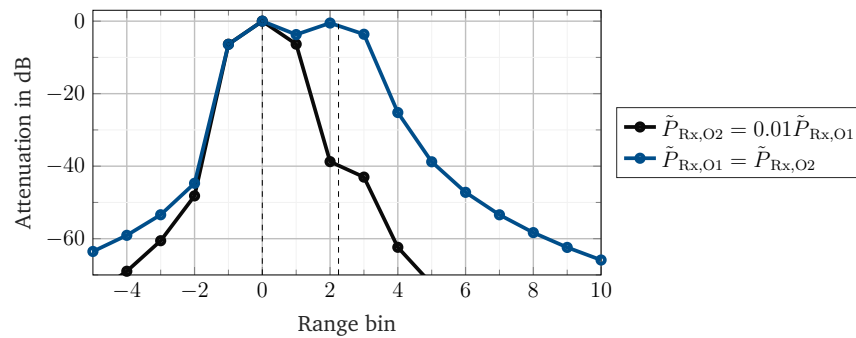


Figure 4.13.: Masking of two objects that are separated by  $2.25 \delta r$ . No discrimination of objects with low backscatter is possible. Range bin 0 indicates the range to the object closest to the sensor.

In the first mentioned case a typical “false negative” situation is obtained, as the second object is not detectable from the measurement under the condition that no separation criterion is fulfilled even in the angular or Doppler domains. Regarding separability for the object having similar backscatter characteristics, the previously described rules apply.

### 4.4.4. Conservation of RCS profiles for calibration objects

For verification purposes, the RCS profile of simple geometries such as flat plates can be obtained from a radar simulation to match that of the analytical solution. This process must verify two aspects: On the one hand, the basic ability of a radar simulation to map

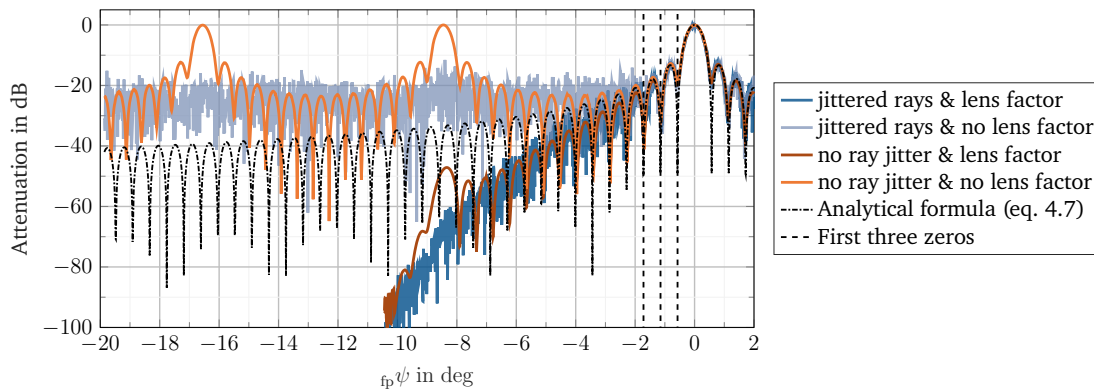


Figure 4.14.: RCS profile of flat plate ( $h_{fp} = 0.2$  m) obtained in simulation. Introducing jitter and the lens factor inspired by the Phong function improve the ability of Fourier tracing to render its RCS profile along with its first zeros.

known RCS profiles and, on the other hand, the ability of the ray tracing portion in Fourier tracing to handle the ambiguities w.r.t the sampling problem in ray tracing, as mentioned above.

A flat square plate of  $h_{fp} = 0.2$  m is placed at 30 m in front of the radar and rotated around its vertical axis in simulation. Multiple reflections over the pavement are not allowed, so that prerequisites for the validity of the analytical RCS profile according to eq. 4.7 are given. The influence of jittering and lens factor is tested by considering them mutually, cf. 4.14.

The figure shows the expected pattern. It is dominated by the sinc function and its shape is reminiscent of the Grundtvig's Church<sup>128</sup>. Without jitter and lens factor ambiguities can be observed: These can be suppressed by jittering the angular increments between rays because the corresponding phases of each ray can only undergo constructive superposition for the rotation angle around 0 deg where the major path length deviates less between all rays. Superpositions of the sinc functions prevents the received amplitude from decaying noticeably and also jittering can affect this. The proposed amplitude reduction according to the Phong idea is an adequate solution as it pushes the disturbing superimpositions into the noise floor. Even without measures, the zero points match the analytical model. Due to jittering, however, they can only be reproduced up to the third zero before they become noisy.

<sup>128</sup> Sennott, R. S.: Encyclopedia of 20th century architecture (2004), p. 567.

#### 4.4.5. Propagation paths

A conventional trihedral CCR that is located at boresight w.r.t. the sensor is suitable for validating the propagation paths calculated by ray tracing: Reflection processes inside the geometry cause tips remain in the corners from which no reflection to the sensor is possible, as shown in figure 4.15a. Points where a ray interacts with the geometry are shown in blue and points from which a reflection to the sensor is calculated are shown in red. The correct reproduction of this phenomenon verifies the reflection paths identified by Fourier tracing, see figure 4.15b.

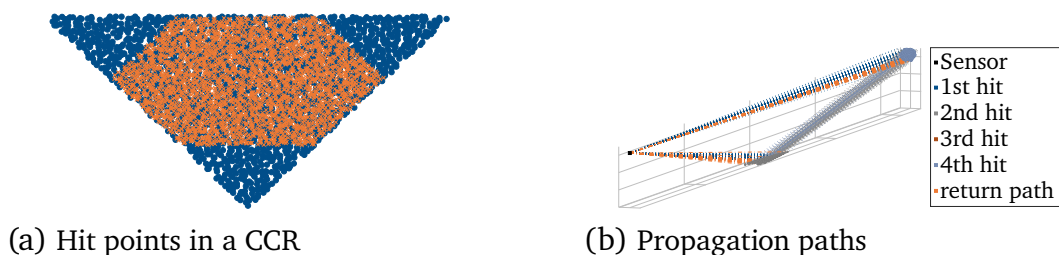


Figure 4.15.: Visualization of hit points for a trihedral CCR obtained by ray tracing. Principal ray interaction points are shown in blue, points from which a reflection to the sensor is calculated are shown in red.

A raytracing-specific problem in phase calculation is addressed in the work of Taygur et al. <sup>129</sup>: For large geometries, ray tracing finds correct propagation paths in theory, but the hit point for a direct and indirect path may not be the same. The resulting different phase differences manifest themselves in phase errors of the indirect path. Because in addition to the length extension by the indirect path (which establishes the superposition pattern) an additional, indeterminable path length is added as the hit point for the indirect path differences. This makes it difficult to correctly simulate the wave superposition behavior of large geometries with Fourier tracing. However, the practical impact is minimal. As the investigations in section 3.7 have shown, multipath superposition related fluctuations manifested by the shaking factor are measurably indistinguishable from specific noise patterns when vehicles are considered.

---

<sup>129</sup> Taygur, M. M.; Eibert, T. F.: Computation of Exact Ray Paths with Bidirectional Ray-Tracing (2020).

## 4.5. Assumptions for a tractable sensor simulation within currently available virtual environments

---

This section reviews a number of assumptions required to apply Fourier tracing in modern automotive simulation environments. They concern the virtual scenery as well as the radar sensor itself.

### 4.5.1. Virtual scenery and 3D geometries

In a virtual world, complex geometric bodies such as vehicles often consist of about 50 000 vertices<sup>130</sup>. This vertex count is a compromise between the level of detail and the required computational resources when loading multiple instances into memory. The surface discretization into meshes plays a significant role for ray tracing in the calculation of reflection paths, since these are determined by the surface normals. A virtual world consists of instances of repetitive 3D geometries and a limited number of textures. In particular for vegetation and associated clutter, this “monotony” at the roadside is countered by the described Russian roulette mechanism. It is, however, the subject of further investigation to what extent characteristic, local properties of the environment, such as those required in simultaneous localization and mapping (SLAM) applications, can be mapped. Dirt on vehicles and damage to the bodywork or other elements are not considered in automotive simulation environments. In terms of environmental conditions, which are addressed by level 5 in the Sauerbier et al.<sup>39</sup> definitions, it is assumed that the virtual scenery represents well-tended conditions, i.e. no adverse effects due to rain, snow, or fog.

#### Pavement reflection properties

Road surface reflectivity must be taken into account to model multipath propagation and related wave superposition effects. For the road surface, a reflection model for road pavement at mm wavelengths is known from Schneider’s work<sup>117b</sup>. Its validity is implied by the fact that this model has been adopted by the open simulation interface (OSI) standardization committee.<sup>131</sup> It calculates the surface reflectivity as a function of the angle of the incident ray by means of coefficients for Fresnel reflectivity, fine roughness, unevenness, and lens effects that are tuned to match a given road condition.

---

<sup>130</sup> Hum3D.com a ParaART, L. c.: Volkswagen Golf Mk5 5-door 2004 3D Model (2020).

<sup>131</sup> <https://github.com/OpenSimulationInterface/open-simulation-interface/pull/133/files>

The reflectivity model calculates the resulting intensity as a function of the angle of incidence or fall-out, i.e. exactly like a BRDF as known from photorealistic rendering.

##### **Vehicle body materials**

For vehicles, it is assumed that the visible outer shell, including the license plate, is completely made of metallic material with the highest reflectivity. Accordingly, this does not take into account the material mix of plastics, steel, and aluminum that is common in modern vehicle body construction.<sup>132</sup> In the course of the simplifications made during 3D modeling, there is no detailing of the vehicle underbody, as it is considered to be ideally smooth. For glass panes, a strong attenuation is expected and perfectly absorbing behavior can be assumed. This makes ray tracing easier because the “any hit” shader used to calculate transparencies does not have to be used: As a ray penetrates glass, the material-specific (but unknown) attenuation would have to be taken into account. If damping of signal amplitude is assumed to be too high, there are no advantages over modeling it as ideally absorbing. Conversely, there is a risk that a propagation path to an occluded object through glass panes will be found. Thus, it would also be possible that multiple occluded vehicles become visible through their glass panes. This is not in line with the observations from measurements, which show clear indications for wave propagation by reflection off the road surface.

Though a (reflective) steel belt can be found in tires beneath the tread, measurements carried out by Marx<sup>133</sup> do not indicate significant contributions from the tires compared to those from the rim. This justifies the choice of marking the rubber material at tires as absorbent. Figure 4.16 shows the material composition (left) of vehicles in a Fourier tracing simulation implemented in Vires Virtual Test Drive (VTD) and the reflectivity (right) that considers the lens factor described on page 101.

Vehicles’ complex geometric shapes makes it difficult to form (specular) multiple reflections by reflection from the sensor in simulation. For this reason, a reflective plate is attached in front of the ego vehicle, see figure 4.17. This plate is modeled as an ideal specular reflection for incoming rays, i.e. rays that are reflected back toward the ego vehicle from the scenery. The damping factor is assumed to be the sensor size in relation to the size of a vehicle, i.e. -13 dB see eq. 3.15.

---

<sup>132</sup> Kirtzakis, S. et al.: *Das Beste aus der MRA- Architektur* (2017), p. 108.

<sup>133</sup> Marx, B. J.: *Ph.D. thesis, Radareigenschaften von Personenkraftwagenkarosserien* (2013), p. 30.

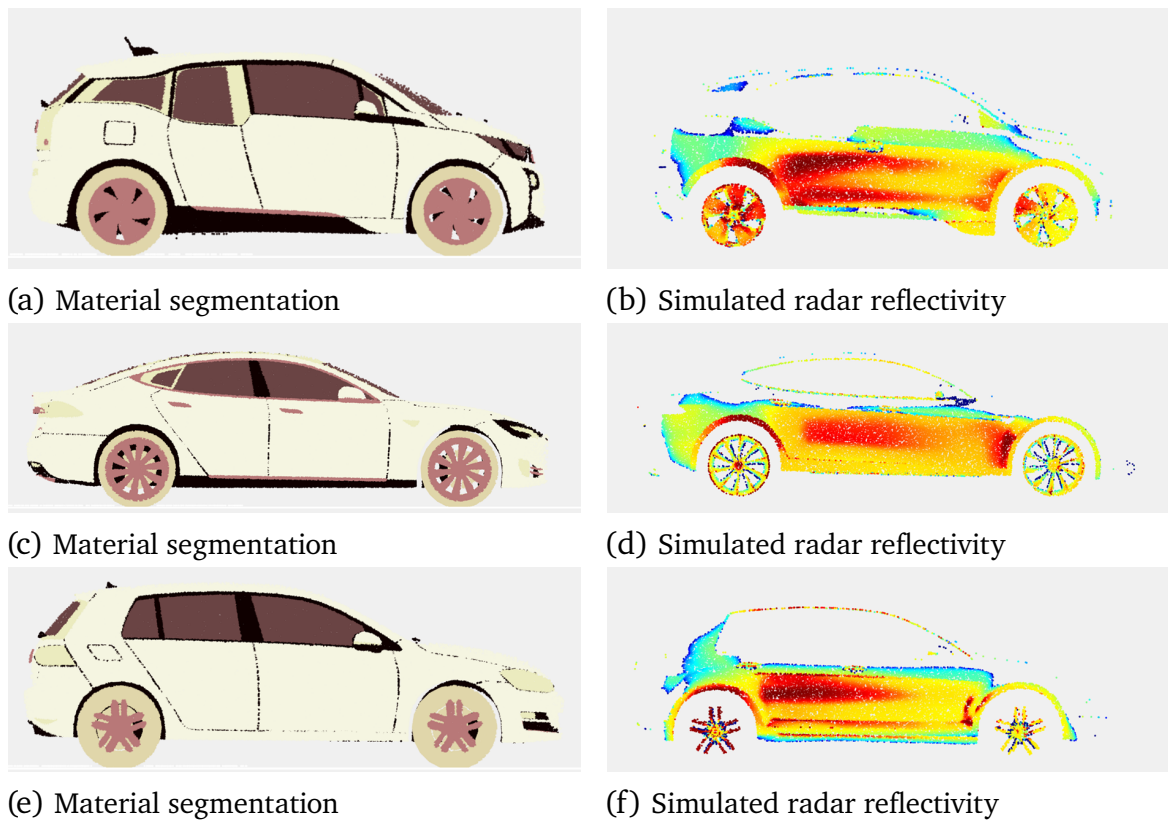


Figure 4.16.: Example of material segmentation and simulation radar reflectivity for a BMW i3, Tesla Model S and VW Golf Mk6.

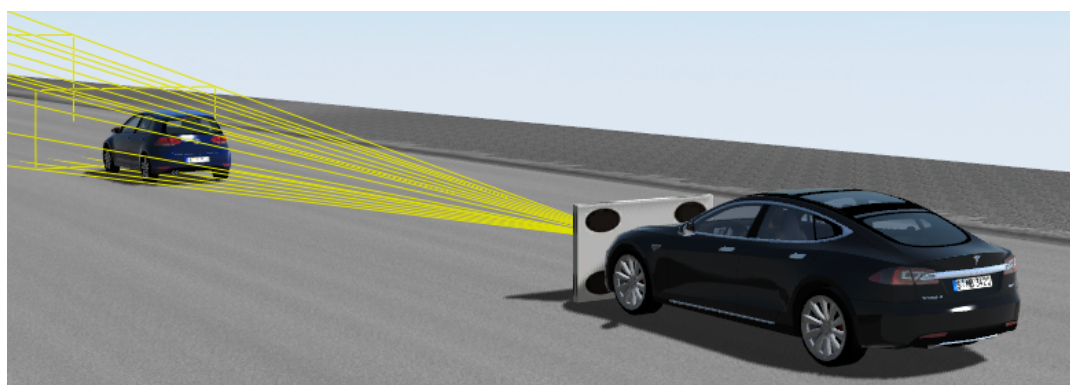


Figure 4.17.: Reflective plate at the ego vehicle to facilitate repeated reflections.

### 4.5.2. Radar sensor

The sensor is assumed to be a point source of radiance. The receiving antenna array is not explicitly modeled, but is assumed to be at the height of the transmitting antenna. No real-time capability is required for simulation, i.e. the time period for synthesis of one measurement cycle may be longer than the measurement cycle of the real sensor. This constraint can be gradually lifted with the introduction of dedicated ray tracing hardware. Fourier tracing has so far only considered the periodogram as available from the squared magnitude of the DFT. Advanced methods such as subspace methods or compressed sensing are not yet considered.

In the presented version of Fourier tracing, only the azimuth angle was considered, i.e. the elevation angle is neglected. The extension of Fourier tracing to radar sensors with measurement capability in elevation direction is straightforward: If the elevation angle is included in the list of  $\delta$ -peaks, it can be transferred into spectral data under consideration of its window function, thus exactly the same as in the other measurement dimensions.

Wave polarization is assumed to be horizontal. Different polarizations of radar waves are not considered in Fourier tracing. Research work has been going on for over 20 years on the application of fully polarimetric radars in automotive radar.<sup>134</sup> The advantage is additional gain of information when illuminating the scene with both vertical and horizontal polarizations. This results in advantages for object classification<sup>135</sup> and localization<sup>136</sup>. This technology has not yet entered the automotive market at scale. The consideration of polarimetric effects with ray tracing is possible and shown by Deep et al.<sup>137</sup> on the example of the reflectivity of human skin.

Excluded effects in the simulation model include batch-to-batch variations of the sensor during manufacturing and dirt on the radome. Interference effects by other radars have also not been considered. This is motivated by the advanced state of the art which allows a high degree of mitigation. Time jittering effects due to the varying cycle time of the radar, which depends on the current computing load caused by the complexity of the current scenery, are ignored as well.

---

<sup>134</sup> Wenger, J. et al.: A Polarimetric 76 GHz Radar-Sensor for Automotive Applications (1997).

<sup>135</sup> Trummer, S. et al.: A polarimetric 76–79 GHz radar-frontend in automotive use (2016).

<sup>136</sup> Weishaupt, F. et al.: Polarimetric Radar for Automotive Self-Localization (2019).

<sup>137</sup> Deep, Y. et al.: Polarimetric Radar Cross-Sections of Pedestrians (2019).

## 4.6. Chapter conclusion: Generating spectral radar data with ray tracing

---

This chapter dealt with research question **RQ4**: *How can one use ray tracing to generate spectral radar data?* which can be answered from the highlighted findings as follows:

The Fourier tracing approach showed a promising foundation for generating radar data on a spectral level from currently available 3D vehicle models and simple texture descriptions. For this purpose, the ray tracing algorithm is used to model the propagation paths of the radar wave through a scene. Fourier tracing divides the simulation of a radar sensor into two parts: In the rendering step, the 3D scene is first divided into pixels. For each pixel, a ray is sent into the scene and a maximum number of interactions are allowed in which this ray can identify a path back to the sensor. For a ray received by the sensor the measured variables are transferred as  $\delta$ -peak according to a radar (range, radial velocity, azimuth angle, signal amplitude). In the second step, the  $\delta$ -peaks are transferred to the radar cubic representation. It is only at this point that sensor-specific properties regarding measuring ranges and resolutions must be considered. The verification section has shown that elementary properties of radar regarding separability, masking of weak objects, and the RCS profile of a flat plate are reproduced correctly.

However, a fundamental weakness of ray tracing for radar simulation became apparent: The aliasing problem requires high ray densities for maintaining high radiance. In short distances, this would lead to an excessive ray density. Due to the even spacing between rays, there are initially considerable sampling gaps between rays, especially with large distances. The lens factor and jittering angular increments between rays have proven to be effective countermeasures.

The angle-dependent backscatter condition in the Fourier tracing algorithm can cause inaccuracies when calculating propagation paths in special geometries such as spheres or CCRs: As soon as the backscatter condition is fulfilled, no further ray iteration is calculated. Due to the wave character, however, in real radar the signal strength would split up according to the conservation of energy. This cannot be achieved with Fourier tracing because the absorption coefficients or reflection losses due to materials are not known.

When allowing  $\hat{U}_{\iota_h} \geq 0$ , those  $\delta$ -peaks that carry  $\hat{U}_{\iota_h} = 0$  can be interpreted as a principal hit, similar to an “ideal lidar”. Thereby, a (supersampled) rendering image of the scenery ready for further processing in lidar sensor simulation is a side product of Fourier tracing.



## 5. Radar sensor model test for falsification

---

Chapter 3 presented a set of “features” that a radar simulation for virtual testing of autonomous driving must include. In this context, falsification experiments and test scenarios for a radar simulation model were postulated. In order to test whether model assumptions prove to be true, this chapter presents a falsification benchmark. The chapter investigates *RQ5: Which requirements are not fulfilled by Fourier tracing?*

Errors in synthetic data can be divided into different categories: Implementation errors due to programming errors include software bugs and can be identified by software engineering methods. Parameterization and calibration errors can be identified by verification tests. Examples are the resolution and separation capability or the irradiation pattern of the sensor. Modeling errors occur when assumptions underlying the model are violated. The research objective of this chapter is to reveal modeling errors in synthetic data and to provide an impact assessment of the identified errors in synthetic data. It is presumed that an existing sensor model is implemented and calibrated without errors, so that deviations between synthetic and measured data can be narrowed down to modeling errors.

For this purpose, a hypothesis is made about the validity of a partial aspect of the model. By means of a falsification experiment, the validity range of the hypothesis is determined. The experiment is set up in the simulation environment and synthetic sensor data is then compared to real measurements. The hypothesis is considered falsified if measurements show contradictory results compared to simulation.

There is no benchmark available yet that allows comparison between radar sensor models. For this reason, the Fourier tracing model developed in chapter 4 is implemented in Vires Virtual Test Drive (VTD) and compared to measurement results and another radar sensor model. The “CarMaker 9 raw signal interface (RSI)” radar sensor model is chosen as a comparative model because, according to the manufacturer, it has been validated in a comprehensive measurement campaign.<sup>138</sup>

---

<sup>138</sup> IPG Automotive: CarMaker 9 Press Release (2020).

### Comparative figures from measurement and simulation

The sensor to be modeled is the radar installed in the test vehicle. Its specification is given in the table 3.1. The parameter set of the Fourier tracing model is given in table A.1 shown in appendix A.4. The radar cubic is available from both the measurement and the simulation with Fourier tracing. For comparability, the signal-to-noise ratio (SNR) value is used in obtained by the calculation rule in appendix A.2.

To identify the radar cubic cells occupied by the object of interest (OOI), its state vector, which indicates the (real) pose of the OOI w.r.t. the ego, is required. In real measurement, this is available via the automotive dynamic motion analyzer (ADMA) devices mounted and calibrated in both the ego and OOI, see also A.7 in the appendix. According to the calibration in the stationary case as shown in appendix A.6, a lateral or longitudinal accuracy of 2-3 cm is achieved. In simulation, there is access to ground truth via “ideal sensors” and thus to the required states of the OOI relative to the virtual radar sensor in the ego vehicle. Based on respective relative distance, speed and angular position, all cells occupied by the OOI in the radar cubic can now be selected.

In CarMaker 9, only the target level (as defined in figure 2.2) is accessible from the radar sensor model. It is reported by means of a target list, i.e. radar data in physically interpretable quantities after applying a constant false alarm rate (CFAR) algorithm. Still, a SNR value can be obtained from the intensity that is reported for every target. All targets belonging to the OOI are available by filtering the target list w.r.t. the state of the OOI given by the “ideal sensor”.

### Structuring of the sensor model test aspects

The experiments are designed to investigate specific aspects of a radar sensor model. They are split into three parts, which are initially independent of each other and illuminate partial aspects of the sensor model:

**1) Wave propagation** measures the ability of the radar model to simulate multipath propagation. This is reflected in wave superposition and corresponding characteristic wave superposition patterns, influences on radial velocity determination, and the formation of mirror targets.

**2) Reflectivity behavior** of geometries and materials is analyzed: Fluctuations of the radar cross section (RCS) over the aspect angle are examined by means of 360 deg RCS profiles of a set of vehicles and during a slalom run of a large vehicle. The reflectivity behavior of pavement determines the visibility of occluded objects.

**3) Sensor uncertainties** related to intrinsic and extrinsic influences are investigated w.r.t. noise in the received power when observing static vehicles, and to range accuracy in a dynamic experiment.

## 5.1. Wave propagation aspects

---

In this section, the aspects of multipath propagation w.r.t. wave superposition, changes in radial velocity, and formation of mirror targets in the radar simulation model are analyzed.

### 5.1.1. Wave superposition pattern with CCR

Based on the harmonic pattern visible in the received power when approaching a corner cube reflector (CCR), its height can be estimated as shown in paragraph 3.3.3. Therefore, the method for estimating object height, as described in section 3.7.2, is applied to synthetic radar data. It was also shown that wave superposition for non-point targets occurs at the receiver side, i.e. as the waves following the direct and indirect propagation paths merge at the sensor.

Successful demonstration of this feature in simulation indicates that the wave propagation paths between the sensor and the CCR are correctly identified and superimposed by the sensor model. Therefore, the following hypothesis is made:

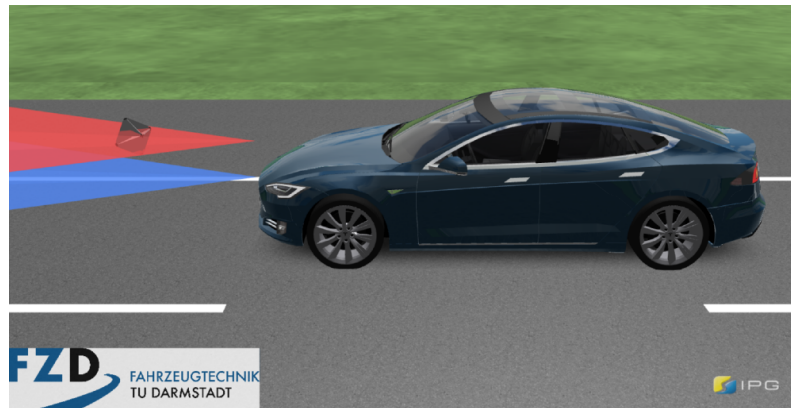
**Hypothesis 1** (Object height estimation). When approaching a CCR in simulation, Fourier tracing generates an wave superposition pattern from which the mounting height of the CCR can be estimated by using the Diewald/Schneider method.

To falsify hypothesis 1, such a scenario is conducted in the simulation environment, see figure 5.1a. The test is conducted with mounting position heights  $h_{\text{CCR,GT}} = 0.63$  m and 1 m, respectively. The sensor (i.e. receiving antenna) is installed at  $h_S = 0.63$  m.

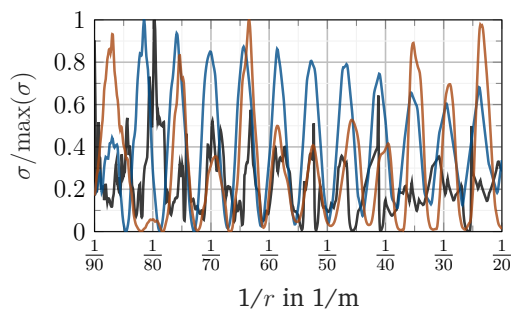
The height spectrum shown in figure 5.1 shows that Fourier Tracing correctly estimates the object height while the CarMaker 9 RSI model shows a slight overestimation of the height. This can be taken as an indication that the mechanism for the formation of wave superposition effects by multipath propagation is correctly represented in both models.

Thereby, hypothesis 1 is not falsified for the studied mounting heights of the CCR.

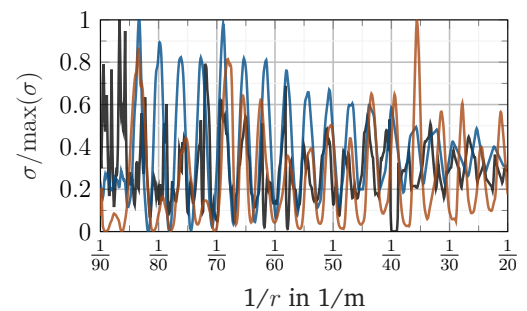
## 5. Radar sensor model test for falsification



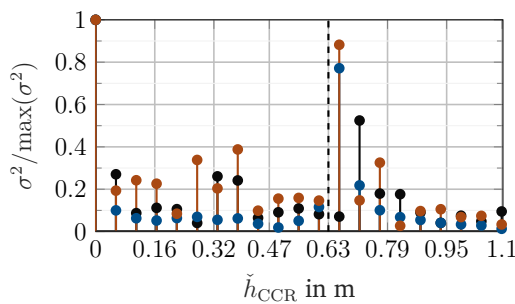
(a) CCR at  $h_{CCR,GT} = 1$  m inserted in CarMaker 9. The colored cones indicate serve as verification of mounting heights for the CCR at 1 m (red, depicted case) and 0.63 m (blue).



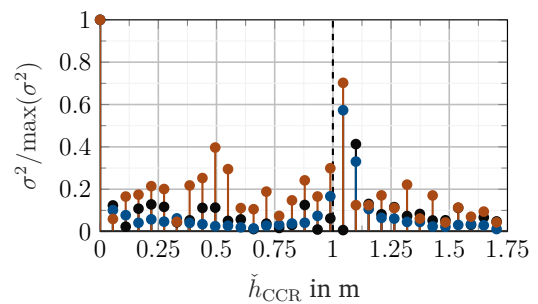
(b) Amplitude characteristic over reciprocal distance with  $h_{CCR,GT} = 0.63$  m



(c) ... $h_{CCR,GT} = 1$  m



(d) Height spectrum for CCR mounted at  $h_{CCR,GT} = 0.63$  m



(e) ... $h_{CCR,GT} = 1$  m

Figure 5.1.: Comparison of CCR height estimation between simulation and measurement. Line color assignment: Measurement (—), Fourier tracing (—), CarMaker 9 RSI (—).

### 5.1.2. Shaking factor

Recall that unlike a CCR, stable wave superposition patterns cannot be observed in compact class vehicles. Instead, the fluctuation of the RCS values can be described by a tilted exponential distribution, cf. 3.19 and table 3.2 in section 3.7. This behavior is also expected from the simulation:

**Hypothesis 2** (Shaking factor). Fourier tracing renders the RCS fluctuation behavior of vehicles according to the tilted exponential distribution in eq. 3.18.

The dynamic scenario, as described in figure 3.15c, is simulated with three different vehicles in the simulation environments. 3D models representing a BMW i3, Audi A3 and VW Golf are used for the Fourier tracing model. These vehicles were not available as 3D models in CarMaker 9. Instead, a Citroen C3, Mercedes A-Class and Peugeot 105 are used as substitutes. As it was found in figure 3.18, the characteristics of the shaking factor is of similar stochastic nature for all compact class vehicles under investigation. This justifies the selection of different vehicle models from the compact class segment in simulation.

For each simulation cycle, the target showing the highest RCS is selected from the set of those assigned to the OOI. As with the procedure for measurement data (see section 3.7), the simulation results of all vehicles examined are aggregated to create the data basis for the statistical analysis. After deducting the moving median value over 10 s, the fluctuating part of the RCS (denoted  $\sigma_\xi$ ) is available which is statistically evaluated, see eq. 3.16. The RCS values calculated from the radar targets are transferred to the  $\log(1 - \text{ECDF}(\sigma_\xi))$  representation.

In addition to the measured and simulated values, figure 5.2 shows a regression line for the tilted exponential distribution, where both the Fourier tracing and the CarMaker 9 model show high agreement with the measurement. A CCR measurement representing a harmonic wave superposition pattern is given as reference. Both sensor models include sections with locally higher agreement between synthetic and real sensor data. The measurement data for the CCR show clearly visible harmonic wave superposition patterns when plotted over reciprocal range, deviating from the approximately linear course required by the  $\log(1 - \text{ECDF}(\sigma_\xi))$  representation.

The results indicate that the fluctuation of RCS is implemented in high agreement with the measurement in both Fourier tracing and the CarMaker 9 RSI model. Both models show portions with a higher qualitative agreement with the measurement. A falsification of hypothesis 2 cannot be determined from this result.

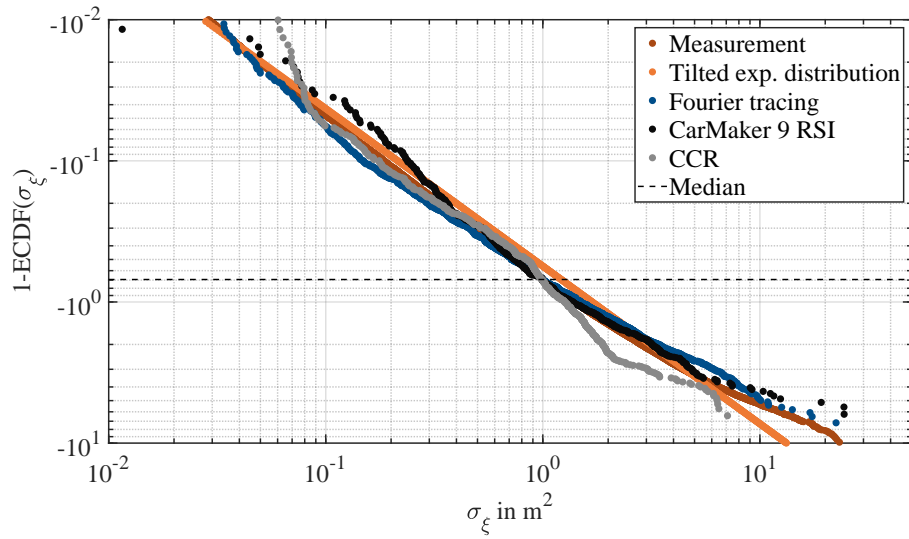


Figure 5.2.: Qualitative analysis of shaking factor via the 1-ECDF plot of simulated RCS quantities. The tilted exponential distribution proposed in eq. 3.18, measured RCS values for vehicles and CCR scenario are given for reference.

### 5.1.3. Relative velocity measurement under multipath propagation

It was shown in section 3.6 that both the indirect-indirect multipath combination (II) and direct-indirect multipath combination (DI)/indirect-direct multipath combination (ID) cases occur in the course of horizontal multipath propagation and reflection off guardrails. Therefore, the following hypothesis is formulated:

**Hypothesis 3** (Doppler under multipath). Fourier tracing renders stable mirror targets from which a radial velocity corresponding to their angular position and the propagation path is obtained.

For falsification, such a scenario is created in the simulation, see figure 5.3a. The OOI overtakes the ego vehicle with a relative speed of 5.6 m/s to reflect the same relative velocity and conditions as in section 3.6. The lane is limited to the left by a reflective wall that allows the establishment of indirect propagation paths. This experiment also serves to evaluate the ray tracer w.r.t. its ability to find II and DI/ID paths between OOI and sensor. The radial velocity information for each hit point is available from the rendering step of Fourier tracing. Because the ray history, i.e. all impact points in the course of the

ray recursion, is known, it is also possible to distinguish between direct and indirect hits. Such information is not available with the CarMaker 9 model. Because this sensor model operates on target level, ray tracing hit points are obtained indirectly: To avoid that an actual occurring reflection is hidden in noise, the noise level and the detection threshold is set to a minimum value while the transmitted power is increased. Targets reported by the sensor model are still discretized according to the radar's resolution cells, but now all ray tracing hit points are expected to be converted into targets. Because the focus is on the principal presence of hit points from the ray tracer, this avoids that searched targets are cut off by the detection threshold.

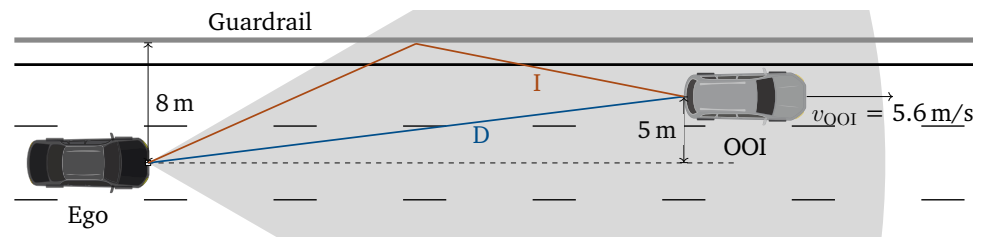
The results are shown in figure 5.3, which is structured as follows: The actual relative longitudinal velocity of the OOI is constant at 5.6 m/s. Radial velocity under multipath is calculated according to eq. 3.8 and 3.9 assuming the hit points are located in the geometrical center of the rear of the OOI cf. 5.3a

It can be seen in figure 5.3b that the Fourier tracing model fundamentally represents all propagation possibilities, as hit points that report the desired velocity are present. However, the II part clearly predominates as a significantly higher number of hit points is present. In case of ID/DI propagation, hit points were only found up to 25 m. The higher number of hit points in the II case indicates that detections for this case are more likely to be found with Fourier tracing. It is expected that a mirror object will form from the targets that results from the hit points during tracking.

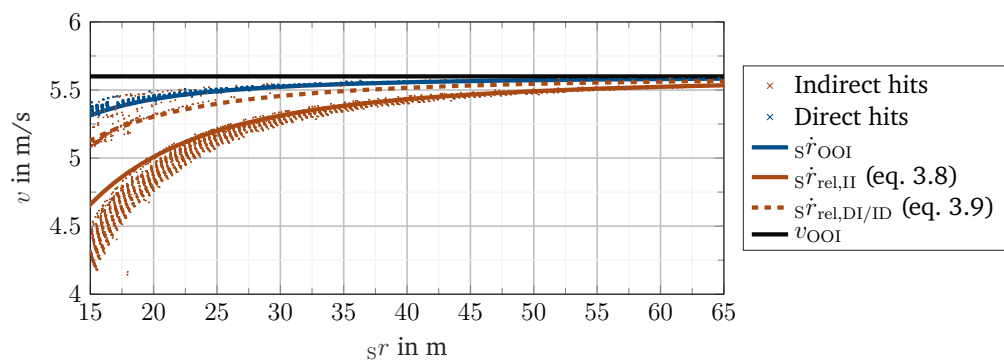
With the CarMaker 9 model, it is exactly the opposite: Here, the ID/DI portion predominates, while only a few measurements can be linked to the II path. Depending on balancing between amplitude and detection threshold, a target is formed from a hit point. The irregular appearance of the targets will potentially hamper the formation of a mirror object by an object tracking filter.

These results are not in contradiction to the measurements in which both II and ID/DI cases were observed. Because the reported relative velocities are not significantly outside the theoretically determined model values, no falsification of hypothesis 3 is evident.

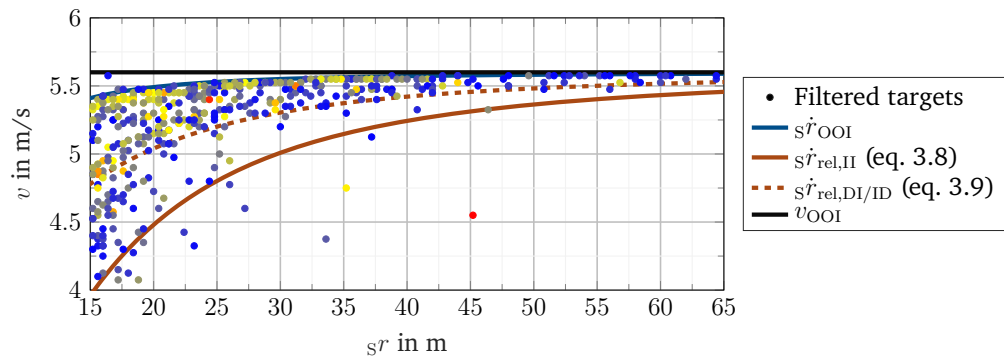
## 5. Radar sensor model test for falsification



(a) Bird's eye view on the evaluation scenario showing direct (D, —) and indirect (I, —) path via a guardrail. The ego vehicle is overtaken by the OOI on the left lane.



(b) Fourier tracing



(c) CarMaker 9 RSI

Figure 5.3.: Range-Doppler plot with simulated quantities showing direct and indirect hits and their respective velocity in a horizontal multipath scenario. Discrete simulation steps lead to data gaps.

#### 5.1.4. Repeated reflections

During repeated reflection off the sensor under multipath propagation, the decrease of signal amplitude is composed of the doubled path length and the ratio of object to sensor size. At the same time, the measured velocity along the path of the radar wave adds up, resulting in twice the radial velocity for the mirror target. Referring to the result from section 3.5, it is claimed:

**Hypothesis 4** (Repeated reflection). Fourier tracing forms stable mirror targets by repeated reflection at twice the distance and twice the speed of the OOI. Their SNR value differs by a median of 25 dB.

In the falsification experiment conducted in simulation, the OOI moves away from the ego vehicle with  $s_{v_{rel,OOI}} = 10$  km/h. This results in  $2 s_{v_{rel,OOI}}$  for the mirror target. The identification criterion for the mirror targets reported by simulation is twice the velocity compared to those induced by the OOI. This verifies the correctness of the assumption that the radial velocity components sum along their paths in the course of multiple reflections.

It can be seen in figure 5.4 that Fourier tracing consistently reports the mirror object at distances up to 35 m for all three vehicles studied. The SNR for the mirror object is determined to be -25 dB less, which is consistent with the results of the measurement (see figure 3.12).

In the CarMaker 9 model, the mirror object shows fewer targets that can be associated with up to 50 m with the OOI. The drop in SNR for the mirror object is about -50 dB and exceeds the expected range from the measurement, which is about -25 dB.

The appearance of the mirror object in a repeated reflection can be assessed as follows: Above a distance of  $s_r = 40$  m the mirror object can no longer be identified by Fourier tracing for the selected vehicles.

The measurements show a homogeneous characteristic for the visibility of the mirror targets. This cannot be confirmed in the simulation, since the Golf Mk7 induces mirror targets over a greater distance: Here, 90% of the mirror targets are visible up to 35 m, compared to 25 m for the BMW i3 and Audi A3. The CarMaker simulation shows a worse visibility of the mirror object w.r.t. its induced targets. Based on the significantly lower SNR compared to the OOI, it can be assumed that the signal drop in the context of multiple reflections is modeled as too strong. As a consequence, the CarMaker simulation shows less frequent occurrence of mirror targets than is the case in the measurement.

Hypothesis 4 could thereby not be falsified for either of the investigated vehicles with Fourier tracing.

## 5. Radar sensor model test for falsification

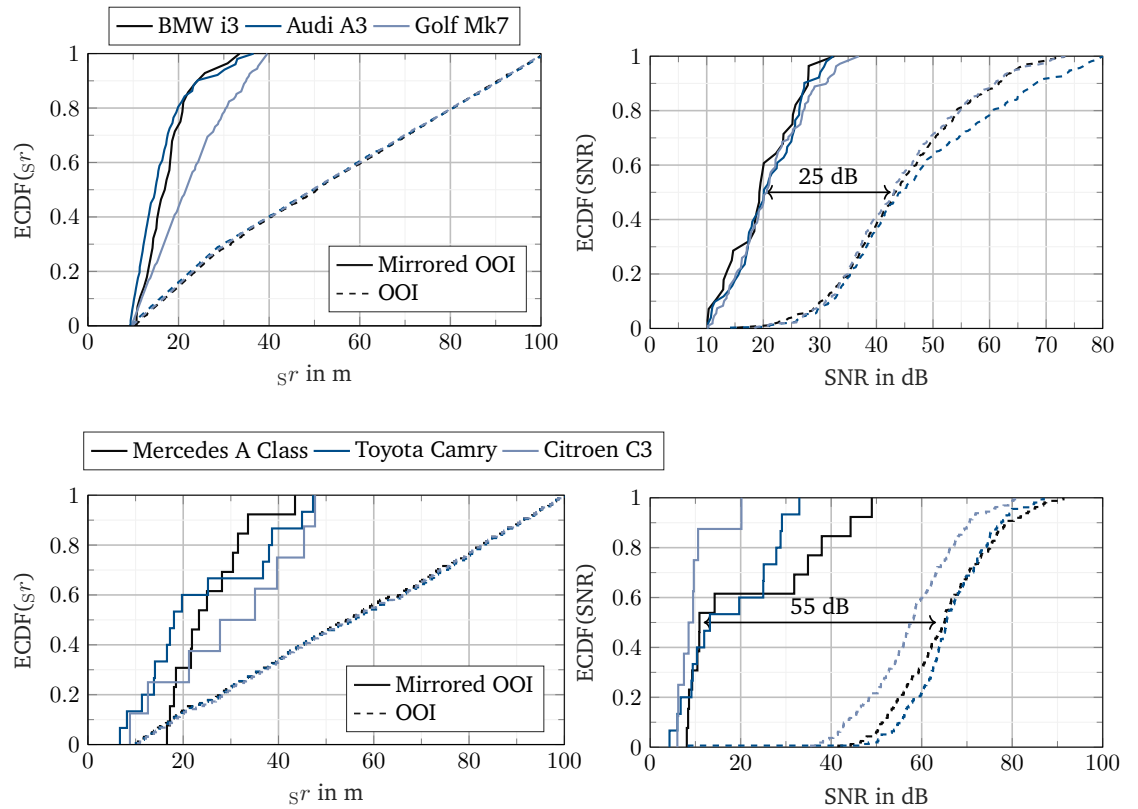


Figure 5.4.: Repeated path scenario in simulation. Fourier tracing (top), CarMaker 9 RSI (bottom).

## 5.2. Reflectivity behavior of geometries and materials

---

### 5.2.1. Sensitivity of RCS to aspect angle

Concerning the reflectivity, in section 4.5.1 the assumption was made that the outer body of a vehicle is mainly made of reflective metallic material. The simulated backscatter property of vehicles is approximated by the reflectance function derived from the Phong reflection model, see eq. 4.12. Therefore, the following hypothesis is stated:

**Hypothesis 5** (RCS characteristics). The proposed reflection function for vehicles reflects the sensitivity of their RCS to aspect angle. Simulated RCS profiles shows clear peaks at 90 and 270 deg, several larger signal drops, and a dynamic range of about 20 dBm<sup>2</sup>.

Two experiments are proposed for falsification: In the first, RCS profiles of different vehicles are generated from a 360 deg rotation around their vertical axis. As such RCS profiles are only theoretical in nature, the reflectivity behavior in real traffic is investigated by measuring a vehicle ahead that is following a slalom course. The OOI is a VW Crafter, whose box-shaped body promises a higher specularity than a compact class vehicle and therefore the changes in signal amplitude during the slalom drive are particularly pronounced.

#### RCS profiles

In contrast to calibration objects such as flat plates, spheres or CCR, analytically calculated RCS profiles for complex geometries such as vehicles are suitable for radar simulation only to a limited extent. Their analytical calculation requires detailed 3D models with fine mesh sizes and material allocations, which are usually not available in automotive simulation environments. Instead, the qualitative comparison of the simulated RCS profile with one obtained by measurements is used. Their metrological determination is carried out by measuring the RCS profile during a 360 deg rotation of the vehicle: It is placed on a turntable which is embedded in the floor of an anechoic chamber. This method is used by Schuler<sup>61</sup>, Schipper et al.<sup>139</sup>, and Mesow<sup>126b</sup>. To avoid disturbing influences of the turntable during measurements outside anechoic chambers, Toss et al.<sup>140</sup> propose a method in which the radar is mounted on a self-driving trolley that moves in a circle around the vehicle. The influence of ground reflection can be compensated by a reflectivity model as demonstrated by Karlsson et al.<sup>141</sup>.

---

<sup>139</sup> Schipper, T. et al.: RCS measurement results for automotive related objects at 23-27 GHz (2011).

<sup>140</sup> Toss, H.; Karlsson, K.: Radar reflectivity spatial profile of 3D surrogate targets and real vehicles (2019).

<sup>141</sup> Karlsson, K. et al.: Reducing influence from ground reflection during RCS characterization (2019).

## 5. Radar sensor model test for falsification

---

Two RCS profiles from literature recorded with radar sensors operating at  $f_c = 77$  GHz are available for comparison: A Mazda 6 profile from the work of Mesow<sup>126c</sup> and a Volvo V40 profile from the work of Karlsson<sup>142</sup>. 3D vehicle models of these vehicles for use in simulation are, however, not available. Other reasons for expected deviations are explained by their measurement methodology: Mesow and Karlsson each measure at different sensor heights (0.9 m with Mesow, approx. 0.5 m with Karlsson) and distances (14 m with Mesow, 30 m with Karlsson).

RCS profiles are generated for different vehicles from the simulation with Fourier tracing or CarMaker and compared in a qualitative analysis. The OOI is placed in 30 m in front of the radar, which is mounted at a height of 0.63 m. Expected characteristics of the RCS profiles are distinct peaks at 90 and 270 deg, a dynamic range of 20 dBm<sup>2</sup>, and a pronounced fluctuation, as seen in the RCS profiles in the literature. For direct comparison, 3D models of Tesla Model S, Mercedes Sprinter, Mercedes Vito, Mercedes S-Class, Chevrolet Silverado, and BMW 5 Series are available in both VTD and IPG CarMaker 9. At this point, only the Tesla Model S and Mercedes Sprinter profiles will be discussed. The other profiles are shown in appendix A.5.

It can be seen from the simulated RCS profiles shown in figure 5.6a that Fourier tracing renders their expected characteristics and no falsification of hypothesis 5 can be deduced. Discrepancies between Fourier tracing and CarMaker in the RCS profile can be explained by differences in the 3D model in terms of surface meshing and details, which renders in different surface normal vectors and respective reflectivity behavior of materials. For a VW Crafter, or Mercedes Sprinter<sup>143</sup>, the 3D models in the virtual environments show the characteristics of a panel van, despite differences in detail, see figure 5.5.



(a) Real vehicle



(b) Vires Virtual Test Drive



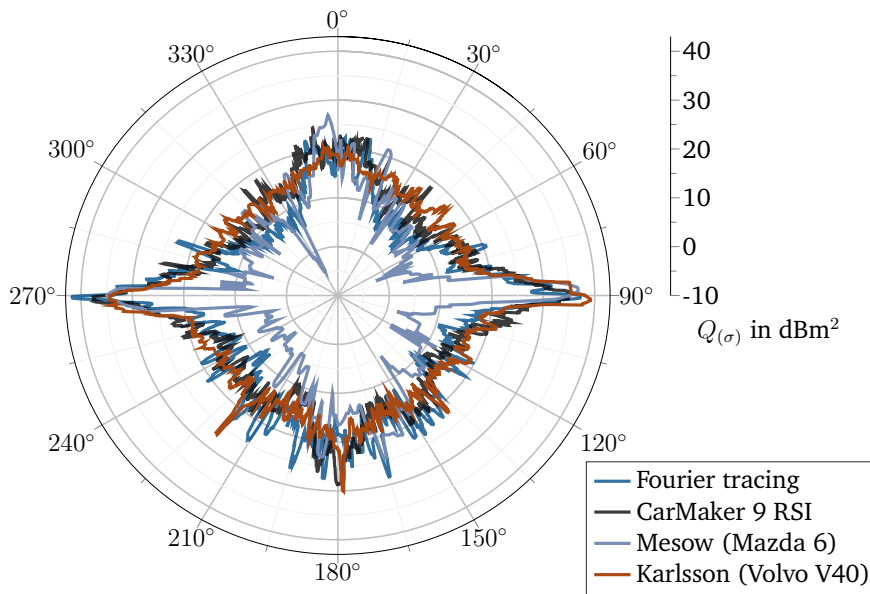
(c) CarMaker 9

Figure 5.5.: VW Crafter / Mercedes Sprinter as an example of a box shaped panel van.

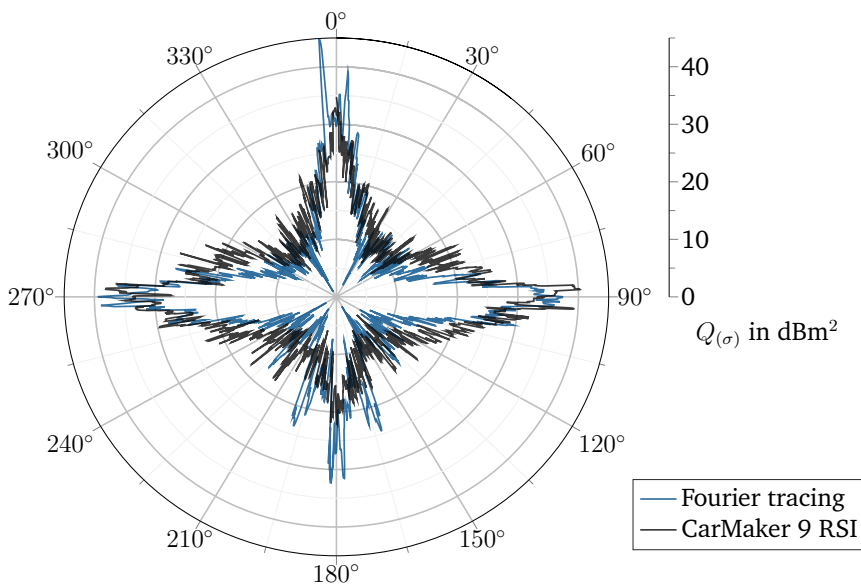
---

<sup>142</sup> Karlsson, K.: Radar Cross Section (2018), p. 10.

<sup>143</sup> Mercedes Sprinter is also marketed as VW Crafter.



(a) Telsa Model S, smoothed with a 11 sample moving median filter for readability.



(b) VW Crafter/ Mercedes Sprinter, smoothed with a 4 sample moving median filter for readability.

Figure 5.6.: RCS profiles obtained via Fourier tracing in VTD and CarMaker 9 RSI. Data of Mesow (recorded in an anechoic chamber) and Karlsson (recorded by a rotating trolley) were provided by the respective authors for use in this dissertation.

### Slalom drive

The “Measurement2Sim” method developed by the author is used to transfer the slalom drive of a VW Crafter shown in figure 5.7 to simulation. With this method, the relative positions and velocities of different agents can be transferred from the measurement to the simulation environment<sup>144</sup>.

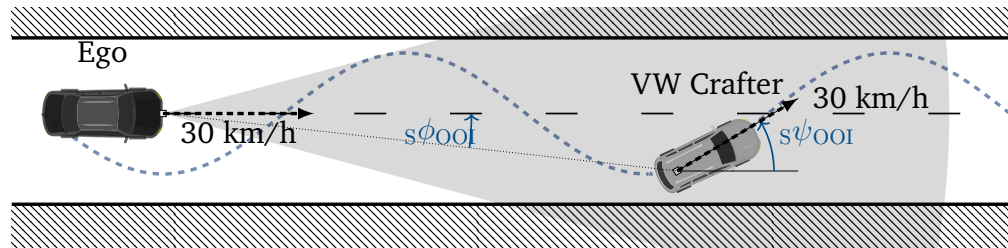


Figure 5.7.: Illustration of the slalom drive: A sine sweep motion is superimposed to the longitudinal movement of the VW Crafter which drives at about 30 km/h. The ego vehicle, carrying the radar sensor, is traveling with about 30 km/h.

The azimuth angle  $s\phi_{OOI}$  and yaw angle  $s\psi_{OOI}$  between sensor and the reference point (center of rear axis) of the VW Crafter is made available via ADMAs which are installed in both vehicles.

Figure 5.8 shows measurement and simulation results obtained during the slalom drive. The basic characteristics regarding highest RCS for heading angles of about 0, as well as the strong drop at heading angle unequal 0 are present. It can be seen that the periodic fluctuation in RCS spans about 20 dBm<sup>2</sup> and are thus more pronounced in the simulation with Fourier tracing than in the measurement. In the latter, it shows a fluctuation range of about 10 dBm<sup>2</sup>, see figure 5.8d and 5.8g.

The aspect angle sensitivity of the reflectivity modeling assumed in Fourier tracing can hence be partly confirmed in the sense of the hypothesis 5. The results for the 360 deg RCS profiles do not show a clear indications of falsification. In the slalom case shown here, however, there are indications that the sensitivity of the reflectivity model in Fourier tracing is too high.

<sup>144</sup> For CarMaker this is only possible with the OOI. For the ego vehicle, it is possible to specify set values for position and speed as input for the vehicle dynamics model. Due to the behavior of the underlying low-level controllers for the vehicle actuators, reference trajectories generally cannot be tracked without a residual tracking error. To achieve an identical behavior within the simulation and the real-world test drives, the models for vehicle dynamics, tires, and low-level controllers have to be adapted towards the real ego vehicle.

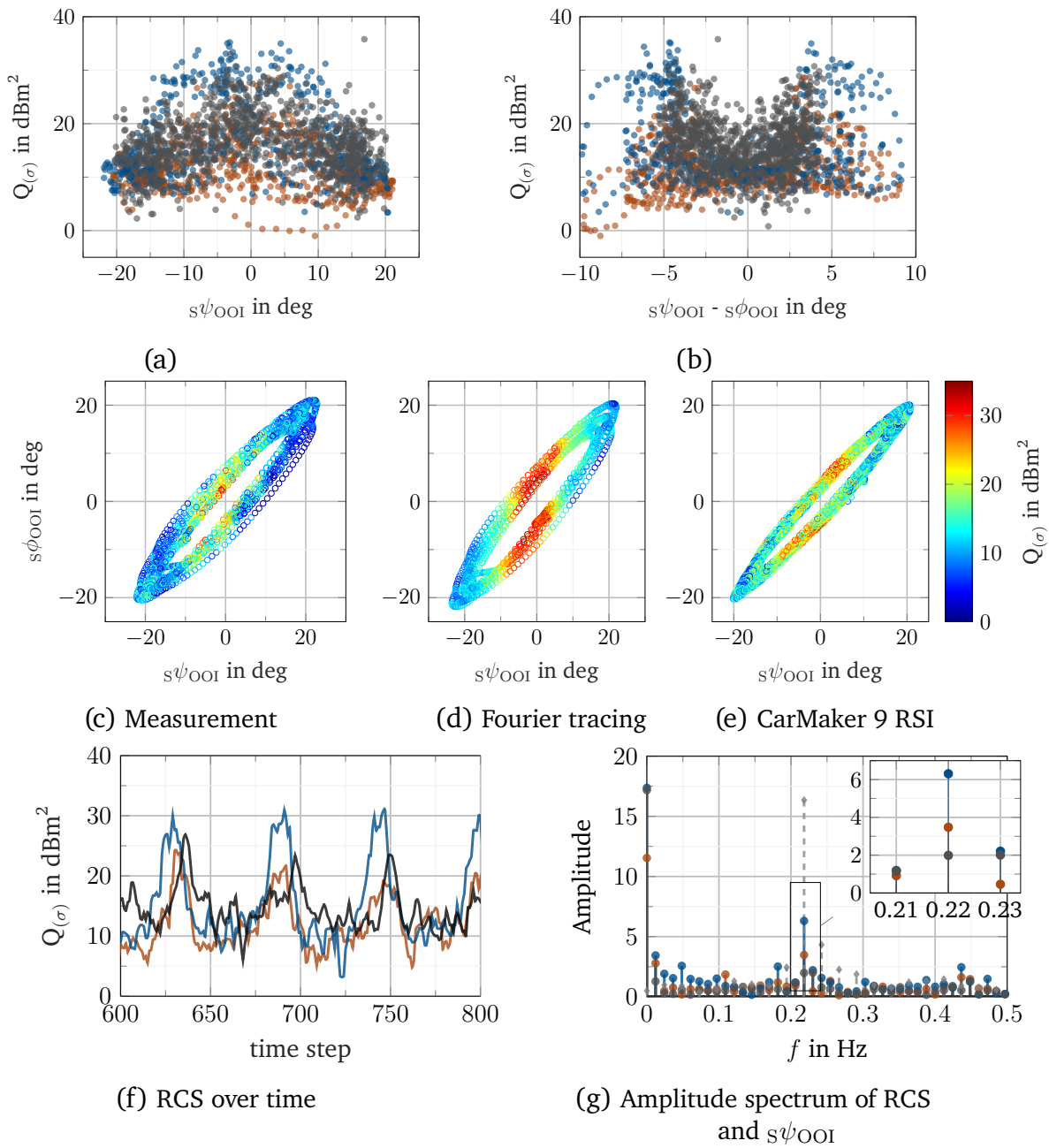


Figure 5.8.: Results of slalom drive with different representations of RCS over heading  $s\psi$  and azimuth  $s\phi$ . Line color assignment: Measurement (—), Fourier tracing (—), CarMaker 9 RSI (—).

### 5.2.2. Occluded objects

As outlined in section 3.4, the OOI can be measured by multipath propagation even if it is occluded, i.e. not within the line of sight (LoS) of the sensor. One possible propagation path is reflection off the pavement if the vehicle in front has sufficient ground clearance. The road reflectivity model according to Schneider is used for the wave propagation over the pavement in Fourier tracing. A simplification is that the road is perceived as specularly reflective because it is assumed to be ideally smooth. It is known that this simplification is not valid: In the case of purely specular reflection, the ground clearance of the forefront vehicle and the overall height of the OOI limit its visibility. This results in a visibility of up to 175 m for the VW Crafter for the scenario investigated in section 3.4. However, the reflection properties of occluded objects must be correctly rendered within the range of validity of specular pavement reflections. It is assumed that this is the case with Fourier tracing:

**Hypothesis 6** (Reflectivity of occluded vehicles). It is possible to identify occluded vehicles by specular reflection off the pavement with Fourier tracing.

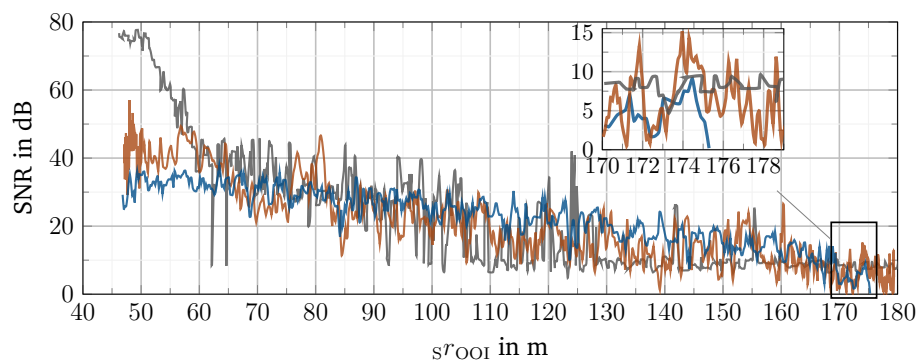


Figure 5.9.: SNR of OOI (here: occluded VW Crafter) obtained by and measurement (—), Fourier tracing (—), CarMaker 9 RSI (—).

The analysis of the experiment, as shown in figure 5.9, shows that Fourier tracing reproduces a linear decay of SNR with less pronounced fluctuations compared to the measurement. As expected, the OOI is no longer visible from about 175 m, although it remains visible in the measurements. The CarMaker 9 RSI model reproduces the course in an unsatisfactory way: After a very strong drop in SNR the OOI remains at a SNR of 10 dB from about 125 m onwards. The assigned targets are thereafter approximately at the level of the detection threshold for which an SNR of 6 dB is set. Thereby, hypothesis 6 cannot be rejected in this setup, where a distance to the OOI of up to 175 m is examined.

### 5.2.3. Material properties: Opacity of glass

The ray tracing algorithm underlying Fourier tracing treats glass as non-transmissive to radar waves. Thereby rays can reach occluded objects only via multipath propagation. In section 4.5.1, it was argued that this simplifies ray tracing since there is no need to calculate wave transmission and diffraction.

**Hypothesis 7** (Opacity of glass panes). In a radar simulation, glass may be modeled as fully opaque to radar.

Hypothesis 7 is tested by installing radiation-absorbent material (RAM) at the rear of a vehicle in simulation. This prevent propagation paths via pavement reflections, see figure 5.10. Therefore, the visibility of a CCR located in front of a stationary vehicle but within the LoS of a radar sensor is possible only by diffraction of radar waves at this vehicle or by penetration of the glass panes.



(a) VW Golf Mk5 with RAM



(b) Carton serves as RAM in simulation

Figure 5.10.: Experiment setup for studying opacity of glass: A CCR is placed either inside or at various distances in front of the vehicle. RAM is installed for preventing reflections under the vehicle.

The results in terms of SNR for near scan (NS) and far scan (FS) by conducting the experiment with a VW Golf Mk5 and BMW i3 are depicted in figure 5.11 and falsify hypothesis 7. If the CCR is mounted inside the vehicle, i.e. between the front seats, the SNR increases, indicating higher backscatter intensity. A further peak, located inside the vehicle, is formed in NS measurement mode. This contradicts the hypothesis of full opacity of glass for radar. If the CCR is placed in front of the vehicle, it is visible to the radar during all measurement trials. In addition to the permeability of glass, diffraction effects not accounted for in the Fourier tracing regime presented may also contribute.

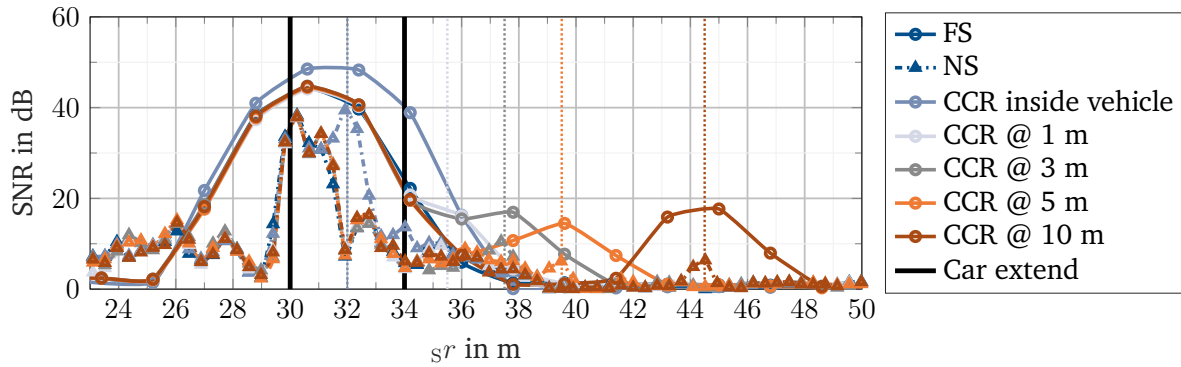
It would be necessary to isolate the space around the OOI with RAM to separate wave diffraction from penetration through glass.

Because neither Fourier tracing nor the CarMaker simulation can display an increase of received power due to the presence of the CCR in the scenery, a modeling error is identified for both models.

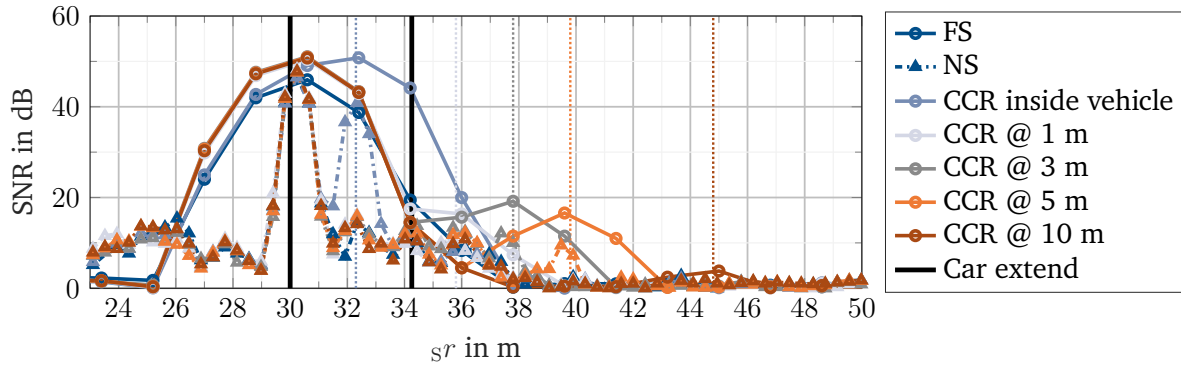
As radar waves show the ability to penetrate the vehicle's outer shell, the range bin that shows the strongest backscatter is to be discussed. For this, the situation shown in figure 5.11 is considered in detail. It is visible that radar targets, as found by quadratically interpolated FFT (QIFFT) from the spectral power in respective range bins, are located inside the vehicle bounding box as shown in figure 5.12. The result is confirmed for both BMW i3 and VW Golf Mk5.

This behavior is only partially represented by Fourier tracing. The hit points are found on the trunk lid, which is slightly indented w.r.t. the vehicle bounding box. Since the rays cannot penetrate into the vehicle, the target found by QIFFT is only slightly offset from the edge of the bounding box.

Figure 5.13 shows hit points and spectral power over range bins on the rear of a BMW i3 from simulation with Fourier tracing. Unlike the measurements, the difference between NS and FS is marginal with Fourier tracing, i.e. 0.16 m and 0.2 m for NS and FS, respectively, whereas 0.6 m and 0.78 m is obtained from the measurements. Backed on these additional remarks, hypothesis 7 can be considered falsified.



(a) Vehicle under test: BMW i3



(b) Vehicle under test: VW Golf Mk5

Figure 5.11.: Measurement results for opacity of glass experiment. A static vehicle has RAM at the rear and is placed at 30 m (tape measure precision) in front of the sensor and a CCR with  $Q_{(\sigma)} = 23.6 \text{ dBm}^2$  is either mounted inside the vehicle, or at distances between 1 and 10 m in front of the vehicle. Solid and dash dotted lines refer to NS and FS respectively. Dotted vertical lines indicate ground truth position of CCR.

## 5. Radar sensor model test for falsification

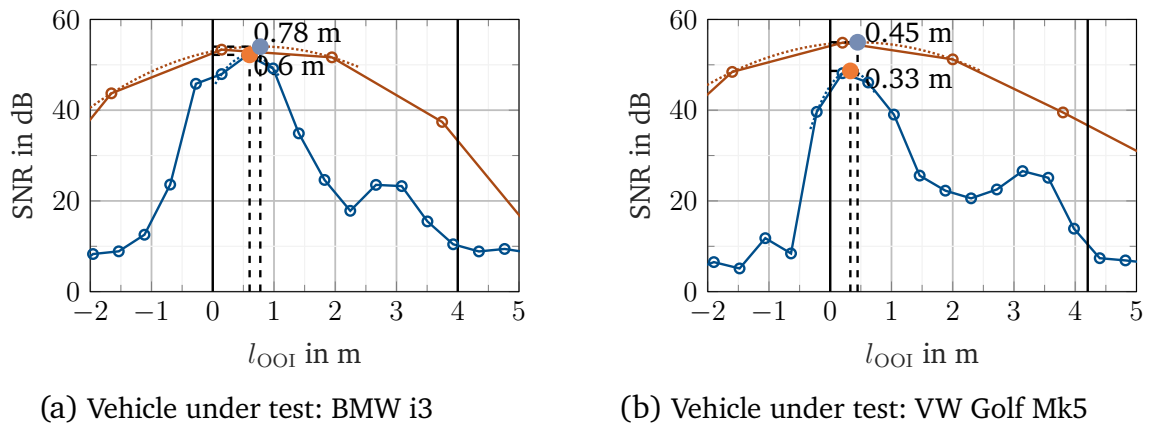


Figure 5.12.: Range accuracy considering the measurement of a stationary BMW i3 or VW Golf Mk 5 located at 25 m in front of the radar (tape accuracy). Line color assignment: NS ( $\text{---}\circ\text{---}$ ), FS ( $\text{---}\circ\text{---}$ ), targets found by QIFFT: NS( $\bullet$ ) and FS ( $\bullet$ ), vehicle dimension ( $\text{---}$ ).

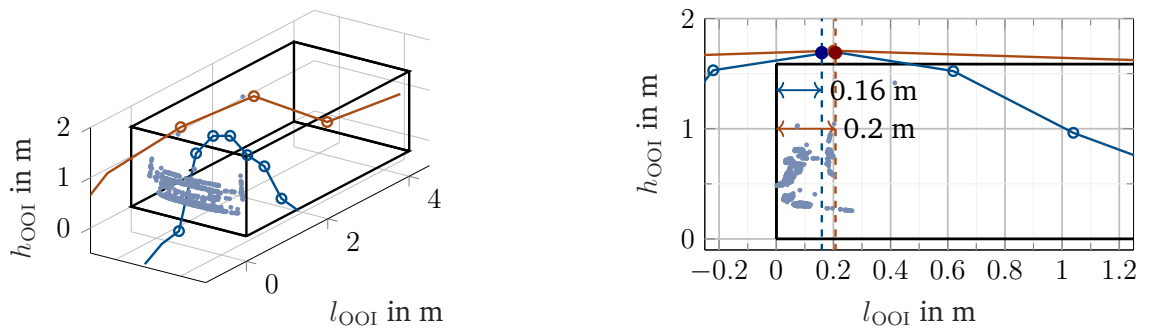


Figure 5.13.: Range accuracy in simulation on the example of a BMW i3 showing an overlay of hit points, bounding box, and the spectral power for NS and FS. Line color assignment: Hit points from ray tracer ( $\bullet$ ), NS ( $\text{---}\circ\text{---}$ ), FS ( $\text{---}\circ\text{---}$ ), interpolated targets found by QIFFT ( $\bullet$ ), vehicle bounding box ( $\text{---}$ ).

### 5.3. Measurement uncertainties

---

The resolution of measurements in radar is increased by spectral interpolation methods such as QIFFT. Its precision is, however, influenced by the amount of noise that shifts the interpolated peak value between adjacent bins. It was found in section 3.8.2 that measurements of the static RCS of vehicles in close range to the sensor fluctuates within  $\pm 0.5$  dB. According to section 3.9.1, vibrations of the vehicle body cause a fluctuation of about 2 dB in RCS of the OOI. It was also shown in section 3.9.2 that extrinsic state uncertainty is introduced by the driving style of other road users. Motivated by these factors, Fourier tracing avoids explicit modeling of noise processes in received power under the following hypothesis:

**Hypothesis 8** (Measurement uncertainties). With Fourier tracing, it is possible to model noise superposed on range accuracy by modeling unsteady motion of traffic participants.

The falsification of hypothesis 8 is based on two scenarios: First, the fluctuating range of RCS in a stationary scenario is analyzed. This indicates the fluctuation of RCS present in the synthetic radar data in the absence of other influences such as the shaking factor or extrinsic uncertainty.

Secondly, the achievable range accuracy is investigated by means of an adaptive cruise control (ACC) scenario. Here, both the ego vehicle and the OOI travel at a set speed of 50 km/h. This results in a distance of about 25 m between the vehicles. This scenario is simulated in two variants: On the one hand, under idealized conditions, i.e. both the ego and OOI are driving with constant speed and distance between the vehicles. On the other hand, the “Measurement2Sim” method is applied to transfer the test drive used to evaluate the measurement results into the simulation. Extrinsic uncertainties in the trajectory and velocity profile of the ego vehicle and OOI as presented in section 3.9.2 are propagated into the simulation in this way.

Then, the quality of the interpolated range measurement using the QIFFT method for parabolic interpolation (see appendix A.8) is analyzed. The quantification of accuracy and precision is done by estimating a normal distribution using the maximum likelihood estimation (MLE) method. The mean value then indicates the accuracy, while the precision is given by the standard deviation, denoted as  $\varsigma$ .

### 5.3.1. Noise in received power

The power values in those cells of the radar cubic occupied by the OOI are considered for a static vehicle. The RCS value is calculated and noise fluctuation is obtained according to eq. 3.20. Noise fluctuation  $Q_{(\sigma),\xi}$  is given as a box plot shown in figure 5.14. A considerable spread in noise level is visible when considering the interquartile range. Both with the Fourier tracing model and the CarMaker 9 RSI model, the noise level exceeds the observation from measurements (see figure 3.21), where it was consistently found within  $\pm 0.1 \text{ dBm}^2$ .

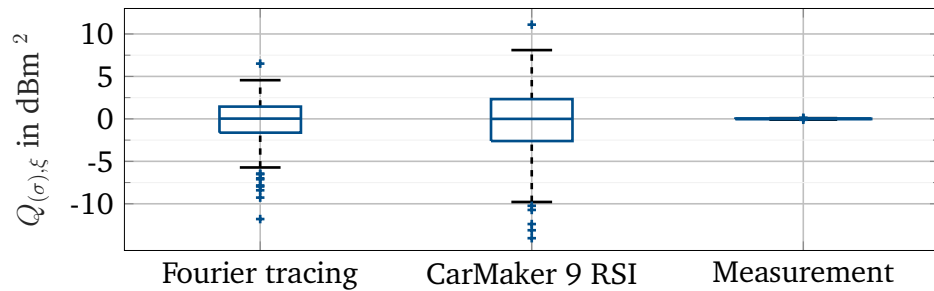


Figure 5.14.: Box plot of RCS fluctuation for a static vehicle located at  $s_r = 25 \text{ m}$ . A measurement result previously shown in figure 3.21 is given as reference.

Apparently, ray jittering in Fourier tracing prevents the same propagation path to form in successive cycles. With different ray paths determined in each cycle, there are also different phases. This may lead to significant differences resulting from the complex addition used to calculate simulated received power. Obviously, an unreasonably high radiance would have to be chosen in order to observe the same propagation paths and thus a more uniform backscattering despite jittering. Therefore, Fourier tracing does not capture the stationary noise behavior as it would correspond to the real sensor. The CarMaker 9 RSI model offers an extensive noise parameterization. It can be assumed that the noise behavior can be further improved by parameter tuning.

### 5.3.2. Range accuracy

An ACC scenario is used to evaluate the range accuracy obtained in simulation. The interpolated range between the sensor and the OOI  $s\check{r}_{OOI}$  is found by applying the QIFFT method on the radar cubic<sup>145</sup>. It is compared to the reference distance  $sr_{OOI,GT}$  that is available from either the ADMA or simulation ground truth. The procedure shown in more detail in the section A.7 in the appendix.

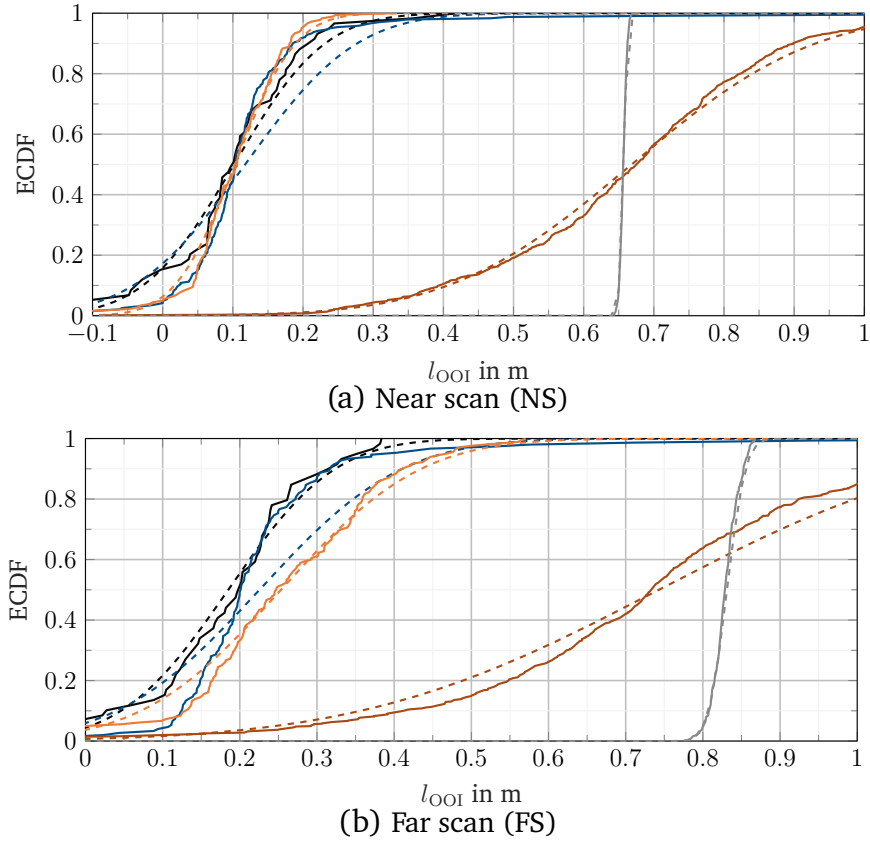
Two aspects of the results shown in figure 5.15 are highlighted: With measured data, the precision of the range measurement decreases in the dynamic case by one order of magnitude, while the accuracy is hardly changed. Regarding the simulation with Fourier tracing, the application of “Measurement2Sim” (denoted M2S) shows no noticeable additional uncertainty compared to the static or dynamic case. The results are well transferable between NS and FS.

Falsification of hypothesis 8 follows from these investigation in two ways: First, the noise floor in Fourier tracing is too high due to ray jittering. As a result, the accuracy of range estimation achieved by the real sensor is not reached in simulation. Second, the consideration of extrinsic uncertainties by the “Measurement2Sim” method does not affect the quality of range measurement with Fourier tracing. The desired reduction in the accuracy of the range measurement in the studied ACC scenario, as observed in the measurement, is not reflected in simulation.

---

<sup>145</sup> This experiment cannot be conducted with CarMaker as in this case only the detection plane, i.e. after application of the CFAR threshold, is accessible. However, the QIFFT method requires access to immediately adjacent cells. These are not available if an adjacent value is below the detection threshold.

## 5. Radar sensor model test for falsification



NS   FS	Fourier tracing, stat.	Fourier tracing, dyn.	Fourier tracing, M2S	Measurement, dyn.	Measurement, stat.
$\bar{r}$ in m	0.10   0.18	0.12   0.23	0.10   0.25	0.67   0.83	0.66   0.83
$\varsigma$ in m	0.10   0.11	0.12   0.14	0.07   0.14	0.20   0.30	0.01   0.02

Figure 5.15.: Range accuracy for FS (top) and NS (bottom) for static and dynamic scenario in measurement and simulation along with estimated normal distribution. Line color assignment: Static scenario with Fourier tracing (—), Dynamic scenario with Fourier tracing (—), Measurement2Sim scenario with Fourier tracing (—), static scenario with measurement (—), dynamic scenario with measurement (—).

## 5.4. Interim conclusion: Revealed modeling errors

---

The research question discussed in this chapter addressed which of the requirements identified in chapter 3 are met by a radar model that uses the Fourier tracing approach. During modeling, a number of assumptions were made regarding multipath effects, reflectance characteristics, and measurement uncertainties. Experiments were conducted to falsify hypotheses about the simulation result when using Fourier tracing. The simulation results obtained with Fourier tracing were compared to measurements and the CarMaker 9 RSI radar sensor model.

Based on the scenarios examined regarding multipath propagation, the Fourier tracing model withstood the tests for falsification. Object height estimation by wave superposition patterns with CCR delivered the expected result for two investigated object heights. The shaking factor showed only slight deviations from the stochastic behavior known from measurements. Mirror targets due to repeated reflection off the sensor occur at up to about 40% of the maximum sensor range. Here, the loss of signal strength is within the theoretically expected range and is in line with the measurement. Regarding horizontal multipath propagation, all combinations of direct and indirect propagation could be identified by the respective deviations in radial velocity.

Regarding the sensitivity of the RCS to the aspect angle, an oversensitivity was identified by a slalom run of a VW Crafter. However, the overall trend in sensitivity of RCS profiles in terms of peaks at 90 and 270 deg, dynamic range, and fluctuations is present. This can be seen from the RCS profiles obtained from the simulation, even if they are more theoretical in nature.

Model deviations became apparent in both accuracy and precision of the range measurement. Due to a missing noise process and the assumption that radar waves cannot penetrate into vehicles, deviations between the simulation and measurements became visible. The precision in range measurement with Fourier tracing is too high compared to the measurements. Measurements also show that radar waves can penetrate into a vehicle, which cannot be represented with Fourier tracing in the present form. Therefore, there is an offset in the distance measurement between simulated and measured data.

If these findings are considered in isolation, deviations between simulation and measurement are identified and quantified. For this reason, the second part of the chapter examines the effects using object detection and tracking as an example. It is examined whether the same logical conclusions can be drawn from the data despite “erroneous” input data.

Considering the hypotheses on radar simulation using Fourier tracing, the results of the falsification experiments are summarized in table 5.1.

Table 5.1.: Results of testing the Fourier tracing radar model for falsification

Feature	Feature demonstrable?	Quantitative agreement
Object height estimation from wave superposition pattern	yes	Fourier tracing estimates mounting heights of CCR from wave superposition pattern for investigated heights within 3 cm
Shaking factor	yes	No full congruence, but regions with apparent agreement with the measurements
Adulteration of Doppler measurement under multipath	yes	Stable mirror targets are present, adulteration of radial velocity according to angular position, Fourier tracing emphasizes II propagation
Mirror targets due to repeated reflection	yes	Mirror targets exist up to 40 m and with an SNR difference of 25 dB which is in agreement with the measurements.
RCS characteristics of vehicles	partly	Overestimation of about 10 dBm <sup>2</sup> (peak to peak) between measurement and Fourier tracing for VW Crafter
Measurement uncertainties	no	Overestimation of range accuracy and precision in the order of one magnitude. The reason was identified as the assumed non-penetrability of glass for radar waves and the lack of additional noise processes.

## 5.5. Stimulation of object tracking with synthetic data

---

Based on the identified discrepancies between synthetic and real sensor data, their impact on sensor data processing is now investigated. Object tracking is a typical and widespread application of radar ever since its use in ACC. Advantageous for tracking is the utilization of radial velocity measurement, which provides a spatial prediction for the next measurement cycle. Object tracking typically makes use of estimation algorithms from the field of recursive Bayesian estimation. Their goal is to estimate the object state vector using the predictor-corrector method. Hereby, the information at the future time step  $t_1$  is estimated using the measured values available up to the current time step  $t_0$ .

This paragraph is therefore subject to **RQ6**: *What is the sensitivity of an object tracking algorithm to deviations between simulation and measurements?*

A number of discrepancies between simulation with Fourier tracing and measurement were identified in the previous section. In an object tracking algorithm, measured data is gradually replaced by estimated data. It is assumed that in this way deviations between measurement and simulation can be compensated. Ideally, the same object list in terms of accuracy, precision, and cardinality would result when a tracking filter is stimulated with measured or synthetic sensor data. Under these circumstances, synthetic radar data from Fourier tracing could not be regarded as falsified w.r.t. the extraction of an object list from this data.

The implementation of the object tracking algorithm based on radar targets used in this section is provided by Zaman<sup>146</sup>. It is based on an extended Kalman filter that estimates the object state vectors. After target clustering, a bounding box of the size 4 m by 2 m is fitted. This corresponds to the dimensions of a compact class passenger car. Identical filter settings were used when stimulating the tracking filter with measurement data and simulation data generated by the Fourier tracing model. Details on the parameterization of the filter can be found in Zaman's thesis. The "Measurement2Sim" method is used again to transfer real-world test drives to simulation.

### 5.5.1. Object tracking evaluation tools

The question of objective evaluation criteria for tracking algorithms can hardly be answered from a sensor modeling perspective. One may assume that a tracking algorithm and a corresponding parameter set exists, which solves the tracking task in the required quality of objectively selected evaluation criteria. The tracking algorithm used here can

---

<sup>146</sup> Zaman, Z.: Master's thesis, Stimulation eines Radar-Trackingverfahren (2020).

therefore only be seen as an exemplary representative of such an algorithm.

Tracking performance can be evaluated using metrics that penalizes localization errors and cardinality errors (false objects, missed objects). The widely used generalized optimal subpattern assignment (GOSPA) metric introduced by Rahmathullah et al.<sup>147</sup> shall be mentioned here as an example. Such a metric is only of limited use if no calibration values or design targets are available. Instead, descriptive aspects are extracted from evaluation scenarios that are curated to reflect falsified modeling aspects. The evaluation of the object list is made under two criteria:

**1) Accuracy and precision:** The object tracking algorithm specifies the state variables of objects in a sensor-centered Cartesian coordinate system. These are compared to the ground truth values available from the ADMA. The state vector for the entry in the object list that refers to the OOI holds estimated quantities and is specified with

$$\mathcal{O}_{OOI,sim/meas} = [s\check{x}_{OOI,sim/meas}, s\check{y}_{OOI}, s\check{\dot{x}}_{OOI,sim/meas}, s\check{\dot{y}}_{OOI,sim/meas}, s\check{\psi}_{OOI,sim/meas}]^T. \quad (5.1)$$

Ground truth, which is available from ADMA, can also be abstracted as an element of the object list:

$$\mathcal{O}_{OOI,GT} = [sx_{OOI,GT}, sy_{OOI}, s\dot{x}_{OOI,GT}, s\dot{y}_{OOI,GT}, s\psi_{OOI,GT}]^T. \quad (5.2)$$

The tracking filter is stimulated with synthetic sensor data as well as measurement data while retaining its respective parameters. The data source is identified by label “meas” or “sim” in the index. Ground truth is denoted with “GT”. This results in three pairs of object state vectors available for comparison:  $\mathcal{O}_{OOI,sim}$  vs.  $\mathcal{O}_{OOI,meas}$  vs.  $\mathcal{O}_{OOI,GT}$

Similar to the procedure in section above, their difference is statistically evaluated by estimating a multivariate Gaussian distribution. This assumes a normal distributed error characteristics. The respective mean values and standard deviations are used as indicators for accuracy and precision.

**2) Cardinality:** The number of objects within the object list can be considered a finite set. Cardinality measures the number of objects regardless of their respective state. It is suitable for comparing object lists, each obtained when the tracking algorithm is stimulated with real or synthetic sensor data. Ideally, for each object present in the measuring range of the radar, an entry is created in the object list. In reality, however, the object list contains wrong objects (e.g. mirror targets), unrecognized objects (missed objects), or present objects are temporarily not recognized (false negative) or no longer recognized (object dropout).

---

<sup>147</sup> Rahmathullah, A. S. et al.: Generalized optimal sub-pattern assignment metric (2017).

### 5.5.2. Slalom drive

An oversensitivity of the RCS to aspect angle was determined in the **slalom drive** illustrated in figure 5.8. During a slalom run, the lateral position and speed of the reference point at the OOI in a sensor centered coordinate frame, denoted as  $sy_{OOI}$  and  $s\dot{y}_{OOI}$ , takes the form of a harmonic oscillation, cf. 5.16a. The spectral noise power density (SNP) is obtained from the spectrum shown in figure 5.16b. It is assumed that above a frequency of 0.6 Hz the spectrum is dominated by noise components.

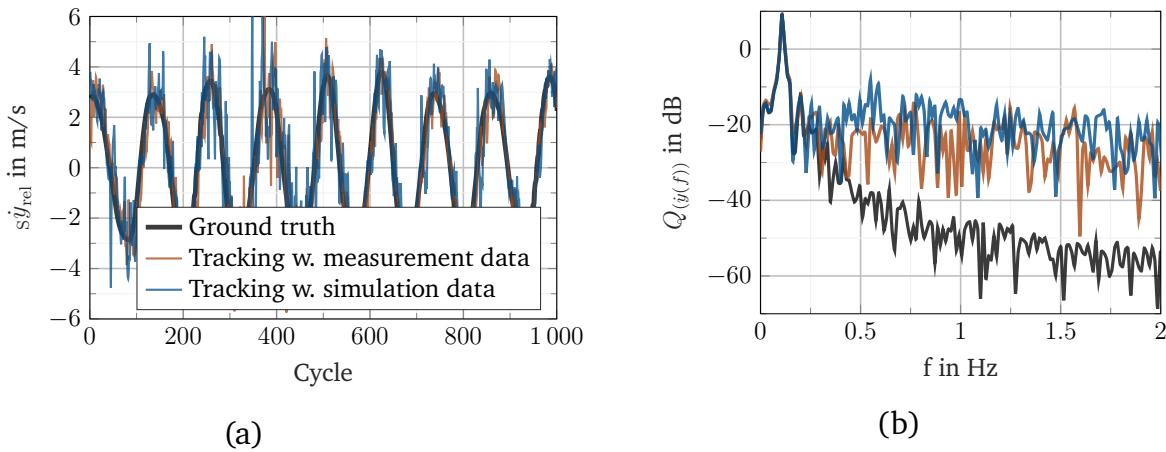


Figure 5.16.: Lateral velocity over time (left) and as spectrum (right).

The quantitative results are shown in table 5.2 where the absolute pose error (APE) is used for quantifying differences between measurement, simulation, and ground truth. The overall impression is that the tracker performs slightly worse when stimulated with synthetic data. The analysis of noise power density does not show a homogeneous picture. Although both measurement and simulation show increased values compared to ground truth, the values differ depending on the quantity. This is seen as an indication of different noise processes underlying the synthetic and real data, respectively. In terms of absolute error, the underestimation of the longitudinal distance shows that the assumption that the reflection occurs at the outer body of the vehicle and that the radar wave does not propagate into the vehicle is not correct. The lateral estimation error from the simulation can be explained by the assumption of non-penetrability. As in the longitudinal case, it is less than 10% of the vehicle dimensions. The estimation of the longitudinal velocity is provided at a precise level. The derivation of lateral velocity is more pronounced. This can be explained by the input data to the filter: Radar reports the velocity component via Doppler effect in radial direction. The azimuth angle is re-

## 5. Radar sensor model test for falsification

---

quired for obtaining the lateral velocity component, but this is measured with lower accuracy compared to radial velocity. The estimated multivariate Gaussians for the APE are illustrated in figure 5.17.

Table 5.2.: Quantitative tracking results from slalom drive scenario

SNP above 0.6 Hz in W/Hz	$s\check{x}_{OOI}$	$s\check{y}_{OOI}$	$s\check{\dot{x}}_{OOI}$	$s\check{\dot{y}}_{OOI}$
Ground truth	0.19	0.31	0.22	0.34
Simulation	1.86	0.98	0.82	1.47
Measurement	1.85	1.05	0.63	1.84
Estimated 2D Gaussians	$s\check{x}_{OOI} - s\dot{x}_{GT}$	$s\check{y}_{OOI} - s\dot{y}_{GT}$	$s\check{\dot{x}}_{OOI} - s\dot{x}_{GT}$	$s\check{\dot{y}}_{OOI} - s\dot{y}_{GT}$
$\text{Mean}_{\text{sim}}$	-0.46 m	0.21 m	0.08 m/s	0.01 m/s
$\text{Mean}_{\text{meas}}$	0.26 m	-0.31 m	0.06 m/s	-0.04 m/s
$\varsigma_{\text{sim}}$	0.01 m	0.17 m	0.07 m/s	1.38 m/s
$\varsigma_{\text{meas}}$	0.05 m	0.08 m	0.14 m/s	0.48 m/s

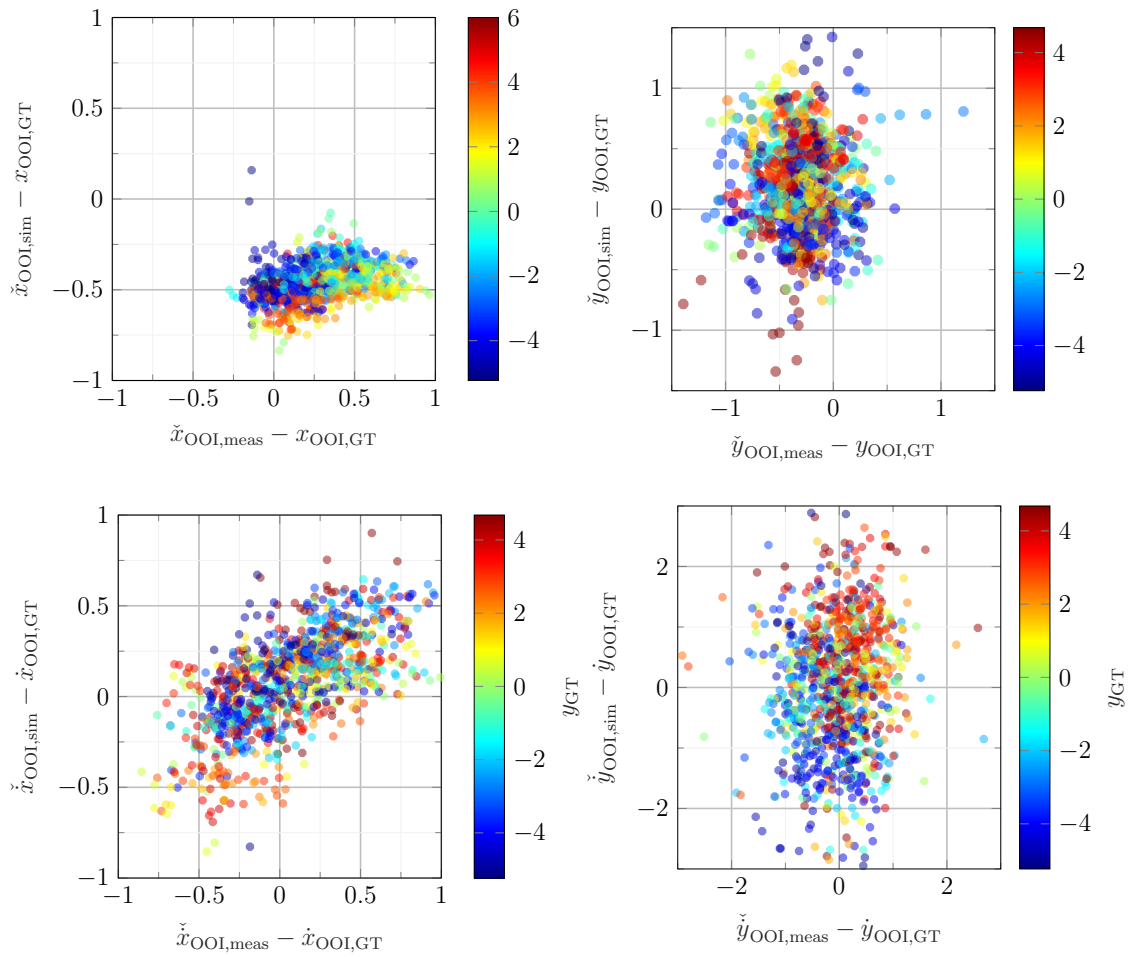


Figure 5.17.: Scatter plots for visualization of tracking performance in slalom scenario. To check the sensitivity to the lateral position, it is highlighted as a color code and given in m.

### 5.5.3. Car following and evasion

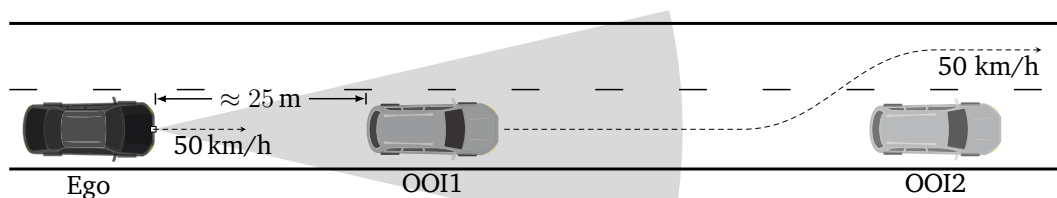


Figure 5.18.: Car following and evasion scenario for object tracking evaluation.

The second scenario for evaluating object tracking with real and synthetic data is illustrated in figure 5.18. It consists of two parts: A following drive behind OOI1 (represented by a BMW i3) outside the visibility range of OOI2 (represented by a VW Golf Mk5), which remains stationary. Based on the first part, statements can be made about the quasi-stationary behavior of the tracker when observing OOI1. The evaluation aspect is the effect of the identified higher accuracy of Fourier tracing compared to the measurement, which was identified in section 5.3.2. In the second part, OOI2 is within the theoretical measurement range of the radar. The duration until successful object detection and assigning an entry on the object list is compared. This highlights the effect of reduced visibility because only specular reflections off the pavement are possible in simulation. Three test repetitions (denoted trial 1,2 and 3) are performed. Due to the determinism of the simulation, only one repetition of the experiment is carried out in simulation.

The general tracking behavior known from the slalom test is confirmed during the car-following phase, see table 5.3. High accuracy and precision, which can be expected from the fidelity of Doppler measurement, is shown in the estimation of longitudinal velocity. The error in longitudinal direction corresponds to the deviations found in the analysis of the range error or non-penetrability of glass, see section 5.3. The lateral estimation error is more pronounced in the simulation. It slightly exceeds the extrinsic uncertainty limits of  $|s\check{y}_{OOI} - sy_{GT}| < 0.4$  m when driving behind another vehicle, see section 3.9.2.

Obviously, there is a higher uncertainty in the angle estimation in Fourier tracing. This leads to an offset when estimating the lateral position of the bounding box. Regarding the object drop-out behavior of the hidden object, figure 5.19 shows that OOI2 appears for a short time already at a distance of about 155 m in the measurements. Constant object detection is possible in the simulation starting at about 84 m while the first occurrence of the object on the object list occurs at about 102 m. This corresponds to the distance at which constant object detection can be achieved for all measurement trials.

When analyzing the test repetitions, it can be seen that the object dropout behavior is different in each repetition. This illustrates the difficulty of repeatability of radar measurements. It remains to be noted that the object dropout behavior is more evident in the simulation until distances with constant detectability of the object are reached.

Table 5.3.: Quantitative tracking results in quasi-stationary scenario. Multivariate Gaussian estimates (top), object drop out characteristics (below).

Tracking of OOI1	$s\check{x}_{OOI} - sx_{GT}$	$s\check{y}_{OOI} - sy_{GT}$	$s\check{\dot{x}}_{OOI} - s\dot{x}_{GT}$	$s\check{\dot{y}}_{OOI} - s\dot{y}_{GT}$
Mean <sub>sim</sub>	0.34 m	-0.67 m	0.04 m/s	-0.04 m/s
Mean <sub>meas</sub>	0.66 m	0.16 m	<0.1 m/s	<0.1 m/s
$\varsigma_{sim}$	0.02 m	0.10 m	0.10 m/s	0.41 m/s
$\varsigma_{meas}$	0.02 m	0.10 m	0.10 m/s	0.41 m/s

Tracking of OOI2	Trial 1	Trial 2	Trial 3	Simulation
First seen	154.3 m	103.2 m	132.7 m	102.2 m
Constant track	103.8 m	84.3 m	104.1 m	83.5 m

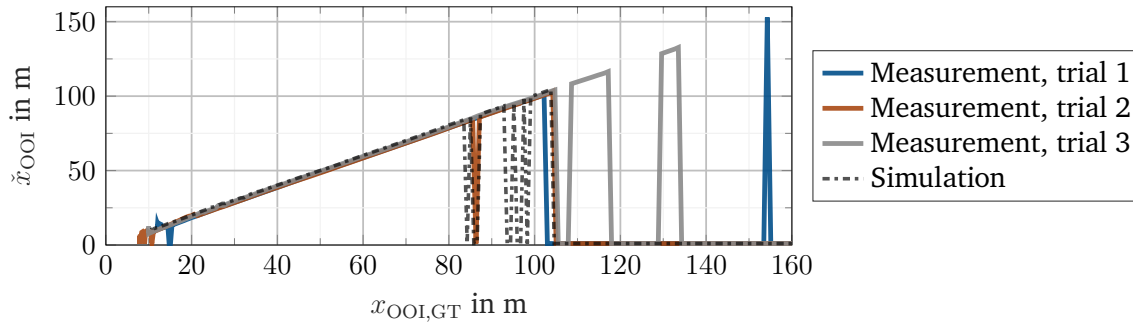


Figure 5.19.: Tracking of (occluded) OOI2 w.r.t. object dropout behavior in occluded object scenario.

### 5.5.4. Object separability

During object tracking, algorithm specific artifacts occur, as mentioned in section 3.10. The origin of these artifacts is the interaction between sensor performance parameters (e.g. resolution and separation capability) and the parameterization of the data processing algorithm. One consequence are estimation errors in cardinality, e.g. if several objects cannot be separated from each other.

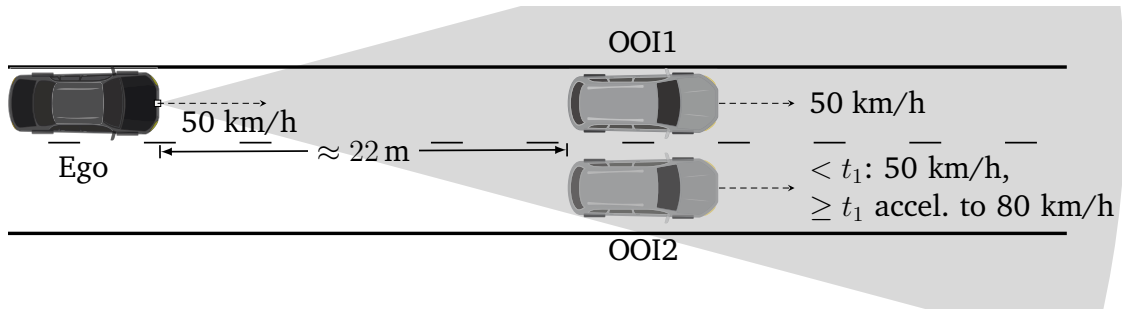


Figure 5.20.: Illustration of object separability test scenario in FS mode.

Object separation ability is tested using a scenario in which two vehicles (OOI1 and OOI2) travel side by side at approximately the same speed (regulated by a speedometer) and offset by one lane. The ego vehicle follows OOI1 in ACC mode. Such a scenario is depicted in figure 5.20. At a given time  $t_1$ , OOI2 accelerates so that the separation condition is given via velocity and range.

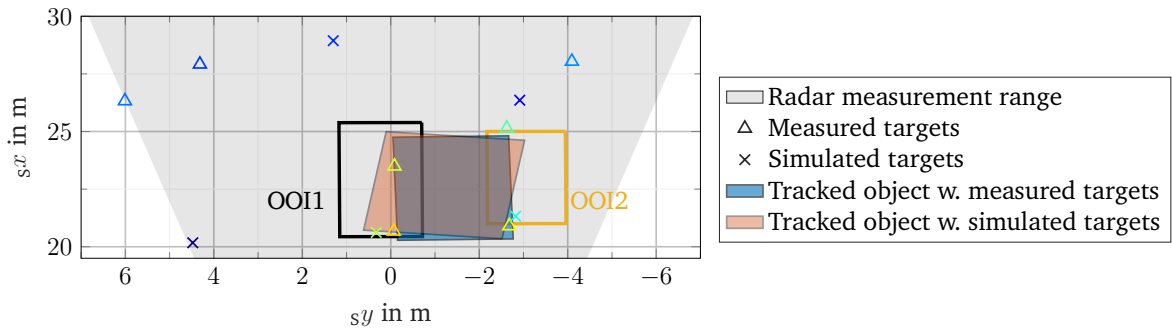


Figure 5.21.: Visualization of radar targets obtained in simulation and measurement, resulting objects and bounding boxes of the vehicles at a time step before  $t_1$ .

When inspecting the radar targets, it can be seen that both objects generate distinguishable radar targets in both measurement and simulation. This is shown in figure 5.21

which considers a time step  $< t_1$ . Because of the lack of further separability criteria, the tracking algorithm is not able to create separate objects. Instead, the radar targets are combined into one object that appears to be located in the middle of the actual objects.

After reaching the separability condition via velocity, the tracking algorithm is now able to identify two separated objects. The results shown in figure 5.22 are in agreement with the expected results: Object separation occurs as the longitudinal speed is sufficiently different, i.e. 2 m/s in the present case. Before successful object separation, the lateral position of the non-separated object is estimated as 1.8 m. This roughly corresponds to the mean distance between the vehicles, given a lane width of 3.5 m. The result is confirmed for the measurement and simulation as well as at the repeated test (right column). As the objects cannot be separated from the tracker's point of view prior to time step  $t_1$ , the occurrence of a data processing specific artifact is evident in both the measurements and the simulation.

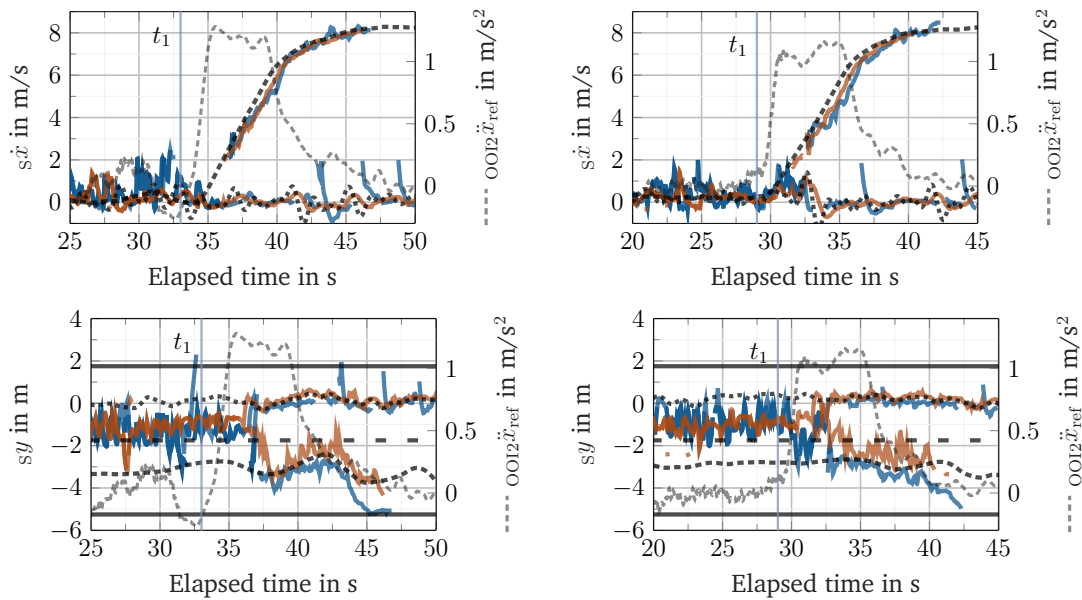


Figure 5.22.: Qualitative results of object separability experiment (Left: trial 1, right: trial 2). The acceleration of OOI2 is given as a reference for the time step at which object separability can be expected. In each trial, after time  $t_1$ , OOI2 shows an increase in its longitudinal acceleration. In the bottom plots, lane markings are shown for identification of lanes. Line color assignment: Tracker with measured targets (—) and simulated targets (—), trajectories of OOI1 and OOI2 (----).

## 5.6. Final remarks on object tracking with synthetic data

---

The second part of the chapter investigated **RQ6**: *What is the sensitivity of an object tracking algorithm to deviations between simulation and measurements?*

As a starting point, Fourier tracing was known to yield discrepancies with measurements w.r.t. the sensitivity of the RCS to aspect angle, the accuracy of the range measurement, and the detectability of occluded objects.

The deviation in the sensitivity of the RCS of the VW Crafter as obtained in the slalom scenario remained without noticeable influence on the object tracking performance. Object drop out would only be expected if its RCS value drops to a level where it would be indistinguishable from noise. Regarding the dynamics of the tracked object in the slalom scenario, no apparent difference was found between tracking with measured and synthetic data: It was possible to continuously track the object with measured and synthetic data. The noise of the object states w.r.t. their noise power density is in the same order of magnitude when tracking with measured or synthetic data.

The previously identified deviations between measurement and simulation in terms of accuracy and precision were propagated to the object list. Estimated object states show higher accuracy and precision when the tracking filter is stimulated with synthetic data. Occluded objects can be tracked within the validity of the assumption of specular reflections off the pavement. Object tracking artifacts in terms of separability are formed in the same way for measured and synthetic data. The separability of objects shows the same qualitative course for measured and synthetic data: Although there are targets found that can be assigned to individual objects, the object tracking algorithm cannot detect separate objects until a certain velocity difference is reached.

## 6. Conclusion

---

This chapter summarizes the conclusions drawn from the investigations of the research questions posed in this dissertation. For this purpose, the core findings of each research question are highlighted and discussed.

---

### 6.1. Modeling scope

---

**RQ1:** *What is necessary for an automotive radar simulation and what is not yet available from existing models?*

Previous research on radar sensor modeling was structured w.r.t. modeling approach and model input and outputs. There is a traditional debate within the sensor modeling community about the achievable simulation quality with “stochastic” versus “physical” models that claim higher accuracy. A list of shortcomings of previous modeling methods was curated based on a review of known variants of sensor models and modeling approaches. It contains elements that these models lack when it comes to their deployment within virtual validation of automated or autonomous driving (AD). The most significant observation was that there is no uniform model scope, i.e. the basic set of features that sensor models provide. In particular, there is no systematic proof of the fidelity with which a desired model feature is actually represented in the model. As there is currently no benchmark for objective evaluation of model performance, many sensor models proclaim their validity based on an instantaneous observation made in a selected scenario, especially one in which particularly appealing results can be achieved.

**RQ2:** *What are the relevant features for the virtual test of AD that a radar simulation must demonstrate?*

Deviations of the sensor measurement from ground truth, which are caused by the sensor measurement principle, are considered as artifacts. The correct representation of an artifact by a sensor model is considered a “feature” of the model. Within this dissertation, a methodology for the quantification of artifacts was presented. This method transfers artifacts, e.g. from observations in measurements, into a falsifiable validation

criteria for a radar sensor model.

It is not possible to prove the completeness of a list of relevant model features. This is due to the fact that in the course of advancing technology development, further application areas of radar in the autonomous vehicle will arise, which may lead to previously unknown artifacts. Nevertheless, already from the understanding of the operation of radar sensors, a set of features can be derived that a meaningful sensor model must cover. This set of features represents basic performance parameters of the sensor such as measurement and unambiguous intervals. Another group of features is characterized by the fact that they can be easily observed in simple scenario constellations. These include effects attributable to multipath propagation, such as mirror targets and variations in received power caused by wave superposition.

In this dissertation, artifacts originating from multipath propagation and measurement uncertainties were transferred into model requirements using the presented methodology.

**RQ3:** *How are the relevant characteristics defined and what are the requirements and test criteria for modeling?*

A descriptive model was derived for each artifact and confirmed by performing repeated measurements. A falsification experiment can be derived from the cause of origin, i.e. a scenario constellation under which the artifact must occur in the simulation in a qualified manner. The identified mathematical description models of the artifacts provide a physical justification. This includes a model expression that is in accordance with the physical principles of radar sensors. Therefore, it is justified to consider the modeling approach chosen in this dissertation as physical modeling of artifacts.

This dissertation delivered justified and verifiable quality requirements as well as falsification criteria for a set of artifacts to be reproduced by a radar simulation model. However, each description model has respective ranges of validity. The specular reflection model of the pavement is mentioned as an example. This captures the reflection conditions only within those intervals where the visibility of hidden objects is given by specular reflection. It is not always possible to trace the cause of an artifact to a determinism in the cause of its origin. The reasons are interactions with other influences that cannot be isolated. This was clearly visible in the multiple measurement repetitions that were carried out with different vehicles when studying the shaking factor. Obviously, small variations in the repeated execution of the experiment are sufficient to turn the determinism behind the formation of wave superposition patterns into randomness. Using the tilted exponential distribution, it was possible to find a stochastic description model for the fluctuation of the received power, which is justified by physical principles, namely the randomness of the phase of the reflected wave.

## 6.2. Radar modeling

---

**RQ4:** *How can one use ray tracing to generate spectral radar data?*

Enhancing ray tracing methods for radar simulation was demonstrated by the Fourier tracing approach introduced in this dissertation. With this approach, it is possible to generate spectral radar data that appears to be realistic from currently available 3D geometries, including the associated, albeit rudimentary, material mapping. The mathematical core of Fourier tracing was successfully verified. However, the use of ray tracing for synthesizing radar data showed limitations that are inherent to its principle. In ray tracing, a ray represents a discrete, infinitely thin sampling point along the wavefront. This is accompanied by a number of challenges:

- Due to the perspective distortion in the spherical coordinate system, sampling gaps occur in the areas between rays when launching with constant ray increments.
- Due to the inverse distance law, the ray intensity per area (i.e. radiance) decreases with distance, resulting in the aliasing problem known from signal processing
- Due to the perspective, most rays hit the pavement in the immediate vicinity of the sensor and do not provide any additional information. To circumvent the aliasing problem, a high number of rays is required, which makes ray tracing fairly inefficient.

To solve these problems, the ray increments were superimposed with a stochastic jitter that reduces sampling gaps at greater distances. In order to overcome the aliasing problem, a weighting factor was designed following the Phong reflection model. It draws its physical motivation from the irradiation profile of a flat plate having an analytical RCS characteristic. Based on this, the backscattered intensity was weighted w.r.t the aspect angle to the sensor. This so-called “lens factor” reduces the influence of aliasing. It also ensures that the known RCS profile of a flat plate is maintained within the unambiguous interval in radar simulation with Fourier tracing.

The wavelength used in radar (i.e.  $\approx 4$  mm) leads to a very high sensitivity of the reflectivity to the aspect angle in real geometries. Thus, already with a deviation of  $1/20$  deg in the aspect angle, no reproducibility of the backscattered intensity obtained by radar measurements can be expected. It is unrealistic to expect that a reliable agreement between simulation and measurement can be achieved. Therefore, it is not worthwhile to strive for a higher modeling quality outside the peak of the analytical RCS profile of a flat plate than a descriptive statistical value would provide. The proposed parameterization of the lens factor overfulfills this postulation by reproducing the first three zeros of the RCS profile of a flat plate. At larger aspect angles, a transition to noise occurs.

### 6.3. Sensor model evaluation

---

*RQ5: Which requirements are fulfilled by Fourier tracing?*

The dissertation presented a standard set of simulation experiments to detect errors in a radar sensor model. This was applied to the presented Fourier tracing model and, where applicable, to the IPG CarMaker 9 RSI radar model. These experiments potentially serve as a benchmark for the sensor model community in future radar sensor model development. It could be shown that Fourier tracing represents all required artifacts in a binary sense, as respective aspects are principally present in synthetic data. However, the qualitative evaluation revealed deviations of the simulation compared to the measurements: For example, the simulation of slalom driving with a VW Crafter showed an oversensitivity of the backscatter intensity w.r.t. the aspect angle. The assumption that radar waves cannot penetrate vehicles leads to an error in the distance accuracy. The absence of a dedicated noise process implies higher accuracy than the sensor being modeled. Jittering of rays, which is necessary from a Fourier tracing point of view, introduces significant noise in the received power for stationary objects.

*RQ6: What is the sensitivity of an object tracking algorithm to deviations between simulation and measurements?*

In the experiments shown, no deviations in object tracking behavior between synthetic and real data could be found that have no explanation by the deviations previously observed. When stimulating an object tracking algorithm with synthetic data generated with Fourier tracing, the known deviations remain: The overestimation of the accuracy and precision of radar targets is reflected in the estimated object states. The error compared to ground truth is slightly larger than the extrinsic measurement uncertainty. However, the usability of tracking filters for model testing for falsification is limited. Fundamental modeling errors can already be determined during previous sensor data processing stages with appropriate tests. Tracking behavior with synthetic data will be very similar to that with measured data as long as the input data satisfies the same measurement model assumptions. This cannot be taken as an indication for equality of input data, since the algorithm compensates for modeling errors by making additional model assumptions (e.g. the motion model in the tracking filter). For example, the tracking filter could also provide plausible results if there is at least one target reported for each object in the sensor's measurement range whose states correspond to ground truth. Thus, the tracking result can be objectively correct even if the model input data is fundamentally flawed. Errors in synthetic sensor data can be identified through rigorous testing. In short, a data processing algorithm, whether it is a tracking filter or any other application, cannot detect additional modeling errors, it can only suppress existing ones.

## 6.4. Recommendations for large-scale data acquisition for sensor models

---

Recorded real-world measurement data is the foundation of sensor modeling. For this reason, large, expandable, calibrated, and referenced databases of sensor recordings from a variety of perception sensors are desirable. Hereby it would be possible to have a comparable database for creation and calibration of sensor models, similar to KITTI, nuscenes<sup>148</sup> or Oxford Radar RobotCar<sup>149</sup> for data processing algorithms. Currently available perception sensor datasets that contain radar data can only be used as a data source for sensor models to a limited extent. Based on continuous recordings made in complex, real-world scenarios, it is hardly possible to examine artifacts in isolation.

It is therefore recommended that dedicated calibration experiments for sensor models will become a part of future data sets. A (non exhaustive) list of such experiments is accompanied by the artifacts that are presented in chapter 3. These experiments can be conducted with different radar sensors and mounting positions while maintaining other test conditions. This would allow characteristics such as wave superposition patterns to be studied simultaneously with different sensors in the same scenario.

The quality of the ground truth supplied for each OOI should be documented according to the calibration procedure described in this dissertation. Labeling should also contain infrastructure elements, such as distances to guardrails, tunnel walls, as well as their shape and material composition. This would allow an in-depth study of the process of forming mirror targets. A referenced point cloud containing the calibrated intensities of multiple lidar scanners would facilitate this investigation.

The data used in this work were obtained from measurements taken over a large period of time and with different human drivers of the OOI. The randomness in radar measurements was then superimposed by different extrinsic uncertainties introduced by human drivers. One challenge was the impossibility of maintaining a constant speed or lateral deviation in the lane with human drivers. Advanced driver assistance systems (ADAS) systems such as ACC and lane keeping lead to respective extrinsic uncertainties. For this reason, the use of driving and steering robots is recommended in scenarios where artifacts (e.g. mirror targets due to multipath propagation) would otherwise be overlaid by extrinsic uncertainties.

---

<sup>148</sup> Caesar, H. et al.: nuScenes: A multimodal dataset for autonomous driving (2019).

<sup>149</sup> Barnes, D. et al.: The Oxford Radar RobotCar Dataset (2019).

## 6.5. Further research directions

---

More in-depth research is advised in the area of wavelength-specific rendering of virtual scenes. So far, there are no databases on the reflection properties of materials at mm-waves. As these become available, transfer of established techniques from the field of photorealistic image synthesis for radar sensor simulation can also be further investigated. In this context, further investigation of diffraction effects is recommended. These were neglected in the Fourier tracing approach developed in this work, although the visibility of occluded objects due to reflections off the pavement proves their relevance.

When further expanding the Fourier tracing approach, additional considerations can be made to simulate the reflective behavior of geometries for radar: So far, a ray provides the normal vector of the elementary cell of a geometry of unknown size at the hit point. The sampling problem is resolved by suppressing backscatter angles outside the ambiguity range. An alternative solution would be to parameterize the backscatter function according to the radiance at the hit point, which is given by  $\rho = \Delta\phi \cdot \Delta\theta \cdot r^2$ . The backscatter is then determined taking into account the orientation of the plate to the sensor, which gives the efficient dimension of the plate. The total backscatter of an arbitrary geometry is obtained from the phase sensitive superposition of all backscatter. Additionally, the mesh geometry and the size of the vertex holding the hit point could be reported via the payload of the ray for post-processing. This would also yield a parameterization for the backscatter function describing the vertex. Similarly, transmission calculations could also be performed for wave-transparent materials. These considerations are to be made against the background of necessary simplifications of the real geometry in its 3D modeling. Instead of fixed or jittered angular increments, it should be investigated whether a distribution of the rays according to the Fibonacci lattice method<sup>150</sup> could resolve the sampling problem. This method projects the Fibonacci spiral onto a sphere, resulting in equal sampling points on its surface.

Additional research is needed on the necessary quality of synthetic sensor data. The problem of reproducibility in real-world measurements is reflected in the problem of the impossibility to achieve complete equality between measured and synthetic data. For use within closed-loop virtual validation chains, software in the loop (SiL) models of sensor data processing algorithms used and the AD function are required. If these are available, error rates between simulation and measurement can be compared and an ultimate statement about the uncertainty of the simulated data can be made.

---

<sup>150</sup> González, Á.: Areas on a Sphere Using Fibonacci and Latitude–Longitude Lattices (2009), p. 4.

An open research problem is to identify test cases for AD that are executed in virtual environments and do not require additional real-world tests to confirm the findings obtained in simulation. This results in a confrontation with the well-known test dilemma of the billions of test kilometers to be driven, as the simulation models must also be validated by real sensor data obtained in measurements. The vision of sensor modeling must therefore be to create simulation models of sensors for which no real sensors exists at first. Based on the sensor specification determined in the simulation, requirements for the real sensor setup can then be derived. Simulation serves thus to validate the real sensor, and its capabilities can be fully leveraged by simulating any scenario under any conditions in parallel. The introduction section quoted George Box aphorism “all models are wrong”, which he and Draper expanded in 1987 to include the phrase “but some are useful”<sup>151</sup>. This aphorism also applies in the utopian view, where sensors and the AD system should first be designed in simulation. As shown in this dissertation, however, it is possible to find areas where radar sensor models can generate synthetic data with fidelity. This brings that goal a little bit closer.

---

<sup>151</sup> Box, G. E. P.; Draper, N. R.: Empirical model-building (1987), p. 424.



# A. Appendix

---

## A.1. Estimating object height from wave superposition pattern

---

To estimate the object height  $h_{OOI}$ , scenarios are used in which the radar, mounted at a known sensor height  $h_S$ , approaches the object with constant<sup>152</sup> speed. The lower the speed, the higher the number of samples. Within this dissertation, a speed of about 3 m/s was chosen which results in a sufficient number of sampling points. This speed can be comfortably realized by driving in idle gas. The data processing steps for determining the object height starting from radar targets are presented below. A more detailed description can be found in Diewald's dissertation<sup>153</sup>.

**Target filtering:** The targets are selected from the list of targets that can be clearly assigned to the object, e.g. based on their angular position, relative velocity or range. Filtering via radar cross section (RCS) is only successful if the object RCS is consistently significantly larger than the RCS of surrounding objects.

**Linearization of RCS:** RCS investigation is carried out after delogartimization into linear RCS range. This has an advantageous effect on the spectral analysis, since harmonic components can be clearly identified as the RCS varies over several dBm<sup>2</sup>.

**Equidistant resampling:** For each target, the information about its radial distance  $r$  to the radar is available. If the object is approached at constant speed, the result is a regular sampling over the distance  ${}_S r$ . The wave superposition pattern expresses itself as an oscillation over the reciprocal distance, i.e.  $1/{}_S r$ . A regular sampling over  $1/r$  can be achieved by linear interpolation at equidistant interpolation points. A fast Fourier transformation (FFT) requires a power of two at sampling points. For this reason  $2^{10} = 1024$  sampling points are suggested. The reciprocal distance extends over  $1/90$  1/m to  $1/20$  1/m. This is an overlapping range between near scan (NS) and far

---

<sup>152</sup> absolute constancy cannot be achieved w.r.t. extrinsic uncertainties

<sup>153</sup> Diewald, F.: Ph.D. thesis, Objektklassifikation und Freiraumdetektion auf Basis bildgebender Radarsensoren (2013), pp. 49-59.

scan (FS) and is not violating the critical distance identified in paragraph 3.3.3.

**Filtering:** A Savitzky-Golay finite impulse response (FIR) smoothing filter of polynomial order 3 and frame length 5 is applied on the linearized data for noise suppression.

**FFT:** Based on the FFT applied on the RCS values of the targets, which are organized over a equidistant  $1/sr$ , the height spectrum is obtained from the squared magnitude of the single sided spectrum. The goal of the spectral analysis is the identification of the dominant frequency  $f_{mp} = \frac{h_{OOI}h_S}{\lambda}$  (see eq. 3.11) which conveys the searched object height  $h_{OOI}$ . The frequency binning results from the equidistant sampling points, i.e.

$$h_{OOI} = \lambda f_{mp} / h_S \quad (\text{A.1})$$

The frequency bin containing the highest power density represents an estimate for the searched object height.

---

## A.2. Obtaining SNR

---

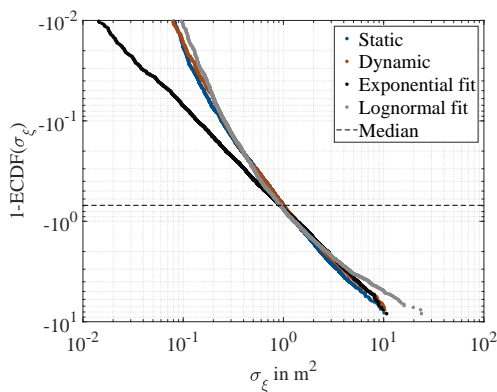
The signal-to-noise ratio (SNR) provides a range compensated quantity that is suitable for comparing received power readings between measurement and simulation. In order to obtain the SNR value, which is frequently used within this dissertation, the following formula is applied:

$$\text{SNR} = 10 \cdot \log_{10} (P_{Rx} \cdot sr^4) - 10 \cdot \log_{10} (P_{\xi} \cdot sr^4) \quad (\text{A.2})$$

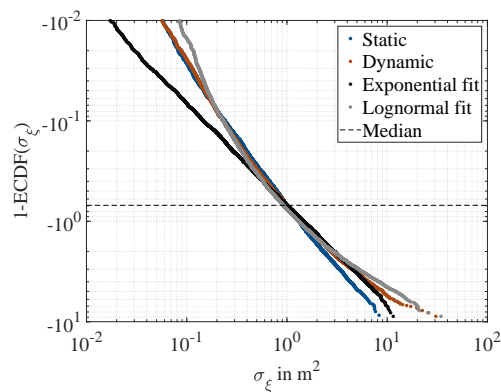
The noise quantity  $P_{\xi}$  is determined by the (known) noise floor level. If this is not known, the minimal power value observed reduced by a small margin for considering a potential detection threshold can be used.

### A.3. 1-ECDF plots for shaking factor determination with different vehicles

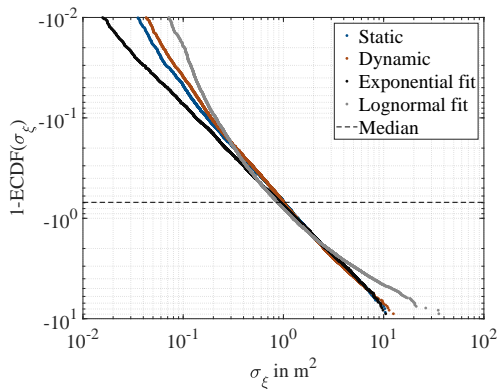
The 1-ECDF plot shows the distribution of RCS values measured by the sensor during the static or dynamic experiment to determine the shaking factor. Each experiment was repeated three times at four different locations on the runway of August Euler airfield (see figure 3.1a).



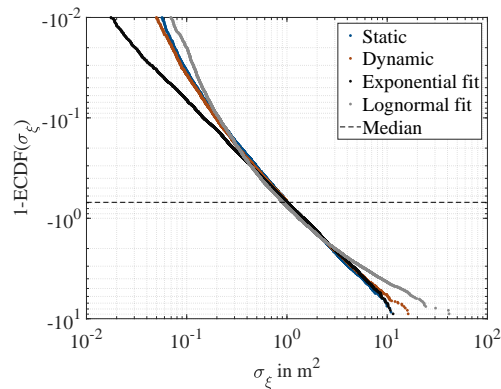
(a) Audi A3



(b) BMW i3



(c) VW Golf Mk5



(d) VW Golf Mk7

Figure A.1.: (1-ECDF) plots for the RCS fluctuation observed during the static and dynamic wave superposition experiment along with exponential and log-normal distribution fit.

## A.4. Sensor model parameters

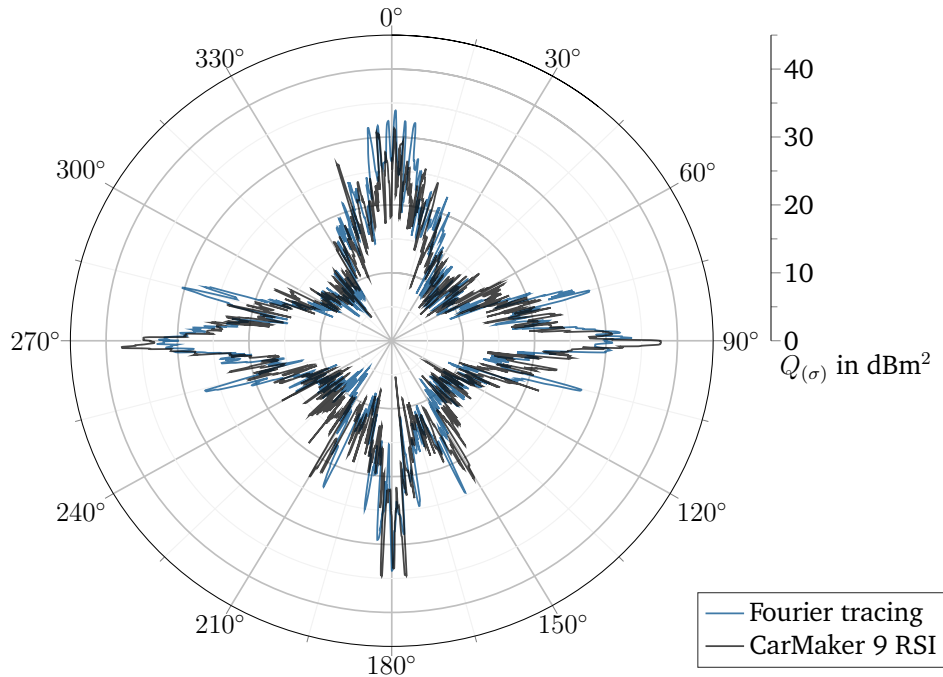
The Fourier tracing radar sensor model was integrated into the Nvidia OptiX ray tracing framework available in Vires Virtual Test Drive (VTD) 2.2. It was executed on a desktop computer with Intel i7 6700K as central processing unit (CPU) and Nvidia GeForce GTX 1080 as graphics processing unit (GPU). The operating system was Ubuntu 18.04. LTS. The parameters used in the radar sensor model are given in table A.1.

Table A.1.: Parametrization of the sensor model for the radar used in this thesis

<b>Radar sensor</b>	
General parameters	see table 3.1
Antenna gain map	provided by manufacturer
Window functions	Hanning
<b>Ray tracing parameters</b>	
Frustum size	$\pm 60$ deg horizontal, $\pm 20$ deg vertical
Ray increments	0.025 deg (horizontal and vertical)
Ray jittering	$0.001 \cdot \mathcal{U}(-0.5, 0.5)$ rad
Reflection depth	5
Maximum ray length	105% of max. sensor range
<b>Lens function parameters</b>	
$k_{\text{sm}}$	$5 \cdot 10^2$
$k_{\text{spec}}$	$5 \cdot 10^{-2}$
$k_{\text{diff}}$	$5 \cdot 10^{-5}$
$k_{\text{edge}}$	1.5

## A.5. Simulated RCS profiles of vehicles

All RCS profiles given below underwent smoothing with a moving median filter of length 4 samples for enhancing readability.



(a) Simulated RCS profile

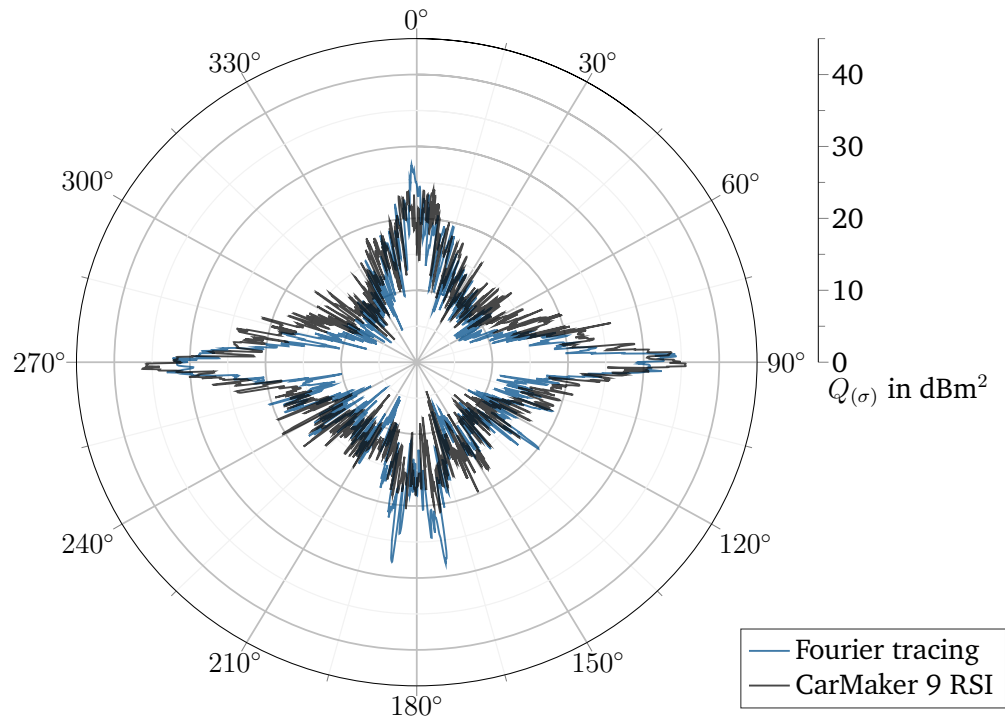


(b) Vires Virtual Test Drive



(c) CarMaker 9

Figure A.2.: BMW G30 (“BMW 5 Series”).



(a) Simulated RCS profile

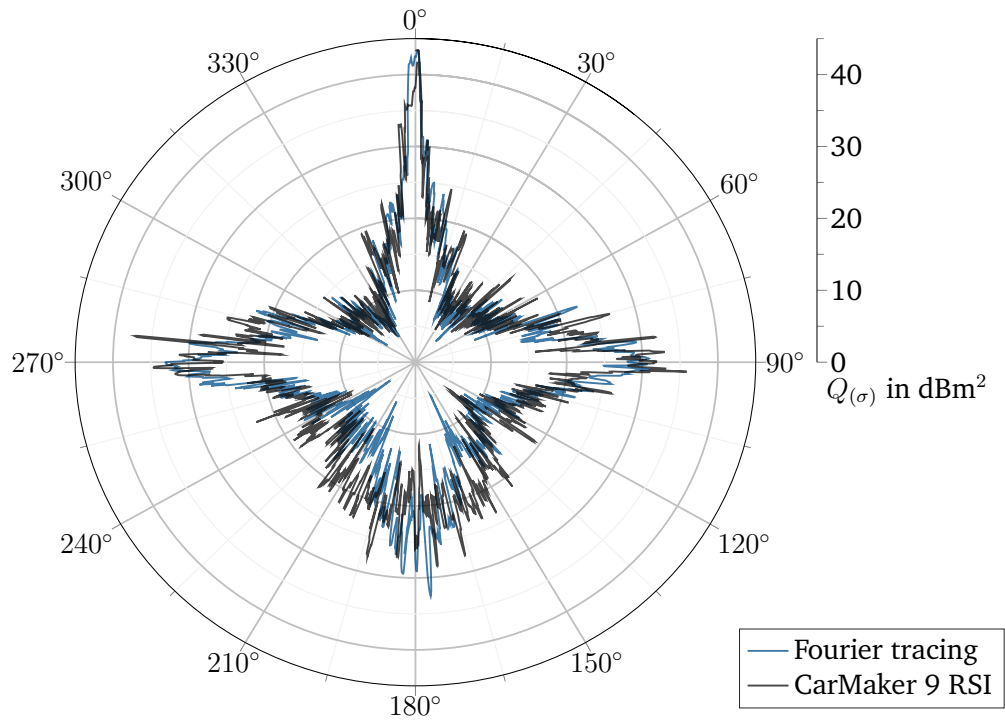


(b) Vires Virtual Test Drive



(c) CarMaker 9

Figure A.3.: Mercedes Benz W222 (“S-Class”).



(a) Simulated RCS profile

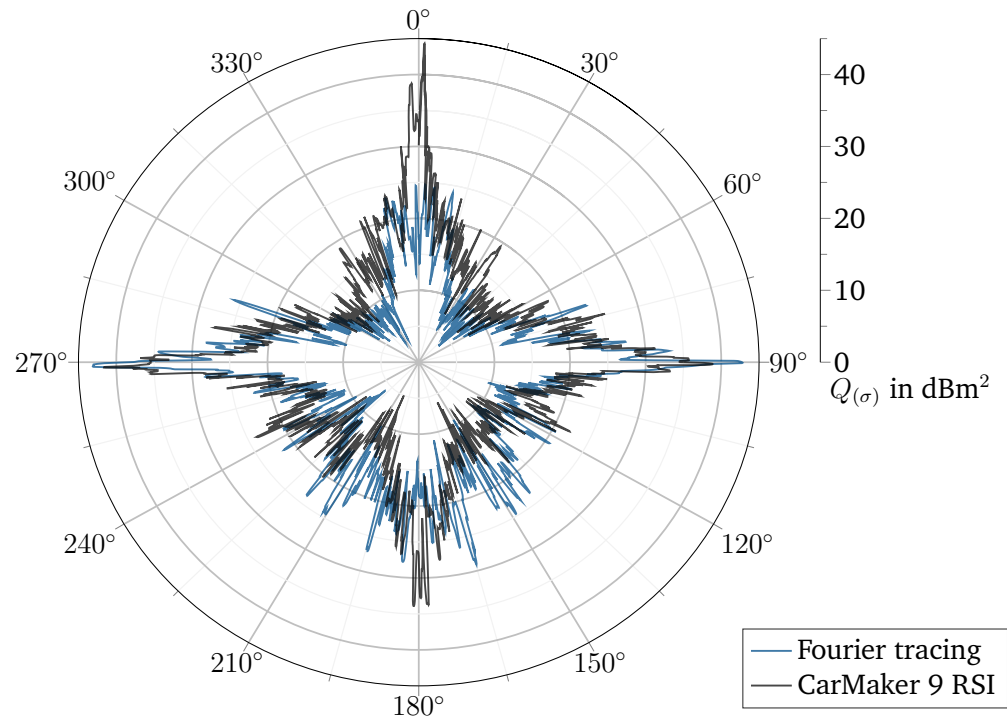


(b) Vires Virtual Test Drive



(c) CarMaker 9

Figure A.4.: Chevrolet Silverado.



(a) Simulated RCS profile



(b) Vires Virtual Test Drive



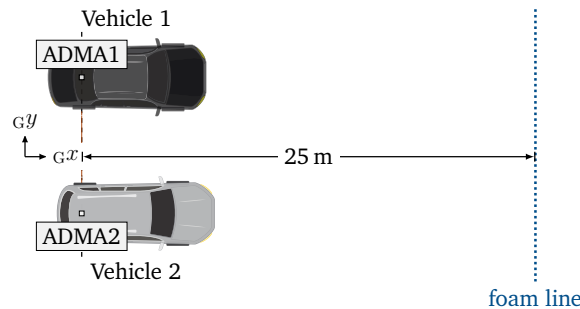
(c) CarMaker 9

Figure A.5.: Mercedes Benz W447 (“Vito”).

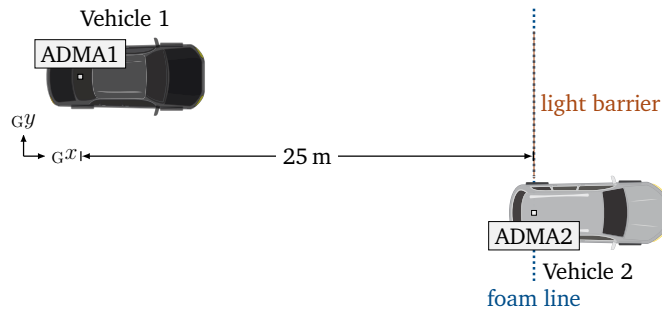
## A.6. Calibration of the “Measurement2Sim” method

The automotive dynamic motion analyzer (ADMA) used in the thesis promises a positioning accuracy of  $< 5$  cm under ideal conditions. This can be achieved if both the installation position of the ADMA in the vehicle and the relative positioning of the antenna is known with  $< 1$  cm accuracy. The state estimation filter in the ADMA must be settled into a steady state so that global navigation satellite system (GNSS) information can be fused with the build-in acceleration and gyro sensors. In addition, undisturbed GNSS reception and GNSS correction data according to the real-time kinematic positioning (RTK) procedure must be available. The achievable accuracy is now dependent on the distance to the base station that sends the correction data, e.g. via the SAPOS service. The accuracy depends on the distance to the base station: The closer the base station to the rover (i.e. the device carrying the GNSS receiver), the higher the accuracy. In an optimal setup, the base station would be located in close proximity, i.e.  $< 1$  km from the rover. When recording raw GNSS data, it is possible to increase the accuracy by means of post-processing routines. For this purpose programs like “RTKLIB” are available. The achievable accuracy with which relative movements between vehicles can be recorded is of interest when using the “Measurement2Sim” method. To determine the accuracy of the position measurement, the method shown below is used:

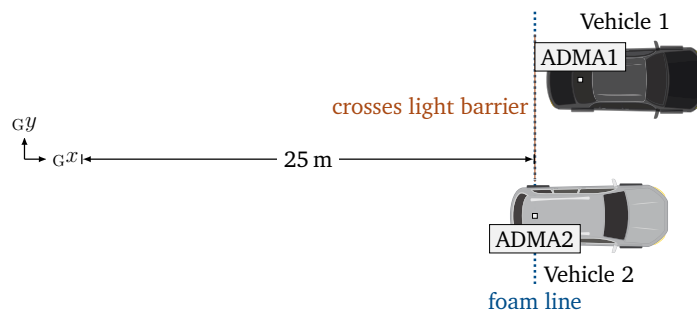
A light barrier is mounted on the vehicles along the lateral axis of the reference point, which is, for example, the center of the rear axle. It is assumed that reaction times are negligibly short. The light barrier sensor is connected to the ADMA, which adds a GNSS-based time reference when sampling the signal from the light barrier sensor at 100 Hz.



**Step 1:** Two vehicles are positioned parallel to each other. This is the zero position for the longitudinal offset. The lateral position is determined with a tape measure (or similar) between the reference points. A foam line is drawn perpendicular to the longitudinal axis of the vehicles at a certain distance (e.g. 25 m).



**Step2:** Vehicle 2 now moves to the foam line and the light barrier sends a trigger signal just as vehicle 2 starts moving. The light barrier is aligned so that it is at the same height as the foam line.



**Step 3:** Vehicle 1 performs a longitudinal movement and crosses the foam line. By this, it also passes over the light barrier, which gives a further trigger signal. The tire tracks in the foam caused by vehicle 1 are only used to determine the lateral offset at the time of crossing the light barrier.

In simulation, the light barrier is implemented as a trigger that is activated when the objects have zero lateral offset in the coordinate system centered on one of the vehicles. The calibration results obtained by conducting the method above are given in table A.2.

For lateral direction and longitudinal direction, an offset of 2 cm is visible. The temporal offset is found as 15 samples. As the ADMA samples at 100 Hz, this corresponds to an temporal offset of 0.15 s.

The determined deviation between the distance according to GNSS positions and the measured values is subject to influences by measurement inaccuracies: Positioning of the light barrier at the reference point on both vehicles, determination of the mean point from the foam tracks, placement and orientation of the foam line. The summed up errors are estimated with 3 cm. The offsets found by calibration are within this estimated accuracy.

Table A.2.: Calibration values of “Measurement2Sim” method

<b>Lateral</b>	Tape	GNSS	Simulation
Initial	3.345 m	3.321 m	3.345 m
Final	3.79 m	3.77 m	3.77 m
<b>Longitudinal</b>			
Initial	0 m	-0.02 m	<-0.01 m
Final	25 m	25.0005 m	25.025 m

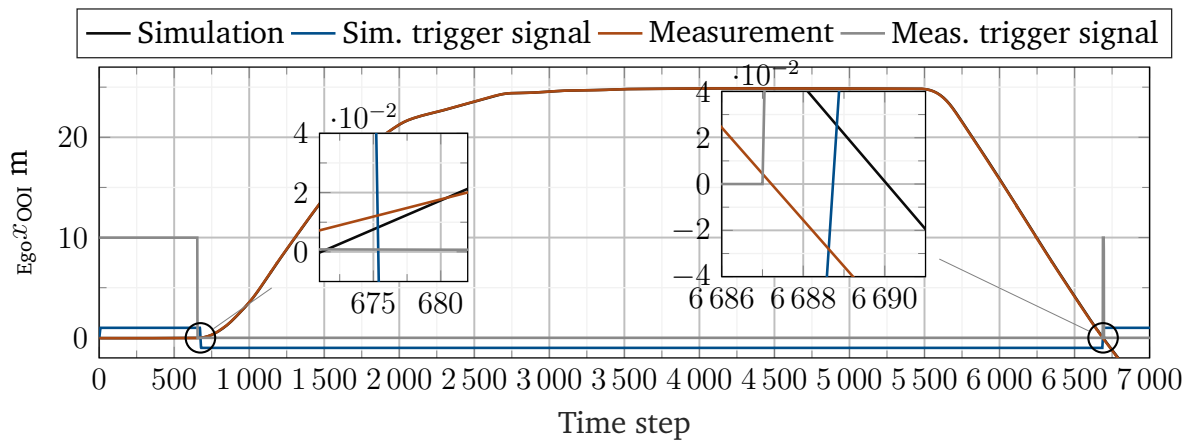


Figure A.6.: Signal reading during calibration recorded at 100 Hz. Longitudinal distance between Ego and OOI are shown for measurement and simulation. Trigger signal is activated when different from 0.

So far, the method only focuses on the calibration of positioning accuracy. When using two light barriers (e.g. on the front and rear axles), the yaw angle can also be calibrated. Calibrating the speed is not possible without further ado: Although the delay of the light barrier can be determined, results shown in section 3.9.2 show that it is not possible to maintain a constant speed with regular speedometers. The speed variations exceed the resolution ranges of the speed measurement of the ADMA. Due to the fact that speed measured with GNSS and radar shows high accuracy and precision, a calibration of the speed is not considered necessary.

The lateral offset can also be determined using a lidar sensor, for which distance measurement accuracies in the range  $< 3$  cm can be expected. This sensor is then placed between the vehicles. In this case, it is advisable to select a prominent and well-defined reflection point (e.g., a highly reflective foil) on the vehicles that can be easily identified from the point cloud based on its intensity. The method is also suitable for calibration if the position of the vehicles is not detected via GNSS but via other methods such as lidar, radar, camera, or ultrasound.

## A.7. Conditioning of ground truth

To determine the ground truth distance between ego and object of interest (OOI) (denoted  $s_{r_{OOI,GT}}$ ), the position determination by the ADMA in the respective vehicles is used. This requires information about the (longitudinal) installation position of the ADMA device in the vehicles as well as the vehicle dimensions (i.e. the distance between the measuring center of the ADMA and the radar in the ego and distance between the measuring center of the ADMA in the OOI and its rear). This determines  $\Delta x_{ADMA1,OOI}$  and  $\Delta x_{ADMA2,OOI}$  which is shown in figure A.7. If there is a lateral offset in the mounting positions, this is to be considered in the same way. The radial distance  $s_{r_{OOI,GT}}$  results from transforming the Cartesian quantities ( $\Delta x_{OOI,GT}$  and  $\Delta y_{OOI,GT}$ ) into a sensor centered polar coordinate frame.

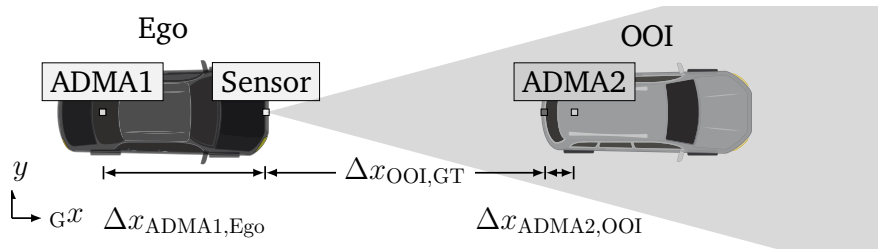


Figure A.7.: Geometric relationships for ground truth conditioning. It is assumed that each ADMA is mounted above the center of the rear axle. For simplification, only quantities in longitudinal direction are shown.

Based on the range measurement with radar, spectral power values are available in the radar cubic at discrete range bins. With knowledge of  $s_{r_{OOI,GT}}$  and the vehicle dimensions, the range bins occupied by the OOI can be found. This is done by searching for the maximum peak in the vicinity (e.g. 1-2 bins) around  $\lfloor s_{r_{OOI,GT}}/\delta r \rfloor$  and applying the quadratically interpolated FFT (QIFFT) procedure outlined in paragraph A.8. Since the ADMA measurement is also used to measure heading angle, angular position, and relative velocity, the Doppler and azimuth bins can be determined in an analog way. By corresponding coordinate transformations, which are not shown here, rotations and lateral displacements between the ego vehicle and OOI can be considered as well.

An estimate of the distance between radar and OOI is available from the QIFFT method, i.e.  $s_{\check{r}_{OOI}}$ . Statistical evaluations can be made when considering the ground truth value  $s_{r_{OOI,GT}}$ . This procedure can be applied to synthetic data in the same fashion. Instead of the ADMA, the ground truth state vector is used to describe the position and speed of the ego or OOI.

## A.8. Quadratic interpolation of spectral peaks

The following describes the spectral estimation method via the QIFFT method. The explanations are based on the work of Smith<sup>154</sup> with adaptation of the nomenclature.

The basic idea of the QIFFT procedure is to estimate the actual location of the frequency peak in the spectrum. In the discrete Fourier transformation (DFT) spectrum there are discrete values and the actual maximum can lie between the discrete bins, see figure A.8. Note that, without limiting the generality,  $x$  and  $y$  are used in this context for the ordinate and abscissa respectively. The peak location  $x_{\text{peak}}$  can be interpreted as the dominant (continuous) frequency in the underlying (discrete) frequency spectrum. In QIFFT a parabola is used as an approximate solution for various window functions. In fact, in case of a Gaussian window, the peak would be reconstructed exactly by the QIFFT method.

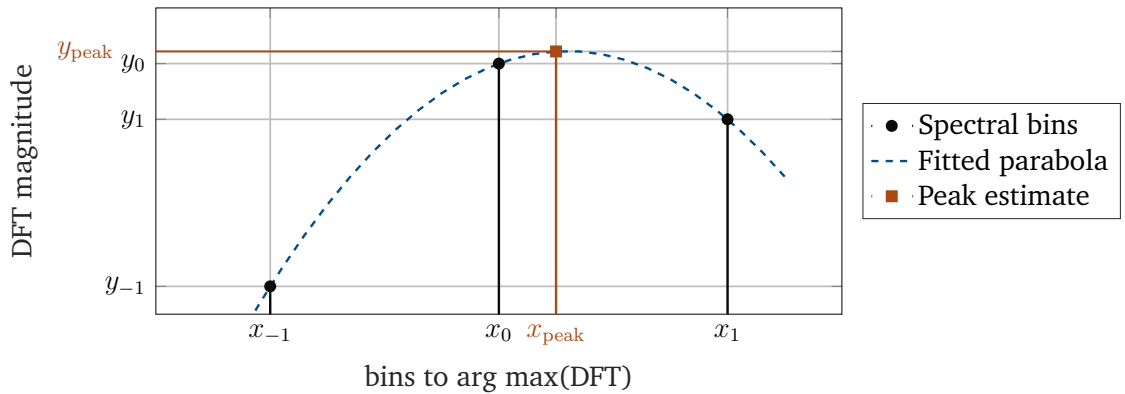


Figure A.8.: Illustration of parabolic peak interpolation using the three samples of the DFT nearest the peak value of the DFT (denoted  $x_0$ . Index denotes the distance to the nearest peak in bins).

The general formula for a parabola may be written as

$$y_{\text{par}} = k_1(x - x_{\text{peak}})^2 + k_2 \quad (\text{A.3})$$

where  $x_{\text{peak}}$  is the center point, i.e. the interpolated peak location and  $k_1$  and  $k_2$  are shape parameters. The left and right neighbor at abscissa position  $x_{-1}$  and  $x_1$  of the bin showing the highest magnitude, denoted  $x_0$ , are taken. Using the three known points

<sup>154</sup> Smith, J. O.: Spectral Audio Signal Processing: Quadratic Interpolation of Spectral Peaks (2020).

from the DFT, the three unknown quantities in eq. A.3, i.e.  $k_1$ ,  $k_2$ , and  $x_{\text{peak}}$  can be solved for the center point:

$$x_{\text{peak}} = \frac{1}{2} \frac{x_{-1} - x_1}{2x_{-1} - 2x_0 + x_1} \quad (\text{A.4})$$

In general,  $y_{\text{peak}} > y_0$  and thus the magnitude of the interpolated peak can be calculated:

$$y_{\text{peak}} = x_0 - \frac{1}{4} (x_{-1} - x_1) x_{\text{peak}} \quad (\text{A.5})$$

For the application on the radar cubic, the method can be applied to any dimension (range, range rate, angular position). If no Gaussian window is used, the QIFFT procedure does not guarantee that the true center point is identified. In this case, the QIFFT procedure provides an estimated peak position, denoted as  $\check{x}_{\text{peak}}$ . To increase the quality of the ordinate estimate, influences of the window function must be eliminated. The procedure for this is described in the literature of Smith et al.



# Bibliography

---

**Abou-Jaoude, R.: ACC Radar Sensor Technology, Test Requirements, and Test Solutions (2003)**

Abou-Jaoude, R.: ACC Radar Sensor Technology, Test Requirements, and Test Solutions, in: IEEE Transactions on Intelligent Transportation Systems, Vol. 4, pp. 115–122, 2003

**Ackermann, F.: Abstandsregelung mit Radar (1980)**

Ackermann, Fritz: Abstandsregelung mit Radar, in: Spektrum der Wissenschaft, pp. 24–34, 1980

**Adams, M.: Robotic Navigation and Mapping with Radar (2012)**

Adams, Martin: Robotic Navigation and Mapping with Radar, Artech House, 2012

**Andres, M. et al.: Extraction of Micro-Doppler Signatures using Automotive Radar Sensors (2012)**

Andres, Markus; Ishak, Karim; Menzel, Wolfgang,; Bloecher, Hans-Ludwig: Extraction of Micro-Doppler Signatures using Automotive Radar Sensors, in: Frequenz, Vol. 66, 2012

**ASAM: OpenCRG (2020)**

ASAM: OpenCRG, ASAM Association for Standardization of Automation and Measuring Systems e.V. URL: <https://www.asam.net/standards/detail/opencrg>, 2020, visited on 05/13/2020

**ASAM: OpenDRIVE (2020)**

ASAM: OpenDRIVE, ASAM Association for Standardization of Automation and Measuring Systems e.V. URL: <https://www.asam.net/standards/detail/opendrive>, 2020, visited on 05/13/2020

**ASAM: OpenSCENARIO (2020)**

ASAM: OpenSCENARIO, ASAM Association for Standardization of Automation and Measuring Systems e.V. URL: <https://www.asam.net/standards/detail/openscenario>, 2020, visited on 05/13/2020

**Aust, P.: Masterthesis, Entwicklung eines lidartypischen Objektlisten-Sensormodells (2019)**

Aust, Philip: Entwicklung eines lidartypischen Objektlisten-Sensormodells, Master's Thesis TU Darmstadt, 2019

**Automobil-Entwicklung: David und die Goliaths: Simultaneous Engineering (1999)**

Automobil-Entwicklung: David und die Goliaths: Simultaneous Engineering - Firmen-Profil: A.D.C. In: Automobil-Entwicklung, pp. 34–36, 1999

**Barnes, D. et al.: The Oxford Radar RobotCar Dataset (2019)**

Barnes, Dan; Gadd, Matthew; Murcutt, Paul; Newman, Paul,; Posner, Ingmar: The Oxford Radar RobotCar Dataset: A Radar Extension to the Oxford RobotCar Dataset, in: arXiv preprint arXiv: 1909.01300, 2019

**Belgiovane, D. et al.: Micro-Doppler characteristics of pedestrians and bicycles (2017)**

Belgiovane, Domenic; Chen, Chi-Chih: "Micro-Doppler characteristics of pedestrians and bicycles for automotive radar sensors at 77 GHz," in: *2017 11th European Conference on Antennas and Propagation (EUCAP)*, 2017

**Berger, C. et al.: Nutzung der GPU für automotive Sensorsimulationen (2009)**

Berger, Christian; Rumpel, Bernhard: Nutzung von projektiven Texturen auf einer GPU zur Distanzmessung für automotive Sensorsimulationen, in: Gesamtzentrum für Verkehr Braunschweig eV, editor, AAET, pp. 319–329, 2009

**Berk, M. et al.: Reliability Assessment of Safety-Critical Sensor Information (2019)**

Berk, Mario; Schubert, Olaf; Kroll, Hans-Martin; Buschardt, Boris,; Straub, Daniel: Reliability Assessment of Safety-Critical Sensor Information: Does One Need a Reference Truth? In: *IEEE Transactions on Reliability*, Vol. 68, pp. 1227–1241, 2019

**Bernsteiner, S. et al.: Radar Sensor Model for the Virtual Development Process (2015)**

Bernsteiner, Stefan; Magosi, Zoltan; Lindvai-Soos, Daniel,; Eichberger, Arno: Radar Sensor Model for the Virtual Development Process, in: *ATZelextronik worldwide*, Vol. 10, pp. 46–52, 2015

**Berthold, P. et al.: An Abstracted Radar Measurement Model for Extended Object Tracking (2018)**

Berthold, Philipp; Michaelis, Martin; Luettel, Thorsten; Meissner, Daniel,; Wuensche, Hans-Joachim: "An Abstracted Radar Measurement Model for Extended Object Tracking," in: *2018 21st International Conference on Intelligent Transportation Systems (ITSC)*, 2018

**Bonek, E.: MIMO Propagation and Channel Modeling (2011)**

Bonek, Ernst: MIMO Propagation and Channel Modeling, Elsevier, 2011

**Box, G. E. P.: Robustness in the Strategy of Scientific Model Building (1979)**

Box, George Edward Pelham: Robustness in the Strategy of Scientific Model Building, in: Launer, Robert L.; Wilkinson, Graham N. (eds): Robustness in Statistics, Elsevier, 1979

**Box, G. E. P.; Draper, N. R.: Empirical model-building (1987)**

Box, George Edward Pelham; Draper, Norman Richard: Empirical model-building and response surfaces, John Wiley & Sons, 1987

**Brisken, S. et al.: Elevation Estimation with a High Resolution Automotive Radar (2019)**

Brisken, Stefan; Gutlein-Holzer, Johanna,; Hohne, Felix: "Elevation Estimation with a High Resolution Automotive Radar," in: *2019 IEEE Radar Conference (RadarConf)*, 2019

**Buddendick, H. et al.: Bistatic scattering center models (2010)**

Buddendick, Hermann; Eibert, Thomas,; Hasch, Jürgen: "Bistatic scattering center models for the simulation of wave propagation in automotive radar systems," in: *German Microwave Conference Digest of Papers*, IEEE, pp. 288–291, 2010

**Bühren, M. et al.: Simulation of Automotive Radar Target Lists (2006)**

Bühren, Markus; Yang, Bin: "Simulation of Automotive Radar Target Lists using a Novel Approach of Object Representation," in: *2006 IEEE Intelligent Vehicles Symposium*, 2006

**Caesar, H. et al.: nuScenes: A multimodal dataset for autonomous driving (2019)**

Caesar, Holger; Bankiti, Varun; Lang, Alex H.; Vora, Sourabh; Liong, Venice Erin; Xu, Qiang; Krishnan, Anush; Pan, Yu; Baldan, Giancarlo,; Beijbom, Oscar: nuScenes: A multimodal dataset for autonomous driving, in: arXiv preprint arXiv:1903.11027, 2019

**Cao, P.: Dissertation, Modeling Active Perception Sensors (2018)**

Cao, Peng: Modeling Active Perception Sensors for Real-Time Virtual Validation of Automated Driving Systems, Dissertation TU Darmstadt, TUpriints, 2018

**CARLASimulator: CARLA Talks 2020 - The External Sensor Interface (ESI) (2020)**

CARLASimulator: CARLA Talks 2020 - The External Sensor Interface (ESI), <https://www.youtube.com>, URL: <https://youtu.be/5hXHPV9FIeY>, 2020, visited on 06/10/2020

**Deep, Y. et al.: Polarimetric Radar Cross-Sections of Pedestrians (2019)**

Deep, Yoshana; Held, Patrick; Ram, Shobha Sundar; Steinhäuser, Dagmar; Gupta, Anshu; Gruson, Frank; Koch, Andreas,; Roy, Anirban: Polarimetric Radar Cross-Sections of Pedestrians at Automotive Radar Frequencies, in: arXiv preprint arXiv: 1910.13706, URL: <https://arxiv.org/pdf/1910.13706>, 2019

**Dickmann, J. et al.: Radar for Autonomous Driving (2019)**

Dickmann, Jürgen; Lombacher, Jakob; Schumann, Ole; Scheiner, Nicolas; Dehkordi, Saeid K.; Giese, Tilmann,; Duraisamy, Bharanidhar: Radar for Autonomous Driving – Paradigm Shift from Mere Detection to Semantic Environment Understanding, in: Bertram, Torsten (eds): Fahrerassistenzsysteme 2018, Springer Fachmedien Wiesbaden, 2019

**Dictionary.com: Definition of Artifact at Dictionary.com (2020)**

Dictionary.com: Artifact | Definition of Artifact at Dictionary.com, <https://www.dictionary.com>, URL: <https://www.dictionary.com/browse/artifact?s=t>, 2020, visited on 08/09/2020

**Dietmayer, K.: Predicting of Machine Perception for Automated Driving (2016)**

Dietmayer, Klaus: Predicting of Machine Perception for Automated Driving, in: Maurer, Markus; Gerdes, J. Christian; Lenz, Barbara,; Winner, Hermann (eds): Autonomous Driving, Springer Berlin Heidelberg, 2016

**Diewald, F.: Dissertation, Objektklassifikation und Freiraumdetektion auf Basis bildgebender Radarsensorik (2013)**

Diewald, Fabian: Objektklassifikation und Freiraumdetektion auf Basis bildgebender Radarsensorik für die Fahrzeugumfelderfassung, Dissertation Universität Ulm, <https://oparu.uni-ulm.de/xmlui/handle/123456789/2538>, 2013

**Doerry, A. W.: Noise and Noise Figure for Radar Receivers (2016)**

Doerry, Armin W: Noise and Noise Figure for Radar Receivers, <https://www.osti.gov>, URL: <https://www.osti.gov/servlets/purl/1562649>, 2016, visited on 05/18/2020

**Dörr, D.: Radar Sensor in IPG CarMaker (2017)**

Dörr, Dominik: Using Virtualization to Accelerate the Development of ADAS & Automated Driving Functions, GTC Europe 2017, URL: <http://on-demand.gputechconf.com/gtc-eu/2017/presentation/23293-dominik-d%C3%B6rr-using-virtualization-to-accelerate-the-development-of-adas-and-automated-driving-functions.pdf>, 2017, visited on 09/28/2017

**Dudek, M.: Dissertation, Towards automotive safety applications based on radar sensors (2015)**

Dudek, Manuel: Towards future automotive safety applications based on phased-array FMCW-radar sensors: A holistic simulative approach incorporating RF-frontend impairments, Dissertation Verlag Dr. Hut, 2015

**Eder, T. et al.: Data Driven Radar Detection Models (2019)**

Eder, Thomas; Hachicha, Rami; Sellami, Houssem; van-Driesten, Carlo; Biebl, Erwin: "Data Driven Radar Detection Models: A Comparison of Artificial Neural Networks and Non Parametric Density Estimators on Synthetically Generated Radar Data," in: *Kleinheubacher Tagung 2019*, 2019

**Engels, F.: Dissertation, Multidimensional Frequency Estimation in Automotive Radar (2016)**

Engels, Florian: Multidimensional Frequency Estimation with Applications in Automotive Radar, Dissertation Karlsruher Institut für Technologie (KIT), Forschungsberichte aus dem Institut für Nachrichtentechnik des Karlsruher Instituts für Technologie, 2016

**Engels, F. et al.: Framework on high-resolution frequency estimation (2017)**

Engels, Florian; Heidenreich, Philipp; Zoubir, Abdelhak M.; Jondral, Friedrich K.; Wintermantel, Markus: Advances in Automotive Radar: A framework on computationally efficient high-resolution frequency estimation, in: *IEEE Signal Processing Magazine*, Vol. 34, pp. 36–46, 2017

**Fan, W. et al.: Measured characteristics of indoor channels at millimetric bands (2016)**

Fan, Wei; Carton, Ines; Nielsen, Jesper Ø.; Olesen, Kim; Pedersen, Gert F.: Measured wideband characteristics of indoor channels at centimetric and millimetric bands, in: *EURASIP Journal on Wireless Communications and Networking*, Vol. 2016, 2016

**Feilhauer, M. et al.: A multi-sensor model to validate ADAS in a virtual environment (2017)**

Feilhauer, Marius; Häring, Jürgen: A real-time capable multi-sensor model to validate ADAS in a virtual environment, in: Isermann, Rolf (eds): *Fahrerassistenzsysteme 2017*, Springer Fachmedien Wiesbaden, 2017

**Felbecker, R. et al.: Electromagnetic wave propagation using OptiX GPU ray tracing (2012)**

Felbecker, Robert; Raschkowski, Leszek; Keusgen, Wilhelm; Peter, Michael: "Electromagnetic wave propagation in the millimeter wave band using the NVIDIA OptiX GPU ray tracing engine," in: *2012 6th European Conference on Antennas and Propagation (EUCAP)*, 2012

**FileFormat.info: Wavefront OBJ: Summary from the Encyclopedia of Graphics File Formats (2020)**

FileFormat.info: Wavefront OBJ: Summary from the Encyclopedia of Graphics File Formats, <https://www.fileformat.info>, URL: <https://www.fileformat.info/format/wavefrontobj/egff.htm>, 2020, visited on 09/02/2020

**Fleming, B.: Recent Advancement in Automotive Radar Systems (2012)**

Fleming, Bill: Recent Advancement in Automotive Radar Systems, in: IEEE Vehicular Technology Magazine, Vol. 7, pp. 4–9, 2012

**Fonck, K.: Radar bremst bei Gefahr (1955)**

Fonck, KH: Radar bremst bei Gefahr, in: Auto, Motor & Sport, p. 30, 1955

**Gadringer, M. E. et al.: Virtual reality for automotive radars (2018)**

Gadringer, Michael E.; Schreiber, Helmut; Gruber, Andreas; Vorderderfler, Michael; Amschl, Dominik; Bösch, Wolfgang; Metzner, Steffen; Pflügl, Horst,; Paulweber, Michael: Virtual reality for automotive radars, in: e & i Elektrotechnik und Informationstechnik, Vol. 135, pp. 335–343, 2018

**Gamba, J.: Radar Target Detection (2019)**

Gamba, Jonah: Radar Target Detection, in: Gamba, Jonah (eds): Radar Signal Processing for Autonomous Driving, Springer Singapore, 2019

**Geiger, A. et al.: Are we ready for Autonomous Driving? The KITTI Vision Benchmark Suite (2012)**

Geiger, Andreas; Lenz, Philip,; Urtasun, Raquel: “Are we ready for Autonomous Driving? The KITTI Vision Benchmark Suite,” in: *Conference on Computer Vision and Pattern Recognition (CVPR)*, 2012

**González, Á.: Areas on a Sphere Using Fibonacci and Latitude–Longitude Lattices (2009)**

González, Álvaro: Measurement of Areas on a Sphere Using Fibonacci and Latitude–Longitude Lattices, in: *Mathematical Geosciences*, Vol. 42, pp. 49–64, 2009

**Goulianos, A. A. et al.: Measurements and Characterisation of Surface Scattering at 60 GHz (2017)**

Goulianos, Angelos A.; Freire, Alberto L.; Barratt, Tom; Mellios, Evangelos; Cain, Peter; Rumney, Moray; Nix, Andrew,; Beach, Mark: “Measurements and Characterisation of Surface Scattering at 60 GHz,” in: *2017 IEEE 86th Vehicular Technology Conference (VTC-Fall)*, 2017

**Gourova, R. et al.: Analysis of rain clutter detections in commercial 77 GHz automotive radar (2017)**

Gourova, Rossiza; Krasnov, Oleg,; Yarovoy, Alexander: “Analysis of rain clutter detections in commercial 77 GHz automotive radar,” in: *2017 European Radar Conference (EURAD)*, 2017

**Haider, A. et al.: Automotive Radar Sensor Behavioral Models (2019)**

Haider, Arsalan; Kim, Jihoon; Sachse, Marcel; Zeh, Thomas; Schneider, Stefan Alexander,; Eryildirim, Abduelkadir: “Automotive Radar Sensor Behavioral Models for Closed Loop Simulations,” in: *Proceedings of the 5th International Symposium on Future Active Safety Technology toward Zero Accidents*, 2019

**Hammarstrand, L. et al.: Extended Object Tracking using a Radar Resolution Model (2012)**

Hammarstrand, Lars; Svensson, Lennart; Sandblom, Fredrik,; Sorstedt, Joakim: Extended Object Tracking using a Radar Resolution Model, in: *IEEE Transactions on Aerospace and Electronic Systems*, Vol. 48, pp. 2371–2386, 2012

**Hanke, T. et al.: Generic architecture for simulation of ADAS sensors (2015)**

Hanke, Timo; Hirsenkorn, Nils; Dehlink, Bernhard; Rauch, Andreas; Rasshofer, Ralph,; Biebl, Erwin: “Generic architecture for simulation of ADAS sensors,” in: *2015 16th International Radar Symposium (IRS)*, 2015

**Hanke, T. et al.: Open Simulation Interface (2017)**

Hanke, Timo; Hirsenkorn, Nils; van Driesten, Carlo; Garcia Ramos, Pilar; Schiementz, Mark; Schneider, Sebastian,; Biebl, Erwin: Open Simulation Interface: A generic interface for the environment perception of automated driving functions in virtual scenarios. URL: <https://www.hot.ei.tum.de/forschung/automotive-veroeffentlichungen/>, 2017

**Hasch, J.: Driving towards 2020: Automotive Radar Technology Trends (2015)**

Hasch, Jurgen: “Driving towards 2020: Automotive radar technology trends,” in: *2015 IEEE MTT-S International Conference on Microwaves for Intelligent Mobility (ICMIM)*, 2015

**Herrmann, M. et al.: Sensor Development Using Raw Signal Interfaces (2019)**

Herrmann, Martin; Schön, Helmut: Efficient Sensor Development Using Raw Signal Interfaces, in: Bertram, Torsten (eds): *Fahrerassistenzsysteme 2018*, Springer Fachmedien Wiesbaden, 2019

**Herz, G. et al.: Sophisticated Sensor Model Framework (2017)**

Herz, Gabriel; Schick, Bernhard; Hettel, Rolf; Meinel, Holger: Sophisticated Sensor Model Framework Providing Real Sophisticated Sensor Model Framework Providing Realistic Radar Sensor Behavior in Virtual Environments, in: 10th Graz Symposium Virtual Vehicle (GSVF), Graz, Austria, 2017

**Hirsenkorn, N. et al.: A non-parametric approach for modeling sensor behavior (2015)**

Hirsenkorn, Nils; Hanke, Timo; Rauch, Andreas; Dehlink, Bernhard; Rasshofer, Ralph; Biebl, Erwin: "A non-parametric approach for modeling sensor behavior," in: *2015 16th International Radar Symposium (IRS)*, 2015

**Hirsenkorn, N. et al.: Ray launching for modeling an FMCW radar system (2017)**

Hirsenkorn, Nils; Subkowski, Paul; Hanke, Timo; Schaermann, Alexander; Rauch, Andreas; Rasshofer, Ralph; Biebl, Erwin: "A ray launching approach for modeling an FMCW radar system," in: *2017 18th International Radar Symposium (IRS)*, 2017

**Hollander, Y.: Foretellix Blog: M-SDL, the autonomous vehicles verification language (2020)**

Hollander, Yoav: M-SDL, the autonomous vehicles verification language, is now open, The Foretellix Blog, URL: <https://blog.foretellix.com/2019/09/23/m-sdl-the-autonomous-vehicles-verification-language-is-now-open/>, 2020, visited on 05/13/2020

**<http://carla.org>: Carla v: 0.9.9 Radar Detection (2020)**

<http://carla.org>: Python API reference - CARLA Simulator, [carla.readthedocs.io](http://carla.readthedocs.io), URL: [https://carla.readthedocs.io/en/0.9.9/python\\_api/#carlaradardetection](https://carla.readthedocs.io/en/0.9.9/python_api/#carlaradardetection), 2020, visited on 08/06/2020

**<http://lgsvlsimulator.org>: Lidar sensor plugin - LGSVL Simulator (2020)**

<http://lgsvlsimulator.org>: Lidar sensor plugin - LGSVL Simulator, <https://www.lgsvlsimulator.com>, URL: <https://www.lgsvlsimulator.com/docs/python-api/#lidar-sensor>, 2020, visited on 08/06/2020

**Hülsmeier, C.: Verfahren um metallische Gegenstände mittels elektrischer Wellen zu melden (1904)**

Hülsmeier, Christian: Verfahren, um entfernte metallische Gegenstände mittels elektrischer Wellen einem Beobachter zu melden, in: European Patent Office, Patentschrift DE165546, Vol. 30, 1904

**Hum3D.com a ParaART, L. c.: Volkswagen Golf Mk5 5-door 2004 3D Model (2020)**

Hum3D.com a ParaART, LLC company: Hum3D 3D Models - Volkswagen Golf Mk5 5-door 2004 3D Model - Vehicles on Hum3D, <https://hum3d.com>, URL: <https://hum3d.com/3d-models/volkswagen-golf-mk5-5-door-2004/>, 2020, visited on 06/10/2020

**Ioffe, A. et al.: RCS characteristics of street curbs (2016)**

Ioffe, Alexander; Doerr, Wolfgang; Yan, Honghui; Vu, Duc H.; Arage, Alebel Hassen: "RCS characteristics of street curbs and the applications in automotive radar classification," in: *2016 European Radar Conference (EuRAD)*, IEEE, pp. 241–244, 2016

**IPG Automotive: CarMaker 9 Press Release (2020)**

IPG Automotive: IPG Automotive Releases Version 9.0 of the CarMaker Product Family, <https://press.ipg-automotive.com>, URL: [https://press.ipg-automotive.com/fileadmin/user\\_upload/content/Download/Press/Press\\_Release/2020/IPG\\_Automotive\\_PM\\_Release\\_9.0\\_EN.pdf](https://press.ipg-automotive.com/fileadmin/user_upload/content/Download/Press/Press_Release/2020/IPG_Automotive_PM_Release_9.0_EN.pdf), 2020, visited on 05/18/2020

International Organization for Standardization. Road vehicles – Data communication between sensors and data fusion unit for automated driving functions – Logical interface. Standard. Status: Under development, 30.60: Close of voting / comment period. Geneva, CH, Oct. 2019.

**Kamann, A. et al.: Automotive Radar Multipath Propagation in Uncertain Environments (2018)**

Kamann, Alexander; Held, Patrick; Perras, Florian; Zaumseil, Patrick; Brandmeier, Thomas.; Schwarz, Ulrich T.: "Automotive Radar Multipath Propagation in Uncertain Environments," in: *2018 21st International Conference on Intelligent Transportation Systems (ITSC)*, 2018

**Karlsson, K.: Radar Cross Section (2018)**

Karlsson, Kristian: HiFi Radar Target High fidelity soft targets and radar simulation for more efficient testing (real and virtual), <https://site.ieee.org>, URL: <https://site.ieee.org/sweden/files/2018/09/IEEE-EMC-20180914-HiFi-Radar-Target-Kristian-Karlsson.pdf#page=10>, 2018, visited on 09/09/2020

**Karlsson, K. et al.: Reducing influence from ground reflection during RCS characterization (2019)**

Karlsson, Kristian; Toss, Henrik.; Costagliola, Francesco: "Reducing influence from ground reflection during RCS characterization of automotive targets," in: *2019 13th European Conference on Antennas and Propagation (EuCAP)*, IEEE, pp. 1–5, 2019

**Kellner, D. et al.: Wheel extraction based on micro doppler distribution (2015)**

Kellner, Dominik; Barjenbruch, Michael; Klappstein, Jens; Dickmann, Jurgen,; Dietmayer, Klaus: "Wheel extraction based on micro doppler distribution using high-resolution radar," in: *2015 IEEE MTT-S International Conference on Microwaves for Intelligent Mobility (ICMIM)*, 2015

**Kirtzakis, S. et al.: Das Beste aus der MRA- Architektur (2017)**

Kirtzakis, Stylianos; Johanns, Torge; Colmsee, Harald,; Bolgert, Alex: Das Beste aus der MRA- Architektur, in: Liebl, Johannes (eds): Mercedes-Benz E-Klasse, Springer Fachmedien Wiesbaden, 2017

**Knott, E.: Radar cross section measurements (1993)**

Knott, Eugene: Radar cross section measurements, Van Nostrand Reinhold, 1993

**Koch, W.: Advanced Sensor Models for Tracking Applications (2007)**

Koch, Wolfgang: Verfeinerte Sensormodelle für Tracking-Anwendungen (Advanced Sensor Models for Tracking Applications), in: tm – Technisches Messen, Vol. 74, 2007

**Kunert, M.: The EU project MOSARIM (2012)**

Kunert, Martin: "The EU project MOSARIM: A general overview of project objectives and conducted work," in: *2012 9th European Radar Conference*, pp. 1–5, 2012

**Lutz, A. et al.: Simulation methods supporting homologation of Electronic Stability Control (2017)**

Lutz, Albert; Schick, Bernhard; Holzmann, Henning; Kochem, Michael; Meyer-Tuve, Harald; Lange, Olav; Mao, Yiqin,; Tosolin, Guido: Simulation methods supporting homologation of Electronic Stability Control in vehicle variants, in: *Vehicle System Dynamics*, Vol. 55, pp. 1432–1497, 2017

**Maier, F. M. et al.: Adapting Phong into Stimulation of Automotive Radar Sensors (2018)**

Maier, F. Michael; Makkapati, Vamsi P.,; Horn, Martin: "Adapting Phong into a Simulation for Stimulation of Automotive Radar Sensors," in: *2018 IEEE MTT-S International Conference on Microwaves for Intelligent Mobility (ICMIM)*, 2018

**Maier, F. M. et al.: Environment perception simulation for radar stimulation (2018)**

Maier, F. Michael; Makkapati, Vamsi P.,; Horn, Martin: Environment perception simulation for radar stimulation in automated driving function testing, in: *e & i Elektrotechnik und Informationstechnik*, Vol. 135, pp. 309–315, 2018

**Marx, B. J.: Dissertation, Radareigenschaften von Personenkraftwagenkarosserien (2013)**

Marx, Benjamin Jakob: Bewertungsverfahren für die Radareigenschaften von Personenkraftwagenkarosserien, Dissertation TU Darmstadt, Fortschrittberichte VDI: Reihe 12, Nr. 775, VDI-Verlag, Düsseldorf, 2013

**Matsunami, I. et al.: RCS measurements for vehicles and pedestrian at 26 and 79GHz (2012)**

Matsunami, Isamu; Nakamura, Ryohei; Kajiwara, Akihiro: "RCS measurements for vehicles and pedestrian at 26 and 79GHz," in: *2012 6th International Conference on Signal Processing and Communication Systems*, 2012

**Mcmullin, E.: What do Physical Models Tell us? (1968)**

Mcmullin, Ernan: What do Physical Models Tell us?, in: Van Rootselaar, B.; Staal, J.F. (eds): *Logic, Methodology and Philosophy of Science III*, Elsevier, 1968

**Meinel, H. H. et al.: Radar Sensors in Cars (2016)**

Meinel, Holger H.; Bösch, Wolfgang: Radar Sensors in Cars, in: Watzenig, Daniel; Horn, Martin (eds): *Automated Driving*, Springer International Publishing, 2016

**Mesow, L.: Dissertation, Multisensorielle Datensimulation (2007)**

Mesow, Lars: Multisensorielle Datensimulation im Fahrzeugumfeld für die Bewertung von Sensorfusionsalgorithmen, Dissertation TU Chemnitz, Forschungsberichte der Professur Nachrichtentechnik, Band 4, Shaker Verlag, 2007

**Miegler, M. et al.: Hardware-in-the-loop test of advanced driver assistance systems (2009)**

Miegler, Maximilian; Schieber, Reinhard; Kern, Andreas; Ganslmeier, Thomas; Nentwig, Mirko: Hardware-in-the-loop test of advanced driver assistance systems, in: *ATZelektronik worldwide*, Vol. 4, pp. 4–9, 2009

**Orsay Consulting: The Autonomous Vehicles Landscape (2020)**

Orsay Consulting: A Widely Referenced Landscape of the Autonomous Vehicle Ecosystem, <https://www.orsayconsulting.net/mobility-resources-en>, URL: [https://s3.amazonaws.com/spoke-profiles-prod-assets/uploads/49b8874568037c7f73397632383a38a0a7578d09/original/AV-High\\_Res.pdf](https://s3.amazonaws.com/spoke-profiles-prod-assets/uploads/49b8874568037c7f73397632383a38a0a7578d09/original/AV-High_Res.pdf), 2020, visited on 08/26/2020

**Parker, S. G. et al.: OptiX: A general purpose ray tracing engine (2010)**

Parker, Steven G.; Bigler, James; Dietrich, Andreas; Friedrich, Heiko; Hoberock, Jared; Luebke, David; McAllister, David; McGuire, Morgan; Morley, Keith; Robison, Austin; Stich, Martin: OptiX: A general purpose ray tracing engine, in: *ACM Transactions on Graphics*, Vol. 29, pp. 1–13, 2010

**Patole, S. M. et al.: Automotive radars: A review of signal processing techniques (2017)**

Patole, Sujeet Milind; Torlak, Murat; Wang, Dan.; Ali, Murtaza: Automotive radars: A review of signal processing techniques, in: *IEEE Signal Processing Magazine*, Vol. 34, pp. 22–35, 2017

**Peddie, J.: Ray-Tracing Hardware (2019)**

Peddie, Jon: Ray-Tracing Hardware, in: Peddie, Jon (eds): *Ray Tracing: A Tool for All*, Springer International Publishing, 2019

**Peinecke, N. et al.: Phong-like lighting for MMW radar simulation (2008)**

Peinecke, Niklas; Doehler, Hans-Ullrich.; Korn, Bernd R.: “Phong-like lighting for MMW radar simulation,” in: *Millimetre Wave and Terahertz Sensors and Technology*, 2008

**Phong, B. T.: Illumination for computer generated pictures (1975)**

Phong, Bui Tuong: Illumination for computer generated pictures, in: *Communications of the ACM*, Vol. 18, pp. 311–317, 1975

**Poggenhans, F. et al.: Lanelet2 (2018)**

Poggenhans, Fabian; Pauls, Jan-Hendrik; Janosovits, Johannes; Orf, Stefan; Naumann, Maximilian; Kuhnt, Florian.; Mayr, Matthias: “Lanelet2: A high-definition map framework for the future of automated driving,” in: *2018 21st International Conference on Intelligent Transportation Systems (ITSC)*, 2018

**Ponn, T. et al.: Systematic Analysis of the Sensor Coverage of Automated Vehicles (2019)**

Ponn, Thomas; Müller, Fabian.; Diermeyer, Frank: “Systematic Analysis of the Sensor Coverage of Automated Vehicles Using Phenomenological Sensor Models,” in: *2019 IEEE Intelligent Vehicles Symposium (IV)*, 2019

**Prophet, R. et al.: Instantaneous Ghost Detection Identification in Automotive Scenarios (2019)**

Prophet, Robert; Martinez, Javier; Michel, Juan-Carlos Fuentes; Ebel, Randolph; Weber, Ingo.; Vossiek, Martin: “Instantaneous Ghost Detection Identification in Automotive Scenarios,” in: *2019 IEEE Radar Conference (RadarConf)*, 2019

**Rahmathullah, A. S. et al.: Generalized optimal sub-pattern assignment metric (2017)**

Rahmathullah, Abu Sajana; Garcia-Fernandez, Angel F.; Svensson, Lennart: “Generalized optimal sub-pattern assignment metric,” in: *2017 20th International Conference on Information Fusion (FUSION)*, 2017

**Rasshofer, R. et al.: Generalized modeling of radar sensors (2005)**

Rasshofer, Ralph; Rank, Johann,; Zhang, Guangyu: "Generalized modeling of radar sensors for next-generation virtual driver assistance function prototyping," in: *12th World Congress on Intelligent Transport Systems*, 2005

**Reway, F. et al.: Test Methodology for ADAS Algorithms with an Automotive Camera (2018)**

Reway, Fabio; Huber, Werner,; Ribeiro, Eduardo Parente: "Test Methodology for Vision-Based ADAS Algorithms," in: *2018 IEEE International Conference on Vehicular Electronics and Safety (ICVES)*, 2018

**Rohling, H. et al.: OS CFAR performance in a 77 GHz radar sensor for car application (1996)**

Rohling, Hermann; Mende, Ralph: "OS CFAR performance in a 77 GHz radar sensor for car application," in: *Proceedings of International Radar Conference*, 1996

**Roos, F. et al.: Ghost target identification by analysis of the Doppler distribution (2017)**

Roos, Fabian; Sadeghi, Mohammadreza; Bechter, Jonathan; Appenrodt, Nils; Dickmann, Jurgen,; Waldschmidt, Christian: "Ghost target identification by analysis of the Doppler distribution in automotive scenarios," in: *2017 18th International Radar Symposium (IRS)*, 2017

**Rosenberger, P. et al.: Benchmarking and Functional Decomposition of Lidar Sensor Models (2019)**

Rosenberger, Philipp; Holder, Martin; Huch, Sebastian; Winner, Hermann; Fleck, Tobias; Zofka, Marc Rene; Zollner, J. Marius; D'hondt, Thomas,; Wassermann, Benjamin: "Benchmarking and Functional Decomposition of Lidar Sensor Models," in: *2019 IEEE Intelligent Vehicles Symposium (IV)*, 2019

**Rosenberger, P. et al.: Towards a Validation Methodology for Sensor Models (2019)**

Rosenberger, Philipp; Wendler, Jan Timo; Holder, Martin Friedrich; Linnhoff, Clemens; Berghöfer, Moritz; Winner, Hermann,; Maurer, Markus: "Towards a Generally Accepted Validation Methodology for Sensor Models - Challenges, Metrics, and First Results," in: *Grazer Symposium Virtuelles Fahrzeug*, 2019

**Roth, E. et al.: Analysis and Validation of Perception Sensor Models (2011)**

Roth, Erwin; Dirndorfer, Tobias J; Knoll, Alois; Neumann-Cosel, Kilian von; Ganslmeier, Thomas; Kern, Andreas,; Fischer, Marc-Oliver: "Analysis and Validation of Perception Sensor Models in an Integrated Vehicle and Environment Simulation," in: *22nd International Technical Conference on the Enhanced Safety of Vehicles (ESV) National Highway Traffic Safety Administration*, 2011

**Sauerbier, J. et al.: Definition of Scenarios for Safety Validation of Automated Driving Functions (2019)**

Sauerbier, Jan; Bock, Julian; Weber, Hendrik; Eckstein, Lutz: Definition of Scenarios for Safety Validation of Automated Driving Functions, in: *ATZ worldwide*, Vol. 121, pp. 42–45, 2019

**Schaermann, A. et al.: Validation of vehicle environment sensor models (2017)**

Schaermann, Alexander; Rauch, Andreas; Hirsenkorn, Nils; Hanke, Timo; Rasshofer, Ralph; Biebl, Erwin: “Validation of vehicle environment sensor models,” in: *2017 IEEE Intelligent Vehicles Symposium (IV)*, 2017

**Scheiner, N. et al.: Non-Line-of-Sight Detection and Tracking Using Doppler Radar (2020)**

Scheiner, Nicolas; Kraus, Florian; Wei, Fangyin; Phan, Buu; Mannan, Fahim; Appenrodt, Nils; Ritter, Werner; Dickmann, Jurgen; Dietmayer, Klaus; Sick, Bernhard, et al.: “Seeing Around Street Corners: Non-Line-of-Sight Detection and Tracking In-the-Wild Using Doppler Radar,” in: *The IEEE Conference on Computer Vision and Pattern Recognition (CVPR)*, 2020

**Schipper, T. et al.: RCS measurement results for automotive related objects at 23-27 GHz (2011)**

Schipper, Tom; Fortuny-Guasch, Joaquim; Tarchi, Dario; Reichardt, Lars; Zwick, Thomas: “RCS measurement results for automotive related objects at 23-27 GHz,” in: *Proceedings of the 5th European Conference on Antennas and Propagation (EUCAP)*, IEEE, pp. 683–686, 2011

**Schneider, R.: Method for processing radar signals (1999)**

Schneider, Robert: Method for processing radar signals, European Patent Office, Patentschrift EP0968441B1, 1999

**Schneider, R.: Dissertation, Modellierung der Wellenausbreitung für ein Kfz-Radar (1998)**

Schneider, Robert: Modellierung der Wellenausbreitung für ein bildgebendes Kfz-Radar, Dissertation Universität Karlsruhe, 1998

**Schreier, M.: Environment representations for automated on-road vehicles (2018)**

Schreier, Matthias: Environment representations for automated on-road vehicles, in: *Automatisierungstechnik*, Vol. 66, pp. 107–118, 2018

**Schuler, K. et al.: Extraction of Virtual Scattering Centers (2008)**

Schuler, Karin; Becker, Denis; Wiesbeck, Werner: Extraction of Virtual Scattering Centers of Vehicles by Ray-Tracing Simulations, in: *IEEE Transactions on Antennas and Propagation*, Vol. 56, pp. 3543–3551, 2008

**Schumann, O. et al.: Semantic Segmentation on Radar Point Clouds (2018)**

Schumann, Ole; Hahn, Markus; Dickmann, Jurgen; Wohler, Christian: "Semantic Segmentation on Radar Point Clouds," in: *2018 21st International Conference on Information Fusion (FUSION)*, 2018

**Schumann, O. et al.: Scene Understanding with Automotive Radar (2019)**

Schumann, Ole; Lombacher, Jakob; Hahn, Markus; Wohler, Christian; Dickmann, Jurgen: Scene Understanding with Automotive Radar, in: *IEEE Transactions on Intelligent Vehicles*, pp. 1–1, 2019

**Sefi, S.: Ray tracing tools for high frequency electromagnetics simulations (2003)**

Sefi, Sandy: Ray tracing tools for high frequency electromagnetics simulations, 2003

**Sennott, R. S.: Encyclopedia of 20th century architecture (2004)**

Sennott, R. Stephen: Encyclopedia of 20th century architecture, Fitzroy Dearborn, 2004

**sergi-e et al.: Carla LIDAR raycast sensor (2020)**

sergi-e; DSantosO: LIDAR raycast sensor - Retrieve simulation data - CARLA Simulator, carla.readthedocs.io, URL: [https://carla.readthedocs.io/en/0.9.9/tuto\\_G\\_retrieve\\_data/#lidar-raycast-sensor](https://carla.readthedocs.io/en/0.9.9/tuto_G_retrieve_data/#lidar-raycast-sensor), 2020, visited on 08/06/2020

**sergi-e et al.: Carla v: 0.9.9 Radar sensor (2020)**

sergi-e; DSantosO: Radar sensor - Retrieve simulation data - CARLA Simulator, carla.readthedocs.io, URL: [https://carla.readthedocs.io/en/0.9.9/tuto\\_G\\_retrieve\\_data/#radar-sensor](https://carla.readthedocs.io/en/0.9.9/tuto_G_retrieve_data/#radar-sensor), 2020, visited on 08/06/2020

**Skolnik, M. I.: Introduction to Radar Systems (2001)**

Skolnik, Merrill I.: Introduction to Radar Systems, Third edition. Auflage, McGraw Hill, 2001

**Smith, J. O.: Spectral Audio Signal Processing: Quadratic Interpolation of Spectral Peaks (2020)**

Smith, Julius O.: Quadratic Interpolation of Spectral Peaks, <https://ccrma.stanford.edu>, URL: [https://ccrma.stanford.edu/~jos/sasp/Quadratic\\_Interpolation\\_Spectral\\_Peaks.html](https://ccrma.stanford.edu/~jos/sasp/Quadratic_Interpolation_Spectral_Peaks.html), 2020, visited on 08/06/2020

**Smulders, P. et al.: Characterisation of propagation in 60 GHz radio channels (1997)**

Smulders, P.F.M.; Correia, L.M.: Characterisation of propagation in 60 GHz radio channels, in: *Electronics & Communication Engineering Journal*, Vol. 9, pp. 73–80, 1997

**Stellet, J. E. et al.: Statistical Modelling of Object Detection (2015)**

Stellet, Jan Erik; Schumacher, Jan; Lange, Oliver; Branz, Wolfgang; Niewels, Frank;; Zöllner, J. Marius: “Statistical Modelling of Object Detection in Stereo Vision-Based Driver Assistance,” in: *Proceedings of the 13th International Conference on Intelligent Autonomous Systems (IAS)*, pp. 749–761, 2015

**Stellet, J. E. et al.: Derivation of performance bounds of autonomous emergency brake systems (2016)**

Stellet, Jan Erik; Vogt, Patrick; Schumacher, Jan; Branz, Wolfgang;; Zollner, J. Marius: “Analytical derivation of performance bounds of autonomous emergency brake systems,” in: *2016 IEEE Intelligent Vehicles Symposium (IV)*, 2016

**Stolz, M. et al.: Fast generic sensor models for testing highly automated vehicles (2018)**

Stolz, Michael; Nestlinger, Georg: Fast generic sensor models for testing highly automated vehicles in simulation, in: *e & i Elektrotechnik und Informationstechnik*, Vol. 135, pp. 365–369, 2018

**Straßer, W.: Dissertation, Kurven-und Flächendarstellung auf grafischen Sichtgeräten (1974)**

Straßer, Wolfgang: Schnelle Kurven-und Flächendarstellung auf grafischen Sichtgeräten, Dissertation TU Berlin, 1974

**Sun, S. et al.: MIMO Radar for Advanced Driver-Assistance Systems and Autonomous Driving (2020)**

Sun, Shunqiao; Petropulu, Athina P.; Poor, H. Vincent: MIMO Radar for Advanced Driver-Assistance Systems and Autonomous Driving: Advantages and Challenges, in: *IEEE Signal Processing Magazine*, Vol. 37, pp. 98–117, 2020

**Sutherland, I. E. et al.: A characterization of ten hidden-surface algorithms (1974)**

Sutherland, Ivan E; Sproull, Robert F;; Schumacker, Robert A: A characterization of ten hidden-surface algorithms, in: *ACM Computing Surveys (CSUR)*, Vol. 6, pp. 1–55, 1974

**Swerling, P.: Probability of detection for fluctuating targets (1960)**

Swerling, Peter: Probability of detection for fluctuating targets, in: *IEEE Transactions on Information Theory*, Vol. 6, pp. 269–308, 1960

**Taygur, M. M. et al.: Computation of Exact Ray Paths with Bidirectional Ray-Tracing (2020)**

Taygur, Mehmet Mert; Eibert, Thomas F.: A Ray-Tracing Algorithm Based on the Computation of (Exact) Ray Paths with Bidirectional Ray-Tracing, in: *IEEE Transactions on Antennas and Propagation*, pp. 1–1, 2020

**Thiel, C. et al.: Vehicle fleet CO2 emission regulation in the European Union (2014)**

Thiel, Christian; Schmidt, Johannes; Zyl, Arnold Van,; Schmid, Erwin: Cost and well-to-wheel implications of the vehicle fleet CO2 emission regulation in the European Union, in: *Transportation Research Part A: Policy and Practice*, Vol. 63, pp. 25–42, 2014

**Thieling, J. et al.: Scalable and Physical Radar Sensor Simulation (2020)**

Thieling, Jörn; Frese, Susanne,; Rossmann, Jürgen: Scalable and Physical Radar Sensor Simulation for Interacting Digital Twins, in: *IEEE Sensors Journal*, pp. 1–9, 2020

**Toss, H. et al.: Radar reflectivity spatial profile of 3D surrogate targets and real vehicles (2019)**

Toss, Henrik; Karlsson, Kristian: “Radar reflectivity spatial profile of 3D surrogate targets and real vehicles,” in: *2019 13th European Conference on Antennas and Propagation (EuCAP)*, IEEE, pp. 1–5, 2019

**Trummer, S. et al.: A polarimetric 76–79 GHz radar-frontend in automotive use (2016)**

Trummer, Stefan; Hamberger, Gerhard F.; Siart, Uwe,; Eibert, Thomas F.: “Polarimetric 76–79 GHz radar-frontend for target classification,” in: *2016 46th European Microwave Conference (EuMC)*, 2016

**van Driesten, C. et al.: Overall Approach to Standardize AD Sensor Interfaces (2019)**

van Driesten, Carlo; Schaller, Thomas: Overall Approach to Standardize AD Sensor Interfaces: Simulation and Real Vehicle, in: Bertram, Torsten (eds): *Fahrerassistenzsysteme 2018*, Springer Fachmedien Wiesbaden, 2019

**Wachenfeld, W. et al.: The Release of Autonomous Vehicles (2016)**

Wachenfeld, Walther; Winner, Hermann: The Release of Autonomous Vehicles, in: Maurer, Markus; Gerdes, J. Christian; Lenz, Barbara,; Winner, Hermann (eds): *Autonomous Driving*, Springer Berlin Heidelberg, 2016

**Wald, I. et al.: Embree: a kernel framework for efficient CPU ray tracing (2014)**

Wald, Ingo; Woop, Sven; Benthin, Carsten; Johnson, Gregory S.,; Ernst, Manfred: Embree: a kernel framework for efficient CPU ray tracing, in: *ACM Transactions on Graphics*, Vol. 33, pp. 1–8, 2014

**Weinmann, F.: Ray Tracing with PO/PTD for RCS Modeling (2006)**

Weinmann, Frank: Ray Tracing With PO/PTD for RCS Modeling of Large Complex Objects, in: *IEEE Transactions on Antennas and Propagation*, Vol. 54, pp. 1797–1806, 2006

**Weishaupt, F. et al.: Polarimetric Radar for Automotive Self-Localization (2019)**

Weishaupt, Fabio; Werber, Klaudius; Tilly, Julius; Dickmann, Jurgen; Heberling, Dirk: "Polarimetric Radar for Automotive Self-Localization," in: *2019 20th International Radar Symposium (IRS)*, 2019

**Wenger, J. et al.: A Polarimetric 76 GHz Radar-Sensor for Automotive Applications (1997)**

Wenger, Josef; Stotz, Michael; Barth, H.; Neef, H.; Wanielik, Gerd; Schneider, R.: "A Polarimetric 76 GHz Radar-Sensor for Automotive Applications," in: *27th European Microwave Conference, 1997*, 1997

**Werber, K. et al.: Automotive radar gridmap representations (2015)**

Werber, Klaudius; Rapp, Matthias; Klappstein, Jens; Hahn, Markus; Dickmann, Jürgen; Dietmayer, Klaus; Waldschmidt, Christian: "Automotive radar gridmap representations," in: *2015 IEEE MTT-S International Conference on Microwaves for Intelligent Mobility (ICMIM)*, 2015

**Weston, R. et al.: Probably Unknown: Deep Inverse Sensor Modelling Radar (2019)**

Weston, Rob; Cen, Sarah; Newman, Paul; Posner, Ingmar: "Probably Unknown: Deep Inverse Sensor Modelling Radar," in: *2019 International Conference on Robotics and Automation (ICRA)*, 2019

**Wheeler, T. A. et al.: Deep stochastic radar models (2017)**

Wheeler, Tim A.; Holder, Martin; Winner, Hermann; Kochenderfer, Mykel John: "Deep stochastic radar models," in: *2017 IEEE Intelligent Vehicles Symposium (IV)*, 2017

**Winner, H.: Automotive RADAR (2015)**

Winner, Hermann: Automotive RADAR, in: Winner, Hermann; Hakuli, Stephan; Lotz, Felix; Singer, Christina (eds): *Handbook of Driver Assistance Systems*, Springer International Publishing, 2015

**Wintermantel, M.: Radar system with elevation measuring capability (2013)**

Wintermantel, Markus: Radar system with elevation measuring capability, US Patent US8390507B2, 2013

**Yun, Z. et al.: Ray Tracing for Radio Propagation Modeling (2015)**

Yun, Zhengqing; Iskander, Magdy F.: Ray Tracing for Radio Propagation Modeling: Principles and Applications, in: *IEEE Access*, Vol. 3, pp. 1089–1100, 2015

**Zaman, Z.: Masterthesis, Stimulation eines Radar-Trackingverfahren (2020)**

Zaman, Zahra: Stimulation eines Radar Objekterkennungs- und Trackingverfahren mit synthetischen Daten, Master's Thesis TU Darmstadt, 2020

**Zec, E. L. et al.: Statistical Sensor Modelling for Autonomous Driving (2018)**

Zec, Edwin Listo; Mohammadiha, Nasser;; Schliep, Alexander: "Statistical Sensor Modelling for Autonomous Driving Using Autoregressive Input-Output HMMs," in: *2018 21st International Conference on Intelligent Transportation Systems (ITSC)*, 2018



# Own Publications

---

Wheeler, Tim Allan; **Holder, Martin Friedrich**; Winner, Hermann; Kochenderfer, Mykel John (2017): “Deep stochastic radar models” in: *2017 IEEE Intelligent Vehicles Symposium (IV)*, 2017

**Holder, Martin Friedrich**; Rosenberger, Philipp; Bert, Felix; Winner, Hermann (2018): “Data-driven Derivation of Requirements for a Lidar Sensor Model” in: *Grazer Symposium Virtuelles Fahrzeug*, 2018

**Holder, Martin Friedrich**; Rosenberger, Philipp; Winner, Hermann; D’hondt, Thomas; Makkapati, Vamsi Prakash; Maier, Michael; Schreiber, Helmut; Magosi, Zoltan; Slavik, Zora; Bringmann, Oliver; Rosenstiel, Wolfgang (2018): “Measurements revealing Challenges in Radar Sensor Modeling for Virtual Validation of Autonomous Driving” in: *2018 21st International Conference on Intelligent Transportation Systems (ITSC)*, 2018

Rosenberger, Philipp; **Holder, Martin Friedrich**; Zirulnik, Marina; Winner, Hermann (2018): “Analysis of Real World Sensor Behavior for Rising Fidelity of Physically Based Lidar Sensor Models” in: *2018 IEEE Intelligent Vehicles Symposium (IV)*, 2018

**Holder, Martin Friedrich**; Slavik, Zora; D’hondt, Thomas (2019): “Radar Signal Processing Chain for Sensor Model Development”, in: Leitner, Andrea; Watzenig, Daniel; Ibanez-Guzman, Javier (eds): *Validation and Verification of Automated Systems*, Springer International Publishing 2019

Rosenberger, Philipp; **Holder, Martin Friedrich**; Zofka, Mark Rene; Fleck, Tobias; D’hondt, Thomas; Wassermann, Benjaming; Prstek, Juraj (2019): “Functional Decomposition of Lidar Sensor Systems for Model Development”, in: Leitner, Andrea; Watzenig, Daniel; Ibanez-Guzman, Javier (eds): *Validation and Verification of Automated Systems*, Springer International Publishing 2019

**Holder, Martin Friedrich**; Linnhoff, Clemens; Rosenberger, Philipp; Winner, Hermann (2019): “The Fourier Tracing Approach for Modeling Automotive Radar Sensors” in: *2019 20th International Radar Symposium (IRS)*, 2019

**Holder, Martin Friedrich;** Linnhoff, Clemens; Rosenberger, Philipp; Popp, Christoph; Winner, Hermann (2019): “Modeling and Simulation of Radar Sensor Artifacts for Virtual Testing of Autonomous Driving” in: *9. Tagung Automatisiertes Fahren*, Lehrstuhl für Fahrzeugtechnik mit TÜV SÜD Akademie, 2019

**Holder, Martin Friedrich;** Hellwig, Sven; Winner, Hermann; (2019): “Real-Time Pose Graph SLAM based on Radar” in: *2019 IEEE Intelligent Vehicles Symposium (IV)*, 2019

Rosenberger, Philipp; **Holder, Martin Friedrich;** Huch, Sebastian; Winner, Hermann; Fleck, Tobias; Zofka, Marc Rene; Zöllner, Marius; D’hondt, Thomas (2019): “Benchmarking and Functional Decomposition of Automotive Lidar Sensor Models” in: *2019 IEEE Intelligent Vehicles Symposium (IV)*, 2019

Rosenberger, Philipp; Wendler, Jan Timo; **Holder, Martin Friedrich;** Linnhoff, Clemens; Berghöfer, Moritz; Winner, Hermann; (2019): “Towards a Generally Accepted Validation Methodology for Sensor Models - Challenges, Metrics, and First Results” in: *Grazer Symposium Virtuelles Fahrzeug*, 2019

**Holder, Martin Friedrich;** Thielmann, Jan; Rosenberger, Philipp; Linnhoff, Clemens; Winner, Hermann; (2020): “How to evaluate synthetic radar data? Lessons learned from finding driveable space in virtual environments” in: *13. Workshop Fahrerassistenzsysteme und automatisiertes Fahren*, 2020

Rosenberger, Philipp; **Holder, Martin Friedrich;** Cianciaruso, Nicodemo; Aust, Philip; Tamm-Morschel, Jonas Franz; Linnhoff, Clemens; Winner, Hermann; (2020): “Sequential lidar sensor system simulation: a modular approach for simulation-based safety validation of automated driving” in: *Automotive and Engine Technology*, 2020

Meister, David; **Holder, Martin Friedrich;** Winner, Hermann; (2020): “A Track-Before-Detect Approach to Multi-Target Tracking on Automotive Radar Sensor Data” in: *Late-Breaking Result at the 21st IFAC World Congress 2020*, 2020

# Supervised Student Theses

---

**Ackermann, Stefan:** “Systematic Analysis of Radar Tracking Algorithms”, Master’s Thesis, 2016

**Berger, Christian:** “Analysis of Algorithms for Lidar based Object Detection”, Master’s Thesis, 2017

**Bert, Felix:** “Identification of Applicable Lidar Feature for Object Detection with Learning Algorithms”, Independent research assignment, 2017

**Chen, Rui:** “Design and Implementation of a Closed-Loop Test Environment for the Realization and Evaluation of Driver Assistance Functions”, Master’s Thesis, 2017

**Chen, Gaoxiang:** “Development of a Calculation Tool for Secondary Surface Influence on Short Range Radar including verification and validation, Master’s Thesis, 2018

**Chen, Xing:** “Enhancement of a Software Tool for Annotation of Sensor Data”, Master’s Thesis, 2018

**Cram, Sophie:** “Conception of a proper Motion Estimator of a Perception Sensor”, Bachelor Thesis, 2017

**Gu, Penguri:** “Sensor Data Fusion for an Autonomous Driving Teaching Platform”, Master’s Thesis, 2018

**Hellwig, Sven:** “Development of a Radar SLAM Algorithm”, Master’s Thesis, 2018

**Hoyer, Tobias:** “Comparisons between Measured and Simulated RCS Profiles of Vehicles”, Bachelor Thesis, 2018

**Hu, Xiaojing:** “Investigations for Improvement of Backscattering Models for Radar Sensor Modeling”, Master’s Thesis, 2018

**Klingenstein, Markus:** “Analysis and Implementation of Thresholding- and Estimation Algorithms for Application in a Radar Simulation Model”, Master’s Thesis, 2019

**Knerr, Jonathan:** “Development of a Tracking Algorithm for a Lidar Sensor Model”, Master’s Thesis, 2017

- Krüger, Jonas:** “Learning Algorithms for Object Detection with Radar”, Master’s Thesis, 2018
- Leinberger, Moritz:** “Quantification of Uncertainties in Measurements with Automotive Radar with Applications in Automated Driving”, Bachelor Thesis, 2019
- Linnhoff, Clemens:** “Development of a Radar Sensor Model”, Master’s Thesis, 2018
- Lotz, Dominik:** “Machine learning on spectrum-level annotated synthetic radar data”, Master’s Thesis, 2020
- Makansi, Faried:** “Control Design of a Car Turntable”, Bachelor Thesis, 2017
- Mayer, Christoph:** ‘Investigations on using Deep Learning Algorithms in Radar Signal Processing”, Master’s Thesis, 2018
- Meister, David:** “Implementation of a Track-Before-Detect Algorithm for Synthetic and Real Radar Data for Sensor Model Assessment”, Master’s Thesis, 2019
- Müller, Till:** “Combined Prediction of Speed and Power in a Deep Learning Radar Model”, Bachelor Thesis, 2018
- Müller, Jochen:** “Construction and Development of a Test Stand for Identification of Radar Reflection Properties of Vehicles”, Master’s Thesis, 2017
- Ngo, Anthony:** “Enhancement of a Lidar Sensor Model for Simulation-based Development and Testing of Object Detection Algorithms”, Master’s Thesis, 2018
- Popp, Christoph:** “Development of a Method for Automatic Detection of Ghost- and Mirror-Targets in Automotive Radar”, Master’s Thesis, 2019
- Ruppert, Timm:** “Evaluation of the State of the Art of Automated Driving Functions Regarding the Transferability for the Darmstadt Tram System”, Master’s Thesis, 2017
- Scheiwe, Gunnar:** “Characterization of Radar Sensors for Autonomous Driving”, Bachelor Thesis, 2018
- Struck, Merten:** “Object Classification with Radar”, Master’s Thesis, 2019
- Stäcker, Lukas:** “Development of an Information System for Segmentation and Tracking of Objects based on Lidar Sensor Data for Autonomous Driving”, Master’s Thesis, 2017
- Thielmann, Jan:** “Analysis of Radar Sensor Model Accuracy by Stimulation of a Free Space Estimation Algorithm with Real and Simulated Sensor Data”, Master’s Thesis, 2019
- Yoon, Ji Su:** “Incorporating Speed Prediction into a Deep Stochastic Radar Model”, Master’s Thesis, 2017

---

**Zaman, Zahra:** “Stimulation of Radar Object Detection and Tracking with Synthetic Data”, Master’s Thesis, 2020

**Zirulnik, Marina:** “Analysis of Multiple Distance Measurement Characteristics and Noise Behavior of Automotive Lidar Sensors”, Master’s Thesis, 2017



# Danksagung

---

Die Erstellung dieser Arbeit während meiner Zeit als wissenschaftlicher Mitarbeiter am Fachgebiet Fahrzeugtechnik der Technischen Universität Darmstadt wurde von vielen Menschen begleitet und ermöglicht, denen ich einige Dankesworte widmen möchte.

Ich bedanke mich bei Prof. Dr. rer. nat. Hermann Winner für die Betreuung meiner Promotion. Wie auch alle anderen Arbeiten bei FZD profitierte meine Arbeit ungemein vom intensivem Gedankenaustausch mit Ihnen und Ihrem kritischen Feedback, das zum weiteren Nachdenken anregt, auch wenn hierzu Ausflüge in den Frequenzraum nicht immer zu vermeiden sind.

Herrn Prof. Dr.-Ing. Erwin Biebl von der Technischen Universität München danke ich für die Übernahme des Koreferates und den damit verbundenen fachlichen Diskussionen zu meiner Arbeit.

Ich bedanke mich bei allen "FZD"lern für das tolle Arbeitsklima und die vielen gemeinsamen Erlebnissen, die diese Zeit unvergesslich machen. Ein besonderer Dank spreche ich den anderen "Sensenheinis" nämlich Philipp Rosenberger, Clemens Linnhoff und Nicodemo Cianciaruso aus. Als Sparring Partner profitierten wir sehr viel voneinander und konnten uns stets über unsere Ideen austauschen, nicht nur über sensortechnische Dinge. Das hat dieser Zeit bei FZD eine besondere Qualität gegeben.

Im Laufe der Zeit hatte ich das Glück eine Vielzahl von sehr begabten Studierenden als Bachelor-, Masterarbeiter, oder ADPLer betreuen zu können. Es bereitete mir stets große Freude mit euch an Problemen zu knobeln, Ideen zu entwickeln, eure Zuarbeiten einzupflegen und Inspiration aus euren Arbeiten ziehen zu können. Allen meinen Studis gebührt mein ausdrücklicher Dank.

Für ihren langjährigen und unermüdlichen Einsatz als Hiwi bedanke ich mich bei Tobias Homolla, Sebastian Raab, Albert Schrotschneider, Hanyu Sun, Christoph Stähler und Hatéf Tahvildari. Durch eure hohe Motivation und euer Talent habt ihr in vielerlei Hinsicht wichtige Beiträge für das Gelingen dieser Arbeit geleistet.

Auf Seiten der ADC Automotive Distance Control Systems GmbH bedanke ich mich bei Rainer Aue, Dr.-Ing. Markus Wintermantel, Dr.-Ing. Thomas Breitenberger, und Dirk Ulbricht für den regelmäßigen Austausch rund um Radarsensoren und deren Simulation.

Dem Bundesministerium für Wirtschaft und Energie bzw. dem Bundesministerium für Bildung und Forschung danke ich für die Förderung der Forschungsprojekte PEGASUS, SET Level4to5 sowie ENABLE-S3 wodurch sich für mich, aber auch für viele andere Doktoranden erst die Möglichkeit zur Promotion ergab.

Auch möchte ich mich beim Deutschen Akademischen Auslandsdienst für die Ermöglichung meines Forschungsaufenthaltes am Stanford Intelligent Systems Lab bedanken. Ich bin sehr glücklich über die fachlichen und persönlichen Horizonterweiterungen, die ich während meines Aufenthaltes bei Prof. Mykel Kochenderfer, dem ich ebenfalls für die vielen wichtigen Denkanstöße für meine Forschung verdanke, und im Silicon Valley machen konnte.

Schließlich bedanke ich mich bei meiner Familie, meiner Mutter Hildegard, meinem Vater Manfred und meiner Schwester Angelika, die meinen akademischen Ausbildungsweg, egal ob in Darmstadt, Göteborg oder Stanford unterstützt und mich in meinen Entscheidungen ermutigt haben. Ich bin froh, dass ich dank eurer Unterstützung den Weg, den ich eingeschlagen habe, nun mit Erfolg zu Ende bringen konnte.

Der größte Dank gebührt meiner Partnerin Frauke, die mich bei allen Etappen seit dem Bachelorstudium durch Höhen und Tiefen begleitet. Insbesondere während der Fertigstellung dieser Dissertation hast du eine besondere Last auf dich genommen um mir den Rücken freizuhalten. Ohne deine Unterstützung und deinen Rückhalt hätte ich meine Ziele nie erreichen können. Ich bin sehr froh dich an meiner Seite zu haben.

Darmstadt, im November 2020